



Máster Universitario en Ingeniería Industrial

Trabajo Fin de Máster

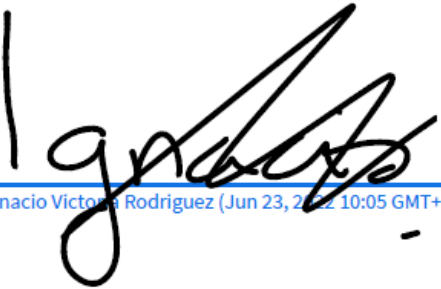
Modelling of gear surface roughness impact on electrified
transmissions' efficiency

Ignacio Victoria Rodríguez

Supervisor:
Foteini Xanthi

Madrid
June de 2022

Declaro, bajo mi responsabilidad, que el Proyecto presentado con el título “Modelling of gear surface roughness impact on electrified transmissions’ efficiency” en la ETS de Ingeniería - ICAI de la Universidad Pontificia Comillas en el curso académico 2021/22 es de mi autoría, original e inédito y no ha sido presentado con anterioridad a otros efectos. El Proyecto no es plagio de otro, ni total ni parcialmente y la información que ha sido tomada de otros documentos está debidamente referenciada.




Ignacio Victoria Rodríguez (Jun 23, 2022 10:05 GMT+2)

Fdo.: Ignacio Victoria Rodríguez

Fecha: 24/06/2022

Autorizada la entrega del proyecto
EL DIRECTOR DEL PROYECTO



Foteini Xanthi (Jun 23, 2022 09:59 GMT+2)

Fdo.: Foteini Xanthi

Fecha: 24/06/2022

MODELLING OF GEAR SURFACE ROUGHNESS IMPACT ON ELECTRIFIED TRANSMISSIONS' EFFICIENCY

Autor: Victoria Rodríguez, Ignacio

Director: Xanthi, Foteini

Entidad Colaboradora: Volvo Car Corporation

Resumen ejecutivo

A. Introducción

La motivación detrás de este proyecto era entender como la rugosidad de las superficies de los engranajes afecta su rendimiento al engranar. En pos de este objetivo, se construyó una herramienta capaz de predecir y analizar el contacto entre superficies rugosas de los dientes de los engranajes; el régimen de lubricación, así como la estimación del espesor de la capa de lubricante; las fuerzas de fricción y resistencia de rodadura. Finalmente, se computa la deformación de las superficies, calentamiento debido a la fricción y se analizan los parámetros de rugosidad más representativos para generar superficies con modelos de aprendizaje supervisado.

B. Cuestiones principales

Durante el transcurso de esta investigación hubo una pregunta que surgió muy temprano: ¿Puede una superficie predecirse a partir de un set de parámetros? Por lo tanto, una parte de los esfuerzos de investigación se dirigieron hacia ésta. En otras palabras, la pregunta principal a resolver era:

- ¿Cuál es la relación entre la superficie y el rendimiento (eficiencia y gripado) en el engrane de dos ruedas dentadas?

De esta pregunta se derivaron otras tres:

- ¿Cuáles son los mecanismos de lubricación para un lubricante cualquiera y cómo pueden predecirse de una manera precisa?
- ¿Puede el comportamiento de una superficie modelarse de manera precisa bajo distintos regímenes de lubricación?
- ¿Puede una superficie ser caracterizada por una pequeña lista de parámetros?

C. Motivación

La motivación de este proyecto puede explicarse muy brevemente con la creciente importancia del diseño al detalle de engranajes ya que las transmisiones eléctricas disponen de menos elementos que sus equivalentes térmicas y, por lo tanto, efectos que antes se perdían en las inestabilidades del sistema ganan relevancia.

D. Estado del Arte

Esta sección contiene un breve resumen de la literatura revisada para comenzar este proyecto:

a. Modelos de contacto sin lubricación

Primero, se desarrolló una herramienta basada en las teorías de Lamé. Ésta se refinó hasta alcanzar el modelo de contacto rugoso en seco de las referencias (Sosa, 2017) and (L. Xiao, 2007).

Éstas desarrollan el método propuesto en (Björklund, 1995) para un contacto plano y semi-elíptico, considerando ambas superficies deformables. La deformación superficial puede expresarse como:

$$\bar{u}_{zi} = \frac{1}{\pi E^*} \sum_{j=1}^n C_{ij} p_j$$

Donde \bar{u}_{zi} es el vector de deformaciones perpendiculares a la superficie i , mientras que C_{ij} es la matriz de rigidez de la población superficial y p_j es vector de estrés originado por el contacto con la superficie j . En tanto que, la matriz de rigidez puede describirse como:

$$C_{ij} = (x_{\Delta} - a_L) \left[\ln \left(\frac{x_{\Delta} - a_L}{a_L} \right) \right]^2 - (x_{\Delta} + a_L) \left[\ln \left(\frac{x_{\Delta} + a_L}{a_L} \right) \right]^2 + C_o$$

$$x_{\Delta} = |x_i - x_j|$$

Donde a_L es la mitad del tamaño de un diferencial; x_{Δ} es el valor absoluto de la diferencia de coordenadas en el eje de las abscisas, relacionando todos los puntos de la superficie i con todos los puntos de la superficie j , de tal manera que sólo en la diagonal principal x_{Δ} es nulo. Por último, C_o es un valor arbitrario no detallado en la referencia, por lo tanto, se tomó como nulo. Así mismo, el campo de presiones en sendos materiales se describe como:

$$\bar{p} = \pi E^* C^{-1} (\delta - \bar{h})$$

Siendo \bar{p} el estrés a lo largo del contacto, \bar{h} es un vector que contiene las diferencias discretas de las alturas entre ambas superficies y δ es la penetración de una superficie en otra (Sosa, 2017). Esta definición es compatible con solucionadores numéricos.

Por lo tanto, la fuerza en el contacto es, inevitablemente:

$$F_C = \int \bar{p} dx$$

En la referencia (Sosa, 2017) también se demuestra que el estrés cortante:

$$\tau_i = -\frac{p_i}{a} (z - z^2(a^2 + z^2)^{-\frac{1}{2}})$$

Esto permite reducir el coste computacional, teniendo un máximo en $z=a$ donde el estrés cortante subsuperficial será un 20.7% del estrés de contacto, siguiendo el contorno del mismo.

La novedad introducida en esta sección radica en la reconversión de contacto plano y semi-elíptico para aceptar 2 superficies genéricas, pudiendo así aceptar 2 superficies rugosas.

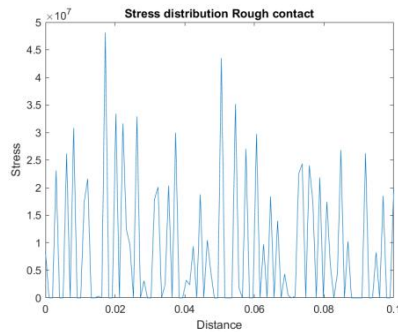


Ilustración Resumen 1 Estrés de contacto

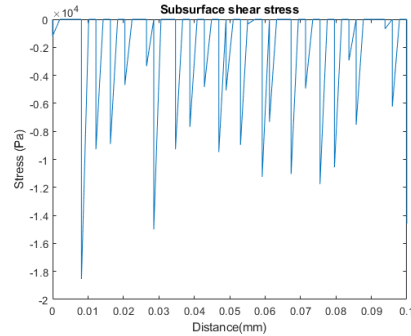


Ilustración Resumen 2 Estrés cortante subsuperficial

b. Resistencia de rodadura y fricción

Las fuerzas cortantes actuando sobre las superficies (como resultado de la rotación del diente con respecto al lubricante) se puede calcular usando la base de fórmulas clásicas de fluidos newtonianos con flujo turbulento como en (Wei, 2015):

$$\tau = \mu \frac{\partial u}{\partial h} - \frac{1}{2} h(x) \frac{\partial p(x)}{\partial x}$$

Donde τ es el estrés cortante y $\frac{\partial u}{\partial h}$ es la derivada del campo de velocidades en el fluido respecto a la altura mientras que el segundo término describe el efecto de la turbulencia.

En lugar de estudiar el contacto en cada diferencial de la superficie, junto los errores que ello puede conllevar, una convergencia a nivel global se puede encontrar en (al H. e., 2007), donde la fuerza de fricción y la resistencia a la rodadura se describen (en contactos bola-disco):

$$F_s = \mu * F_C$$

$$F_r = \frac{4.318 \varphi_T (\tilde{G} \tilde{U})^{0.658} \tilde{Q}^{0.0126} R}{\alpha}$$

Donde F_r es la resistencia a la rodadura; φ_T es el factor de reducción térmico para compensar el incremento de temperatura a altas velocidades (al H. e., 2007). Sin embargo, la definición de este factor no se da en la referencia (al H. e., 2007) sí que se discute en detalle en (Chapter 2: Overall Methodology, 2005). \tilde{G} es el parámetro adimensional del material; \tilde{U} es la velocidad adimensional; \tilde{Q} es la carga adimensional y α es el coeficiente presión-viscosidad. F_s es la fuerza de fricción, μ es el coeficiente de fricción y F_C es la normal.

En esta publicación (al H. e., 2007), el coeficiente de fricción del lubricante se describe con una precisión del 94% y el error global del modelo es inferior al 0.1%. La aproximación al coeficiente de fricción proviene de las ecuaciones (al H. e., 2007):

$$\begin{cases} \mu = e^{f(SR, P_h, \nu_o, S)} P_h^{b_2} |SR|^{b_3} V_e^{b_6} \nu_o^{b_7} R^{b_8} \\ f(SR, P_h, \nu_o, S) = b_1 + b_4 |SR| P_h \log_{10}(\nu_o) + b_5 e^{-|SR| P_h \log_{10}(\nu_o)} + b_9 e^S \end{cases}$$

Donde μ es el coeficiente de fricción; SR es el ratio rodadura-deslizamiento en el engrane, P_h es la máxima presión de Hertz en el contacto; ν_o es la viscosidad absoluta (en cPs) a la temperatura de entrada del lubricante; V_e es la velocidad de arrastre; R es el radio equivalente del contacto; S es el RMS equivalente de la rugosidad mientras que $b_i \mid i = 1, 2, \dots, 9$ pertenecen a un vector derivado de la regresión lineal de las propiedades del lubricante, el cual, en la referencia (al H. e., 2007) se describe como el aceite estándar en test FZG.

Esto permite adaptar el coeficiente de fricción a las características del contacto el cualquier momento, por lo tanto, mitigando los efectos dinámicos ya que este modelo depende de una concatenación de simulaciones estáticas.

La novedad aportada por esta sección es la aplicación en un sistema de coordenadas rotado, ya que la formulación considera una vista perpendicular al contacto, mientras que este proyecto considera la aplicación pormenorizada a cada elemento de la superficie. Así mismo, y basándose en la referencia (Pandurangi, 2020) se definió un algoritmo propio para extrapolar las propiedades de los lubricantes empleados, más allá del de referencia aportado por FZG.

c. Régimen de lubricación

Un elemento crucial a la hora de desarrollar herramientas para el estudio de los contactos son los regímenes de lubricación. Existen 3 principales:

- Lubricación elastohidrodinámica (“EHL” por sus siglas en inglés “Elastohydrodynamic lubrication”): Las superficies no están en contacto directo, existe una fina capa de lubricante entre ambas. Suele ser el objetivo en todo proceso de diseño ya que previene el gripado de las superficies. Está asociado con un incremento del coeficiente de fricción.
- Lubricación mixta (“ML” por sus siglas en inglés “Mixed lubrication”): Existe contacto entre ambas superficies, aunque limitado, habiendo contacto metal-metal en ciertos puntos. Está asociado con un decremento del coeficiente de fricción.
- Lubricación límite (“BL” por sus siglas en inglés “Boundary lubrication”): Hay principalmente contacto directo entre las superficies, con pequeños depósitos de lubricante debido a las imperfecciones de la superficie. Presenta un coeficiente de fricción constante.

Como se puede ver en la curva de Stribek en la Ilustración Resumen 3, el régimen de lubricación es extremadamente sensible a las propiedades del lubricante (Wang, 2013). El estudio contenido en (Jonny Hansen, 2021) también indica que la rugosidad y deformación de las superficies afectan al régimen de lubricación. En dicha publicación, se propone un nuevo estimador de estado, Λ^* , dicho parámetro predice un 60-80% de participación de EHL en ML para cualquier contacto bola-disco y predijo con correctamente el 100% EHL cuando se evaluó un contacto con lubricación completa.

Este estimador, Λ^* , consideraba la rugosidad de superficies reales de ingeniería, aunque, no bilateralmente deformables, considerando una superficie perfectamente plana e infinitamente rígida contra una superficie rugosa y deformable (Jonny Hansen, 2021). Se adaptó de la referencia (Jonny Hansen, 2021) para aceptar una pareja de engranajes con superficies deformables y rugosas:

$$\Lambda^* = \frac{h^*}{S_{pk}}$$

En la ecuación superior Λ^* es el ya mencionado estimador del régimen de lubricación donde $\Lambda^* \geq 1$ implica EHL mientras que $\Lambda^* < 1$ implica ML o BL. La separación total de las superficies es h^* y la máxima altura del perfil rugoso es S_{pk} . Además, en la publicación (Jonny Hansen, 2021), los autores dedican especial interés a redefinir este parámetro h^* en función de parámetros tradicionales de EHL, llegando a:

$$h^* = h_m + h_c f_q$$

Al modificar la formulación para superficies de engranajes, los radios $R'_{y,b}$ y R'_y son ∞ ya que los engranajes en la dirección de engrane representan circunferencias equivalentes con centros colineales en la línea de presión mientras que en la dirección perpendicular son una línea recta, y, por lo tanto, una circunferencia de radio infinito, lo cual permite simplificar las ecuaciones a (reduciendo en el proceso el coste computacional):

$$h_m = 3.63U^{0.68}G^{0.49}W^{-0.073}$$

$$h_c = 2.69U^{0.67}G^{0.53}W^{-0.067}$$

$$f_q = \left(\frac{R'_{x,a}}{R'_{x,b}} \right)^\alpha \left(1 - \gamma_1 e^{-\gamma_2 \left(\frac{R'_{y,a}}{R'_{x,a}} \right)^{\gamma_3}} \right)$$

En estas ecuaciones, los parámetros α , γ_1 , γ_2 y γ_3 dependen de la direccionalidad de la rugosidad de la superficie con respecto a la dirección de engrane; U , G y W son las ya mencionadas velocidad, material y carga adimensional respectivamente. La variable X es el exponente correspondiente a la velocidad adimensional en cada ecuación. La variable R' representa los radios efectivos en varias direcciones, donde los subíndices x e y representan la dirección de engrane y su perpendicular, respectivamente, así mismo, a y b representan el radio de las asperidades superficiales y el radio de la superficie respectivamente (cuando no se muestran los subíndices a o b , la variable hace referencia a la superficie perfecta de referencia).

La novedad introducida en esta sección reside en la adaptación del estimador EHL a geometrías de dientes de engranajes y la adaptación de un modelo sólido deformable contra un plano infinitamente rígido a una configuración con superficies deformables bilateralmente.

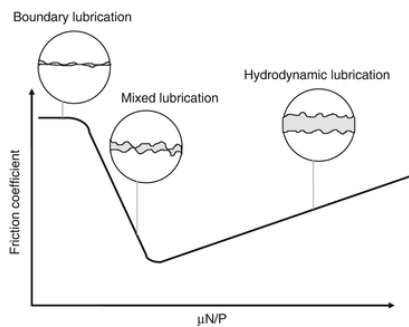


Ilustración Resumen 3 Curva de Stribeck (Wang, 2013)

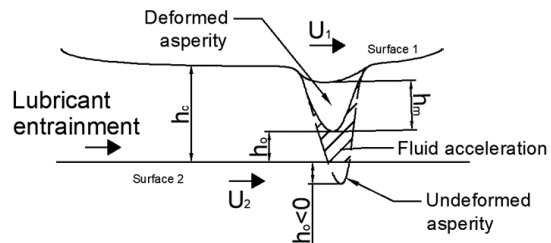


Ilustración Resumen 4 Lubricación EHL

d. Presión a través de la película de fluido

Las aproximaciones de película de lubricantes aceptan la ecuación de Reynold, una simplificación de las ecuaciones de Navier-Stokes donde se asume que una de las tres dimensiones espaciales es despreciable, aunque, en engranajes de transmisiones en el sector de la automoción, debido a su pequeño módulo, al comenzar el engrane, esto no es necesariamente cierto. Además, en ciertas transmisiones, el ancho del diente puede llegar a ser sólo un par de módulos, siendo por lo tanto dos dimensiones espaciales con un orden de magnitud similar, lo cual, en la fase de aproximación puede hacer que a altura del fluido sea comparable a las otras dos dimensiones. Por lo tanto, se procedió a revisar una solución basada en Navier-Stokes.

Así mismo, la ecuación de Reynold asume que la distribución de presión a lo largo de la película es uniforme (lo cual se quiso evitar desde un primer momento).

Otro elemento clave a la hora de descartar este formato de dinámica de fluidos aplicada proviene de la referencia (C-Therm, 2022). En esta tesis doctoral el autor explica cómo el elemento principal a la hora de determinar el coeficiente de fricción es la capa límite. Dicha capa límite es, además, increíblemente sensible a la composición química del lubricante y condiciones previas, principalmente la rugosidad superficial resultante de diferentes procesos de manufactura, incluyendo liberación de viruta, bruñido y lijado, por lo tanto, no se pueden aceptar de base las simplificaciones de la ecuación de Reynold.

e. Efectos térmicos

Es de sobra sabido que superficies en contacto tienden a calentarse debido a la fricción. Este incremento de temperatura es conocido en la literatura anglosajona como “flash temperature” o temperatura instantánea en castellano (Rowe, 2014). De tal modo que la temperatura superficial puede ser descrita como:

$$T_i = T_b + \Delta T$$

Donde T_i es la temperatura superficial; T_b es la temperatura del núcleo y ΔT es el incremento de temperatura instantáneo.

Dado que el modelo se basa en diferenciales verticales deformables, el problema puede dividirse en 2 tipos de transmisión de calor: conducción en el contacto directo y convección en el lubricante.

El incremento instantáneo de temperatura debido al contacto directo es:

$$T_f = \frac{q + T_{b1}R_2 + T_{b2}R_1}{R_1 + R_2}$$

Donde q es el calor generado por la fricción ($q = v_s * \mu W$); R_i es la resistencia térmica a la conducción y los subíndices 1,2 corresponden a cada superficie respectivamente. Esta resistencia sigue la fórmula (C-Therm, 2022):

$$R = \frac{L}{Ak}$$

Tal que L es la longitud (en esta aplicación la longitud de un diferencial de superficie), A es el área de transferencia (área de un diferencial) y k es la conductividad térmica del material.

No se consideró una resistencia de contacto ya que por definición representa la dificultad de transmisión del calor entre 2 superficies debido al área de contacto siendo menor que la nominal (Ishizaki & Nagano, 2020). Dado que el código sólo aplica estas ecuaciones cuando hay contacto directo se pueden obviar. Esta definición se corresponde también con los hallazgos detallados en (Kadiric P. R., 2019) donde la temperatura en la superficie depende del deslizamiento.

Para desarrollar la temperatura instantánea en diferenciales lubricados, se revisaron las propuestas de (Zhou, Xing, & Hu, 2021) y se implementaron. En esta publicación, el flujo de calor a través

de un diente de engranaje se divide en diferenciales circulares a lo largo de la altura del diente y se resuelven un conjunto de sistemas de transmisión lineares, ver Ilustración Resumen 5. En este artículo (Zhou, Xing, & Hu, 2021), su nuevo modelo fue comparado con el modelo de Blok y el modelo ISO con buenos resultados. Por lo tanto, el problema se puede describir siguiendo el símil eléctrico:

$$T_f - T_b = \frac{Q}{A} \left(\frac{1}{h_1} + \frac{L}{k_s} + \frac{1}{h_2} \right) \quad h_m = 0.288Re^{0.731}Pr^{1/3} * \frac{k_f}{d_i}$$

Donde Pr es el número de Prandtl. Y, por lo tanto, la temperatura instantánea es:

$$T_f = T_{bi} + \frac{Q_i}{A} \left(\frac{2}{h_i} + \frac{L}{k_s} \right)$$

Donde los subíndices i representan cada superficie. Siguiendo (Masse, 2019) el reparto de calor entre ambas superficies sigue las ecuaciones:

$$\begin{aligned} T_{b1} - T_{b2} &= \frac{h}{2k_f} (1 - 2\vartheta)Q \quad | \quad h = h_1 + h_2 \\ Q_1 &= \vartheta Q \\ Q_2 &= (1 - \vartheta)Q \end{aligned}$$

Tal que ϑ es la fracción de calor absorbido por la superficie 1.

La novedad aportada en esta sección es la reformulación del problema de transferencia de calor, operando como pseudo-transitorio superponiendo configuraciones estáticas.

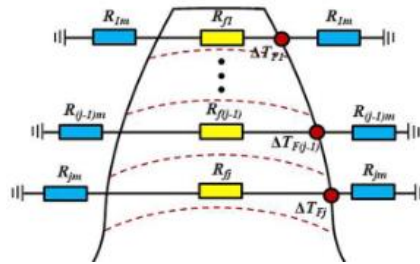


Ilustración Resumen 5 Aproximación de la transferencia de calor a través de un diente de engranaje (Zhou, Xing, & Hu, 2021)

f. Generación de las superficies

El objetivo principal de este proyecto era estudiar el impacto de la rugosidad superficial en la eficiencia y como dicha rugosidad puede ser caracterizada de una manera adecuada por los parámetros de rugosidad para estudiar como varía en manufactura y operación.

Esta sección contiene todas modificaciones a los modelos revisados y propuestos, así como desarrollos propios ad hoc. Para realizar este estudio, primero se realizó una preselección de modelos basándose en el estado del arte. Los modelos considerados son:

- Redes Neuronales Recurrentes (“Recurrent Neural Networks”, RNN)
- Redes Generativas Antagónicas (“Generative Adversarial Networks”, GAN)
- Regresión lineal multivariable
- Regresión de Procesos Gaussianos (“Gaussian Process Regression”, GPR)

Tanto las RNN como las GAN son redes neuronales empleadas comúnmente para la clasificación y generación de imágenes, pero, como se explica en (Fumo, 2017) y (Brownlee, Machine Learning Mastery, 2019) admiten regresiones secuencia-secuencia. La gran diferencia entre ambas son sus operaciones internas. Las RNN admiten un módulo de memoria interna capaz de retener los datos más relevantes de las entradas y de las iteraciones anteriores. Dicho módulo se

conoce como Memoria Corta de Larga duración (“Long-Short Term Memory”, LSTM). Dicho modulo se conoce como Memoria Corta de Larga duración (“Long-Short Term Memory”, LSTM). Esta célula puede generar una salida o iterar sobre sí misma, realizando siempre la misma operación, de ahí el recurrente”. Para entrenar y validar la red se empleó la técnica de retro propagación (“backpropagation”), la cual consiste en recorrer la red en sentido inverso, obteniendo la entrada original de su salida, en otras palabras, verificando la biyectividad de la red (Donges, 2021).

Las redes GANs por otro lado se basan en el juego del gato y el ratón, o juego de ganancia nula entre 2 redes opuestas (Brownlee, Machine Learning Mastery, 2019). Se las conoce comúnmente como Generador (identificador a secuencia) y el Discriminador (secuencia a etiqueta). Basándose en los mismos datos, ambas redes compiten, el Generador busca crear datos falsos que parezcan realistas y el Discriminador descubrir cuales son reales y cuales son falsos, creados por el Generador (al I. G., 2014). Compiten en cada generación y quien pierda recibe una ronda adicional de entrenamiento. Normalmente, una vez el Generador ha sido entrenado el Discriminador es descartado (Hui, 2018). Pese a que las GANs suelen usarse para generar o mejorar imágenes a partir de etiquetas existen varios ejemplos de GANs aplicadas a secuencias de números y generadores de número aleatorios según (Rocca, 2019) y (Marcello De Bernardi, 2018).

Las otras dos alternativas caen en la categoría de “machine learning” siendo la regresión multivariable la más simple de las dos alternativas con una formulación de sobra conocida. Si mayor desafío es la necesidad de predefinir las variables a estudiar y el orden de magnitud de éstas, siendo, por lo tanto, un estudio paramétrico (Williams, 2010). Además, se eliminaría la aleatoriedad de cualquier valor dado que siempre generará una salida del tipo $Y = f(X)$ (Tim, 2017), por consiguiente, toda superficie generada por este método será siempre igual (si disponen de las mismas entradas) a menos que se acepte un valor aleatorio dentro de los intervalos de confianza.

Las regresiones lineales no son la mejor herramienta para lidiar con grandes cantidades de datos con mucho ruido y sin una estructura clara, centrada entorno al cero, como en las muestras presentadas por (James, 2020), ya que los intervalos de confianza se ajustarán a la regresión y excluirán parte de los datos reales

Por último, los GPRs son regresiones no paramétricas, por lo tanto, en lugar de calcular la distribución de probabilidad de una distribución de un parámetro, calcula la probabilidad de todas las posibles funciones con dicho parámetro (Sit, 2019) y as compara con los datos, calculando así, la probabilidad a posteriori, basándose en probabilidad bayesiana. Gracias a la probabilidad asociada a cada función generada, se puede calcular tanto la media de las funciones como los intervalos de confianza en cada punto de la función (Optimization Geeks, 2021). En otras palabras, los métodos GPR cubren los datos con una manta y los kernels, o covarianzas, le dan mayor flexibilidad para adaptarse a los datos, estudiando después si es factible dicha forma.

Ambas redes neuronales fueron descartadas dado que funcionan como cajas negras, es imposible saber exactamente qué ocurre en su interior mientras que la regresión multivariable no es lo suficientemente flexible para estos datos, por lo tanto, se estudiarán GPR con varios kernels.

La novedad aquí introducida es el uso de GPRs para modelar regresiones de parámetros superficiales y su relevancia en lugar de un problema de clasificación típico.

E. Implementación

Esta sección resume la implementación de los distintos módulos y su adaptación al código.

a. Funcionamiento interno

Primero, el modelo estima el coeficiente de fricción, seguido del régimen de lubricación, el cual determina qué solucionador se empleará. Si se ha determinado EHL completo (el cual se sabe de

la literatura siempre preciso) las superficies no estarán en contacto y habrá una pequeña película de lubricante entre ambas superficies, con un espesor mínimo $h_o = h^*$, lo cual generará un campo de presiones en el fluido y actuando sobre ambas superficies (solucionador algebraico). El deslizamiento y la resistencia a la rodadura se distribuirán de manera uniforme ya que lo único actuando sobre las superficies es dicha película de lubricante.

Si, sin embargo, las ecuaciones de lubricación predicen ML o BL, se empleará un solucionador numérico basado en el modelo de contacto rugoso ya mencionado. Este solucionador presiona una superficie contra la otra, empleando la matriz de rigidez para estimar la tensión superficial, a la vez que calcula la presión del fluido extraída de las ecuaciones de Navier-Stokes (donde haya fluido). La suma de la tensión y la presión se integra a lo largo de la superficie para calcular la fuerza de contacto. Se itera hasta que las fuerzas convergen. En paralelo, otros efectos son estudiados e implementados, obteniendo la deformación superficial y eficiencia, como se puede apreciar en la siguiente imagen:

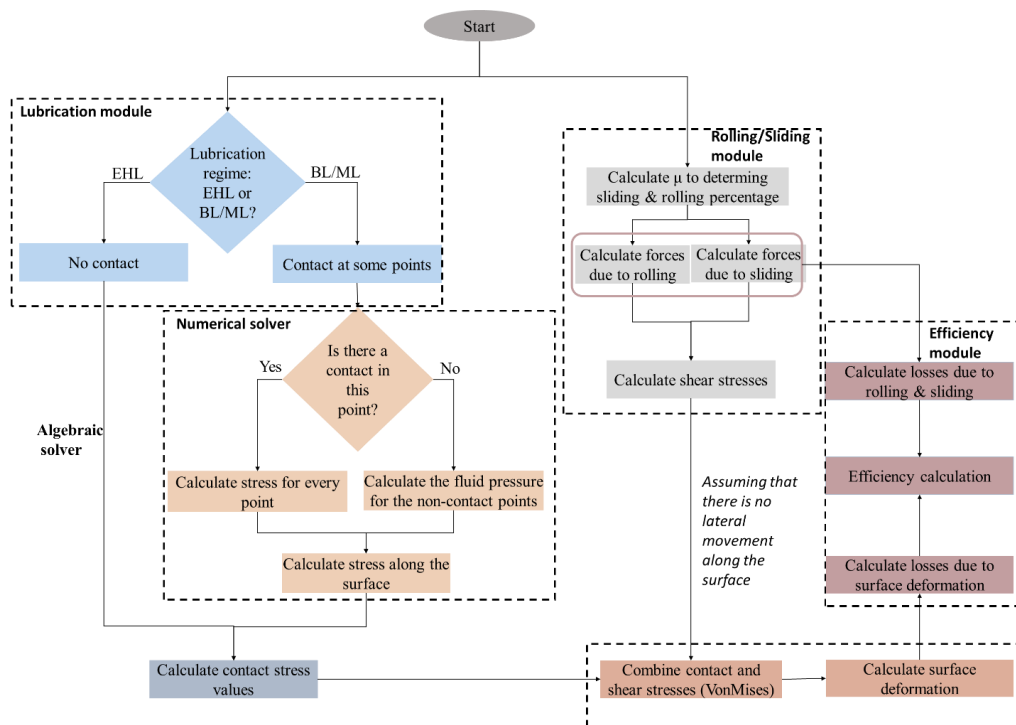


Ilustración Resumen 6 Diagrama de bloques del modelado

Independientemente del solucionar, el modelo procede a calcular la eficiencia (añadiendo las pérdidas por deformación plástica, deslizamiento y rodadura) del contacto, así como otras salidas tales como el momento transmitido, con la fórmula:

$$M_2 = \frac{M_1 \omega_1}{\omega_2} \eta$$

Donde M_2 es el momento de salida; M_1 es el momento de entrada; ω_2 es la velocidad angular de salida; ω_1 es la velocidad de rotación de entrada y η es la eficiencia.

b. Eficiencia

Las pérdidas por rozamiento y agitación del lubricante, aunque estudiadas en la Memoria, no se implementaron ya que son en sí externas al proceso de engrane.

Las pérdidas por deslizamiento y rodadura se describen como:

$$P_\mu = F_s V_s$$

$$P_r = F_r V_e$$

Donde P_μ son las pérdidas debidas a la fricción (F_s) y es dependiente de la velocidad de deslizamiento entre los dientes de los engranajes (V_s), mientras que las perdidas por rodadura dependen de la resistencia de rodadura (F_r) y de la velocidad de engrane (V_e).

La fórmula de las pérdidas por deformación plástica es:

$$P_{si} = \frac{\iint \sigma \delta \cdot ds}{T} \rightarrow \frac{\sigma \delta a^2}{T}$$

Donde P_{si} son las pérdidas por deformación plástica de la superficie i , σ es la tensión equivalente de Von-Mises, la cual puede ser plástica o elástica, δ es la profundidad de deformación en cada punto y T es el periodo de rotación de los engranajes. La formulación teórica con la integral de superficie se sustituyó en el código con la energía de deformación de cada diferencial (diferenciales cuadrados de lado a) para respetar el modelo de contacto rugoso

Por lo tanto, la eficiencia se calcula como:

$$\eta = \frac{M_1 \omega_1 - P_\mu - P_r - P_{s1} - P_{s2}}{M_1 \omega_1}$$

c. Esfuerzos cortantes & asignación de presiones

En el modelo bidimensional de superficies rugosas deformables, la presión del fluido y otras fuerzas actuando sobre la superficie se aplican de manera diferente en función de la lubricación.

Cuando existe EHL complete, la presión del fluido se aplica a ambas superficies siguiendo la solución aproximada de Navier-Stokes, por lo tanto $\sigma = P(r, \theta, \omega_1, \omega_2, \mu, \rho, R_b, h)$ en cada punto de las líneas de superficie, considerando así la variación de presión en el fluido. La tensión cortante debida al deslizamiento y la rodadura se reparten de manera uniforme a lo largo de la superficie ya que el fluido actúa de igual manera sobre la misma (salvo por variaciones de altura).

Si existe BL o ML, el solucionador numérico ya considera los efectos de la presión debidos a la aproximación de Navier-Stokes. Donde existe contacto directo entre las superficies el reparto de deslizamiento y rodadura varía, de tal modo que la rodadura se aplica sólo donde hay contacto directo y el deslizamiento donde hay fluido entre medias (y por lo tanto efecto de la presión también). En los puntos de contacto directo se aplica un deslizamiento de contacto metal-metal, por lo tanto, el reparto entre diferenciales sigue la lógica de convergencia:

$$F_m = \sum \mu_m a^2 w_{con} \quad F_{s_{no}} = \sum \mu a^2 w_{no} \quad F_s = F_{s_{no}} + F_m$$

Donde F_m es el deslizamiento metal-metal, con su coeficiente de fricción, μ_m y w_{con} es la tensión que experimenta cada diferencial en contacto directo. Por otra parte, $F_{s_{no}}$ representa la fricción de elementos lubricados y depende del tamaño del diferencial, a , el coeficiente de fricción del fluido μ y la tensión de cada diferencial lubricado w_{no} . Asegurando que se cumplen los valores predichos por los modelos macroscópicos precisos de la literatura.

d. Implementación de Navier-Stokes

La solución se basa en la aproximación de 2 dientes engranando a dos cilindros rotando, ver Ilustración Resumen 7. Las simplificaciones aceptadas son:

$$\begin{aligned} u_z &= 0 & \frac{\partial^i u_r}{\partial z^i} &= 0 \mid i \in \mathbb{N} \\ \frac{\partial u_i}{\partial t} &= 0 \mid i \in [\vec{r}, \vec{\theta}, \vec{z}] & \frac{\partial^i u_\theta}{\partial z^i} &= 0 \mid i \in \mathbb{N} \\ \vec{g} &= \begin{bmatrix} 0 \\ 3 \times 1 \end{bmatrix} \end{aligned}$$

Estas simplificaciones implican que el fluido no se mueve a lo largo del ancho del diente, lo cual en sí es falso, pero permite modelar el movimiento del fluido a lo largo del engrane de manera más simple. La velocidad en los ejes \vec{r} y $\vec{\theta}$ como independientes de \vec{z} permite solventar el problema como bidimensional, completamente desacoplado en los ejes \vec{r} y $\vec{\theta}$, lo cual representa presión uniforme en las capas de fluido, lo cual, debido a la rugosidad, permite obtener diferentes presiones para puntos con los mismos \vec{r} y $\vec{\theta}$, respetando así la configuración pseudotrídimensional del problema propuesto.

Al considerar que la velocidad del fluido depende tanto del ángulo como del radio permite calcular la compresión a medida que el fluido entra en el engrane, así que 2 puntos en la misma circunferencia podrían tener diferentes presiones ya que tendrían diferentes ángulos, y, por lo tanto, el fluido no se comporta de manera laminar, lo cual sería una definición pobre.

Los efectos de la gravedad se ignoraron en todo el modelo ya que la base del mismo la proveerá el modelo de lubricación calculado.

Efectos dependientes del tiempo fueron ignorados ya que complicarían en demasía el modelo y aumentarían el coste computacional sin añadir demasiado detalle ya que el modelo converge una serie de eventos estacionarios.

Respetando las hipótesis y simplificaciones previas, se necesita un campo de velocidades, asumiendo flujo turbulento, y, por lo tanto, con una distribución parabólica a lo largo del espesor del fluido que se calcula como:

$$h = h_o + (1 - \cos \theta)(r_1 + r_2)$$

De ahí, el campo de velocidades puede describirse en función de la altura (y por lo tanto de θ y el radio), pudiendo resolverse así el siguiente sistema de ecuaciones:

$$\begin{cases} v(h) = Ah^2 + B^2 + C \\ v(\theta = 0, r = r_2) = \omega_2 r_2 \\ v(\theta = 0, r = r_1) = \omega_1 r_1 \end{cases}$$

Donde A, B and C son los coeficientes a calcular, ω_i es la velocidad angular de cada diente. Para resolver el modelo es imperativo basarse en u_∞ la cual es la velocidad del fluido suficientemente alejada de las superficies (y de la capa límite que generan) siendo estable en el tiempo y el espacio.

Al esto describe la velocidad azimutal u_θ , lo cual permite calcular la velocidad radial en base a la ecuación de continuidad del fluido:

$$u_r = -\frac{1}{r}(r_1 + r_2)(2hA \sin \theta + B \sin \theta)(r + D) - C$$

Al aplicar las condiciones de contorno, tal que en el engrane $u_r = 0 \forall r$, entonces:

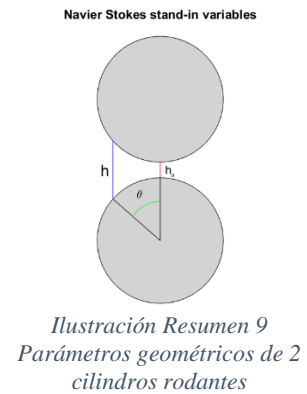
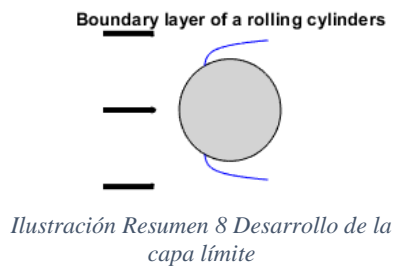
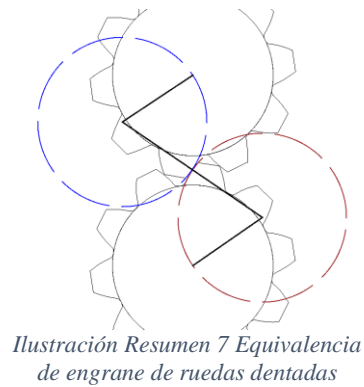
$$u_r = 0 \forall r \Leftrightarrow C = 0$$

Así mismo, una película infinitamente fina de fluido en contacto con una sólido moviéndose, se moverá de manera solidaria al mismo, por lo tanto, iniciando la capa límite:

$$P | \vec{u} = \begin{bmatrix} u_r = 0 \\ u_\theta = u_{wall} \end{bmatrix}$$

Whereby, due to the solidarity in movement, there is no radial component since the wall has exclusively movement in the $\vec{\theta}$ direction, alas, solving for D . Whilst the minimum separation shown in Figure Summary 9 is derived from the EHL model.

Donde, por el movimiento solidario, no existe movimiento radial ya que la pared, en dicho punto, e mueve exclusivamente en $\vec{\theta}$, permitiendo así hallar D . Mientas que la separación mínima vista en Ilustración Resumen 9 se extrae del modelo de lubricación



e. Salidas

El modelo calcula la deformación de las superficies de 2 dientes de sendos engranajes durante el contacto (deformación elástica y plástica) y después del contacto (deformación plástica). De las ecuaciones de lubricación también se puede extraer el espesor de la capa de lubricante y de ella, el campo de presiones en ella. Finalmente, más allá del momento y la velocidad del engranaje de salida, también se estima la eficiencia del engrane además del historial de convergencia.

f. Entrenamiento del generador de superficies

Para entrenar el modelo se realizó una partición 80-20 entrenamiento-test. No se definió una parte de validación ya que, actualmente, al entrenar el modelo GPR los hiper-parámetros se optimizan automáticamente con una partición interna entrenamiento-validación (Scikit learn, 2022).

Antes de revisar las salidas del modelo, se ha de señalar que las mediciones (máquina: KEYNECE VR-500) no cubren toda la medición, lo cual se realiza automáticamente para evitar ruido al comienzo y al final como se ve en Ilustración Resumen 10 e Ilustración Resumen 11.

Por lo tanto, el modelo se entrenará con los valores entre 0.7 mm y 1.5 mm a lo largo de la curva involuta (no es lo suficientemente grande para acomodar más de 1 longitud de corte) y entre 0.5mm y 10.9mm a lo largo del ancho (13 longitudes de corte). Del estudio (Santos, 2022) medidas adquiridas con tecnologías 2D o 3D no son comparables, por lo tanto, se creó un algoritmo en MATLAB que simulase el filtrado físico inherente a las medidas de rugosidad con contacto, ver Ilustración Resumen 12, permitiendo así comparar medidas obtenidas mediante interferencia óptica y con punteros, los cuales suelen usarse en producción.

Los diferentes modelos de GPR fueron ensayados y analizados con su puntuación (porcentaje de explicación) así como la bondad logarítmica del ajuste marginal (como de bien explica los datos).

La máxima puntuación fue del 15% (sin etiquetas de identificación) y un kernel “rotational quadratic”, mientras que, cuando se añadieron las etiquetas (acabado, módulo, flanco, fabricante...) la puntuación cayó al 13.4%. La bondad del ajuste siempre fue mala. Se probaron todas las posibles combinaciones de 3 parámetros.

Los más relevantes fueron R_{max} , R_t y S_m . Para verificar este resultado se realizaron tanto un ADR como un árbol de regresión, obteniendo de ambos R_{max} , S_m y R_{sk} como más relevantes.

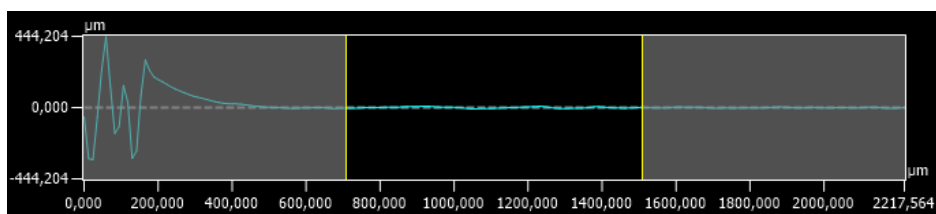


Ilustración Resumen 10 Longitud de evaluación en la dirección del perfil

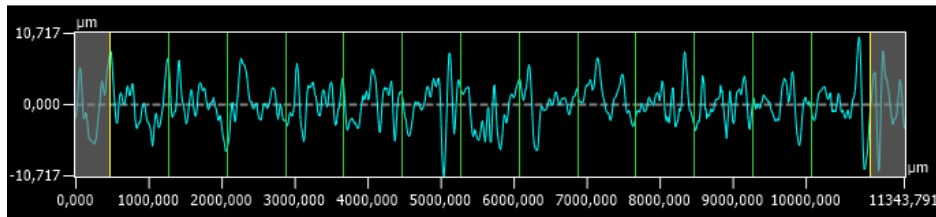


Ilustración Resumen 11 Longitud de evaluación en la dirección principal

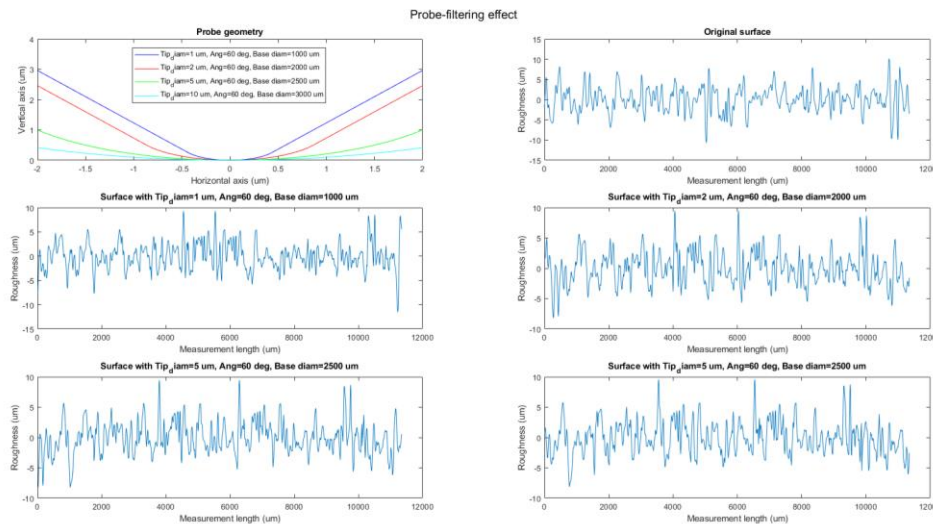


Ilustración Resumen 12 Filtrado físico por diferentes punteros

F. Evaluación & discusión

Ya que el estimador de lubricación es muy sensible a las propiedades del fluido (como el estimador del coeficiente de fricción) así como la rugosidad superficial, cada módulo se evaluó por separado. Una vez el modelo completo se verificó por secciones, se estudió el conjunto con una superficie dañada, ver Ilustración Resumen 13. Convergiendo en menos de 75 segundos en las 100 iteraciones (ver Ilustración Resumen 15) con eficiencias entre el 98.48188% y el 99.4635%, que, si bien son algo elevadas para esta aplicación, son similares a las predichas por programas de simulación especializados como ROMAX y LDP.

Las pérdidas por rozamiento y agitación del lubricante fueron estudiadas, pero no se implementaron en el modelo final ya que añadían error al mismo, reduciendo la eficiencia al 84% (ver Ilustración Resumen 15). También se evaluó el efecto de la aproximación de Navier-Stokes sobre la eficiencia (el campo de presiones en el lubricante). No se encontró que afectase de manera significativa la solución, sin embargo, sí aporta más detalle y realismo al modelo, por lo tanto, se consideró una aproximación válida.

Una vez realizado el análisis de sensibilidad del lubricante, el modelo se ensayó con la misma superficie, pero propiedades realistas de lubricación. La eficiencia fue del 98.87% con la deformación superficial siendo más marcada en los defectos iniciales, lo cual respeta los efectos de propagación descritos en la literatura.

También se aprecia como los defectos actúan como concentraciones de tensiones de hasta 2 órdenes de magnitud superiores al resto de las tensiones (siendo responsables de la propagación del daño superficial, ver Ilustración Resumen 16 e Ilustración Resumen 17), de acuerdo con lo descrito en la literatura. Finalmente, la temperatura instantánea aumentó en hasta 60K donde se dio contacto directo y sólo 24K en las zonas lubricadas, validando el efecto refrigerante.

Si bien es cierto que el módulo de la temperatura instantánea predice temperaturas ligeramente inferiores a las referencias, lo cual se debe a la aproximación estática en lugar de transitoria que se suele aplicar a estos problemas.

El análisis los parámetros superficiales y la generación de superficies mostraron que para 10 ciclos de optimización el más adecuado era el kernel “rotational quadratic”, mientras que le RBF parecía demandar más ciclos de optimización. El kernel tipo “White”, específico para modelar ruido en una señal, no obtuvo resultados, indicando por lo tanto que los datos tienen una estructura inherente, lo cual, era esperado, pues se señala en la literatura, según el tipo de acabado.

Las bajas puntuaciones sugieren que se necesitan más datos para entrenar el modelo.

Esto se apoya también en el hecho de que al añadir las etiquetas las puntuaciones bajasen, dividiendo el set de entrenamiento más, lo cual sugiere falta de entrenamiento. Esto puede mitigarse con más medidas, y, por lo tanto, aumentar el número de datos. Sin embargo, se comprobó que una superficie puede ser modelada con 3 parámetros (los 3 ya mencionados son: R_t , S_m y R_{sk}). La combinación de R_t y R_{max} dio la máxima puntuación (ver Ilustración Resumen 19), pero, como se explica un poco más adelante, son parámetros muy similares, y aportan poca información adicional ya que R_{max} es el máximo de R_t . Así que la combinación más relevante es S_m y R_t , acotando tanto vertical como horizontalmente las superficies.

El kernel “rotational quadratic” dotaba la suficiente anchura y flexibilidad a los intervalos de confianza para aceptar la mayoría de los datos, como se muestra en Ilustración Resumen 18.

R_t es la media de la máxima variación de altura en cada longitud de corte, mientras que R_{max} es el máximo de dichos valores, siendo más inestable. R_{max} ya no se considera en las nuevas versiones de la norma ISO 219201.

S_m es el porcentaje de superficie que intersecciona el plano medio de la distribución.

R_{sk} es el sesgo, si es mayor que 0 la superficie presenta más picos, si es menor más valles.

Es inevitable asociar la combinación de estos 3 parámetros como vertical, horizontal y posicionamiento, sugiriendo, ratio o distribución de material, conclusiones similares a las presentadas en la literatura, referencias a la curva de Abbot-Firestone. Redefinir los requisitos superficiales en función de ésta permitiría, en un futuro, definir nuevos requisitos en todas las direcciones de la superficie.

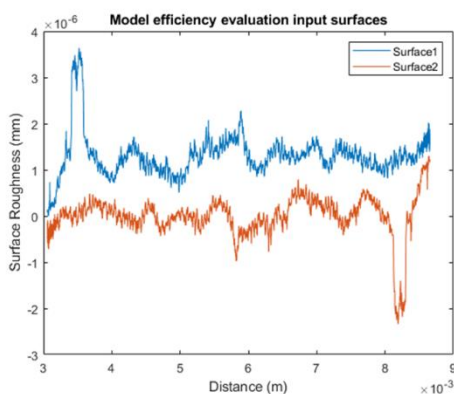


Ilustración Resumen 13 Superficies iniciales

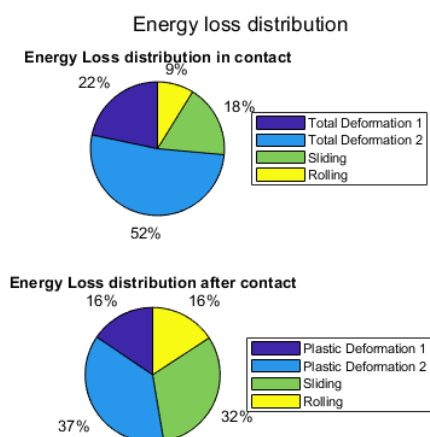


Ilustración Resumen 14 Desglose final de la eficiencia y las pérdidas

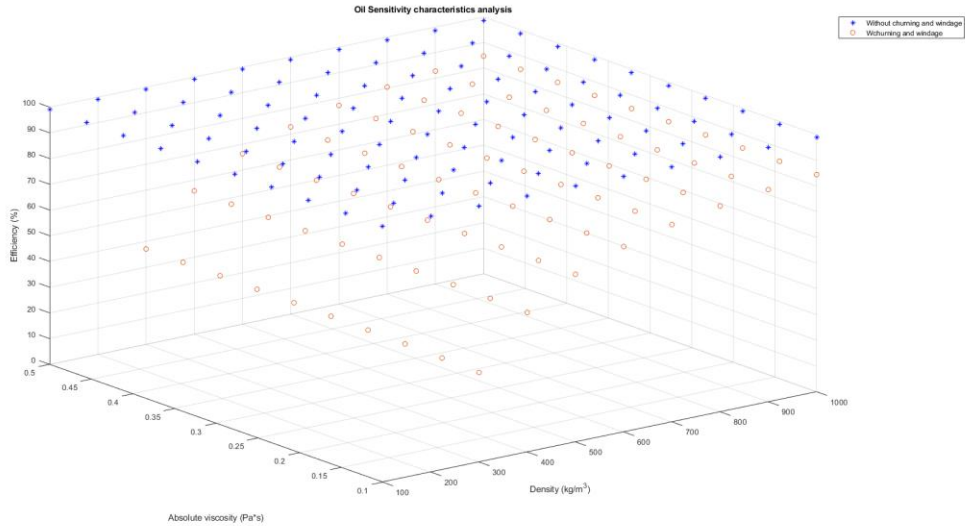


Ilustración Resumen 15 Análisis de sensibilidad al lubricante

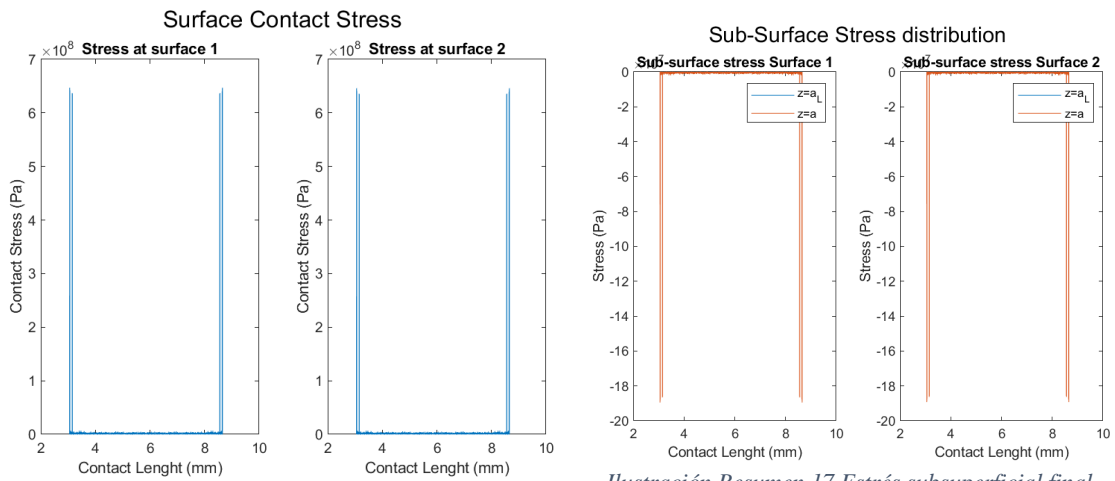


Ilustración Resumen 16 Estrés de contacto final

Ilustración Resumen 17 Estrés subsuperficial final

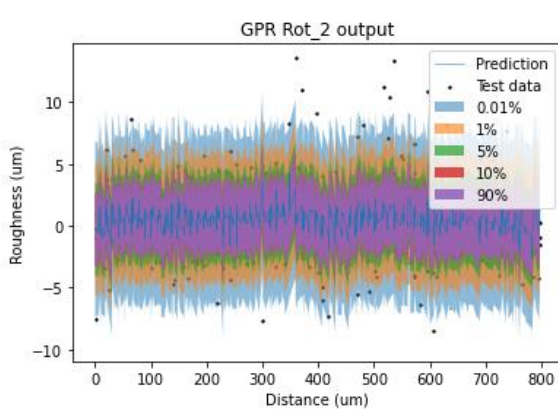


Ilustración Resumen 18 Resultados rotational quadratic

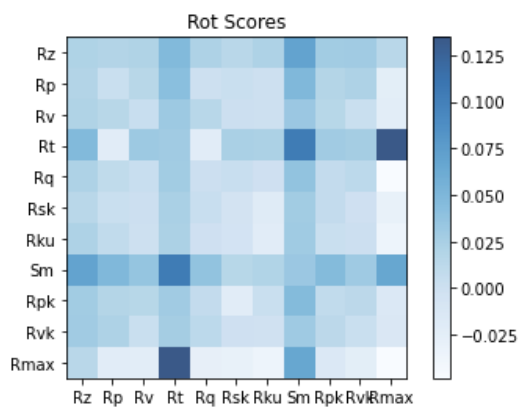


Ilustración Resumen 19 Distribución de puntuaciones rotational quadratic

G. Desarrollos futuros

Claramente, el modelo puede mejorarse incorporando un módulo de temperaturas más preciso, yendo más allá de una simple implementación del modelo de Fourier para concordar con los

resultados de simulaciones en ROMAX y LDP (software comercial empleado en la industria automovilística para diseñar, simular y analizar transmisiones).

El modelo podría pasar de ser un estacionario 2D a pseudo-3D o 3D completo, considerando el área alrededor del contacto (para el pseudo-3D) considerando todas las líneas en la dirección perpendicular y el programa moviéndose en a lo largo de curva involuta o 3D completo si se considera todo el flanco del engranaje como superficie (lo cual requeriría elementos finitos).

Quizás sea más apremiante convertir el modelo en transitorio e implementar efectos temporales tanto en la dinámica del contacto como, en especial, la lubricación, como ya se ha mencionado.

El módulo de generación de superficies también debe ser entrenado con cuantiosas cantidades de series de rugosidad superficial con diversos orígenes, antes, durante y después de ensayos de durabilidad para poder también modelar como las superficies varían a lo largo de su vida útil (en especial en los primeros ciclos cuando se da la mayor deformación por ciclo). Ser capaces de modelar como las superficies varían en la vida real podría a su vez ayudar a mejorar las prestaciones de las transmisiones de vehículos eléctricos.

Furthermore, a refined powder metal gears module should be implemented to allow for further R&D efforts to study their applications in future transmissions, reducing material usage and associated environmental impacts.

Así mismo, el módulo de engranajes de pulvimetalurgia y sinterizado debería mejorar su implementación para facilitar esfuerzos de I+D y su aplicación a futuras transmisiones, reduciendo el desperdicio de material y su impacto medioambiental.

La naturaleza modular del modelo permite su adaptación a varios escenarios y fácil desarrollo futuro, montando, por ejemplo, un módulo de NVH (ruido durante el funcionamiento).

H. Objetivos de Desarrollo sostenible

El Proyecto claramente cae dentro del “Objetivo 9: Industria, innovación e infraestructura” ya que un mejor entendimiento del comportamiento de los engranajes en funcionamiento o tras su manufactura permitirá avanzar en la electrificación, lidiando con la innovación del objetivo. Dado que se ha buscado una mejor definición y entendimiento del comportamiento de las superficies se mejora el apartado de industria. Al comprender relevancia de la rugosidad superficial y su efecto en la eficiencia, el siguiente paso es la adecuación de la cadena de valor y manufactura, lo cual permite la optimización para acomodar los nuevos requisitos superficiales.

Comprender los efectos de varios factores ya discutidos facilita la inclusión en “Objetivo 12: Producción y consumo responsable” ya que busca aportar beneficios tangibles minimizando la utilización innecesaria de recursos. Un buen ejemplo es la nueva definición de requisitos superficiales, ya que los parámetros de producción pueden adecuarse para aumentar la utilización y reducir el desperdicio: velocidades, profundidad de corte, mantenimiento preventivo, desviaciones en producción...

Finalmente, “Objetivo 13: Acción por el clima” está presente en todo el Proyecto. Desde el lado de la producción, donde la reducción de los insumos de material y la utilización de la energía reduce automáticamente la huella de carbono, mejorando el ciclo de vida de las transmisiones de vehículos eléctricos. Además, dado que el número de vehículos eléctricos no hará sino aumentar a medida que los requisitos CAFE se vuelven más exigentes y los motores de combustión interna quedan obsoletos cualquier avance que permita mejorar la eficiencia de la transmisión, reducirá la energía consumida y, por lo tanto, sus emisiones asociadas, ya que a no es 100% renovable, por lo tanto, todo vehículo eléctrico tiene emisiones secundarias asociadas, si bien menores a los de combustión interna.

Resumen Ejecutivo: Referencias

- al, H. e. (2007). Prediction of Mechanical Efficiency of Parallel-Axis Gear Pairs. *Journal of Mechanical Engineering* 129, 58-68.
- al, I. G. (2014). Generative Adversarial Nets. *Proceedings of the International Conference on Neural Information Processing Systems* (pp. 2672-2680). Montréal: International Conference on Neural Information Processing Systems.
- Björklund, S. (1995). *Elastic contacts between rough surfaces*. Stockholm: KTH.
- Brownlee, D. J. (2019, 07 17). *Machine Learning Mastery*. Retrieved from A Gentle Introduction to Generative Adversarial Networks (GANs): <https://machinelearningmastery.com/what-are-generative-adversarial-networks-gans/>
- Brownlee, D. J. (2019, 07 19). *Machine Learning Mastery*. Retrieved from A Gentle Introduction to Generative Adversarial Networks (GANs): <https://machinelearningmastery.com/what-are-generative-adversarial-networks-gans/>
- Chapter 2: Overall Methodology. (2005). In H. Xu, *DEVELOPMENT OF A GENERALIZED MECHANICAL EFFICIENCY PREDICTION METHODOLOGY FOR GEAR PAIRS* (p. 30). Columbus: Ohio State University.
- C-Therm. (2022, 04 25). *C-Therm*. Retrieved from Thermal Resistance and Thermal Conductance: <https://ctherm.com/resources/helpful-links-tools/thermalresistanceandconductivity/>
- Donges, N. (2021, 07 29). *Builtin*. Retrieved from A Guide to RNN: Understanding Recurrent Neural Networks and LSTM Networks: <https://builtin.com/data-science/recurrent-neural-networks-and-lstm>
- Fumo, D. (2017, 08 04). *Towards Data Science*. Retrieved from A Gentle Introduction To Neural Networks Series — Part 1: <https://towardsdatascience.com/a-gentle-introduction-to-neural-networks-series-part-1-2b90b87795bc>
- Hui, J. (2018, 06 19). *Jonathan Hui*. Retrieved from GAN — What is Generative Adversarial Networks GAN?: <https://jonathan-hui.medium.com/gan-whats-generative-adversarial-networks-and-its-application-f39ed278ef09>
- Ishizaki, T., & Nagano, T. I. (2020). Measurement of local thermal contact resistance with a periodic heating method using microscale lock-in thermography. *Review of Scientific Instruments*, 91: 064901.
- James. (2020, 06 24). *Stats Exchange*. Retrieved from Linear Regression for Noisy Data: <https://stats.stackexchange.com/questions/473850/linear-regression-for-noisy-data>
- Jonny Hansen, M. B. (2021). A New Film Parameter for Rough Surface EHL Contacts with Anisotropic and Isotropic Structures. *Tribology Letters* 69:37, 1-17.
- Kadiric, P. R. (2019). The influence of side-roll ratio on the extent of micropitting damage in rolling-sliding contacts pertinent to gear applications. *Tribology Letters*, 67:1-20.
- L. Xiao, S. B. (2007). The influence of surface roughness and the contact pressure distribution on friction rolling/sliding contacts. *Tribology international*, 40:4:694-698.
- Marcello De Bernardi, M. K. (2018). Pseudo-Random Number Generation using Generative Adversarial Networks. *Nemesis 2018, UrbReas 2018, SoGood 2018, IWAISe 2018, and Green Data Mining 2018* (pp. 1-10). Dublin: Springer International Publishing.
- Masse, S. L. (2019). On the flash temperature under the starved lubrication condition of a line Contact. *Tribology International*, 136: 173-181.

- Optimization Geeks. (2021, 10 31). *Youtube*. Retrieved from Easy introduction to gaussian process regression (uncertainty models): <https://www.youtube.com/watch?v=iDzaoEwd0N0>
- Pandurangi, A. B. (2020). *Electric Transmission System efficiency Simulation*. Gothenburg: Chalmer's University of Technology.
- Rocca, J. (2019, 01 07). *Towards Data Science*. Retrieved from Understanding Generative Adversarial Networks (GANs): <https://towardsdatascience.com/understanding-generative-adversarial-networks-gans-cd6e4651a29>
- Rowe, W. B. (2014). 18 - Energy Partition and Temperatures. In W. B. Rowe, *Principle of Modern Grinding Technology* (pp. 381-420). Norwich: William Andrew Publishing.
- Santos, D. J. (2022). *A study on surface characterization of gears and the measurement problem*. Győr: Széchenyi István University.
- Scikit learn. (2022, 04 29). *Scikit learn*. Retrieved from [sklearn.gaussian_process.GaussianProcessRegressor: https://scikit-learn.org/stable/modules/generated/sklearn.gaussian_process.GaussianProcessRegressor.html](https://scikit-learn.org/stable/modules/generated/sklearn.gaussian_process.GaussianProcessRegressor.html)
- Sit, H. (2019, 06 19). *Towards Data Science*. Retrieved from Quick Start to Gaussian Process Regression: [https://towardsdatascience.com/quick-start-to-gaussian-process-regression-36d838810319#:~:text=Gaussian%20process%20regression%20\(GPR\)%20is,uncertainty%20measurements%20on%20the%20predictions.](https://towardsdatascience.com/quick-start-to-gaussian-process-regression-36d838810319#:~:text=Gaussian%20process%20regression%20(GPR)%20is,uncertainty%20measurements%20on%20the%20predictions.)
- Sosa, M. (2017). *Running-in of gears- surface and efficiency transformacion*. Stockholm: KTH.
- Tim. (2017, 01 17). *Stackexcahnge*. Retrieved from Understanding the randomness of y in linear regression model: <https://stats.stackexchange.com/questions/256998/understanding-the-randomness-of-y-in-linear-regression-model>
- Wang, Y. W. (2013). Stribeck Curves. In Y. W. Wang, *Encyclopedia of Tribology* (pp. 3365-3370). Boston: Springer.
- Wei, J. (2015). A Study of Spur Gear Pitting under EHL Conditions: Theoretical ANalysis and Experiments. *Tribology International* 94, 146-154.
- Williams, D. (2010, 09 21). *Talk Stats*. Retrieved from Is there a non parametric alternative to multiple linear regression?: <http://www.talkstats.com/threads/is-there-a-non-parametric-alternative-to-multiple-linear-regression.13721/>
- Zhou, C., Xing, M., & Hu, H. W. (2021). A novel thermal network model for predicting the contact temperature of contact gears. *International Journal of Thermal Sciences*, 161:106703.

Executive Summary

A. Introduction

The motivation for this project was to understand how the surface roughness of gears affects their performance and efficiency when meshing. For this, a holistic contact tool was built, including, lubrication regime and film thickness estimation, sliding and rolling forces calculation, surface deformation computation and contact flash temperature modelling. Finally, a machine learning model to analyze the relevance of several roughness parameters was built, capable of generating surfaces from supervised learning algorithms.

B. Research questions

During the completion of this research, a question arose very early, could a surface be predicted from a small set of parameters, alas, a part of the research efforts were redirected towards that question. In other words, the main research question was:

- What is the relationship between the surface and performance (scuffing and efficiency) of a gear mesh?

From this main question, a number of secondary questions arise:

- What are the lubrication mechanisms for a given lubricant and can it be accurately predicted?
- Can the surface behaviour in different lubrication regimes be accurately modelled?
- Can a surface be directly correlated to a small set of surface characterization parameters?

C. Motivation

The motivation can easily be characterized by the growing importance of detailed gear study as electric transmissions have far less gear pairings than their ICE counterparts, alas, effects which before got lost in the system-level instabilities are gaining relevance.

D. State of the Art

The following section contains a brief summary of the literature review which kickstarted this project:

a. Dry contact model

At first, a purely superficial contact tool based on Lamé theory was developed. This was in turn refined into the dry contact model from the references (Sosa, 2017) and (L. Xiao, 2007).

These develop the method proposed in (Björklund, 1995) for an elliptical-to-half-space contact, considering both to be deformable. Where the surface deformation is described as:

$$\bar{u}_{zi} = \frac{1}{\pi E^*} \sum_{j=1}^n C_{ij} p_j$$

In which \bar{u}_{zi} is the deformation in the perpendicular direction to the contact for surface i , whilst C_{ij} is the population of compliance matrix and p_j is the pressure originating from the contact in surface j .

In turn, the population compliance matrix itself is described as:

$$C_{ij} = (x_{\Delta} - a_L) \left[\ln \left(\frac{x_{\Delta} - a_L}{a_L} \right) \right]^2 - (x_{\Delta} + a_L) \left[\ln \left(\frac{x_{\Delta} + a_L}{a_L} \right) \right]^2 + C_o$$
$$x_{\Delta} = |x_i - x_j|$$

Where a_L is the half-cell size; x_Δ is the absolute value of the difference of coordinates along the x-axis of the contact correlating every point in surface i with every point in surface j so that, only in the main diagonal of C would x_Δ be null. Finally, C_o is an arbitrary value not detailed in the reference, as such, it was given a value of zero.

Therefore, the pressure field in each material can be described as:

$$\bar{p} = \pi E^* C^{-1} (\delta - \bar{h})$$

Such that \bar{p} is the pressure across the surface contact, \bar{h} is the vector containing the discrete height difference between both surfaces and δ is the approach distance between both surfaces (Sosa, 2017). This in turn can be solved via numerical methods.

Consequently, the force on the contact must inevitably be:

$$F_c = \int \bar{p} dx$$

The reference (Sosa, 2017) also demonstrates the subsurface stress follows the algebraic formulation:

$$\tau_i = -\frac{p_i}{a} (z - z^2 (a^2 + z^2)^{-\frac{1}{2}})$$

Thus, reducing computational cost and having a maximum at $z=a$, where the shear stress will be 20.7% of the surface stress, alas, the shear stress contour line will mimic the surface.

The novelty introduced in this section is the conversion from a semi-elliptical contact and a flat plane to the generalization of input surfaces, therefore being able to accept any input 2D rough line as a surface instead of only 1 rough line and a flat one.

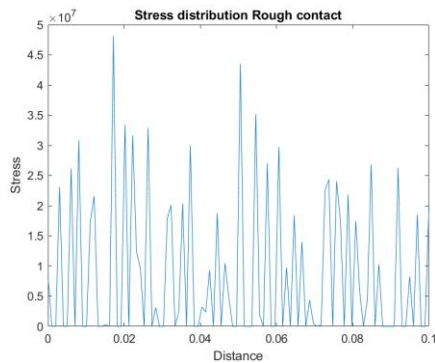


Figure Summary 1 Surface contact stress

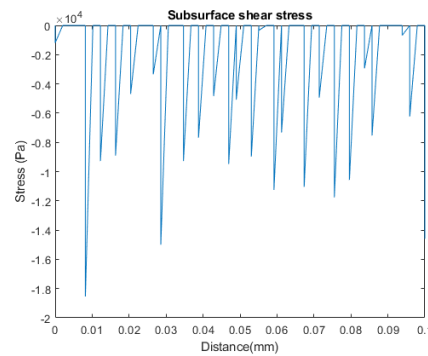


Figure Summary 2 Sub-surface stress

b. Rolling & sliding forces

The shear stress acting on the surfaces (as a result from the rotation of the tooth surface with regards to the lubricant) can be calculated using traditional formulae based on Newtonian fluids with turbulent flow such that (Wei, 2015):

$$\tau = \mu \frac{\partial u}{\partial h} - \frac{1}{2} h(x) \frac{\partial p(x)}{\partial x}$$

Where τ is the shear stress of the fluid and $\frac{\partial u}{\partial h}$ is the derivative of the velocity field in the fluid with regards to the height whilst the second term describes the effect of the turbulence.

Instead of studying every contact point with the inaccuracies which that might entail, a macro-level sliding and rolling resistance descriptions can be found in (al H. e., 2007). The sliding and rolling resistance are therefore described as (for ball-on-disc contacts):

$$F_s = \mu * F_C \qquad F_r = \frac{4.318\varphi_T(\tilde{G}\tilde{U})^{0.658}\tilde{Q}^{0.0126}R}{\alpha}$$

Such that F_r is the rolling resistance; φ_T is the thermal reduction factor to account for the effect of temperature rise at high speed conditions (al H. e., 2007), however, said value isn't disclosed in the reference, but it is described at length in (Chapter 2: Overall Methodology, 2005). \tilde{G} is the dimensionless material parameter; \tilde{U} is the dimensionless speed parameter; \tilde{Q} is the dimensionless load parameter and α is the pressure viscosity coefficient. F_s is the sliding force, μ is the friction coefficient and F_C is the normal force of the contact.

In this publication, (al H. e., 2007), the friction coefficient of the lubricant is described with a 94% accuracy and a model error for the acting forces below 0.1%. The friction coefficient approximation results from the equations (al H. e., 2007):

$$\begin{cases} \mu = e^{f(SR, P_h, \nu_o, S)} P_h^{b_2} |SR|^{b_3} V_e^{b_6} \nu_o^{b_7} R^{b_8} \\ f(SR, P_h, \nu_o, S) = b_1 + b_4 |SR| P_h \log_{10}(\nu_o) + b_5 e^{-|SR| P_h \log_{10}(\nu_o)} + b_9 e^S \end{cases}$$

Such that μ is the friction coefficient; SR is the slip-to-rolling ratio upon the teeth meshing, P_h is the maximum Hertzian contact pressure; ν_o is the absolute viscosity (in cPs for this application) at the oil inlet temperature; V_e is the entraining velocity; R is the equivalent radius of the contact; S is the equivalent RMS surface roughness whilst $b_i \mid i = 1, 2, \dots, 9$ belong to a 9 element coefficient vector derived from a lineal regression of the lubricant properties, which in the reference (al H. e., 2007) is described as the standard FZG set-up.

This allows for the adaptation of the friction coefficient to the contact characteristics at every point in time, therefore, mitigating the dynamic effects as all these models rely on a sequence of static load cases to operate.

The novelty incorporated in this section is the implementation in a rotated coordinate system, as this formulation looks at gear contacts perpendicularly to the contact, whilst this implementation studies every point of the line contact. Furthermore, and following (Pandurangi, 2020), a proprietary algorithm was created to adapt the lubricant properties to the different ones studied, beyond the FZG base lubricant.

c. Lubrication regime

A crucial element when developing contact tools is the existing lubrication regime. For this, there are 3 main regimes:

- Elastohydrodynamic Lubrication (EHL): There exists a thin layer of fluid between both surfaces so there is no direct contact in between each other. This is the go-to since it prevents surface damage such as scuffing. It is typically associated with an increase of the friction coefficient as shown in the Stribeck curve
- Mixed Lubrication (ML): There is some contact between the surfaces, whilst other regions have an oil film in between them. This leads to a decrease of the friction coefficient between both surfaces.
- Boundary Lubrication (BL): There is mostly direct contact between the surfaces, with a constant friction coefficient (solid-to-solid contact) whilst some pockets of lubricant may be found.

As seen in the Stribeck curves below in Figure Summary 3 , the lubrication regime is extremely sensible to the lubricant properties (Wang, 2013). A study conducted in (Jonny Hansen, 2021) also points out the effect of surface roughness and surface deformation on the lubrication regime. In said publication, a new lubrication estimation parameter was proposed, Λ^* , said parameter could predict a EHL contribution of 60-80% in mixed lubrication conditions for any ball-on-disc contact and correctly predict a 100% EHL contact when full-film lubrication was tested.

Furthermore, said parameter, Λ^* , accounted for the roughness of real engineering surfaces, although not bilaterally, one surface was considered to be perfectly flat and infinitely rigid (Jonny Hansen, 2021). Adapted from the reference (Jonny Hansen, 2021), the predictor, for a pair of deformable and rough surface meshing gears is described as:

$$\Lambda^* = \frac{h^*}{S_{pk}}$$

Where Λ^* is the aforementioned lubrication regime estimator where $\Lambda^* \geq 1$ implies full EHL whilst $\Lambda^* < 1$ implies BL or ML. The total surface separation is represented by h^* and the peak surface roughness is represented by S_{pk} .

Furthermore, in the publication (Jonny Hansen, 2021), the authors go into a lot of trouble to describe their newfound height h^* based on traditional EHL parameters, arriving at:

$$h^* = h_m + h_c f_q$$

When modifying the general formulation to gears, the radius $R'_{y,b}$ and R'_y are ∞ since the gears in the entrainment direction represent a circumference centred in the pressure line, but in the perpendicular direction, they are but a flat line, thus having an infinite radius, alas, the equations can be simplified to:

$$\begin{aligned} h_m &= 3.63U^{0.68}G^{0.49}W^{-0.073} \\ h_c &= 2.69U^{0.67}G^{0.53}W^{-0.067} \\ f_q &= \left(\frac{R'_{x,a}}{R'_{x,b}}\right)^\alpha \left(1 - \gamma_1 e^{-\gamma_2 \left(\frac{R'_{y,a}}{R'_{x,a}}\right)^{\gamma_3}}\right) \end{aligned}$$

In this set of equations, the coefficients α , γ_1 , γ_2 and γ_3 depend on the direction of the surface roughness and its direction with regards to the oil entrainment direction; U , G and W are the aforementioned dimensionless speed, material and load variables. The variable X is the corresponding exponent of the dimensionless speed parameter in each equation. The R' represents the effective radii on different directions, where the x and y subindexes represent the oil-entrainment direction and it's perpendicular, respectively and the a and b subscripts represent asperity radius or the macro geometry radius respectively (when no a or b subindexes are present the variable represents the smooth surface effective radius).

The novelty of this section lies in the adaptation of the EHL model to gear teeth geometries and the conversion of a deformable-solid-to-infantile-rigid-plane into a bilateral deformable surface contact.

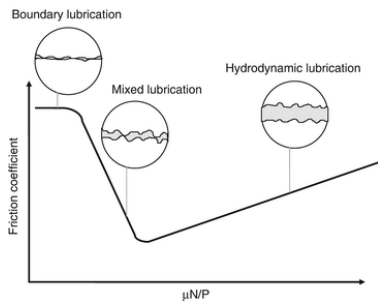


Figure Summary 3 Stribeck curve (Wang, 2013)

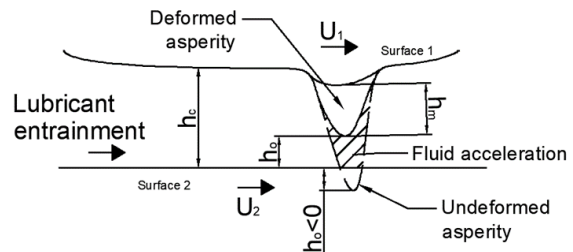


Figure Summary 4 EHL surface depiction

d. Navier-Stokes equations & pressure across the oil film

Thin film lubrication accepts Reynold's equation, a simplification of the Navier-Stokes equations which assume one of the three dimensions in space to be insignificant, although, in automotive

gears, due to their small module, upon approach, this is not necessarily true. As such, a solution to Navier-Stokes is proposed.

Reynold's equation cannot be considered for this application since it assumes the pressure distribution through the height of the film thickness is uniform (which, from the get-go was assumed to be false). Furthermore, it also assumes the thickness of the fluid layer is much smaller than its 2 counterparts in space, which, given the problem configuration is not necessarily true since a gear width might only be a few times the teeth height in some instances and thus, in the approximation phase of 2 flanks, the fluid film thickness can be comparable in magnitude to the other 2 dimensions found in space.

Another key element when discarding this version of applied fluid dynamics comes from the reference (C-Therm, 2022). In this PhD thesis, the author explains that a key element in determining the friction coefficient is the surface boundary layer. On top of that, said surface boundary layer is strongly dependant on the chemical composition of the lubricant and pre-existing conditions, namely, surface roughness after different gear manufacturing operations, which included green-shaving; power honing and grinding, alas, no assumptions about the lubricant can be made, such as the ones in Reynold's equations.

e. Thermal effects

It's common knowledge that surfaces in contact heat up due to friction. Said temperature increase is commonly referred to flash temperature (Rowe, 2014). Alas, the surface temperature in a frictional contact is often described as:

$$T_i = T_b + \Delta T$$

Where T_i is the surface temperature; T_b is the bulk temperature of the material and ΔT is the flash temperature increase.

Since the code works based on vertical deformable differentials it is possible to break the problem down into 2 types of heat transmission: conduction due to direct contact and heat transfer through the fluid layer.

The flash temperature due to direct contact can be described as:

$$T_f = \frac{q + T_{b1}R_2 + T_{b2}R_1}{R_1 + R_2}$$

Where q is the friction-generated heat ($q = v_s * \mu W$); R_i represents the thermal conductivity resistance and the subindexes 1,2 correspond to surface 1 and surface2 respectively. Said resistance follows the well-known formula (C-Therm, 2022):

$$R = \frac{L}{Ak}$$

Such that L is the length (in this application the length of a surface differential in meters), A is the area through which the heat is transferred (once again, adapted to a differential, the area of said differential in meters squared) and k is the thermal conductivity of the material (K/W).

In this application, a contact thermal resistance is not considered since by definition it represents the difficulty heat transfer faces when 2 uneven surfaces are in contact and thus the contact area is smaller than the nominal area (Ishizaki & Nagano, 2020). However, since the code only applies the conductivity equations to calculated direct contact, said resistance is redundant.

This heat definition also respects the findings made in (Kadiric P. R., 2019) where the temperature increase in the gear surface depends on the sliding speed.

To develop the flash temperature of a surface where there is lubrication, the proposition made in (Zhou, Xing, & Hu, 2021) was implemented. Here the heat flux across a gear tooth is divided into

circular differentials across the height of the tooth and a set of linear heat transfer problems as seen in Figure Summary 5.

In this publication (Zhou, Xing, & Hu, 2021), this novel model is compared against both Blok's model and ISO standard model, achieving satisfactory results. As such, the problem can be rewritten following the electrical model equivalent as:

$$T_f - T_b = \frac{Q}{A} \left(\frac{1}{h_1} + \frac{L}{k_s} + \frac{1}{h_2} \right) \quad h_m = 0.288 Re^{0.731} Pr^{1/3} * \frac{k_f}{d_i}$$

Where Pr is Pradnt's number. As such, the flash temperature can be computed as:

$$T_f = T_{bi} + \frac{Q_i}{A} \left(\frac{2}{h_i} + \frac{L}{k_s} \right)$$

Where the i subindexes indicate each surface respectively. To understand how the heat generated due to friction divides amongst both surfaces the equations presented in (Masse, 2019) were used:

$$\begin{aligned} T_{b1} - T_{b2} &= \frac{h}{2k_f} (1 - 2\vartheta) Q \mid h = h_1 + h_2 \\ Q_1 &= \vartheta Q \\ Q_2 &= (1 - \vartheta) Q \end{aligned}$$

Where ϑ is the fraction heat coefficient.

The novelty of this section is the reformulation of the heat transfer problem to, in a dynamic problem, operate as a pseudo-transient by overlapping static configurations.

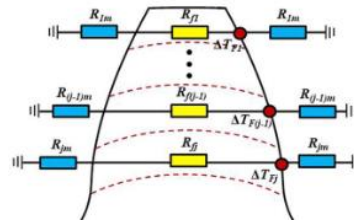


Figure Summary 5 Heat transfer approximation through a gear tooth (Zhou, Xing, & Hu, 2021)

f. Surface generation

One of the main goals of this master thesis was to study the effect of surface roughness in efficiency and how said roughness could be represented by the surface roughness parameters so it can be easily tracked through manufacturing.

This section contains all the adjustment made to the reviewed models and purpose specific complementary developments carried out in this here Master Thesis. To study this a shortlist of suitable candidates was composed, and a literature review was performed. The candidates were:

- Recurrent Neural Networks (RNN)
- Generative Adversarial Networks (GAN)
- Multivariable Linear regression
- Gaussian Process Regression (GPR)

Both RNN and GAN are neural networks commonly used for image classification and generation, but support sequence-to-sequence capabilities as described in (Fumo, 2017) and (Brownlee, Machine Learning Mastery, 2019). The key difference lies on how they operate internally. RNN supports an internal memory function which is carried throughout the model remembering the most relevant elements of both the input and the previous iteration of calculations (Donges, 2021), known as Long-Short Term Memory (LSTM). This cell is able to both generate an output or

iterate in itself to refine the output, thus the name, recurrent. To validate and train the network a technique known as backpropagation is used, which simply put is moving from the output layer to the input layer of the neural network (Seth, 2021), in other words, verifying the bijectivity of the neural network.

GANs on the other hand rely on a cat and mouse game or zero-gain game between two neural networks (Brownlee, Machine Learning Mastery, 2019). These are generally referred to as the Generator (a label-to-sequence neural network) and a Discriminator (a sequence-to-label neural network). Based on a training dataset, both networks are pitted against each other, the Generator aiming to create data as realistic looking as possible based on the training dataset whilst the Discriminator must determine which of the samples which it's been fed are in fact real or false, created by the Generator (al I. G., 2014). They compete in each iteration and whomever losses must improve before the next round. Generally, once the generator has been trained the Discriminator is discarded (Hui, 2018). Although GANs are generally used to recreate or enhance images there are several examples of GANs used to generate sample numerical vectors and random number generators (RNG) as shown in (Rocca, 2019) and (Marcello De Bernardi, 2018).

The other two alternatives fall in the machine learning realm, with multivariable linear regression being the simpler of the two and its formulation being well known, however, the biggest setback is the lack requirement of predetermining the variables to adjust and the order of magnitude of said variables, thus being a parametric study (Williams, 2010). Furthermore, randomness of any given value is inherently removed from any regression since it will always output a function $Y = f(X)$ (Tim, 2017), therefore any line surface generated with this technique will always be equal (given the same input parameters) unless the confidence intervals are considered, and a random value is selected from the range.

It is well known linear regression is not well suited for very noisy large datasets without a clear structure, centred around 0, such as these samples for instance (James, 2020), since the confidence intervals will tighten around the regression model and thus excluding real original values.

Finally, GPR is a non-parametric regression, thus rather than calculating the probability distribution of a parameter it calculates the probability across all possible functions for said parameter (Sit, 2019) and compare those to the sample data, thus, calculating the posterior probability of that function being representative with a Bayesian approach. Thanks to the associated probability of each generated function, the mean function can be derived along with the confidence intervals at every point of the function (Optimization Geeks, 2021). In other words, GPR lies a cloth over the data and the kernels or covariance algorithms give it more flexibility to adapt to the data, evaluating afterwards how likely that shape is.

Both neural networks were discarded since they operate in a black box manner, not fully knowing what's going on behind closed doors and the MLR is not flexible enough to adapt to the data adequately, alas, GPR was employed with a set of kernels which were also studied

The novelty of this section is the usage of GPR to model surface parameter's regression and their relevance instead of a commonplace classification problem.

E. Implementation

This section summarizes the implementation of the different modules and adaptations of the code.

a. Inner workings

The model proceeds to estimate the friction coefficient followed by the lubrication regime, which can then result in one of two solvers. If a full EHL regime is estimated (which, from the literature review is 100% accurate), the surfaces will not be in contact and a thin layer of fluid with a minimum thickness of $h_o = h^*$ is implemented, which, then yields a pressure field across the

fluid acting on the surfaces (algebraic solver). The sliding and rolling forces are then allocated uniformly across the surface of each gear as the only element acting on either surface is said film.

If however, the lubrication equations suggest there is ML or BL, a numerical solver based on the aforementioned rough contact model is implemented. This solver lowers both surfaces into each other and using the compliance matrix estimates stress whilst simultaneously applying the fluid pressure due to the Navier-Stokes solution (where there is fluid). Said stress and pressure are integrated across the entire line contact until the contact force converges. In parallel, other effects are studied and implemented, obtaining a surface deformation and overall efficiency, see below.

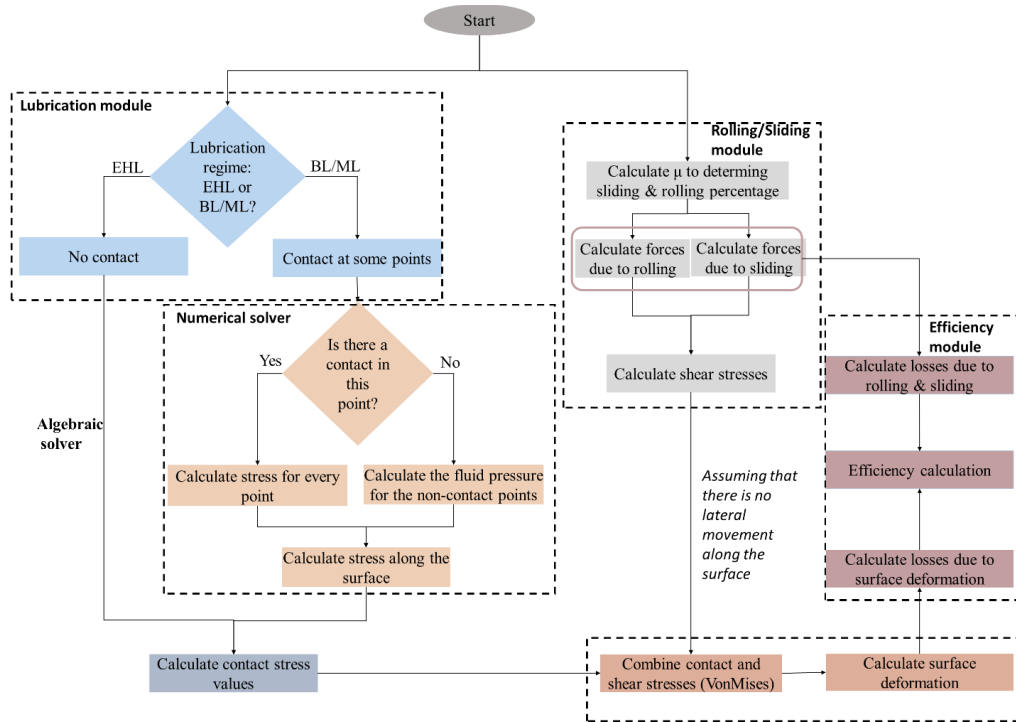


Figure Summary 6 Model's box diagram

Regardless of the solver, the model then proceeds to calculate the efficiency (by adding all losses due to plastic deformations, sliding and rolling losses) of the contact as well as other outputs such as transferred torque by the driven gear with the formulation:

$$M_2 = \frac{M_1 \omega_1}{\omega_2} \eta$$

Where M_2 is the output torque; M_1 is the input torque; ω_2 is the output rotational speed; ω_1 is the input rotational speed and η is the efficiency.

b. Efficiency

Windage and churning losses, although they were reviewed, were not implemented in this model since they are themselves external to a pair of gears meshing.

The sliding and rolling resistance losses were described as:

$$P_\mu = F_s V_s \qquad P_r = F_r V_e$$

Where P_μ are the losses due to sliding friction (F_s) and it's dependent on the sliding speed of the contact between gear teeth (V_s), whilst the rolling resistance losses are dependent on the aforementioned rolling resistance (F_r) and the entrainment speed (V_e).

The surface deformation losses followed the formula:

$$P_{si} = \frac{\iint \sigma \delta \cdot ds}{T} \rightarrow \frac{\sigma \delta a^2}{T}$$

Where P_{si} are the losses due to surface deformation of each surface, σ is the Von Misses surface stress, which can be elastic or plastic, δ is the deformation depth at every point, T is the period of rotation of the gears. The theoretical formulation with a surface integral was substituted in the code with a multiplication of stress and deformation at every point in the line measurements, with a squared differential with side a to concord with the rough deformation contact model.

Finally, the efficiency is thus calculated as:

$$\eta = \frac{M_1 \omega_1 - P_\mu - P_r - P_{s1} - P_{s2}}{M_1 \omega_1}$$

c. Shear stress & pressure allocation

In the 2D deformable, rough line contact the fluid pressure influence and other forces acting on the surface is allocated differently depending on the lubrication regime.

When there is full EHL the pressure of the fluid is applied on both surfaces following the Navier-Stokes solution, as such $\sigma = P(r, \theta, \omega_1, \omega_2, \mu, \rho, R_b, h)$ for every point of the line contact of each surface, therefore, the variation of the pressure across the fluid pressure is considered. The shear stress due to rolling and sliding are then divided even across the entire line contact, as the fluid acts equally on the entire surface, save pressure variations due to height alterations.

In BL or ML cases, the numerical solver already accounts for the pressure effect of the Navier-Stokes solution. If there is contact between surfaces, points where both surfaces touch, the formulation for allocating sliding and rolling resistance varies, such that the rolling resistance is allocated to said points, as for rolling resistance there needs to be surface engagement and the sliding forces are slightly modified to accommodate metal to metal contact, therefore, the surface stress follows the allocation logic and convergence equations:

$$F_m = \sum \mu_m a^2 w_{con} \quad F_{s_no} = \sum \mu a^2 w_{no} \quad F_s = F_{s_no} + F_m$$

Where F_m is the sliding resistance from a metal-to-metal contact, along with the metal-to-metal friction coefficient, μ_m and w_{con} is the stress experienced by every differential in contact with the opposing surface. On the other hand F_{s_no} represents the friction due to the fluid action and it's entirely dependent on the square differential size, a , the fluid's friction coefficient μ and the stress in differentials which are not in contact with the other surface w_{no} . Ensuring thus that the macroscopically calculated forces are verified by the model, since those are the precise formulations.

d. Navier-Stokes implementation

This solution relies on a pair of meshing teeth being approximated to a couple of rolling cylinders as seen below in Figure Summary 7. The simplifications accepted for this model were:

$$\begin{aligned} u_z &= 0 & \frac{\partial^i u_r}{\partial z^i} &= 0 \mid i \in \mathbb{N} \\ \frac{\partial u_i}{\partial t} &= 0 \mid i \in [\vec{r}, \vec{\theta}, \vec{z}] & \frac{\partial^i u_\theta}{\partial z^i} &= 0 \mid i \in \mathbb{N} \\ \vec{g} &= \begin{bmatrix} 0 \\ 3x1 \end{bmatrix} \end{aligned}$$

These simplifications imply the fluid does not move across the flank of the tooth, which, as it well known, is inherently false, however, this allows to model the movement of the fluid across the meshing of the flanks more simply. Considering the velocity in both \vec{r} and $\vec{\theta}$ to be independent

from \vec{z} allows for a fully decoupled two-dimensional model along the \vec{r} and $\vec{\theta}$ directions, which, represents uniform pressure across the fluid “layers”, thus resulting in varying pressures for two points in different z coordinates but same \vec{r} and $\vec{\theta}$ (due to the surface roughness), thus, respecting the pseudo-three-dimensional problem configuration proposed.

Considering the fluid velocity variation to be dependent of the angle position as well as the radius allows for the computation of the fluid compression as the points in the gear surface move closer together, thus 2 points in the same circumference having different pressures as they would be in different angles and therefore, the fluid will not behave as laminar throughout the model, which, would be a poor definition. The effects of gravity have been disregarded throughout the model, since, at its core it will operate with the film thickness provided by the corresponding EHL model.

Time effects have been disregarded since it would overcomplicate the model and increase the computational cost without adding too much information, since the model itself works by converging a set of stationary events.

To further solve the model, a velocity field is required, and for such, being consistent with the previously listed simplifications, the velocity field has been assumed to be turbulent and therefore, it presents a parabolic distribution through the fluid height.

$$h = h_o + (1 - \cos \theta)(r_1 + r_2)$$

As such, the fluid velocity can be rewritten as a function of height (and therefore, inherently, θ and the radius), therefore, the following system of equations can be solved:

$$\begin{cases} v(h) = Ah^2 + B^2 + C \\ v(\theta = 0, r = r_2) = \omega_2 r_2 \\ v(\theta = 0, r = r_1) = \omega_1 r_1 \end{cases}$$

Where A, B and C are the coefficients to be calculated, ω_i is the radial speed of the gear tooth (for the driving and driven gears 1 and 2 respectively). To solve the model, it's imperative to rely on a variable denoted as u_∞ which is widely regarded as the fluid velocity far away from the working surfaces (and the boundary layer thereby generated) and thus stable in time and space.

Either way, accepting, this definition of the fluid velocity represents u_θ , the continuity equation yields the velocity distribution as a function of the radius:

$$u_r = -\frac{1}{r}(r_1 + r_2)(2hA \sin \theta + B \sin \theta)(r + D) - C$$

Which, when applying the contour conditions whereby, in the meshing point $u_r = 0 \forall r$, then:

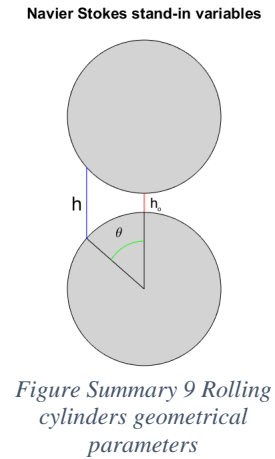
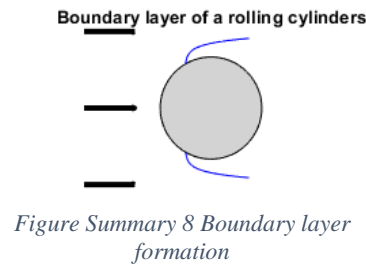
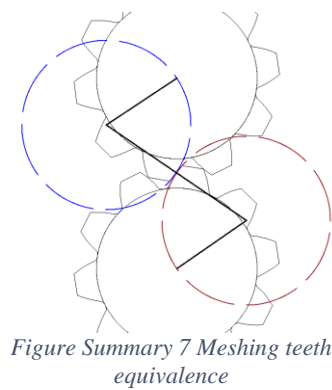
$$u_r = 0 \forall r \Leftrightarrow C = 0$$

Alternatively, an infinitely thin layer of fluid in contact with a moving solid will always move at the wall's speed, alas, the point at which the boundary layer starts can be described as:

$$P \mid \vec{u} = \begin{bmatrix} u_r = 0 \\ u_\theta = u_{wall} \end{bmatrix}$$

Whereby, due to the solidarity in movement, there is no radial component since the wall has exclusively movement in the $\vec{\theta}$ direction, alas, solving for D . Whilst the minimum separation shown in Figure Summary 9 is derived from the EHL model.

The novelty of this section lies in studying the pressure distribution across the thin oil film upon contact whilst also being able to describe both the velocity and pressure fields further away from the contact.



e. Outputs

As such the model can calculate the surface deformations of the contact between 2 gear teeth, both within the contact (elastic and plastic deformation) and after the contact (permanent or plastic deformation). From the lubrication formulations it can also output the oil film thickness and stemming from there, the pressure distribution across the oil film. Finally, other than speed and torque of the driven gear, it can estimate the efficiency of the gears meshing on top of the convergence history.

f. Surface generator training

To train the model, 80% will be allocated to the training set and 20% to the test set, no validation set was defined since the current implementation of the GPR model automatically fits the hyperparameters, making its own train/validation split internally (Scikit learn, 2022).

Before progressing towards model outcomes, it's worth noting the surface parameters extracted by the measurement acquisition instruments (KEYNECE VR-500) do not expand the entirety of the measurement length but a frame in the middle of the aforementioned, most likely to avoid noise due to the start and ending of the measuring length as seen below in Figure Summary 10 and Figure Summary 11.

Alas, the model will only be trained with data from that same range, 0.7 mm to 1.5 mm in the profile direction (there isn't enough distance along the tooth's involute to measure more than 1 cut-off length) and 0.5 mm to 10.9 mm in the lead direction (13 cut-off lengths).

From the literature review presented in (Santos, 2022) 2D and 3D measurements are not comparable, alas, an algorithm was set up in MATLAB to simulate the physical filtering that a stylus tip generates in the measurement data, as seen in Figure Summary 12, thus allowing to compare the 3D acquired measurements with normal 2D measurements which are normally used when tracking production. Alas, now both sets of data are comparable, regardless of their origin.

The GPR models were tested and subsequently analysed, both on their score (which percentage of the testing data they explained) and their marginal log likelihood (how well they explained the data).

The maximum score was 15% (without identifying labels) and a rotational quadratic kernel whilst when labelled, the score dropped to 13.4% (adding information such as finishing procedure, module, manufacturer...). The marginal log likelihood were poor overall. Testing all possible 3 parameter combinations as inputs. The three most relevant variables obtained by GPR were R_{max} , R_t and S_m . To verify the results ADR and regression trees were also employed, yielding both of them R_{max} , S_m and R_{sk} as the most relevant variables.

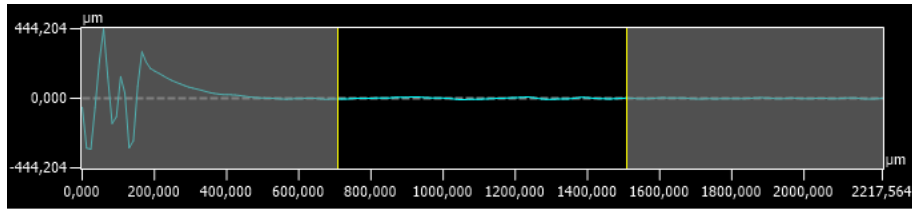


Figure Summary 10 Evaluation length in the profile direction

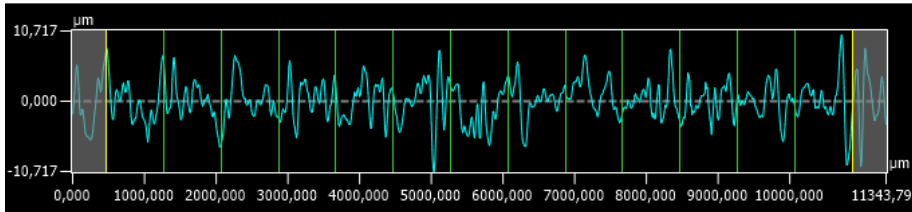


Figure Summary 11 Evaluation length in the lead direction

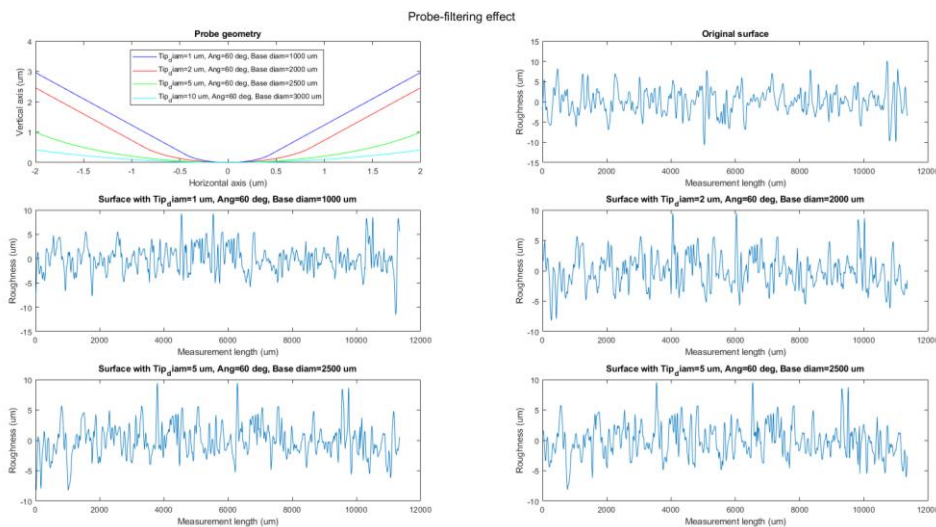


Figure Summary 12 Physical filtering for different probes

F. Evaluation & discussion

Since the lubricant estimator is remarkably sensible to lubricant physical properties (just like the mu coefficient estimator) as well as the surface roughness each module was evaluated separately. Once the entire model was verified by sections it was tested ensemble with a surface with remarkable pitting as seen in Figure Summary 13. Converging in under 75 seconds with every iteration for 100 iterations (Figure Summary 15) and yielding efficiencies ranging from 99.4635% to 98.4188%, which, although they are slightly high, are within the same region ($\pm 0.5\%$) of reference simulation software such as ROMAX and LDP.

Windage and churning losses were studied but ultimate they were deemed to contain too many inaccuracies that would hinder the model, in fact, they dropped efficiency as low as 84%, as seen in Figure Summary 15. The effect of considering pressure variation cross the fluid film thickness was also evaluated (in other words, the Navier-Stokes solution was put to the test). It was found not to affect the efficiency in any significant manner whilst providing a more realistic surface deformation and stress field, alas, it was deemed as a valid approximation.

The model was then tested with the same surface but a realistic lubricant (instead of a range of properties). The overall efficiency was 98.87% with surface deformation and its associated losses being more prominent where the defects were at the start, which agrees with the propagating effect seen in the literature.

It also showed there were stress concentrations up to 2 orders of magnitude greater in both contact stress and sub-surface stress (responsible for pitting propagation, see Figure Summary 16 and Figure Summary 17), alas, in concordance with the literature, where surface defects are a stress concentration point. Finally, the flash temperature increased wup to 60K where there was direct contact but only 24K where there was lubricant, validating its cooling effect.

Granted, the flash temperature module yields temperatures slightly lower than most literature but it's due to the static approximation instead of the transient configuration which these modules typically present.

The surface parameter analysis and generation showed the most appropriate kernel at 10 optimization runs to be the rotational quadratic kernel, whilst the RBF seemed to demand further optimization runs. The White kernel, a random noise specific kernel, failed to yield any significant results, alas, pointing towards some structure in the dataset, as expected from the literature, different finishing techniques will always yield a certain imprint in the surface.

The low score suggests further training data is needed (the 96 measurements were divided on an 80-20 ratio for training and testing).

This is further verified by the fact scores dropped when adding the labels, thus subdividing the dataset even further, which suggests underfitting and undertraining of the model. This can be tackled by adding measurements and therefore increasing the dataset. Overall, however, the surface could be properly depicted with only the 2 or 3 parameters previously listed (Rt, Sm and Rsk). The combination of Rt and Rmax yielded the highest score (see Figure Summary 19), but as discussed further down, they are very similar parameters and provide little in terms of additional information as Rmax is only the maximum of Rt. Therefore, the most relevant combination is that provided by Sm and Rt, framing vertical and horizontal requirements for the surface as seen in Figure Summary 19.

The rotational quadratic kernel also provided enough flexibility and width to the confidence intervals to encompass most of the provided dataset, as depicted in Figure Summary 18.

Rt is the average maximum height variation within of several cut-off length, whereas Rmax refers to the maximum height variation of the evaluation length, therefore, being more unstable. In fact, Rmax is no longer considered in new versions of ISO 219201. Sm refers to the percentage of the surface which is sectioned at the midplane. Rsk is the profile skewness, where is it's greater than 0 the surface tends to have more peaks and more valleys if vice versa.

It is inevitable to think the combination of this three refer to a vertical, horizontal and positioning parameters, suggesting, therefore, material ratio, which agrees with the literary references, as requirements to the Abbott-Firestone curve allow not only to set requirements but specify further requisites of the profile in all directions.

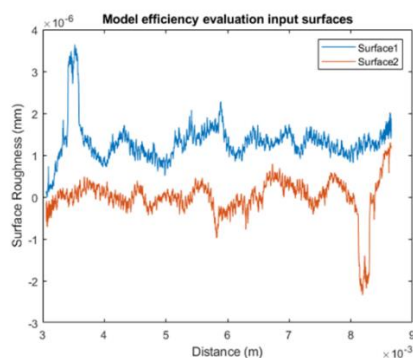


Figure Summary 13 Surface input

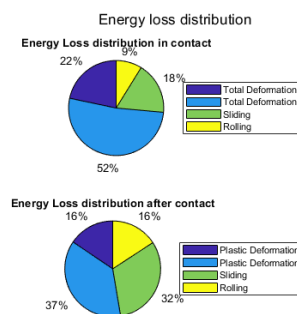


Figure Summary 14 Final efficiency and losses breakdown

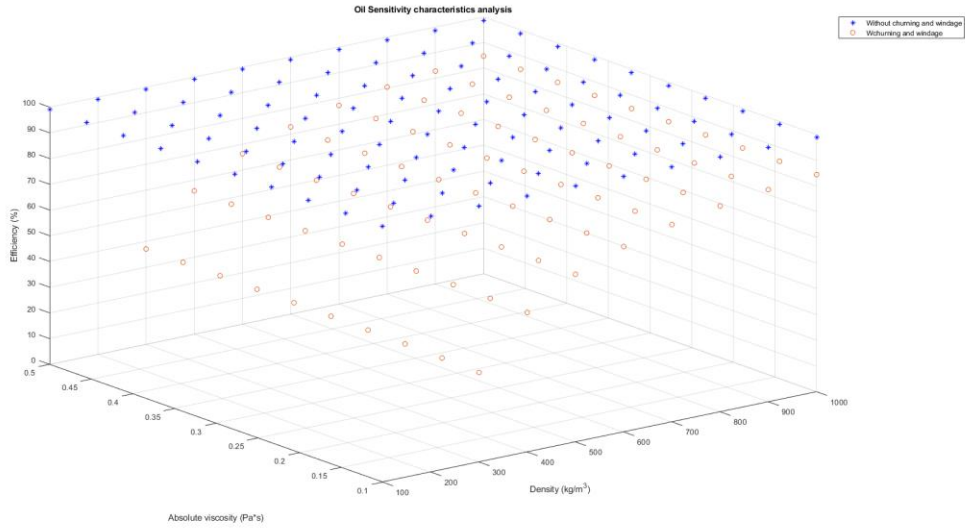


Figure Summary 15 Lubricant sensitivity analysis

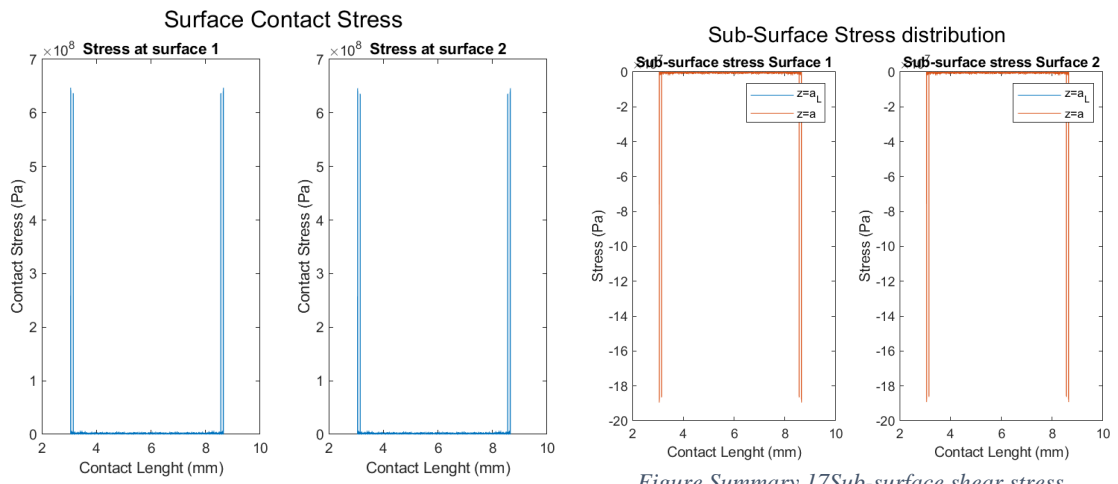


Figure Summary 16 Contact stress

Figure Summary 17 Sub-surface shear stress

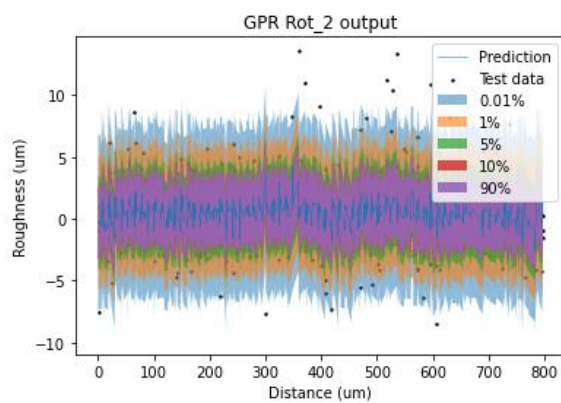


Figure Summary 18 Rotational quadratic results

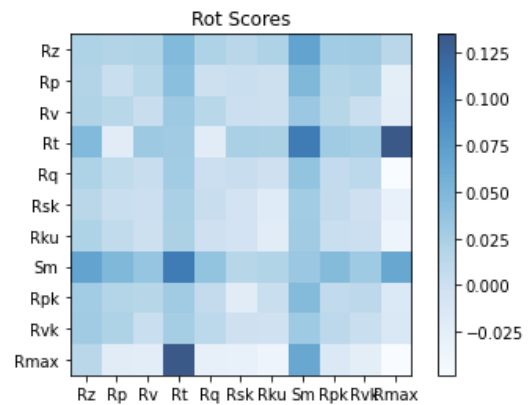


Figure Summary 19 Rotational quadratic Score distribution

G. Outlook

Clearly, the model can be further improved to accommodate a more accurate temperature module beyond the current one from essentially, adaptations of Fourier's law to better mimic the results

of both ROMAX and LDP (commercially available software used in the automotive industry to design, simulate and analyse transmissions).

The model could also be upgraded from a 2D stationary line contact model to a pseudo3D or full 3D by considering the area around the studied contact point (in the case of a pseudo 3D) as every line in the lead direction is considered (with the software running along the profile direction of the gear tooth) or a full 3D by considering the gear flank as a surface body (which would undoubtedly require FEM).

Perhaps it is more pressing the software be made transient and implement time-dependent factors directly into both the contact dynamics and specially in the lubrication definitions, as discussed.

The surface generating model should also be re-trained with heaps of data from a myriad of surface roughness measurements before, during (different stages) and after testing so a more complete picture of how the surface deforms (especially in the first cycles were running-in takes place) and thus it would be able to generate surfaces as they deform and change in real life, helping in the design and understanding of test definition and in turn improve real-life performance of electric transmissions.

Furthermore, a refined powder metal gears module should be implemented to allow for further R&D efforts to study their applications in future transmissions, reducing material usage and associated environmental impacts.

The modular nature of the model allows for further developments and introduction of additional functions such as NVH evaluation.

H. Sustainable development goals

The project is clearly encompassed into “Goal 9: Industry, Innovation and Infrastructure” since it the better understanding of gear behaviour when running and straight out of manufacture allow to push forward any electric vehicle transmission efforts, thus dealing with innovation. Since a better surface definition and a deeper understanding of its behaviour benefit industrial manufacturing processes, allowing for more appropriate and accurate surface requirements, alas, the industry segment of the goal. Having already comprehended the importance of surface roughness and its effect on efficiency the next step is clearly the adequacy of the manufacturing process and value creation chain, thus, yielding an infrastructure optimization to accommodate this new gear surface requirement reality since some current production techniques will undoubtedly be made redundant as they fail to meet requirements.

Understanding of the effect of the several factors hereby discussed on gear efficiency falls in the category of “Goal 12: Responsible Consumption and Production” since it aims to provide all attainable benefits whilst minimizing natural resources utilization. A prime example is the more accurate definition of surface roughness requirements, since all production equipment parameters can be adjusted to increase utilization whilst reducing waste: speeds, cutting depths, pre-emptive maintenance, manufacturing deviation within specifications...

Finally, Goal 13: Climate Action is present across the entire project. From the manufacturing end of the project, where a reduction in material consumption and energy usage amongst others inherently reduces the carbon footprint and ameliorates the lifecycle assessment of any and all electric driveline transmissions. Furthermore, with the number of electric vehicles set to increase as the CAFE requirements tighten on OEMs and combustion engines are left behind, any efficiency increase through the entire power delivery chain not only would increase the drivable range of vehicles but would also reduce wasted energy and thus reduce energy desideratum and associated undesirable climatic side effects as energy production is still not 100% renewable, thus, every time an electric vehicle is recharged, new CO₂ is released, although less than with and ICE.

Executive Summary: References

- al, H. e. (2007). Prediction of Mechanical Efficiency of Parallel-Axis Gear Pairs. *Journal of Mechanical Engineering* 129, 58-68.
- al, I. G. (2014). Generative Adversarial Nets. *Proceedings of the International Conference on Neural Information Processing Systems* (pp. 2672-2680). Montréal: International Conference on Neural Information Processing Systems.
- Björklund, S. (1995). *Elastic contacts between rough surfaces*. Stockholm: KTH.
- Brownlee, D. J. (2019, 07 17). *Machine Learning Mastery*. Retrieved from A Gentle Introduction to Generative Adversarial Networks (GANs): <https://machinelearningmastery.com/what-are-generative-adversarial-networks-gans/>
- Brownlee, D. J. (2019, 07 19). *Machine Learning Mastery*. Retrieved from A Gentle Introduction to Generative Adversarial Networks (GANs): <https://machinelearningmastery.com/what-are-generative-adversarial-networks-gans/>
- Chapter 2: Overall Methodology. (2005). In H. Xu, *DEVELOPMENT OF A GENERALIZED MECHANICAL EFFICIENCY PREDICTION METHODOLOGY FOR GEAR PAIRS* (p. 30). Columbus: Ohio State University.
- C-Therm. (2022, 04 25). *C-Therm*. Retrieved from Thermal Resistance and Thermal Conductance: <https://ctherm.com/resources/helpful-links-tools/thermalresistanceandconductivity/>
- Donges, N. (2021, 07 29). *Builton*. Retrieved from A Guide to RNN: Understanding Recurrent Neural Networks and LSTM Networks: <https://builton.com/data-science/recurrent-neural-networks-and-lstm>
- Fumo, D. (2017, 08 04). *Towards Data Science*. Retrieved from A Gentle Introduction To Neural Networks Series — Part 1: <https://towardsdatascience.com/a-gentle-introduction-to-neural-networks-series-part-1-2b90b87795bc>
- Hui, J. (2018, 06 19). *Jonathan Hui*. Retrieved from GAN — What is Generative Adversarial Networks GAN?: <https://jonathan-hui.medium.com/gan-whats-generative-adversarial-networks-and-its-application-f39ed278ef09>
- Ishizaki, T., & Nagano, T. I. (2020). Measurement of local thermal contact resistance with a periodic heating method using microscale lock-in thermography. *Review of Scientific Instruments*, 91: 064901.
- James. (2020, 06 24). *Stats Exchange*. Retrieved from Linear Regression for Noisy Data: <https://stats.stackexchange.com/questions/473850/linear-regression-for-noisy-data>
- Jonny Hansen, M. B. (2021). A New Film Parameter for Rough Surface EHL Contacts with Anisotropic and Isotropic Structures. *Tribology Letters* 69:37, 1-17.
- Kadiric, P. R. (2019). The influence of side-roll ratio on the extent of micropitting damage in rolling-sliding contacts pertinent to gear applications. *Tribology Letters*, 67:1-20.
- L. Xiao, S. B. (2007). The influence of surface roughness and the contact pressure distribution on friction rolling/sliding contacts. *Tribology international*, 40:4:694-698.
- Marcello De Bernardi, M. K. (2018). Pseudo-Random Number Generation using Generative Adversarial Networks. *Nemesis 2018, UrbReas 2018, SoGood 2018, IWAISe 2018, and Green Data Mining 2018* (pp. 1-10). Dublin: Springer International Publishing.
- Masse, S. L. (2019). On the flash temperature under the starved lubrication condition of a line Contact. *Tribology International*, 136: 173-181.

- Optimization Geeks. (2021, 10 31). *Youtube*. Retrieved from Easy introduction to gaussian process regression (uncertainty models): <https://www.youtube.com/watch?v=iDzaoEwd0N0>
- Pandurangi, A. B. (2020). *Electric Transmission System efficiency Simulation*. Gothenburg: Chalmer's University of Technology.
- Rocca, J. (2019, 01 07). *Towards Data Science*. Retrieved from Understanding Generative Adversarial Networks (GANs): <https://towardsdatascience.com/understanding-generative-adversarial-networks-gans-cd6e4651a29>
- Rowe, W. B. (2014). 18 - Energy Partition and Temperatures. In W. B. Rowe, *Principle of Modern Grinding Technology* (pp. 381-420). Norwich: William Andrew Publishing.
- Santos, D. J. (2022). *A study on surface characterization of gears and the measurement problem*. Győr: Széchenyi István University.
- Scikit learn. (2022, 04 29). *Scikit learn*. Retrieved from `sklearn.gaussian_process.GaussianProcessRegressor`: https://scikit-learn.org/stable/modules/generated/sklearn.gaussian_process.GaussianProcessRegressor.html
- Sit, H. (2019, 06 19). *Towards Data Science*. Retrieved from Quick Start to Gaussian Process Regression: [https://towardsdatascience.com/quick-start-to-gaussian-process-regression-36d838810319#:~:text=Gaussian%20process%20regression%20\(GPR\)%20is,uncertainty%20measurements%20on%20the%20predictions.](https://towardsdatascience.com/quick-start-to-gaussian-process-regression-36d838810319#:~:text=Gaussian%20process%20regression%20(GPR)%20is,uncertainty%20measurements%20on%20the%20predictions.)
- Sosa, M. (2017). *Running-in of gears- surface and efficiency transformacion*. Stockholm: KTH.
- Tim. (2017, 01 17). *Stackexcahnge*. Retrieved from Understanding the randomness of y in linear regression model: <https://stats.stackexchange.com/questions/256998/understanding-the-randomness-of-y-in-linear-regression-model>
- Wang, Y. W. (2013). Stribeck Curves. In Y. W. Wang, *Encyclopedia of Tribology* (pp. 3365-3370). Boston: Springer.
- Wei, J. (2015). A Study of Spur Gear Pitting under EHL Conditions: Theoretical ANalysis and Experiments. *Tribology International* 94, 146-154.
- Williams, D. (2010, 09 21). *Talk Stats*. Retrieved from Is there a non parametric alternative to multiple linear regression?: <http://www.talkstats.com/threads/is-there-a-non-parametric-alternative-to-multiple-linear-regression.13721/>
- Zhou, C., Xing, M., & Hu, H. W. (2021). A novel thermal network model for predicting the contact temperature of contact gears. *International Journal of Thermal Sciences*, 161:106703.

MODELLING OF GEAR SURFACE ROUGHNESS IMPACT ON ELECTRIFIED TRANSMISSIONS' EFFICIENCY

Author: Victoria Rodríguez, Ignacio

Director: Xanthi, Foteini

Entidad Colaboradora: Volvo Car Corporation

Memoir

I. Table of Contents

1.	Introduction	1
1.1.	Master thesis outline.....	1
1.2.	Master thesis objective	1
1.3.	Research questions	1
2.	State of the Art	2
2.1.	Gear History	2
2.2.	Gears in electric drivelines.....	2
2.3.	Gear Properties & Characteristics	3
2.4.	Gear Manufacturing	5
2.4.1.	Forming	5
2.4.2.	Machining.....	6
2.4.3.	Hardening	7
2.4.4.	Finishing.....	8
2.5.	Abbot curve and surface roughness.....	9
2.5.1.	Amplitude parameters	10
2.5.2.	Spacing parameters	10
2.5.3.	Hybrid parameters	10
2.5.4.	Abbott-Firestone curve.....	11
2.6.	Gear surface damage & transformation.....	12
2.6.1.	Scuffing	12
2.6.2.	Micro pitting.....	12
2.6.3.	Pitting	13
2.6.4.	Running-in.....	14
2.7.	Powder Metal Gears	15
2.8.	Sustainability	19
3.	Contact modelling	21
3.1.	Hertzian Contact.....	21
3.2.	Surface deformation modelling.....	22
3.2.1.	Theoretical background.....	22
3.2.2.	Contact model evaluation.....	24
3.3.	Rough contact modelling approximation	26
3.3.1.	Theoretical background.....	26
3.3.2.	Contact model evaluation.....	28
4.	Model adaptation.....	32
4.1.	Rolling and sliding forces modelling	32
4.2.	Navier-Stokes equations & elasto-hydrodynamic lubrication.....	35
4.3.	Stress allocation.....	44
4.4.	Fluid model testing.....	44
4.5.	Thermal effects.....	46
4.6.	Churning and Windage Losses.....	49
4.7.	Model's lubricant sensitivity analysis & validation	53
4.8.	Efficiency and losses calculations.....	55
4.9.	Sintered gears implementation	55
4.10.	Model outputs.....	55
4.11.	Model Summary	61
5.	Surface measurement & characterization.....	62
5.1.	2D measurements	62
5.2.	3D measurements	66
5.3.	Acquisition system comparison and equivalence.....	68

Modelling of gear surface roughness impact on electrified transmissions' efficiency
Index

6.	Surface modelling and generation.....	73
6.1.	Model selection and discussion.....	73
6.2.	Data preparation	82
6.3.	Surface model output and discussion	83
7.	Sustainability and SDG alignment	92
8.	Conclusions	93
9.	Outlook and future work	94
10.	References	95

II. Table of Figures

Figure 1 Involute construction (Glinsky, 2022)	3
Figure 2 Gear tooth geometry (Rackov, Veres, & Kuzmanovic, 2013).....	3
Figure 3 Gear diameters and main geometry (KHK Stock gears, 2022).....	4
Figure 4 Helical gear module (KHK Stock gears, 2022)	4
Figure 5 Maag method (Espinel, 2021).....	7
Figure 6 Fellow's method (Espinel, 2021).....	7
Figure 7 Gear hobbing (Espinel, 2021).....	7
Figure 8 Cut-off and evaluation length	9
Figure 9 Abbot-Firestone curve example (J.C. Vasco, 2006).....	11
Figure 10 Steel powder material and energy flow diagram (José M.C. Azevedo, 2018).....	19
Figure 11 Hertzian Contact representation.....	21
Figure 12 Line contact approximation from Hertzian contact definition (Hansen, 2021)	22
Figure 13 Stiffness variation with length ($E=210\text{GPa}$, $Re=235\text{MPa}$, $A=0.005^2\pi$)	24
Figure 14 Lamé's approximation starting surfaces.....	24
Figure 15 Lamé's approximation convergence history.....	25
Figure 16 Lamé's approximation deformed surfaces	25
Figure 17 Lamé's approximation stress and distortion energy	26
Figure 18 Rough contact stress example.....	27
Figure 19 Subsurface stress example	28
Figure 20 Starting surfaces rough contact model evaluation	29
Figure 21 Rough contact evaluation convergence history	29
Figure 22 Deformed surfaces rough contact evaluation.....	30
Figure 23 Contact stress rough contact model evaluation.....	30
Figure 24 Shear stress rough contact model evaluation	31
Figure 25 Surface deformation energy rough contact evaluation	31
Figure 26 Model's block diagram	32
Figure 27 Gear tooth profile representation (Slogén, 2013)	36
Figure 28 Stribeck curve (Wang, 2013).....	37
Figure 29 Fluid velocity profile over a rolling cylinder (IIT Bombay Alumni, 2022).....	38
Figure 30 Navier-Stokes stand in contour variables	38
Figure 31 Boundary layer representation	40
Figure 32 Traditional EHL parameter depiction (Jonny Hansen, 2021)	41
Figure 33 Adapted h^* model representation	42
Figure 34 Navier Stokes surface pressure divergence.....	45
Figure 35 Navier Stokes surface pressure divergence in large gaps	45
Figure 36 Thermal configuration differential contact	46
Figure 37 Heat flux distribution across the meshing flank (left) and flash temperature solver proposal (right) (Zhou, Xing, & Hu, 2021).....	47
Figure 38 Flash temperature across the contact	48
Figure 39 Surface deformation across the contact	49
Figure 40 CFD-Mauz comparaison (Gorla, 2016).....	50
Figure 41 Changenet & Vexel model validation (al M. N., 2020).....	51
Figure 42 Comparison between tests and modelized windage losses (Diab, 2005).....	52
Figure 43 Real surface measurement example.....	53
Figure 44 Efficiency sensitivity analysis to lubricant properties	54
Figure 45 Sample surface module output.....	57
Figure 46 Sample contact stress output.....	57
Figure 47 Sample detail output of contact stress.....	57
Figure 48 Sample sub-surface stress output	58

Figure 49 Sample detail output of sub-surface stress	58
Figure 50 Sample flash temperature output	58
Figure 51 Sample energy loss distribution output.....	58
Figure 52 Sample convergence history output.....	59
Figure 53 Command prompt messages 1	59
Figure 54 Command prompt messages 2	60
Figure 55 Final model output summary	60
Figure 56 Model block diagram	61
Figure 57 Raw surface measurement data.....	62
Figure 58 Automatic model accuracy selection	63
Figure 59 Nominal form polynomial extracting comparison	63
Figure 60 Surface measurement regression and extracted roughness	64
Figure 61 Surface measurement distribution and cumulative distribution.....	64
Figure 62 Surface roughness calibration sample.....	65
Figure 63 Line roughness calibration sample 1.....	65
Figure 64 Line roughness calibration sample 2.....	65
Figure 65 Smoothing effect in contact profilometry (Cho, 2012).....	66
Figure 66 White light interferometry assembly (nanoScience Instruments, 2022).....	67
Figure 67 Probe mimicking surface roughness	69
Figure 68 Optical measurement acquisition: Lead and profile measurements (right) and surface capture (left of a sun gear).....	70
Figure 69 Meshed sun gear & planet gear.....	70
Figure 70 Planetary assembly CAD	70
Figure 71 Profile shift coefficient visualization	72
Figure 72 Profile crowning visualization	72
Figure 73 Gear profile deviation after testing	73
Figure 74 Unfolded RNN	74
Figure 75 LSTM architecture	75
Figure 76 CGAN structure	76
Figure 77 Linear regression on surface sample.....	77
Figure 78 GPR confidence intervals at 99.9% of a real measurements	78
Figure 79 Fixed boundary optimization kernel comparison	80
Figure 80 Underfitting warning message	83
Figure 81 Evaluation length of 2-line measurements in the profile direction.....	83
Figure 82 Evaluation length of 1line measurements in the lead direction and it's extracted roughness.....	83
Figure 83 Default GPR model results	84
Figure 84 Exponential Sine GPR model results.....	84
Figure 85 Matérn GPR model results.....	84
Figure 86 Rotational Quadratic GPR model results.....	84
Figure 87 White GPR model results	85
Figure 88 RBF GPR model results.....	85
Figure 89 Regression tree for variable significance.....	85
Figure 90 Parameter selection representation (Marghalani, 2010)	86
Figure 91 Reduced default GPR model results	86
Figure 92 Reduced RBF GPR model results.....	86
Figure 93 Reduced White GPR model results.....	87
Figure 94 Reduced Exponential Sine GPR model results	87
Figure 95 Reduced Rotational Quadratic GPR model results	87
Figure 96 Labelled input RBF GPR model.....	88
Figure 97 Labelled input Rotational Quadratic FPR model.....	88

Figure 98 RBF scores colour map without labels	88
Figure 99 RBF score distribution without labels.....	88
Figure 100 RBF Log Margin colour map without labels	89
Figure 101 RBF Log Margin distribution without labels.....	89
Figure 102 Rot scores colourmap without labels	89
Figure 103 Rot score distribution without labels	89
Figure 104 Rot Log Margin colour map without labels.....	89
Figure 105 Rot Log Margin distribution without labels.....	89
Figure 106 RBF scores colourmap with labels	90
Figure 107 RBF score distribution with labels.....	90
Figure 108 RBF Log Margin colour map with labels	90
Figure 109 RBF Log Margin distribution with labels	90
Figure 110 Rot scores colourmap with labels	91
Figure 111 Rot score distribution with labels	91
Figure 112 Rot Log Margin colour map with labels	91
Figure 113 Rot Log Margin distribution with labels.....	91
Figure 114 SDG 9 (United Nations, 2022)	92
Figure 115 SDG 12 (United Nations, 2022)	92
Figure 116 SDG 13 (United Nations, 2022)	92

III. Table of Tables

Table 1 Adimensional EHL coefficients	41
Table 2 Velex and Chagnenet's coefficients	51
Table 3 Variables portrayed example.....	56
Table 4 Surface roughness probe filtering output	69
Table 5 Measured Gears' characteristics	70
Table 6 Input variables for the surface model.....	71
Table 7 Sample kernel evaluation	81
Table 8 First GPR model results	84
Table 9 ARD significance results 1.....	85
Table 10 ARD significance results 2.....	85
Table 11 Refined GPR training with different kernels.....	86
Table 12 Relevant parameters and kernels optimization with labels	87
Table 13 Unlabelled model details	89
Table 14 Labelled model details	91

1. Introduction

For many a century, gears, be it in their most primitive form to modern solutions, have been paramount in the transfer of mechanical power for a plethora of applications.

Alas, it is essential modern gear utilization challenges are dealt with in order to push lightweight automation electrification forward towards an eco-friendly future.

Although a pair of gear meshing is one of the most efficient means of mechanical power transfer, it's paramount the underlying mechanism found therein are fully understood and in turn modified.

OEMs are scrambling to better suit this new mobility, ultra-connected reality where emissions are heavily penalized by the authorities and range anxiety governs consumer behaviour when choosing between a traditional internal combustion engine or a modern solution (hybrid or full electric vehicles).

1.1. Master thesis outline

This Master thesis follows the same structure as the research project followed. Firstly, a brief introduction on the subject of gears and torque transfer has been made, then a literature review on powder metal gears, their applications and limitations. A set of contact models are studied and modified based on available literature and development of new theoretically based equations, verified with newfound literature. Said models' convergence and output are evaluated in a variety of fields, from deformation and stress to surface temperature approximation and lubricant sensitivity without forgetting the end goal, modelling efficiency.

1.2. Master thesis objective

The aim of this Master thesis is to conduct a study on the tribological mechanisms; surface parameters and power transmission of gears, correlating those to scuffing and efficiency in electrified transmissions. To achieve said objective, a surface contact model will be proposed to analyse the surfaces, their losses and their efficiency. Said model will in turn be compared against the available LDP calculations to assess both precision and accuracy. Simultaneously, a machine learning algorithm will be proposed to model and predict surfaces from a small list of surface parameters with measurement data being acquired with 2 and 3 dimensional techniques.

1.3. Research questions

This Master thesis seeks to explore powder metal gears and their application in powertrains and how their surface characteristics might affect their performance. Alas, the main research question of this Project is:

- What is the relationship between the surface and performance (scuffing and efficiency) of a gear mesh?

From this main question, a number of secondary questions arise:

- What are the lubrication mechanisms for a given lubricant and can it be accurately predicted?
- Can the surface behaviour in different lubrication regimes be accurately modelled?
- Can a surface be directly correlated to a small set of surface characterization parameters?

2. State of the Art

2.1. Gear History

It's unclear when the first man-made gears arose but it's reasonable to assume it succeeded the invention of the wheel (Apex Dynamics, 2022). Gears are the continuation of friction wheels, able to transfer more power and remain synchronized without an upper limit determined by the friction coefficient of 2 friction wheels.

The earliest example of a gear implementation dates back to 2700 B.C.E. (Apex Dynamics, 2022), with the renowned Chinese South-Pointing Chariot which contained a gear which would automatically point and arrow south regardless of the chariot's bearing (FGM, 2022). Several differential-like systems are also mentioned in unofficial writings dating back to 800 B.C.E. in China (Apex Dynamics, 2022). These early gears consisted of wooden disks with wooden pegs press fitted in their exterior diameter, allowing for easy maintenance since any broken tooth could be easily and individually serviced (Apex Dynamics, 2022).

Moving forward, in the 400 B.C.E. Aristotle is credited with the first detailed description of a gear (Apex Dynamics, 2022). As per his definition, these elements were capable of reversing the direction of momentum. Artifacts with gears at their core dating back to this time have also been found. As of the year 100 B.C.E. metal gears with cylindrical teeth were commonly used in complex "computing" machines and astronomical calendars such as the Antikythera Mechanism containing upwards of 30 gears (Apex Dynamics, 2022).

As of the 17th century efforts to yield constant velocity ratios between meshing gears resulted in the involute curve (UGEARS, 2022).

By the 19th century cutters and rotating cutters were first used in the manufacture of gears when in 1835 Joseph Whitworth patented the first worm gear hobber which he later perfected along with Christian Schiele (UGEARS, 2022). By 1897 Herman Pfauter invented the first machine of cutting spur and helical gears (UGEARS, 2022).

The next big step forward came in 1975 when the Pfauter Company introduced the first numerically controlled hobbing machines and in 1982 the first full 6-axis CNC (UGEARS, 2022).

2.2. Gears in electric drivelines

Ever since the first Ford model T exited Highland Park Plant the automotive industry boomed and demand for these new machines skyrocketed. Paired with this newfound market, internal combustion engines (ICEs) and its ancillaries also grew. As cars gained in both speed and power the transmission became ever-increasingly complex, from a simple 1-speed model to automatic 8-speed gear boxes without forgetting the classical manual transmissions which dominated 20th century markets along with several differential configurations. All these moving parts increase in number and complexity until the dawn of the electric drivelines.

ICEs rely exclusively on their power-rpm (or torque-rpm) curves. Different speeds aim to keep the engine as close to its optimal working point as possible. However, electric machines can operate in a broader range of speeds with much higher efficiencies (upwards of 98% efficiency) than ICEs (maximum of 35%), alas, the transmissions could be simplified, and the number of gears therein reduced, which in turn aided in vehicle weight reduction. This gear number reduction implies that the remaining gears must operate across the entire rpm-torque domain of the electric machine (adjusted by the reductor).

Most hybrid and early electric vehicles rely on planetary transmissions rather than multi-axial gearbox transmissions since it allows for easy implementation of different driving modes and transmission ratios.

2.3. Gear Properties & Characteristics

Modern gears are governed by 3 key parameters, the module; pressure angle and the number of teeth in each component. The module is a unit of length which determines the size of the teeth, whilst the pressure angle determines the inclination of the line which the contact follows. Finally the number of teeth determines the size of the element and the transmission ratio.

This constant direction which the force follows is thanks to the involute profile of the gear flanks. The involute curve is described as the geometric curve that can be described by the trace of unwrapping a taut string which is tangent to the base circle (Glinsky, 2022).

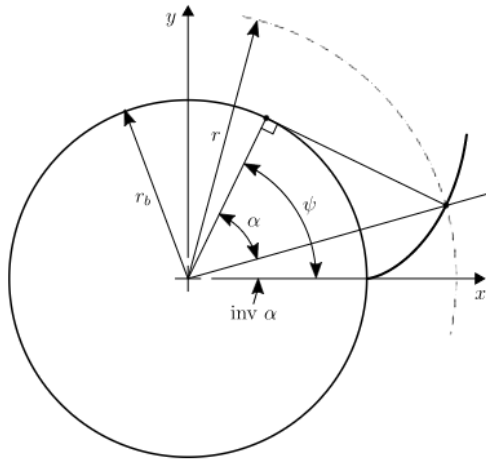


Figure 1 Involute construction (Glinsky, 2022)

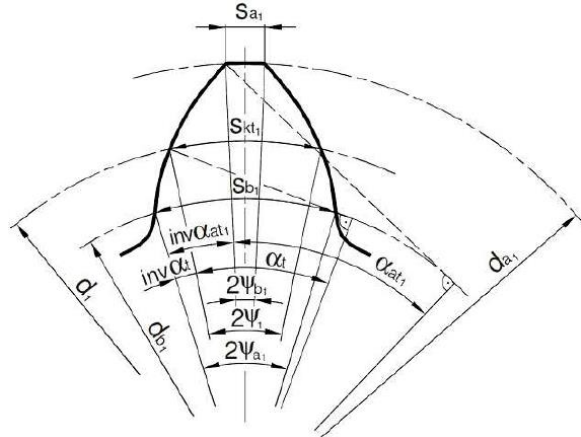


Figure 2 Gear tooth geometry (Rackov, Veres, & Kuzmanovic, 2013)

The involute is described by the involute is described by the pressure angle α , by the function:

$$inv \alpha = \tan \alpha - \alpha$$

As a result of this definition, the contact line is always tangent to the base circle, as such, the base circle for the involute in any gear can be defined as:

$$d_b = zm * \cos (\alpha)$$

The tip of any gear tooth is known as the addendum whilst the bottom is known as the root or dedendum, together they determine the gear tooth height as per the equations:

$$\begin{aligned} h_a &= m \\ h_f &= 1.25m \\ h &= h_f + h_a \end{aligned}$$

The tooth half-thickness (s_y) at any diameter (d_y) can be computed from the following formulae:

$$\begin{aligned} \Psi_y &= \frac{\pi}{2z} + 2 \frac{\tan \alpha}{z} + \tan \alpha - \alpha + \tan \left(\arccos \frac{zm \cos \alpha}{d_y} \right) - \arccos \frac{zm \cos \alpha}{d_y} \\ s_y &= d_y \Psi_y \end{aligned}$$

Where Ψ_y is the half-angle of the tooth width at the given diameter.

To determine the radial limits of a tooth, the tip and root diameters are employed, which, depend purely on the module (m) and number of teeth (z). These are both obtained from minor modifications to the pitch diameter (intersection contact line, centre line):

Modelling of gear surface roughness impact on electrified transmissions' efficiency
 2. State of the Art

$$d = zm$$

$$d_a = m(z + 2)$$

$$d_f = m(z - 2.5)$$

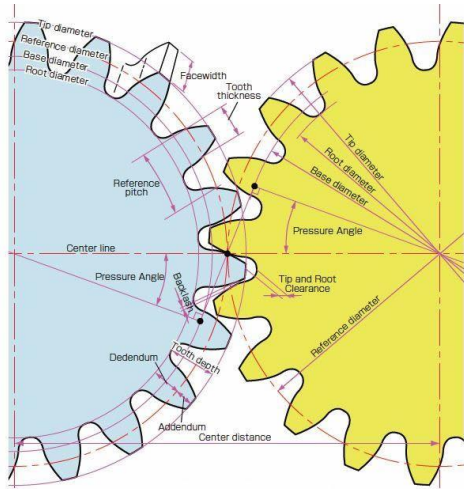


Figure 3 Gear diameters and main geometry (KHK Stock gears, 2022)

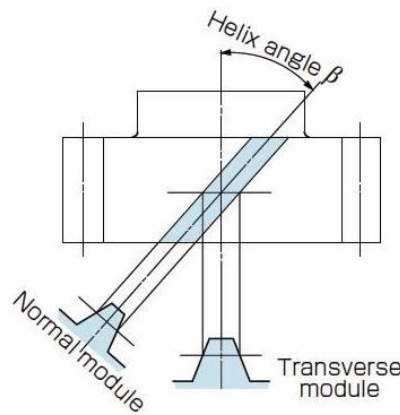


Figure 4 Helical gear module (KHK Stock gears, 2022)

Alas, the centre distance (a) can be calculates as:

$$a = d_1 + d_2 = m(z_1 + z_2)$$

Whilst the tooth clearance, c is:

$$c = 0.25m$$

Any straight tooth gear can be converted to a helical gear employing the helix angle, β .

Helical gears not only are quieter than straight or spur gears but can transfer greater forces (thanks to the increased length due to the angled projection), this follows the formula:

$$m_t = \frac{m_n}{\cos \beta}; \quad \alpha_t = \text{atan} \left(\frac{\tan \alpha}{\cos \beta} \right)$$

Where m_n is the normal module; m_t is the transversal module (and the one to employ in all subsequent calculations) and α_t is the transverse pressure angle.

A final element essential when determining a gear tooth's geometry is the profile shift coefficient, which related to the displacement of the cutting tool, thus modifying the tooth's thickness (KHK Stock gears, 2022), it is commonly referred to as a coefficient multiplying the module and is represented by the symbol X.

In any pair of gears, the transmission ratio a direct function of the number of teeth of each gear:

$$i = \frac{\omega_2}{\omega_1} = \frac{z_1}{z_2}$$

The moment transferred by the gear pair can be expressed in a similar manner, derived from power input-output balance (considering efficiency, represented as η):

$$M_2 = \frac{\omega_1}{\omega_2} M_1 \eta = \frac{z_2}{z_1} M_1 \eta = \frac{M_1 \eta}{i}$$

The force transferred by the teeth, thus becomes (where the i subindex refers to the driving or driven gear respectively):

$$F_i = \frac{2M_i}{mz_i \cos \alpha}$$

2. State of the Art

In any gear, the active flank is always referred to as the driving flank and the opposing flank is known as coast flank. Similarly, the gear flank is divided in 2 directions lead (parallel to the pitch line) and profile (from addendum to dedendum).

It's fairly common to include other modifications in gear teeth to tackle misalignments which can create unfavourable loading conditions. Tip or root relief modifies the involute shape of the flank to facilitate a smoother entrance of the gear into the contact whilst crowning modifies the ends of the flank in the lead direction to ensure the bulk of the load is carried by the centre of the tooth even when misaligned (Slogén, 2013). Crowning also acts as end reliefs, preventing stress concentration on the edges.

Prime amongst all gear parameters lies the working pressure angle (in spur gears, α_w) or radial working pressure angle (for helical gears, α_{wt}), as per the formulae:

$$\alpha_w = \arccos\left(\frac{\cos \alpha}{\frac{2\Delta a}{a} + 1}\right) = \arccos\left(\frac{\cos \alpha}{\frac{2y}{z_1 + z_2} + 1}\right) \mid \Delta a = ym$$

$$\alpha_{wt} = \arccos\left(\frac{\cos \alpha}{\frac{2\Delta a}{a} + 1}\right) = \arccos\left(\frac{\cos \alpha_t}{\frac{2y \cos \beta}{z_1 + z_2} + 1}\right)$$

This allows yields the new pressure angle of the gears for when a radial displacement is encountered Δa modifying the centre distance from the original one defined at the starting pitch point, thus altering the functioning of the gear pair. This Δa can in turn range from $-\cos \alpha$, where both base circles are in contact (and thus $\alpha_w = 90^\circ$) to $2m$ where the gears would be out of mesh and no power would be transferred.

2.4. Gear Manufacturing

Gears can be manufactured with a broad range of technologies; however, the general flowline follows these steps in order:

- Forming
- First heat treatment (if required)
- Machining
- Hardening
- Finishing
- Inspection

2.4.1. Forming

Traditional forming operations allow operators to obtain a rough shape of the gear, reducing material waste if compared to cutting a gear straight from a blank. Depending on the procedure followed different results are possible in industrial applications (Madhusanka, 2021):

Sand casting: Can be employed to obtain a rough blank or a semi-finished gear geometry but with a poor surface finish. This process requires melting the base material; therefore it is somewhat limited on the materials it may use but it also removes any kind of defect the blank may have had prior to the treatment, allowing the manufacturer to control the quality of the material at the start of the manufacture process. Gears can be used straight from this application if noise is not a constraint nor geometrical accuracy but in industrial applications it is only the first step of the process and never the end-step (Madhusanka, 2021).

Die casting: It's particularly important in the manufacture of non-ferrous gears and can be combined into hot and cold chamber castings. These gears have a higher surface quality and

2. State of the Art

accuracy. It's compatible with high volume production in certain situations but tooling costs are remarkably high (Madhusanka, 2021).

Injection moulding is commonly used for plastic gears in toys and low torque applications where precision is not paramount.

Extrusion and cold drawing process are also employed since they do not require a heating component and therefore its material can preserve any heat treatment which was completed upstream. Since there is no heating involved, no thermally induced stress or heat-associated stress are produced, alas, gears manufactured with this technique are more precise and can go straight into machining (Madhusanka, 2021).

Just as with the stamping does not require heat application and allows for higher volume production but it's limited in early shape complexity and thickness (Madhusanka, 2021). As of today, hot stamping in the automotive industry is sprightly limited to Body in White techniques since the high-performance properties of these materials would result in very high tooling and maintenance costs. Gears manufactured from forming techniques typically benefit from unbroken grain-flow patterns and strain hardening (al P. K., 2021).

2.4.2. Machining

There are three main methods employed to manufacture gears: the Sunderland method; gear shaping and gear hobbing (Espinel, 2021).

The Sunderland (or Maag) method uses rack-type cutters with specific rake and clear angles to generate a gear tooth geometry from a blank (Bergstedt, 2021). To do so it relies on a specific relative motion between the tool and the blank during the machining process. Overlapping each cutter pass with a small offset generates the tooth's involute profile. This method excels at creating teeth with a uniform shape, and, if all gears are cut by the same tool (and tool wear is insignificant) the pair of gears should mesh perfectly, even herringbone gears (Espinel, 2021).

Gear shaping (or Fellow's method) uses a rack cutter connected to the blank mechanically by a gear chain so both pieces don't roll together as the cutter reciprocates. Slowly, the cutter starts to penetrate the blank (until it reaches the desired depth) as it generates the tooth profile in the blank.

This method is commonly employed when fabricating spur, herringbone and ratchet gears. It can be used for other types as well but due to the reciprocating gear pair these are the simplest to implement. Due to precision requirements this method may not be suitable for internal gears or worm gears (Espinel, 2021). A great benefit when compared with the Maag method is its ability to manufacture internal gears (Bergstedt, 2021).

Finally, hobbing. It generates a gear by rotating a cylindrically shaped mandrel with slightly overlapped cutters positioned radially and at an angle, said cutter is called a hob. The hob can have several threads depending on the number of teeth cut per revolution. Helical gears tend to be manufactured following this procedure (Espinel, 2021). More appropriately, the hob is a single tooth worm gear cut perpendicularly to the rolling direction in several small sections (Bergstedt, 2021). The hobbing end quality directly depends on the tool quality and wear; workpiece precision and machine kinematics, as an example, dry gear hobbing can produce up to IT 5 DIN quality parts (Krömer, Sari, & Brecher, 2016). Hobbing generates a mesh of surface roughness intersection feed marks and generated cuts, with the first taking place in the lead direction and the later in the profile direction. The height of the feed marks directly depends on the axial speed and outer hob diameter and generally are greater than that of the generated cuts, whose height depends on the gaps and threads of the tool but both them are smaller than the process deviations due to tolerances, clamping and machine kinematics which can go up to 20 μm (Krömer, Sari, & Brecher, 2016), far too great for any reasonable gear application, specially due to NVH (sounds and vibrations) concerns.

2. State of the Art



Figure 5 Maag method (Espinel, 2021)

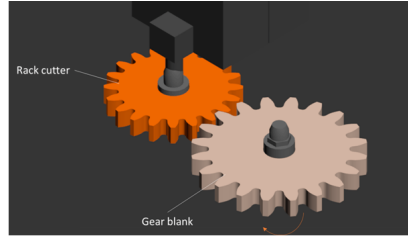


Figure 6 Fellow's method (Espinel, 2021)

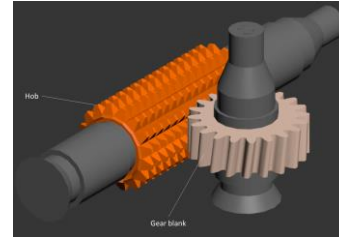


Figure 7 Gear hobbing (Espinel, 2021)

Certain gear forming techniques are also used although more sparingly, these involve the milling of all the material in between 2 azimuthally consecutive gear teeth (Bergstedt, 2021).

2.4.3. Hardening

Shot peening although not a heat treatment it can achieve surface hardening and densification. In this application, small spherical objects (glass, metal or ceramics typically) collide against the surface at high volumes and speeds, plastically deforming it and thus introducing a compressive residual stress which hardens the gears and makes them less susceptible to wear whilst increasing the mechanical properties of the surface layer (Bergstedt, 2021).

Quenching as any basic heat treatment method requires the heating of the element above the austenite transition temperature (723°C) and quickly cooling it down, achieving both martensite and retained austenite which greatly increase the hardness of the material at the expense of its ductility. This can later be adjusted through one or more tempering cycles, where the material is heated at various temperatures for different amounts of time to further refine the crystalline structure of the work piece. Finally normalizing cycles can be performed to reduce or remove any underlying thermal stress.

Through-hardening refers to gears where the entire workpiece is the same hardness, although rare. Normally, only the surface of the gear receives a heat treatment, heating up to a certain depth to achieve a higher toughness whilst keeping costs down and a softer core, this is typically known as case hardening (Mar-Dustrial Sales, 2022).

Flame hardening allows for localized heating of plain carbon (0.45% C) or low alloy steels (Mar-Dustrial Sales, 2022). If managed correctly the flame provides a low-oxygen environment which prevents corrosion without the need of additives such as flux.

Induction hardening is suitable for smaller parts than flame hardening, since the piece is fitted inside an induction coil and a high intensity current is circulated through the coil, which generates a strong magnetic field. Said magnetic field induces Foucault's currents (or Eddy currents) in the gear surface which due to the Joule effect heats the surface. The longer the piece remains in the coil, the deeper the penetration depth of the temperature field.

Carburizing is the most common hardening technique for gear surfaces. The gear is placed in a carbon rich atmosphere and the chamber is slowly heated. This promotes carbon diffusion into the gear (following Fick's law of diffusion). This yields different steel compositions at the core and the surface of the gear, which, allows for differential heat treatments, achieving a harder carbon-rich surface and a soft core, since the martensite is mainly built up in the surface as the core tends to be of a low carbon steel (al N. B., 2022).

Nitriding like carburizing alters the chemical composition of the surface, however, this is performed in a nitrogen-rich chamber rather than a carbon rich environment. Nitriding not only increases the hardness but the thermal and fatigue strength of the gears. Furthermore, high resistance to corrosion, adhesive and abrasive wear can be achieved easily (Koenig, Hoja, Tobie, & Stahl, 2019).

2. State of the Art

Carbonitriding leads to high levels of retained austenite (upwards of 50% by volume) and other precipitates which increase the load carrying capabilities of the surfaces at the expense of more complicated and intensive grinding (al P. K., 2021).

2.4.4. Finishing

Finishing is critical to obtain a correct surface roughness, material and geometrical properties. This is largely due to the poor surface quality after machining and possible deformations and other corrections in case a heat treatment was performed. The surface finish operations generally remove the outermost layer of the material (Bergstedt, 2021). The main finishing techniques are:

Grinding, which is subdivided into 2 types: gear grinding and generation grinding. The first employs a grinding disc tailored to the involute curve of the gear teeth, grinding in the space between 2 teeth whilst the latter is either a single straight edge grinding or multiple grinding wheels where the teeth resemble a toother rack rolling over the reference circle dictate by the gear (Bergstedt, 2021). Grinding can satisfy high tolerance requirements on hardened parts, however, the process, due to the outstanding friction generates a lot of heat which requires cooling or slowing the procedure, thus making it more time consuming (Bergstedt, 2021). A correct grinding technique can improve surface integrity, this techniques can range from grinding tailored to different microstructures to topological grinding which can improve the load carrying capabilities of working surfaces (al P. K., 2021).

Honing uses a grinding stone shaped like a gear which moves across the surface. The resin matrix is often coated in diamond abrasive particulate. The gear is rotated about the grinding tool thus obtaining a surface texture almost parallel to the tooth at both addendum and dedendum and perpendicular at the pitch line (Bergstedt, 2021). As stated in (Rathi, 2013) honing and green-shaving generate a superior surface finish to grinding. This reference (Rathi, 2013) also advocates for honing as finishing step after hobbing since it greatly improves the surface quality, but surfaces generated in such a way are more susceptible to change and variation whilst running under load as grooves resulting from the honing rapidly disappear due to plastic deformation of the flank's surface. This in turn can facilitate the appearance of cracks which can lead to premature gear failure and surface damage, as the cracks are not being actively ground away. Further studies cited in (Rathi, 2013) show that honing does not thermally affect the surface, it does not raise tooth surface temperature, yield heat cracks; burned spots or hardness soft spots in the surface (Rathi, 2013). Neither does it cause internal stress; microstructure change or cold work hardness. Finally, surface roughness parameters decreased as the rotation speed of the tool increased, more cuts per blank rotation, (Rathi, 2013).

Gears finished either by continuous grinding or honing showed marked NVH behaviour deviations, especially vibration-related as different vibration sources were found for different tooth-flank topographies (al P. K., 2021). Most of the here listed tests were performed on dry lubrication, but when tested with oil lubrication their tooth-flank topography-induced vibrations were still found to be predominant.

Lapping essentially uses an abrasive paste in between 2 meshing gears. As the gears turn, they reciprocate on one another at a controlled pressure therefore conforming both surfaces to each other. A master lapping gear is sometimes used as a way of ensuring high accuracy (Bergstedt, 2021).

Shaving can only be performed on non-hardened gears, limiting the accuracy since posterior heat treatments may distort the part. This process' tool is a serrated gear-shaped cutting tool, resulting in a myriad of cutting edges. Initially the cutting tool and the softened gear are placed cross-axially and as the tool drives the gear it slowly penetrates it until the desired centre distance is achieved between both axes (Bergstedt, 2021). This process excels at removing waviness and cutting marks and generates very low heat compared to other finishing techniques (Bergstedt, 2021).

2. State of the Art

Rolling does not remove any material; in this process the surface is merely conformed to a given shape by a tool (with a counter-shape engraved in it). The gear is meshed against the tool, forcing a material flow across the surface with a smoothing effect. Since no material is technically removed, it's not uncommon that excess material forms as lips on the edges of the gear, which requires posterior operations to remove (Bergstedt, 2021).

Superfinishing is a polishing technique which can be performed via several means: mechanical, chemical or a mixture of the 2. It improves the surface quality further after other finishing steps. Regardless of the polishing means, the aim remains the same, remove the surface peaks, leaving a mirror-like finish on the gears, hence the name. Mechanical approaches use a super-fine abrasive paste which polishes the gear as it either rotates or oscillates, which results in cross patterns in the surface. Chemical means etch the surface, where peaks are more susceptible to chemical attack since their surface-to-volume area is greater than the rest of the surface. However, it is slow and costly which only makes it suitable for high performance applications (Bergstedt, 2021).

Commonly, automotive gearboxes have efficiencies ranging from 90%-97% largely due to their surface finishes (al P. K., 2021). Common grinding techniques achieve R_z between 3 and 5 μm , whilst finer finishes lie between 0.5-1 μm along with an R_a of 0.05 μm , thus reducing the R_{pk} by 75% and the R_{mr} reduction is upwards of 90% (al P. K., 2021).

2.5. Abbot curve and surface roughness

Real engineering surfaces are far from perfect. No real-world element has a nominal surface (the surface follows exactly the blueprint requirements), instead any surface is widely regarded as having 3 components (from shortest to longest wavelength):

- Roughness: High frequency components of the surface.
- Waviness: Medium frequency components of the surface.
- Form: Low frequency components of the surface.

The form can generally be extracted from the drawings, whilst the difference between waviness and roughness is purely technical.

Any manufacturing technique inherently has some harmonic components associated which imprint in the surface. These can be caused by the cutting tool, speed, heat treatment or any other variations in the product manufacturing cycle (Santos, 2022). Roughness refers to the smaller of the too, which is considered purely stochastic and random (Santos, 2022).

When recording surface roughness, the difference between surface roughness and waviness is the cut-off length. Any evaluation length (L_e) is composed of several cut-off lengths (L_c), with surface characterization parameters being described at each cut-off length (Santos, 2022), although ISO 21920 recommends 5 cut-off lengths, there is no set parameter to determine the surface waviness (Santos, 2022).

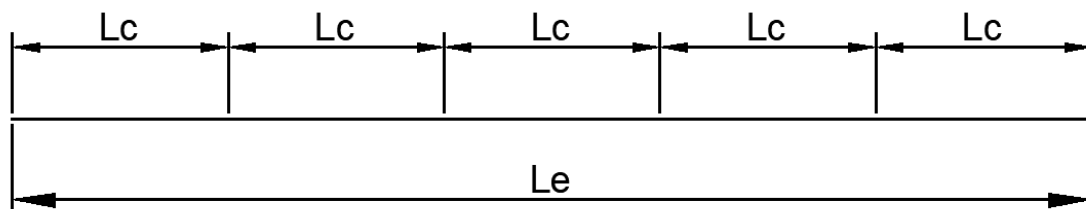


Figure 8 Cut-off and evaluation length

Surface roughness parameters can be widely divided into amplitude, spacing and hybrid parameters.

2.5.1. Amplitude parameters

Some of the surface amplitude parameters listed in the reference are (Santos, 2022):

Maximum profile peak height (R_p) is the maximum height of the profile within the evaluation length measured from the mean reference line (considered for every cut-off length).

$$R_p = \max(Z(X) - M)$$

Maximum profile valley depth (R_v) is the maximum depth of the profile within the evaluation length measured from the mean reference line (considered for every cut-off length).

$$R_v = \min(Z(X) - M)$$

Average maximum profile height (R_z) is the average distance between the highest peak and the lowest valley within each cut-off length, described as:

$$R_z = R_p + R_v$$

Total surface height (R_t) is the difference between the highest point and the deepest valley across the entire evaluation length.

$$R_t = \max(Z(X)) - \min(Z(X))$$

Average surface height (R_a) is the average roughness of the profile, computed as:

$$R_a = \frac{1}{L_c} \int_0^{L_c} |Z(x)| dx$$

Root mean square deviation (R_q) measures the deviation of the surface roughness from the mean line.

$$R_q = \sqrt{\frac{1}{L_c} \int_0^{L_c} Z^2(x) dx}$$

Profile Skewness (R_{sk}) is the average of the first derivative of the surface, denoting if the surface is mainly composed of peaks or valleys.

$$R_{sk} = \frac{1}{L_c \cdot R_q^3} \int_0^{L_c} Z^3(x) dx$$

Profile Kurtosis (R_{ku}) represents the sharpness of the roughness profile distribution from the mean line.

$$R_{ku} = \frac{1}{L_c \cdot R_q^4} \int_0^{L_c} Z^4(x) dx$$

Maximum roughness depth (R_{max}) is the largest R_{ti} from successive values of R_{ti} .

$$R_{max} = \max(Z(i) - Z(i - 1))$$

2.5.2. Spacing parameters

The main surface spacing parameter denoted in the reference is the mean width of profile elements, S_m (Santos, 2022).

$$S_m = \frac{1}{m} \sum_{i=1}^m S_{m_i}$$

2.5.3. Hybrid parameters

These are scarcely employed outside a very niche approach to friction and lubrication. Some of the surface spacing parameters listed in the reference are (Santos, 2022):

Root mean square slope (Rdq) studies the local tilt along the sampling length. It differs from the derivative since this approximation considers a seven-point formula.

$$Rdq = \sqrt{\frac{1}{L_c} \int_0^{L_c} \left[\frac{dZ(x)}{dx} \right]^2 dx}$$

Relative material rate (Rmr) shows the percentage of surface material above the height plane c, over the entire evaluation length.

$$Rmr = \frac{100}{L_e} \sum_{i=1}^m Ml(c)_i$$

2.5.4. Abbott-Firestone curve

Based on the relative material rate, there is a more commonly accepted representation of surfaces, the Abbott-Firestone curve (or Abbott curve for short). This curve describes the material rate distribution across its height, starting at 0 up to 100% in the X-axis (Rmr) and profile height in the Y-axis.

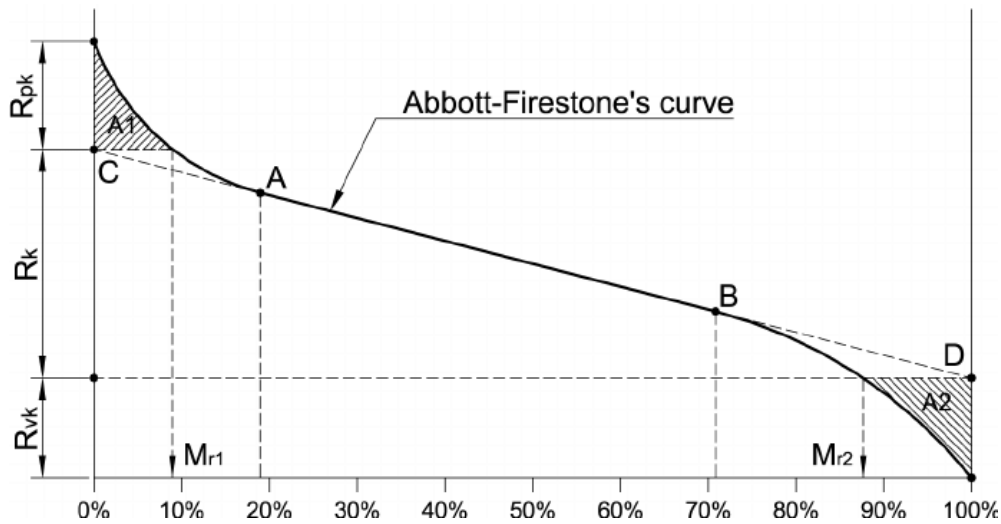


Figure 9 Abbot-Firestone curve example (J.C. Vasco, 2006)

The Abbot curve is typically represented as three interconnected straight lines:

- Section 1: Peaks. Connecting the maximum profile height with the start of the surface core.
- Section 2: Core. Contains most of the surface.
- Section 3: Valleys. Connecting the core of the surface with the lowest points of the surface.

Most high-quality surfaces have a relatively flat core section. Any Abbot curve can be built from the measurement and the selected A and B X-coordinates (or core material ratio range), since the first section can be built from the highest peak to A, the core section is the line connecting A and B and section 3 is the connection of B and the lowest point of the surface (Tomanickova, 2007).

Both C and D can be obtained from extrapolating the AB line to cross with the vertical axis at 0 and 100%. From C and D, the distance to the maximum/minimum of the surface the reduced profile height (Rk) and reduced profile depth (Rvk) can be calculated (Tomanickova, 2007).

If a horizontal line is projected from C or D, the intersection with the Abbott-Firestone Curve yield the smallest material share or the largest material share (Tomanickova, 2007).

2. State of the Art

The vertical difference between C and D is R_k , the functional part of the profile (Tomanickova, 2007).

2.6. Gear surface damage & transformation

2.6.1. Scuffing

Scuffing is a form of surface damage largely due to local temperature increase governed by the contact pressure and sliding velocities (which generally takes place in high speed or high temperature running gears). This process is closely linked to surface temperature, which, itself has 2 main components, bulk temperature (the material temperature prior to the contact) and flash temperature, an instantaneous temperature increase caused by local frictional heat flux (Kahraman, 2021). This sudden increase in temperature is sometimes enough to melt the metal which results in the fusion of both surfaces, also known adhesive contact. When both flanks move apart, this newly formed weld breaks apart damaging both surfaces. The best countermeasure (albeit a preventive measure) is a lubricated contact, ideally under full elastohydrodynamic conditions (EHL for short), where there is a thin layer of fluid in between both surfaces, and thus, direct metal-to-metal contact is avoided (Kahraman, 2021). Scuffing often starts in the dedendum of the driving gear, where there exists more sliding between both teeth (Abraham, 2014).

Scuffing is generally assumed to be caused by a failure of the EHL lubrication regime, draining from the contact either through lateral leakage or near the edges due to a squeeze effect cause by tip reliefs in gears, thus, promoting its appearance in the mating gear's dedendum (Snidle, Evans, & Holmes, 2004).

Another technique to prevent scuffing is the addition of chemically active extra pressure (EP) additives to the lubricant which activate at high temperatures and prevent the lubricant from losing properties as lubricants degrade at temperatures above 100°C (Snidle, Evans, & Holmes, 2004).

Other forms of preventing or mitigating scuffing relies in chemical hardening of the surfaces such as carburizing or nitriding, of which, 2 particularly promising techniques include improvements in surface finishing (preventing peaks, and thus, stress concentration points where flash temperatures are higher) and super-hard surface finishes such as diamond-like carbon (DLC) coatings. Superfinished elements have shown double the scuffing load limit than normally ground elements (Snidle, Evans, & Holmes, 2004). A new version of DLCs includes metal-dropped DLCs, which in both tools and machine elements have shown better adherence and greater toughness.

Furthermore, hard coatings have shown promising results in non-gearing applications in scuffing prevention by improving wear resistance, chemical inertness and low sliding friction coefficients (Snidle, Evans, & Holmes, 2004). Another surface coating which can help prevent scuffing is boron carbide DLCs which increase thermal and chemical stability. On top of that, this coating requires a less reactive gas when produced, which is in itself an advantage (Snidle, Evans, & Holmes, 2004).

2.6.2. Micro pitting

Nowadays, this is the main gear failure mode this is largely due to improvements in modern manufacturing techniques which have all but eliminated sub-surface inclusions which used to be the main cause of gear failure (Matk Devlin, 2006) and there is currently no fixed design technique to avoid it (Kadiric P. R., 2019). As of today, as much as 60% of all damage caused to gearboxes is due to pitting or micro pitting (imbema, 2022).

Still, the mechanism through which micro pitting is initiated remains a mystery. It can be described simply as pitting (rolling contact fatigue) on the scale of the roughness (Snidle, Evans, & Holmes, 2004).

2. State of the Art

Micro pitting is a type of surface damage that occurs in rolling–sliding contacts operating under thin oil film, mixed or dry lubrication conditions, such as those formed between meshing gear teeth (Kadiric P. R., 2019) and/or high loads (Snidle, Evans, & Holmes, 2004).

FZG pitting tests were performed with FZG Type GF-C micro pitting gears instead of the standard FZG Type PT-C pitting gears showed unexpectedly much longer fatigue pitting life. This was largely due to a delay in the pit formation due to extensive micro pitting wear changing the gear tooth profile preventing the formation of a shoulder which could act as a stress concentration, promoting the pit formation, thus suggesting that a wear model should be considered (Matk Devlin, 2006). Furthermore, rougher surfaces showed shortened micro pitting life's which could be due to the extensive plastic deformation their surfaces experienced, as such, a micro pitting life fatigue formulation was proposed based on the Ra (average roughness) of surfaces.

The boundary between micro pitting and pitting is the order of magnitude, where pitting presents surface damage of a similar size to the contact patch. In a series of studies collected in the reference (Kadiric P. R., 2019) lubricant additives were found to affect the extent of micro pitting by suppressing the wearing-in process, which in turn leads to an increased number of asperity stress cycles, and by changing the level of contact friction, which modifies tensile stresses and hence affects crack initiation and propagation. These cracks propagate opposite to the friction force acting on the surface. Wear depth shows a somewhat asymptotic correlation with the number of cycles and an exponential correlation with the sliding distance between gear teeth, regardless of the slide-to-roll ratio, SRR in short (Kadiric P. R., 2019). A negative SRR was found to increase micro pitting damage. A correlation between running-in loads and increased micro pitting was found, this might be due to the folded asperities, which result in sharp angles where they may be stress concentrations (even more so than in the original surface) leading to early crack propagation (Mallipeddi, Norell, & Nyborg, 2019).

Other research efforts aiming to understand the causes of micro pitting were presented in (Hui Long, 2015). In this publication (Hui Long, 2015), the authors studied micro pitting initiation and propagation with varying loads at constant rotational speeds, analysing the results as per several ISO standards and analytical methods. These methods showed that micro pitting starts at the pinion's dedendum but grows more significantly at the addendum, due to the pairing with the mating gear. Analytical results for various surface roughness showed this section of the tooth has the highest loads and the thinnest lubricant film thickness. The specific lubricant film thickness was also found to be strongly related to the surface roughness, which varied with each running cycle. Therefore, the authors concluded that the main factor influencing micro pitting formation were excessive loading; gear tooth micro-geometry; surface roughness and lubricant film thickness (Hui Long, 2015).

Although it is accepted that micro pitting starts at the dedendum, where greater sliding components are present, some publications such as (Abraham, 2014) report no addendum damage (in the mating gear) until much later in the running cycle (22 million cycle approximately). Whilst micro pitting bands grow along the contact pattern of gears which after 630 thousand cycles results in pitting of the gear tooth (pitting in the first tooth takes place long before micro pitting starts in its corresponding meshing gear's addendum). Furthermore, residual stress of the surface decreases with the number of cycles which suggests micro pitting and pitting are reducing the surface treatment depth by removing material from the gear's surface.

2.6.3. Pitting

Pitting or pitting corrosion, like micro pitting, is a type of surface fatigue failure at a larger scale. It is largely due to the recurrent loading of a gear flank with a contact stress which exceeds the surface's fatigue strength. The material in the affected region is thus removed, which results in a pit (hence the name). Since it is inherently associated with a reduction of the contact surface and the creation of new edges, this leads to a stress concentration in the adjacent regions of the

2. State of the Art

gear flank, which, like this first pit, will also, in due time, suffer this phenomenon, thus a chain reaction of sorts takes place until the entirety of the gear flank is damaged. Subsequently, if, at any point, a higher load comes to act on the weakened tooth it might cause it to fracture, having thus, a catastrophic gear failure (Gears Mechon, 2022). The first signs of pitting appear during the running-in period of the gear, where the larger peaks are torn away and small pits remain (typically 25 to 50 μm deep), just below the pitch line. As the gear surface transforms through the running-in period and the contact patch increases in size, the load gets distributed over a larger area which reduces the local stress and thus slows down the pitting process (Gears Mechon, 2022). Pitting can also be caused by a misalignment of the gears and thus an abnormally reduced contact patch which in turn leads to an increase of the contact stress in the gear flank.

If no corrective measure is taken following the first signs of pitting, it will degenerate into destructive pitting (provided the contact loads are high enough). Once this pitting has fully damaged one flank it will start to act incessantly on the mating gear's unpitted surface as the now rouged surface reduces the effective lubrication layer (Gears Mechon, 2022) wither with peaks whose effective height are larger than the fluid film thickness or by creating microscale venturis which accelerate and squeeze the lubricant out of the contact.

The reference (Xi-Hui Liang, 2017) proposes a model to understand pitting propagation across a set of meshing gears, which is then verified with both numerical and statistical methods, mimicking vibrations across the meshing effect based on the size of the pits, although the scope is limited to a single pair of spur gears. The study then interpolates between "states of health" of each flank to represent the pitting effect on each flank and the effect in vibration transmission (Xi-Hui Liang, 2017).

Pitting formation life increases when the austempering temperature decreases as per the reference (Tasgetiren, 2004). Thus the pitting resistance is affected by both the austempering temperature and time. Furthermore, the surfaces from pitting failures do not depend on rolling direction of the contact. The numerical analysis proposed is deemed appropriate for determining pitting resistance. Finite element results prove useful when predicting formation shape. For gears which have undergone austempering, the pitting failure time can be predicted without testing (Tasgetiren, 2004). Austempering is a form of heat treatment which produces bainite in steel gears. It is commonly used to both improve mechanical properties (increased ductility and shock resistance) and reduce or remove distortion in thin parts (Bodycote, 2019).

2.6.4. Running-in

The running-in of gears is not a type of surface damage but rather an inevitable surface modification. Running-in permanently alters the surface of gears at the start of their operating lives.

The running-in of gears generally takes place in the early stages of the gear's life with some authors reporting running-in effects as early as revolution 44 out of almost 21000 (Sosa, 2017). In other references (Mallipeddi, Norell, & Nyborg, 2019) the effects of running-in were limited to the first 10 μm of the surface, where surface asperities were smoothed through plastic deformation. This in turn leads to micro pitting right after the running-in period had finished. Plastic deformation up to 5 μm did verify the corresponding stress up to that depth after the efficiency tests (composed of a running-in period and normal operation) but no cracks were found in said regions, suggesting running-in does not yield sub-surface cracks (Mallipeddi, Norell, & Nyborg, 2019). Finally, running-in was found to increase surface stress in both profile and lead direction but after testing the stress levels in both directions tended to converge, therefore, after the running-in phase no major surface deformation occurs (Mallipeddi, Norell, & Nyborg, 2019). Sub-modelling techniques on gear teeth fatigue simulations (FEM with 20-node brick elements) showed fatigue strength is not particularly sensitive to relative porosity as long as it was above 90% but the generated data is not sufficient to ensure infinite lifetime stress. Furthermore, the

2. State of the Art

authors showed the critical pore tends to be a cluster of near-surface pores whose 3D composition and sharp edges result in stress concentration points (Mallipeddi, Norell, & Nyborg, 2019). Finally, microhardness levels were expected to vary due to the clustering effects (Mallipeddi, Norell, & Nyborg, 2019).

2.7. Powder Metal Gears

Modern automotive applications of sintered gears started with the non-structural elements and pieces with little to no load carrying requirements, since powder metallurgy inevitably alters the internal microstructure of parts, mainly, the residual porosity of the part (Fontanari, Molinari, & Pahl, 2019). As per the reference, (Fontanari, Molinari, & Pahl, 2019) if the relative density between powder metal gears and wrought steel gears is less than 1, the stiffness and tensile stress are negatively affected (as already discussed) along with fatigue and wear properties. Lower stiffness undermines mesh precision, and the mesh power loss factor thus increases, whilst a reduced bending strength decreases bending fatigue and pitting resistance which leads to superior wear rates.

In spongy materials fatigue tends to occur early on at the geometry necks, thus fatigue is diffused rather than localized as with solid materials. When porosity drops below 6% fatigue damage is delayed (Fontanari, Molinari, & Pahl, 2019). A first approximation on crack propagation stress on spongy materials is proposed in the publication (Fontanari, Molinari, & Pahl, 2019), although somewhat limited since it considers single defects with no interaction, therefore, a correction factor for connected porosity was developed:

$$\sigma_W = F_{loc} \frac{HV + 120}{(\sqrt{area})^{\frac{1}{6}}} \left(\frac{1 - R}{2} \right)^{\alpha} \quad | \quad \alpha = 0.226 + \frac{HV}{10^4}$$

Where R is the load ratio; HV is the surface's Vicker's hardness; area represents the negative effect of the fatigue damage triggering defect and it is the area of the defect on the plane of the maximum normal load; F_{loc} is the defect location factor, 1.41 and 1.56 for superficial or internal defects respectively and α is a function of the material's micro-hardness (Fontanari, Molinari, & Pahl, 2019).

Sintered gears substitute the first 2 steps (and sometimes the third as well) steps in the traditional gear manufacturing process. Metal powder is pressed in a mould, then heated and sintered, obtaining a raw part which then moves through the hardening and finishing processes (Bergstedt, 2021).

Sintered powder metal gears, although they might share a material with traditional wrought steel gears, due to the sintered nature, they may not share their mechanical properties. Consequently, several attempts have been made at characterizing the mechanical properties of sintered metal gears based on the fabrication method. According to (Kianian, Comparing Acquisition and Operation Life Cycle Cost of Powder Metallurgy and Conventional Wrought Steel Gear Manufacturing Techniques, 2019) there are 4 main options when it comes to powder metal gears:

- Double pressing, double sintering: Yields a higher strength, reduced porosity and scuffing resistance in self-lubrication composites. It can reach densities up to 7.2 to 7.5 g/cm³.
- Sinter-hardening: Removes the need for a secondary quench, thus reducing part distortion.
- Gear rolling: Applied after sintering, can increase the gear's surface density to levels comparable to wrought steel gears, having the surface reach densities of up to 7.8 g/cm³ and the core up to 7.4 g/cm³.
- FPM single stroke forging: This process can reach densities up to 98-100% when compared with wrought steel.

Both gear rolling and FPM single stroke forging require a posterior heat treatment, a considerable drawback sustainability-wise.

However, the most cost-effective method seems to be a one-step compaction-sintering-hardening (based partly in applications of hot stamping), since no posterior heat treatment is required as martensite and retained austenite are produced with this method (Fontanari, Molinari, & Pahl, 2019).

Earlier studies (Dizdar, 2012) already looked into powder metal gear cores and surface differentiation via surface treatments. Shot peening was found to increase adhesive wear failure in high density powder metal gears, which can be corrected by brushing and thus in some cases outperform wrought steel gears by ISO standards. It concludes powder metal gears to have a 70% pitting resistance when compared to that of wrought steel gears and the required surface densification depth in powder metal gears to be equal to the required case-hardening depth in combination with an appropriate core density. For densities of 7.4 g/cm³ or higher, the gear's behaviour is remarkably similar to that of a wrought steel gear (Dizdar, 2012).

Other papers study the direct application of powder metal gears in electric driveline transmissions with rolled gears and a core density of 6.8 g/cm³ and later upped to 7.5g/cm³ which resulted in a structure-borne noise reduction and there was no need for a heat treatment. The densified surface was described as 98% SSD (Kotthoff, 2018). Furthermore, the reference further analyses the effect of the micro geometry of the gear surface (equivalent to surface roughness), which, when optimized, can significantly reduce the excitation across all rotational speeds, ranging from 0 to 5500rpm (Kotthoff, 2018).

All the efforts to characterize the mechanical properties of powder metal gears yields a literature review presented in (Flodin, 2016) depicts a formulation for the Young's modulus of a powder metal part:

$$E = E_o \left(\frac{\rho}{\rho_o} \right)^{3,4}$$

Where E_o is the material's known Young's modulus, ρ is the powder metal part density and ρ_o is the material's known density and E

This is further developed in (Li, 2016), where a similar formulation for the Poisson coefficient is accepted:

$$v = \left(\frac{\rho}{\rho_o} \right)^{0.16} (1 - v_o) - 1$$

Where v is the part's Poisson coefficient and v_o the material's original Poisson coefficient.

Alas, any gear model originally designed for wrought steel gears can easily be converted to accept powder metal gears, given that there are no significant sub-surface defects of voids which may compromise the surface's behaviour.

As per (Sosa, 2017), most of the running-in of gears takes place at the start of the gear's operation (with the most significant surface roughness variations taking place before cycle 44 of a 20880-cycle test). When comparing ground and superfinished gears, the later do not manifest the effects of running-in, which supports his theory of the elastic-plastic contact (plastic deformation of surface asperities but an overall elastic contact). Ground gears had a significant running-in load which also seemed to be more robust in terms of surface topography and a reduced friction (to lower adhesion forces most likely). To characterize the surface hardness more accurately, Vicker's hardness was recorded and a variance of 30HV was denoted from the commonly available data.

Rough surfaces seem to have the peaks ground away, whilst the valleys remain, which, also points at an improved wear behaviour, since, if there ever is a propagating crack in a rough surface, it'll either break a peak of the surface (since the valleys cannot be considered to be load bearing unless a full fluid pressure distribution is calculated) or the surface asperity is completely ground way

2. State of the Art

thanks to the running-in, thus also removing the crack. This effect, however, cannot be seen in superfinished gears, which is why, they are more prone to micro pitting, since a crack can only propagate inwards and thus, once its path is complete, it'll remove a piece of the densified surface in lieu of a mere peak, as in rough surfaces.

When comparing performance in pure wrought steel; powder metal exclusive or mixed gear boxes configuration the reference (Li, 2016) concludes the most challenging component in rolling-sliding contact is the sliding, with a bigger effect on the root or dedendum. In powder metal gear to powder metal gear contact wear and friction increases with pore size whilst in the hybrid configuration (powder metal gear to wrought steel gear) both friction and wear decrease with pore size. In both cases, friction decreases as the rotational speed increases, most likely due to the mixing regime of the lubricant being treaded by the gears. Due to the solid nature of wrought steel gears, the adhesion forces in wrought steel to wrought steel are larger than a double powder metal gear assembly whilst powder metal to powder metal has greater torque dependent losses. Finally, it concludes the bending stiffness of the powder metal gears does affect the transmission but overall, the elasticity divergence does not seem to influence the overall efficiency.

In (al T. P.-J., 2008) the efficiency variation is correlated to the roughness of the gear's surface (ranging from 0.5-3 μm) and it was found to be much less relevant than the correlation efficiency-module. However, roughness was found to reduce power losses for both fine and rough Ra as well as a cubic relationship between rotational speed and power losses.

The reference (Kianian, A comparative cost analysis of conventional wrought steel and powder metallurgy (PM) gear manufacturing technologies, 2019), the nominal processing routes of both wrought steel gears and powder metal gears are compared, highlighting the following: Wrought steel gears' route is longer (most likely due to longer set-up times), with lower material utilisation and excessive tool wear due to lubrication and cooling limitations. Powder metal gears yield an almost finished shape and have shortened processing routes (Kianian, A comparative cost analysis of conventional wrought steel and powder metallurgy (PM) gear manufacturing technologies, 2019). A new approach toward gear cost calculations is presented, based in performance part costing (PPC), and assessed with a shop-floor level breakdown at its core. Furthermore, this PPC approach can easily be integrated into life cycle costing. Overall, with regards to gear performance and quality, PM gears required additional operations to match traditional wrought steel gears which also resulted in acquisition costs threefold that of traditional gears but there are possibilities for cost reduction, between 12 to 38%.

As per (Dizdar, 2012), powder metal gears would imply a weight reduction of just over 5% with a virtually equal performance, thus reducing emissions and aiding the vehicle meet the CAFE standards imposed by the authorities (European Commission, 2022) and (NHTSA, 2022) for European and American markets respectively.

When comparing the life cycle assessment (LCA) between a wrought steel part and its equivalence in powder metallurgy in (Tengzelius, 2000). The author points out there is clear lack of data to properly compare both manufacturing methods (since PM is still far from mature) therefore, that variability must be considered. The LCA presented (even with the data driven bias) denotes the lower environmental impact of PM processes compared to wrought steel parts when considering manufacturing and recycling operations of automotive components. This advantage is largely due to the lower energy usage whilst environmental key performance indicators (KPIs) such as natural resources depletion; acidification and human toxicity range from 26% to 41% when referenced to the standard manufacturing procedures (Tengzelius, 2000). Whereas estimations from (European Powder Metallurgy Association, 2020) suggests up to a 33% of the supply chain related carbon dioxide reduction.

An economic comparison is detailed in (Kianian, Comparing Acquisition and Operation Life Cycle Costs of Powder Metallurgy and Conventional Wrought Steel Gear Manufacturing

Techniques, 2019). Firstly, there is a remarkable lack of publicly available data concerning PM gears and their costs, alas, not even confidence intervals for the estimations could be provided by the author. The reference estimates PM initial investment costs to be upwards of 40 million SEK (largely due to the specific tooling) compared to traditional wrought steel gears 15 million SEK when excluding heat treatment; grinding and finishing equipment as both technologies use these equipment, although, the author points out, heat treatment procedures need to be optimized for powder metal gears. Based on equipment definitions, the powder metal gear was estimated to produce 400 000 units per annum whilst the traditional wrought steel parts produced 36 000 over 8 and a half years. This suggests that the additional initial investment required for powder metal gears (which often acts as an entry barrier) could be recovered in reduced production costs and cycle times (in some particular applications powder metal equipment could quadruple the production rate of wrought steel equipment). Another factor the author suggests might be key when considering the upgrade to powder metal gears is the vibration characterization and optimization, which, although are easier to optimize with powder metal gear equipment this claim lacks data-driven supports (Kianian, Comparing Acquisition and Operation Life Cycle Costs of Powder Metallurgy and Conventional Wrought Steel Gear Manufacturing Techniques, 2019).

As presented in (José M.C. Azevedo, 2018), the rapid solidification native to sintered gears for high alloy steels. In the reference's (José M.C. Azevedo, 2018) literature review shows powder metallurgy can be three times more energy intensive than its theoretical minimum. In light of this energy usage and the lack of a clear energy output from the manufacturing stages drives the authors to propose a new form of relative efficiency, allowing for intersystem comparison, although irreversibilities inherent to any manufacturing process rend the 100% efficiency objective unattainable. This new efficiency proposal follows the formulae:

$$\eta = \frac{SEC_{theo}}{SEC_{real}} \quad | \quad SEC = \frac{E}{m}$$

Where SEC is the specific energy consumption (theoretical or real); E is the energy required to fulfil any given manufacturing stage and m is the mass output of said process. This formulation allows for later material and energy flows in the publication (José M.C. Azevedo, 2018).

It's stated in (José M.C. Azevedo, 2018) that powder metallurgy is greatly affected by both the size and shape of the metal particles, since the predominant technique (pressing and sintering) only uses irregular particles whilst all others (minor manufacturing methods by volume of production) rely on spherical particles, whose production is strictly one order of magnitude below irregular particles, as they can only be manufactured by gas atomization.

Gas atomization is a metal powder manufacturing procedure in which a molten metal stream is disintegrated into droplets by a high-pressure inert gas stream. Upon dispersion of the metal stream, surface tension forces the metal droplets to acquire a spherical shape (minimum surface energy/tension principle depending on the physical state of the material). During the fall, the droplets cool down and solidify before being collected (Tingskog, 2018). This process can also be done submerged in water; thus it's known as water atomisation.

Since the most common technique as of now, thanks to the automotive industry's large influence, is pressing and sintering, most metal powder is made through water atomisation which uses scrap iron as an input which has a much smaller embodied energy than virgin steel. Although said scrap metal has a lower impact, it's prompt scrap, as such it does not provide the benefits of recycling from end of product life (José M.C. Azevedo, 2018).

Since powder metallurgy is still an incipient technology, only minor produces have specialized manufacturing lines with efficient induction ovens, whereas major produces simply divert a portion of their flame oven-melted metal towards powder metal, which, suffice to say, is less efficient (José M.C. Azevedo, 2018).

Modelling of gear surface roughness impact on electrified transmissions' efficiency

2. State of the Art

After atomization (gas, water or other) the powder is annealed which requires continuous ovens to increase productivity (as they allow for greater element diffusion into the powder and thus lowering the carbon content and increasing that of alloying elements) at the cost of efficiency due to augmented losses (José M.C. Azevedo, 2018).

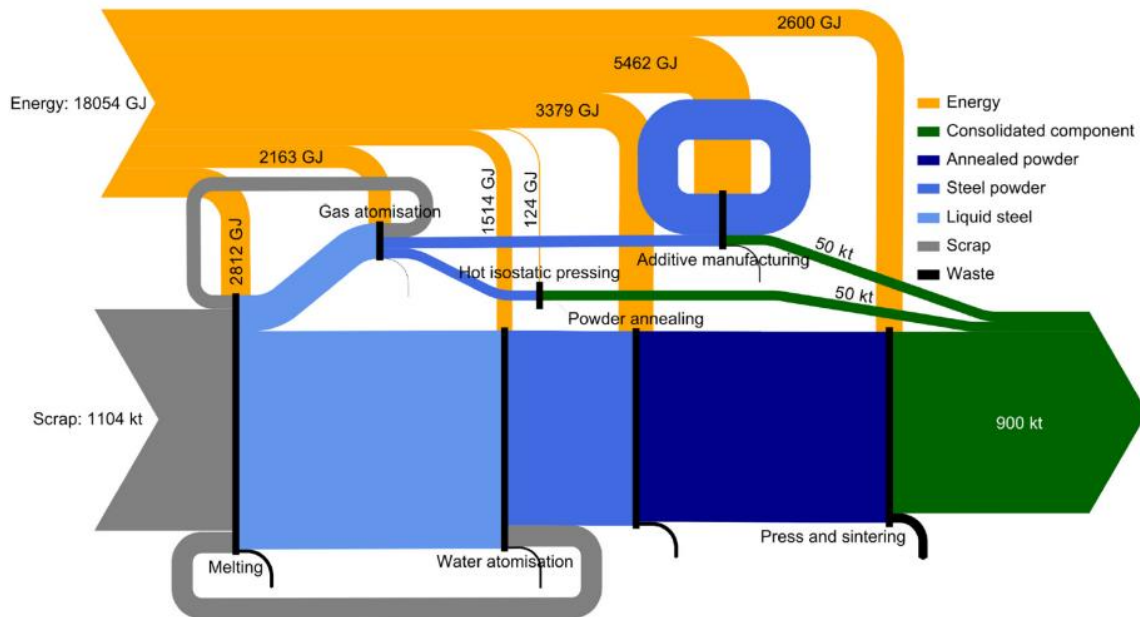


Figure 10 Steel powder material and energy flow diagram (José M.C. Azevedo, 2018)

Some of the benefits proposed by the author to improve efficiency and thus reduce the carbon footprint are (José M.C. Azevedo, 2018):

- Increasing the sintering temperature in batch ovens, reducing the number of cycles and overall energy consumption.
- Swapping hydraulic presses for electrical presses, since hydraulic presses tend to be over-dimensioned to apply a maximum pressure which is very rarely required which could improve efficiency by 2%.

However, energy only accounts to 6.3% of sintered parts, therefore, industrial process have focused in optimizing more cost heavy sections such as tooling and labour. Finally, sintering allows to significantly reduce material waste from atomisation as it can be reinpitted to at the melting stage, reducing overall material usage and therefore, environmental impact and resource depletion is slightly mitigated (José M.C. Azevedo, 2018).

2.8. Sustainability

Although powder metal gears are a great step forward improving gear manufacturing sustainability, it is not the only ongoing process. As exposed in (Jeong & Lee, 2014) hobbing and shaving processes have lower material recovery rates; higher energy consumption and associated carbon emissions relative to forging, which, in turn can lead to lower productivity, increased costs and industrial waste. Some alternatives which can increase material recovery rate and productivity are rolling, extruding aside from forging (Jeong & Lee, 2014).

Alas, in the reference (Jeong & Lee, 2014) gears manufactured by extrusion and machining are compared via LCA (following ISO 14000) and quality via their respective Vicker's hardness.

Although cold extrusion has higher tooling failure rates (dices tend to break due to the higher loads needed) they've been shown to reduce energy usage by 25% and 49% for single or double extrusion respectively (Jeong & Lee, 2014). The authors also detail carbon emissions by each process, where machining released 0.649 kg of CO₂, whilst single extrusion released 0.551 kg of

2. State of the Art

CO₂ and double extrusion 0.459 kg of CO₂. Furthermore, single extrusion entailed an increase of the material recovery rate of 58% whilst with double extrusion yielded a 91.2% increase (Jeong & Lee, 2014).

These sustainability improvements didn't affect the quality of the finished gears either, since the Vicker's hardness increased by an average of 37% across the entire tooth depth from surface to core, therefore, it's safe to state that extruded gears improve sustainability by increasing their durability (Jeong & Lee, 2014).

3. Contact modelling

To properly characterize a surface and its requirements its paramount one understands the forces it will experience during operation, alas, the contact between 2 rough surfaces needs to be accurately modelled.

3.1. Hertzian Contact

The simplest way to describe the contact of 2 meshing spur gear teeth is through the contact of 2 finite, infinitely rigid parallel cylinders. Under said hypothesis, the radii of these cylinders can either be the base diameter of the gears (traditionally denoted as R_b) when considering a macroscopic level or the radii of the teeth's circumference centred on the pressure line of the teeth (assuming an involute geometry) when considering a more detailed approach to the contact. Either way, both can be modelled with the following equations presented in the reference (Sosa, 2017):

$$a = \sqrt{\frac{4F_c R}{b\pi E^*}}$$

$$p_o = \sqrt{\frac{F_c E^*}{b\pi R}}$$

Where a is the semi-contact-width; E^* is the equivalent Young's modulus; R is the equivalent radius stemming from both radii in contact; b is the depth of the contact; F_c is the force which the contact is transmitting and p_o is the maximum contact stress (Sosa, 2017).

Furthermore, these artificial variables can be computed as:

$$\frac{1}{E^*} = \frac{1 - \nu_1}{E_1} + \frac{1 - \nu_2}{E_2}$$

$$\frac{1}{R} = \frac{1}{R_1} + \frac{1}{R_2}$$

Where ν_i represents the Poisson's coefficient of each material (either 1 or 2); E_i represents each material's Young's Modulus and R_i each element's radius.

Below an example is depicted between a two finite cylinders (0.1m in length) both made of steel ($E=210\text{GPa}$, $\nu=0.3$) and 5 mm and 10 mm radii respectively:

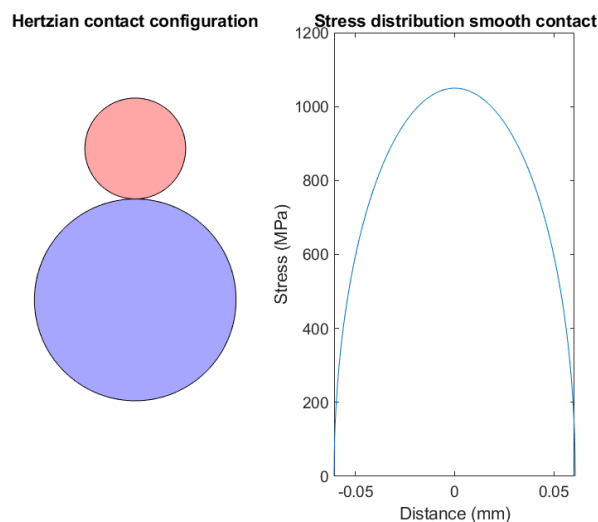


Figure 11 Hertzian Contact representation

Modelling of gear surface roughness impact on electrified transmissions' efficiency
 3. Contact modelling

Alas, for any finite contact length between 2 bodies, the pressure across the entire contact is assumed to be constant as depicted below:

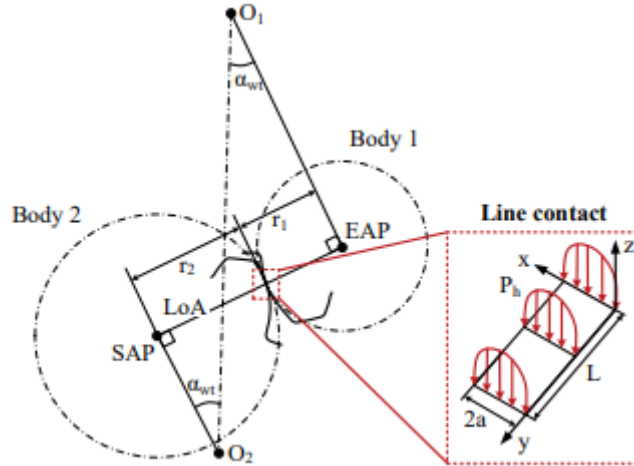


Figure 12 Line contact approximation from Hertzian contact definition (Hansen, 2021)

3.2. Surface deformation modelling

3.2.1. Theoretical background

Following traditional orthotropic linear elasticity formulations, any deformation of the elemental cube along its 3 main directions can be expressed as (Kelly, 2022):

$$\begin{bmatrix} \sigma_1 \\ \sigma_2 \\ \sigma_3 \\ \tau_1 \\ \tau_2 \\ \tau_3 \end{bmatrix} = \begin{bmatrix} \frac{1}{E_1} & -\frac{\nu_{21}}{E_2} & -\frac{\nu_{31}}{E_3} & & & \\ -\frac{\nu_{12}}{E_1} & \frac{1}{E_2} & -\frac{\nu_{32}}{E_3} & [0] & & \\ -\frac{\nu_{13}}{E_1} & -\frac{\nu_{23}}{E_3} & \frac{1}{E_3} & & & \\ & & & \frac{1}{2G_{23}} & 0 & 0 \\ & & & 0 & \frac{1}{2G_{13}} & 0 \\ & [0] & & 0 & 0 & \frac{1}{2G_{12}} \end{bmatrix} \begin{bmatrix} \varepsilon_1 \\ \varepsilon_2 \\ \varepsilon_3 \\ \gamma_1 \\ \gamma_2 \\ \gamma_3 \end{bmatrix}$$

Where the subscripts 1, 2 and 3 refer to the principal directions and the subscripts 12, 21, 31, 23, 13 and 32 refer to the directions along the faces of the elementary cube. In the formulation above, σ_i represents principal stress and τ_i shear stress. E_i represents the different Young's moduli in each direction; ν_i is the Poisson coefficient in each direction and G_{ij} is the shear moduli in each direction, with the formula:

$$G_{ij} = \frac{E_i}{2(1 - \nu_j)}$$

In turn, the matrix equation can be rewritten as:

$$\begin{bmatrix} \vec{\sigma} \\ \vec{\tau} \end{bmatrix} = \begin{bmatrix} [E] & [0] \\ [0] & [G] \end{bmatrix} \begin{bmatrix} \vec{\varepsilon} \\ \vec{\gamma} \end{bmatrix}$$

This in turn allows to de-couple the stress and deformations such that:

3. Contact modelling

$$\begin{aligned} \vec{\sigma} &= [E] \vec{\varepsilon} \\ 3 \times 1 &= 3 \times 3 \ 3 \times 1 \\ \vec{\tau} &= [G] \vec{\gamma} \\ 3 \times 1 &= 3 \times 3 \ 3 \times 1 \end{aligned}$$

Which allows for ease of calculation, thus, reducing the computational cost of the surface deformation model. Keeping in line with more detailed models this will be applied to line contacts between 2 rough surfaces.

Thus, the plane strain hypothesis can be considered, since the out-of-plane deformation can be negligible and the height and length of the surface line represented in the problem is negligible compared to the total flank length, allowing thus to convert the three-dimensional problem into a two-dimensional one. Furthermore, by aligning the principal axes with the pressure line, all deformations will be along the principal axes, alas, the entire shear stress equation can be suppressed, thus the model becomes:

$$\begin{bmatrix} \sigma_1 \\ \sigma_2 \\ \sigma_3 \end{bmatrix} = \begin{bmatrix} \frac{1}{E_1} & -\frac{\nu_{21}}{E_2} & -\frac{\nu_{31}}{E_3} \\ -\frac{\nu_{12}}{E_1} & \frac{1}{E_2} & -\frac{\nu_{32}}{E_3} \\ -\frac{\nu_{13}}{E_1} & -\frac{\nu_{23}}{E_2} & \frac{1}{E_3} \end{bmatrix} \begin{bmatrix} \varepsilon_1 \\ \varepsilon_2 \\ \varepsilon_3 \end{bmatrix}$$

From this equation, it's clear the stress in the surface will depend on only 2 factors, the pressure applied on each element and the expansion of its neighbours due to that same pressure being applied.

To fully develop the model, the only thing that now remains is the contour conditions of the problem, which, being the material a topmost layer of the surface, we can consider to be equivalent to each peak being a cantilever beam.

Said assumption results in an inverse correlation between the height of the roughness element and the stiffness of said element since:

$$\begin{aligned} \varepsilon_{real} = \ln\left(\frac{\Delta L}{L}\right) &\rightarrow K = \frac{F}{L_o e^{\frac{F}{EA}}} \\ \varepsilon_{engineering} = \frac{\Delta L}{L} &\rightarrow k = \frac{EA}{L_o} \end{aligned}$$

A representation of the implications can be seen below:

Modelling of gear surface roughness impact on electrified transmissions' efficiency
 3. Contact modelling

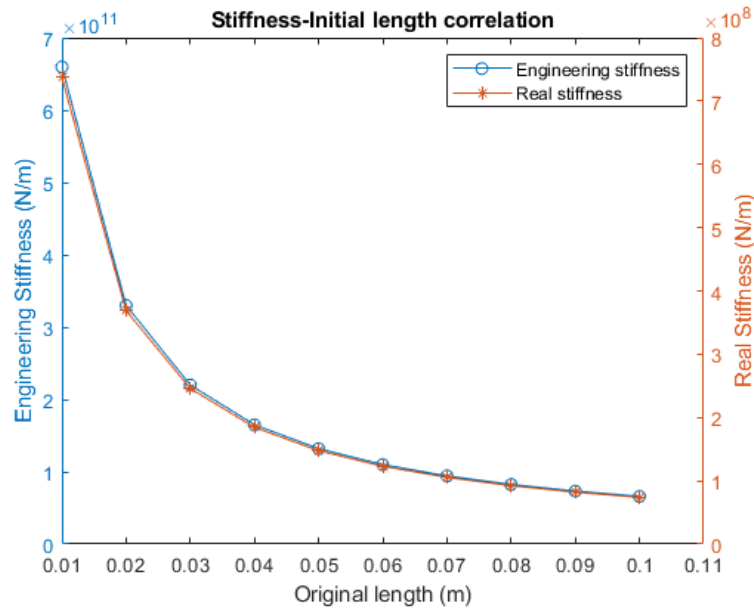


Figure 13 Stiffness variation with length ($E=210GPa$, $Re=235MPa$, $A=0.005^2\pi$)

This is representative of reality since the Surface peaks will always grind away before the Surface proper, largely due to receiving most of the contact and having a smaller stiffness, thus, permanently deforming more easily. Note the different order of magnitude, alas, why the engineering and real strains converge in small deformations, commonly limited to 0.02% to be considered elastic deformation in metals (Materion Bursh Performance Alloys, 2012).

3.2.2. Contact model evaluation

Two randomly generated surfaces were created in MATLAB, which can be seen below at the start of the code, where one is place on top of the other without any contact:

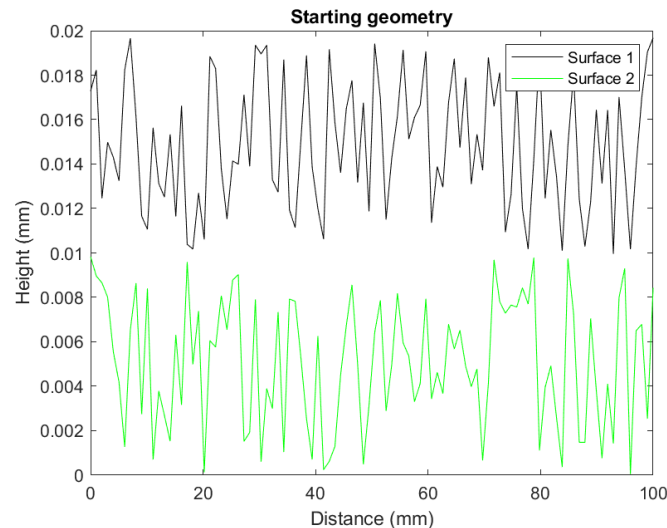


Figure 14 Lamé's approximation starting surfaces

Afterwards, the program would start lowering one surface into the other until there was contact and the objective force in the contact was obtained. In this example a force of 1kN was applied and a step on 0.001mm, thus resulting in the following convergence:

Modelling of gear surface roughness impact on electrified transmissions' efficiency
3. Contact modelling

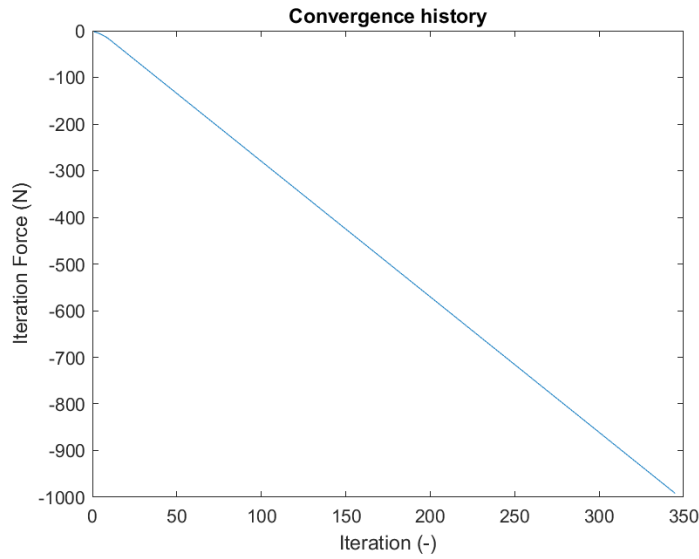


Figure 15 Lamé's approximation convergence history

In the first few iterations the force calculated from the stress integral is null since the pieces are not yet touching. The convergence force is negative since it's a compression effort. This resulted in the following deformed surfaces:

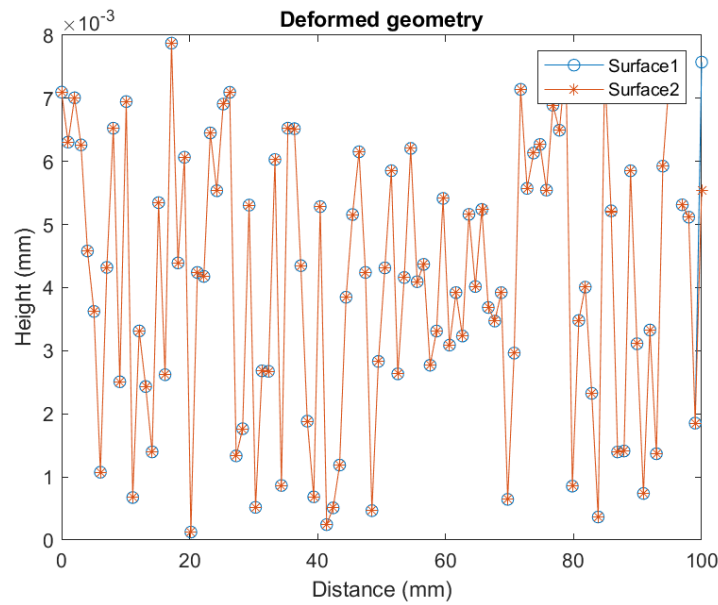


Figure 16 Lamé's approximation deformed surfaces

The surfaces seen above have its minimum point in the last point of the surface height vector (a mere peculiarity of the randomly generated vector), but it's clear the entire surface has deformed save for the valley, since all other points have a significant contact stress as seen below:

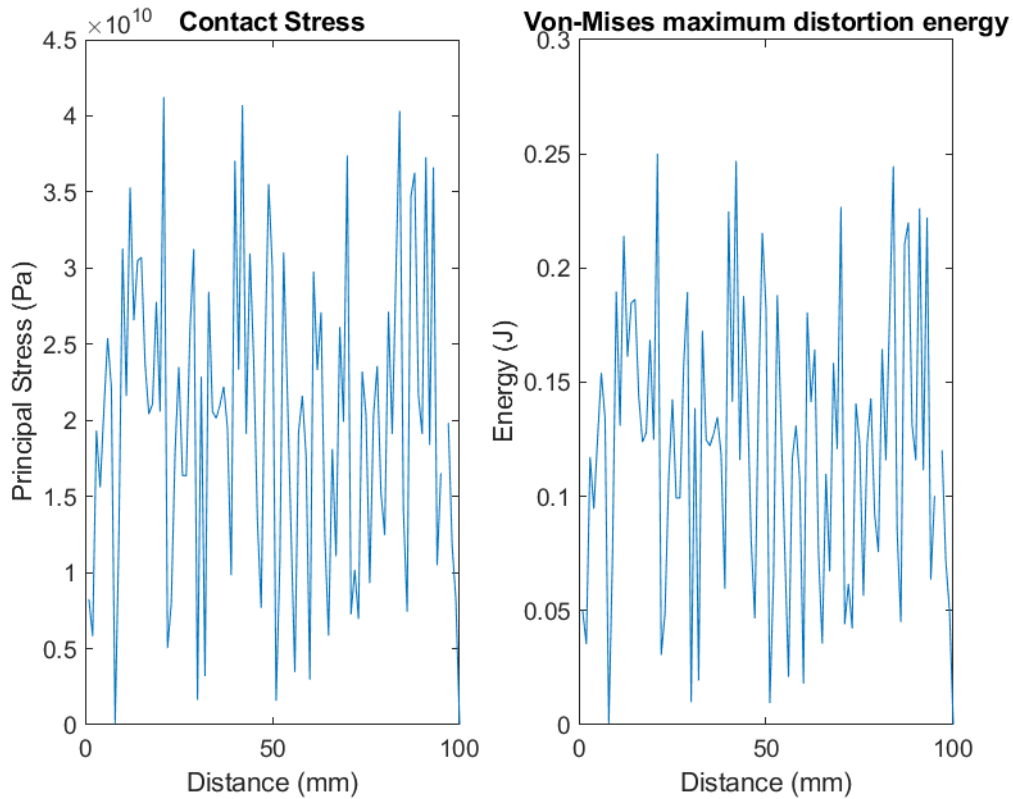


Figure 17 Lamé's approximation stress and distortion energy

Two points in the graph above have a stress of 0, the bottom most point of surface 1, where there isn't any contact with the other surface and the lowest point in surface 2, since, as already discussed, it has height zero and thus infinite rigidity in terms of the strain.

The total distortion energy was: 0.0122 J. The force in the final iteration was 991.7484 N (representing an error below 1%).

Stability-wise the model was remarkably sensible to the surface roughness-lowering step-error correlation, needing to be at least one order of magnitude smaller than the surface roughness to achieve a rough convergence and at least three if a convergence error of less than 1% was the aim. Regardless all parameters could be tuned to achieve a better precision, at the expense of computational cost, since reducing the step even further would quickly result in over 10000 iterations to converge since the difference would always be a power function of 10.

3.3. Rough contact modelling approximation

3.3.1. Theoretical background

In the references (Sosa, 2017) and (L. Xiao, 2007), take it one step further expanding this formulation to an elliptical-to-half-space contact, considering both to be deformable solid with a formulation derived from (Björklund, 1995).

The surface deformation is described as:

$$\bar{u}_{zi} = \frac{1}{\pi E^*} \sum_{j=1}^n C_{ij} p_j$$

In which \bar{u}_{zi} is the deformation in the perpendicular direction to the contact for surface i , whilst C_{ij} is the population of compliance matrix and p_j is the pressure originating from the contact in surface j .

Modelling of gear surface roughness impact on electrified transmissions' efficiency
 3. Contact modelling

In turn, the population compliance matrix itself is described as:

$$C_{ij} = (x_{\Delta} - a_L) \left[\ln \left(\frac{x_{\Delta} - a_L}{a_L} \right) \right]^2 - (x_{\Delta} + a_L) \left[\ln \left(\frac{x_{\Delta} + a_L}{a_L} \right) \right]^2 + C_o$$

$$x_{\Delta} = |x_i - x_j|$$

Where a_L is the half-cell size; x_{Δ} is the absolute value of the difference of coordinates along the x-axis of the contact correlating every point in surface i with every point in surface j so that, only in the main diagonal of C would x_{Δ} be null. Finally, C_o is an arbitrary value not detailed in the reference, as such, it was given a value of zero.

Therefore, the pressure field in each material can be described as:

$$\bar{p} = \pi E^* C^{-1} (\delta - \bar{h})$$

Such that \bar{p} is the pressure across the surface contact, \bar{h} is the vector containing the discrete height difference between both surfaces and δ is the approach distance between both surfaces (Sosa, 2017). This in turn can be solved via numerical methods.

Consequently, the force on the contact must inevitably be:

$$F_C = \int \bar{p} dx$$

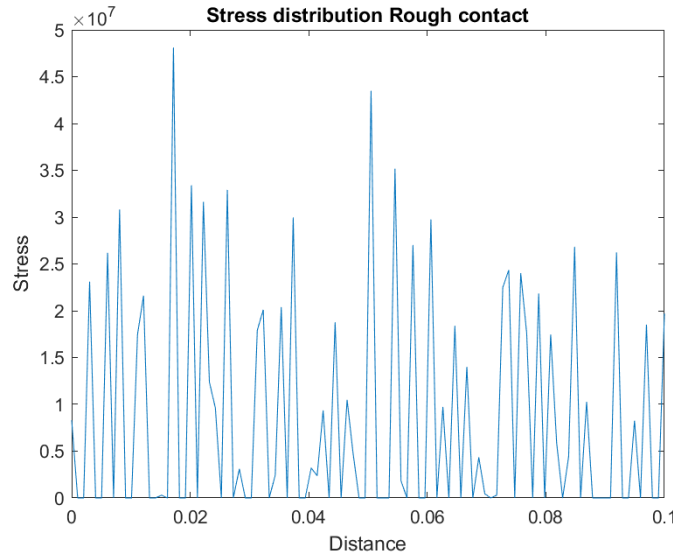


Figure 18 Rough contact stress example

Furthermore, the author (Sosa, 2017) describes a set of equations to calculate sub-surface shear stress based on Johnson's equations (Johnson, 1987):

$$\tau = B_{\tau} \bar{p}$$

Where B_{τ} is in essence an elementary cube rotation matrix to convert principal stress into shear stress (represented as τ in the equation above). The formulation relies on every point in the surface (x_i) having a corresponding depth (subindex k):

$$B_{\tau ik} = \frac{1}{2\pi} [\cos(2\theta_{1,ik}) - \cos(2\theta_{2,ik})]$$

Whereby θ_1 and θ_2 are auxiliary variables used to calculate the shear stress at a depth of z_D , thus:

$$\theta_{1,ik} = \text{atan} \left(\frac{z_{D,k}}{x_i - a_L} \right)$$

$$\theta_{2,ik} = \text{atan}\left(\frac{z_{D,k}}{x_i + a_L}\right)$$

The reference (Sosa, 2017) also demonstrates the results is equal to the algebraic formulation:

$$\tau_i = -\frac{p_i}{a} (z - z^2(a^2 + z^2)^{-\frac{1}{2}})$$

Thus, reducing computational cost and having a maximum at $z=a$, where the shear stress will be 20.7% of the surface stress, alas, the shear stress contour line will mimic the surface.

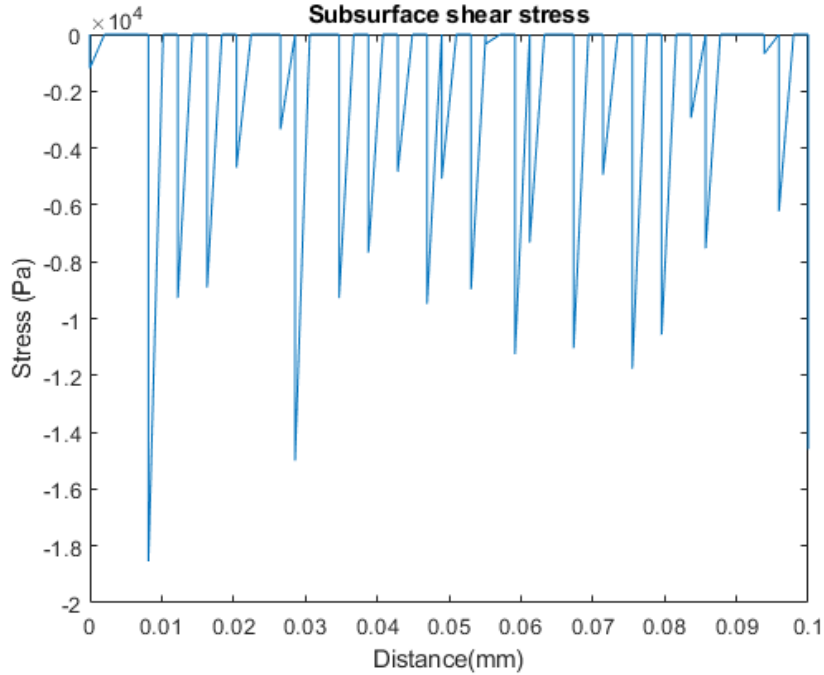


Figure 19 Subsurface stress example

3.3.2. Contact model evaluation

Since the base model works considering a tooth-to-flat-plane contact, it's been adapted to consider the contact between 2 rough contacts lines in two opposing teeth, in other words, works in the plane which contains the pressure line and a parallel to the main axes of both gears.

Two randomly generated surfaces were created in MATLAB, which can be seen below at the start of the code, where one is place on top of the other without any contact:

Modelling of gear surface roughness impact on electrified transmissions' efficiency
3. Contact modelling

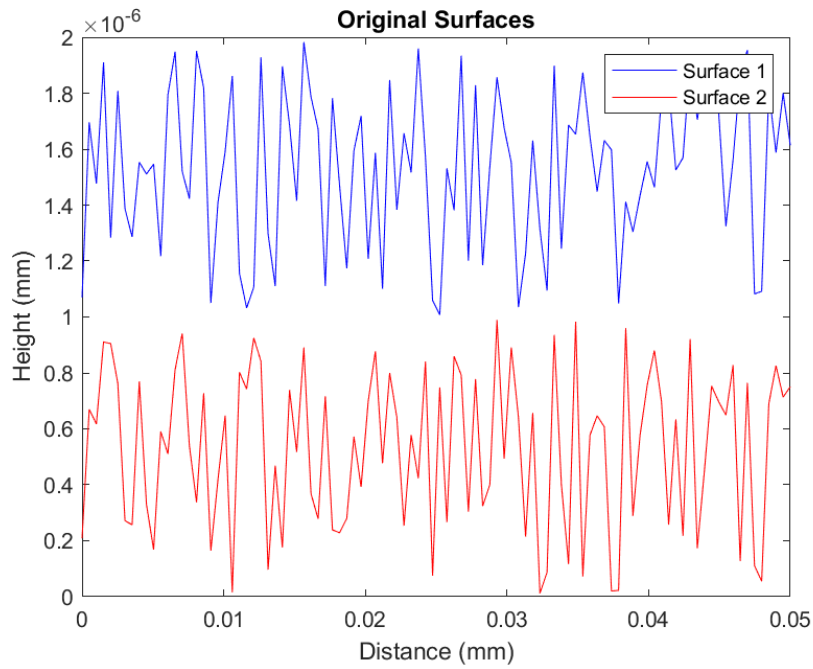


Figure 20 Starting surfaces rough contact model evaluation

Afterwards, the program would start lowering one surface into the other until there was contact and the objective force in the contact was obtained. In this example a force of 1kN was applied and a step on 0.001mm, thus resulting in the following convergence:

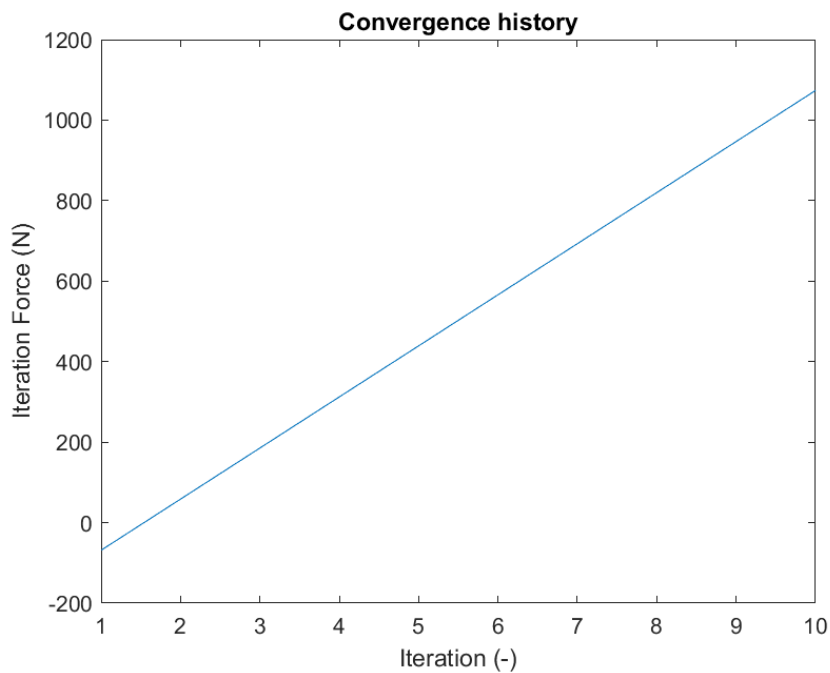


Figure 21 Rough contact evaluation convergence history

In the first few iterations the force calculated from the stress integral is irrelevant since the pieces are not yet touching. The convergence force positive since the iteration force depicts the absolute value of the force (which by convention it should be negative due to it being a compression effort). This resulted in the following deformed surfaces:

Modelling of gear surface roughness impact on electrified transmissions' efficiency
3. Contact modelling

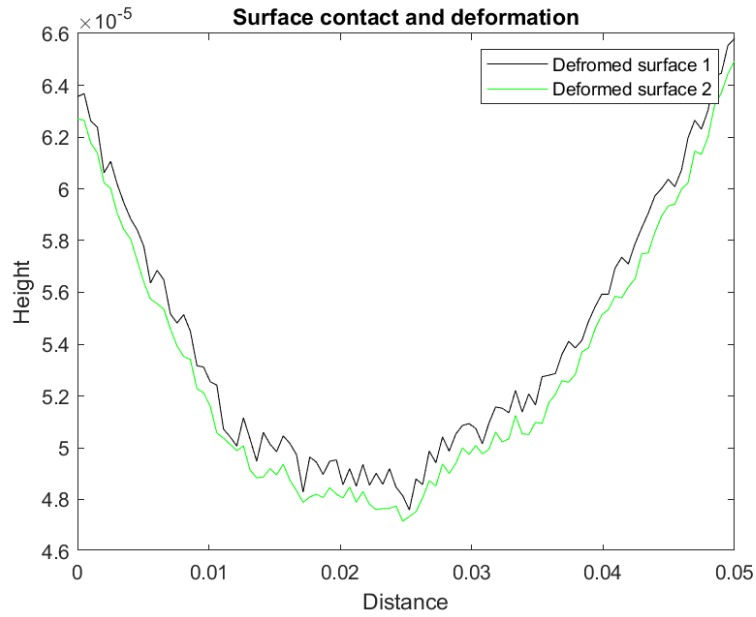


Figure 22 Deformed surfaces rough contact evaluation

The surfaces show a bigger surface deformation at the centre of the flank, which is consistent with the hypothesis explained in several references (Bergstedt, 2021) and (al G.-E. e., 2018), thus why specially in (Bergstedt, 2021) the surface roughness is always measured first at the centre of the flank vertically (addendum to dedendum). Consequently, the surface pressure was computed as:

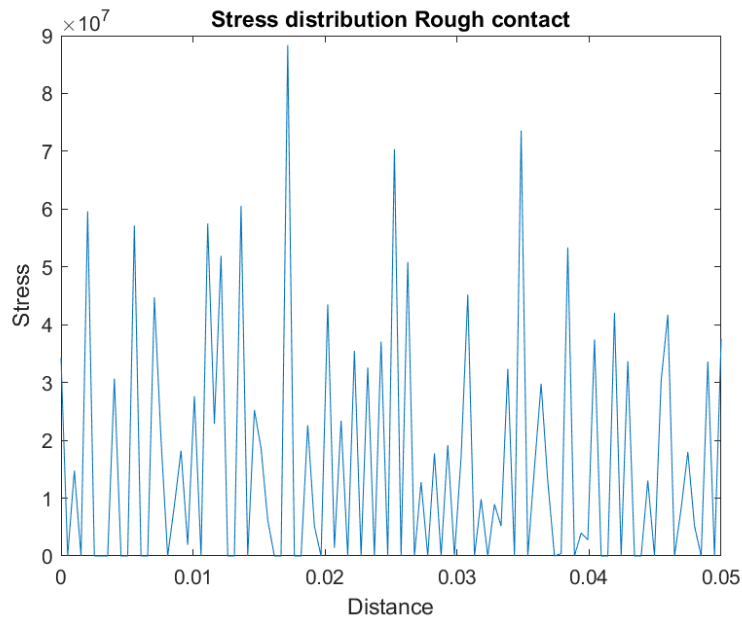


Figure 23 Contact stress rough contact model evaluation

The subsurface shear stress at $z=a$ thus presents a similar shape only toned down as seen below.

Modelling of gear surface roughness impact on electrified transmissions' efficiency
3. Contact modelling

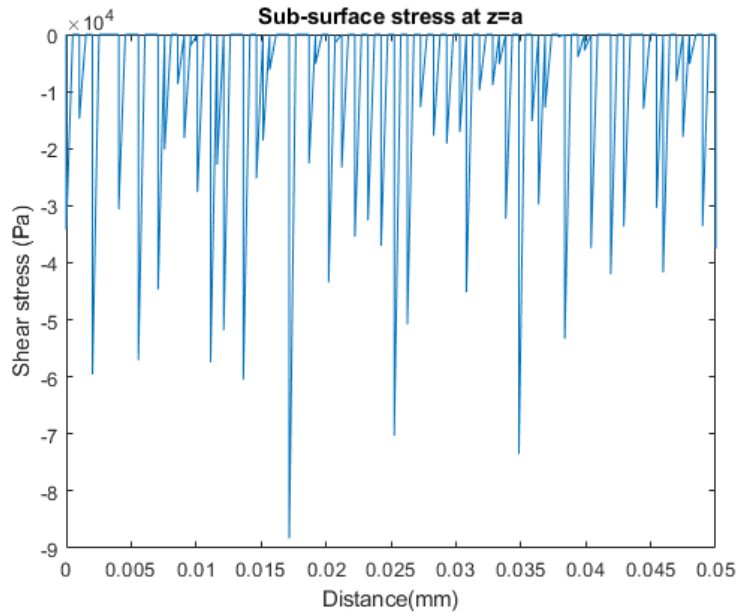


Figure 24 Shear stress rough contact model evaluation

The force in the final iteration was 1073.6 N (representing an error below 7.36%), which is due to the convergence condition. This model, like the previous Lamé-based model, presented some stability issues, being remarkably sensible to the delta, alas, an upper bound convergence condition was not included, since for it to be reliable the delta would have needed to be much smaller and thus the calculation time would have needlessly sky-rocketed.

The total energy spent in the surface deformation was 0.0856 J. With a distribution as follow:

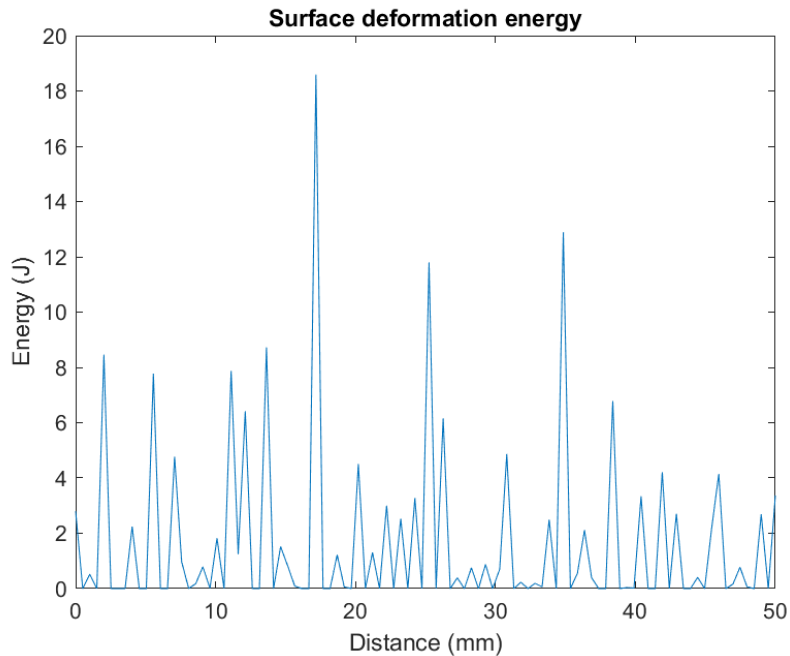


Figure 25 Surface deformation energy rough contact evaluation

4. Model adaptation

Rather than calculate a contact in the reference plane (perpendicular to the axes), the model was rotated 90° so it would contain the pressure plane (thus containing the full depth of the gear flank). On top of that, elastohydrodynamic lubrication was implemented.

The model proceeds to estimate the friction coefficient followed by the lubrication regime, which then result in one of two solvers. If a full EHL regime is estimated the surfaces will not be in contact and a thin layer of fluid with a minimum thickness of $h_o = h^*$ is implemented, which, then yields a pressure field across the fluid acting on the surfaces. The sliding and rolling forces are then allocated uniformly across the surface of each gear.

If however, the lubrication equations suggest there is mixed lubrication (ML) or boundary lubrication (BL), a numerical solver based on the rough contact model is implemented. This solver lowers both surfaces into each other and using the compliance matrix estimates stress whilst simultaneously applying the fluid pressure due to the Navier-Stokes solution. Said stress and pressure are integrated across the entire line contact until the contact force converges. This model's operation is depicted below.

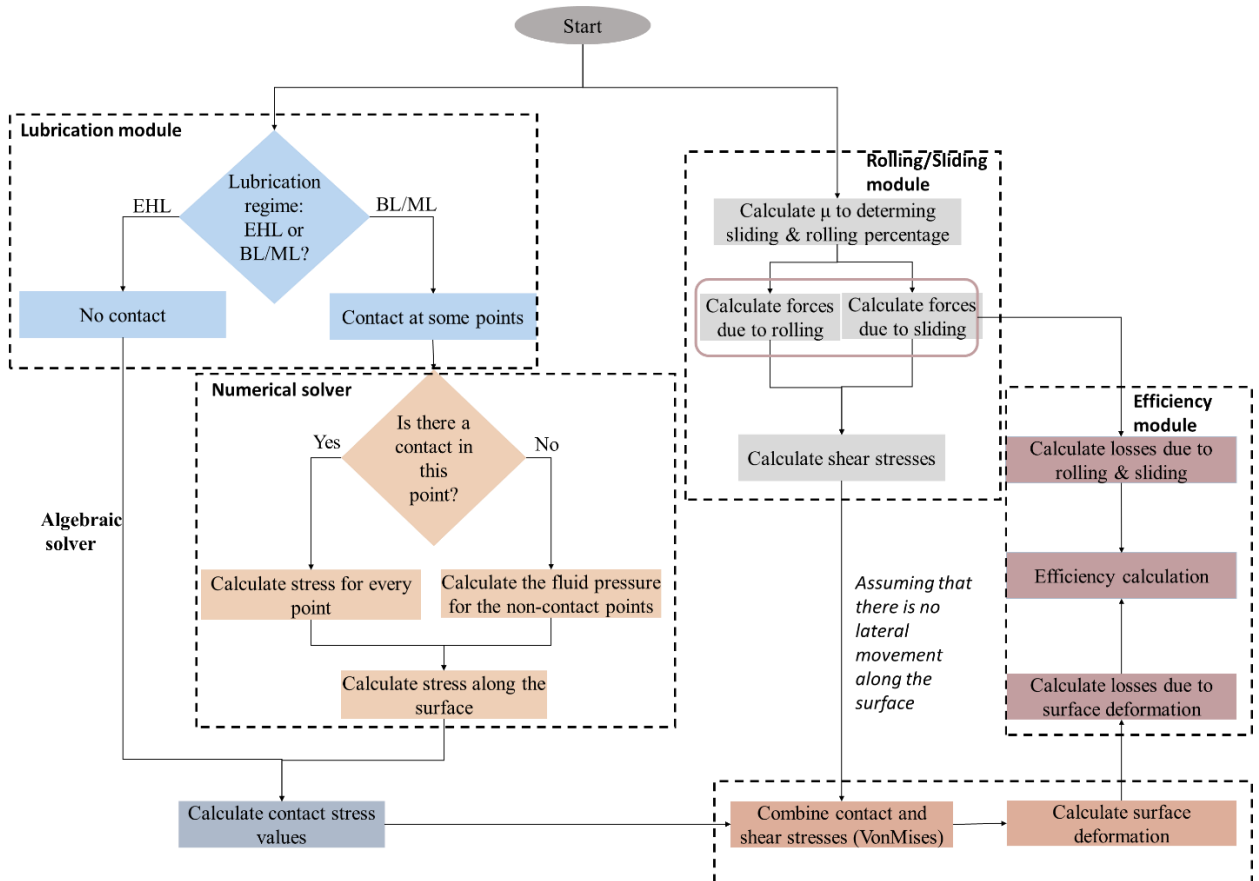


Figure 26 Model's block diagram

4.1. Rolling and sliding forces modelling

There are plenty of examples of dry contact approximations, although in reality, gears very rarely run completely dry since that would greatly reduce their lifespan. There are, nonetheless, some research efforts in this field, such as the one presented by (Sklenak & Brecher, 2021), employing a half-space, optimizable mesh approach to model local friction energy. In lubricated contacts that can easily be done via the fluid shear stress (if there is no contact between 2 points of study).

The shear stress acting on the surfaces (as a result from the rotation of the tooth surface with regards to the lubricant) can be calculated using traditional formulae based on Newtonian fluids such that:

$$\tau = \mu \frac{\partial u}{\partial h}$$

Where τ is the shear stress of the fluid and $\frac{\partial u}{\partial h}$ is the derivative of the velocity field in the fluid with regards to the height.

However, as it's well known, fluids do not always behave in a laminar manner, incurring in turbulences, as such, in the reference (Wei, 2015) the author proposes:

$$\tau = \mu \frac{\partial u}{\partial h} - \frac{1}{2} h(x) \frac{\partial p(x)}{\partial x}$$

Therefore, the shear stress is at least, partially dependent on the oil film pressure, for which, the Navier-Stokes equations need to be solved. The second term is derived from an adaptation of the Reynold's equation whereby, the pressure of a fluid is dependent on its viscous forces (Tribonet, 2016).

A way of bypassing this is presented in the reference (al H. e., 2007), where the friction coefficient of the lubricant is described with a 94% accuracy and a model error for the acting forces below 0.1%. The friction coefficient approximation results from the equations (al H. e., 2007):

$$\left\{ \begin{array}{l} \mu = e^{f(SR, P_h, \nu_o, S)} P_h^{b_2} |SR|^{b_3} V_e^{b_6} \nu_o^{b_7} R^{b_8} \\ f(SR, P_h, \nu_o, S) = b_1 + b_4 |SR| P_h \log_{10}(\nu_o) + b_5 e^{-|SR| P_h \log_{10}(\nu_o)} + b_9 e^S \end{array} \right.$$

Such that μ is the friction coefficient; SR is the slip-to-rolling ratio upon the teeth meshing, P_h is the maximum Hertzian contact pressure (whose calculations have already been previously described); ν_o is the absolute viscosity (in cPs for this application) at the oil inlet temperature; V_e is the entraining velocity; R is the equivalent radius of the contact (as described previously in standard Hertzian contacts); S is the equivalent RMS surface roughness whilst $b_i \mid i = 1, 2, \dots, 9$ belong to a 9 element coefficient vector derived from a lineal regression of the lubricant properties, which in the reference (al H. e., 2007) is described as the standard FZG set-up lubricant.

The equivalent RMS of both surfaces can be computed as:

$$S = RMS_{total} = \sqrt{\sum_{i=1}^n (RMS_i)^2}$$

Granted surfaces can be described as a linear combination of different waveforms (a Fast Fourier Transform) as depicted in several of the references e.g.: (Sosa, 2017) and (al H. e., 2007).

In turn the rolling speed can be described as (Spikes):

$$V_s = |V_1 - V_2|$$

Where V_s is the sliding velocity; V_1 is the linear speed on the first gears and V_2 is the linear velocity of the second gear.

The entraining speed is described as (Spikes):

$$V_e = \frac{V_1 + V_2}{2}$$

Alas, the slide-to-roll-ratio can is described as (Spikes):

$$SR = \frac{V_s}{V_e}$$

In the same reference as the friction coefficient (al H. e., 2007) a global definition for the sliding and rolling forces in a contact are described (acting perpendicularly to the pressure line of the contact):

$$F_s = \mu * F_C$$

Where F_s is the sliding friction force.

This implementation of the friction coefficient agrees with the approximations made in (Kadicic P. R., 2019) where it was shown μ is correlated with the slide-to-roll ratio.

Other papers (Myunster, 2002) estimate a loss coefficient purely dependant on the friction the gears teeth experiment as one moves over the other, in other words, friction as a function of the contact band position along the flank. Said approximation is valid for global approaches, however, when it comes to the study of surfaces and their contacts it's a vast simplification. Similarly, the friction coefficient was sometimes estimated based on classical EHL parameters as explained in (al P. M., 2021), which, although is fairly accurate for ball-to-disc contacts it presents problems in more complex set-ups where the contact area isn't as clear.

The rolling force is derived in (al H. e., 2007) from an empirical formula from (al S. W., 1991):

$$F_r = \frac{4.318\varphi_T(\tilde{G}\tilde{U})^{0.658}\tilde{Q}^{0.0126}R}{\alpha}$$

Such that F_r is the rolling resistance; φ_T is the thermal reduction factor to account for the effect of temperature rise at high speed conditions (al H. e., 2007), however, said value isn't disclosed in the reference, but it is described at length in (Chapter 2: Overall Methodology, 2005). \tilde{G} is the dimensionless material parameter; \tilde{U} is the dimensionless speed parameter; \tilde{Q} is the dimensionless load parameter and α is the pressure viscosity coefficient.

The dimensionless material parameter is described as (Chapter 2: Overall Methodology, 2005):

$$\tilde{G} = \alpha E^*$$

Such that α is the pressure-viscosity coefficient.

The dimensionless speed parameter is (Chapter 2: Overall Methodology, 2005):

$$\tilde{U} = \frac{\nu_o(V_1 + V_2)}{RE^*}$$

The dimensionless load parameter is thus (Chapter 2: Overall Methodology, 2005):

$$\tilde{Q} = \frac{W'}{E^*R}$$

Where W' is the unitary load per unit width in the surface.

The thermal reduction factor is described as (Chapter 2: Overall Methodology, 2005):

$$\varphi_T = \frac{1 - 13.2 \frac{P_h}{E^*} (L^*)^{0.42}}{1 + 0.213(1 + 2.23SR^{0.83})(L^*)^{0.64}} \quad | \quad L^* = - \frac{\partial \nu}{\partial T_o} \frac{(V_e)^2}{K_f}$$

Where ν is the absolute viscosity; T_o is the lubricant temperature at the inlet and K_f is the lubricant's thermal conductivity. Alas, if no thermal events are considered $\varphi_T = 1$.

4. Model adaptation

Having, thus, characterized the macro-level properties of the lubricant, the Navier-Stokes equations can be solved (with their corresponding simplifications) to characterize the pressure field of the lubricant when both teeth have meshed.

A paper detailing a dynamic approximation to line contacts in gears and the effect of the roughness was reviewed (Kolivand, 2020). It correctly points to the divergence of static and dynamic simulations and how surface roughness may affect the tribological conditions of the gear contact, with a friction coefficient defined by sections and threshold pressures, a definition which was previously discarded in this study due to its lack of validation and disregard for other influencing factors.

Other references (Bergseth, 2012) focus more on the correct characterization of lubricants, as there are several additives which can be absorbed by the surface of the gear given the right conditions: contact pressure, temperature... The author goes in depth on the effect of lubricants and additives, since any additive must be able to perform adequately in both the close surface contact and the bulk of the lubricant pool found at the bottom of the transmission casing, alas, for simplicity, the effects of lubricants will be disregarded in the model. As a side note, the author (Bergseth, 2012) also studies the variation of the friction coefficient, which is obviously dependant on the lubricants but the definition of said friction coefficient is the traditional measured friction force over the normal load, thus it will not be implemented in this model since a more detailed version has already been discussed.

The reference (L. Xiao, 2007), however, present alternative definitions of the friction coefficient, describing it as the sum of a constant term and a load-dependent factor, which, when paired with the aforementioned rough contact model is reasonably accurate at high loads. Since the adequacy of the formula and its accuracy could not be assessed this friction coefficient formulation was also discarded as the others considered far more parameters native to rolling-sliding contacts.

4.2. Navier-Stokes equations & elastohydrodynamic lubrication

There is a discussion on whether for thin film lubrication it's more appropriate to use Reynold's equation or Navier-Stokes. Reynold's equations relies on the thickness of the lubricant film being far smaller than its length, which, as per the reference (Tosic, 2019), this tends to agree with the CFD simulations, however, it can present issues and uncertainties when the surface has a high roughness, which, is inherently present in ground or honed gears, more so in powder metal gears, where the surface roughness is more pronounced as seen in (Dizdar, 2012), (Li, 2016) and (Kotthoff, 2018) amongst others. Reynold's equation is shown below (Reynolds, 1886):

$$\frac{\partial}{\partial x} \left(\frac{ph^3}{12\mu} \frac{\partial p}{\partial x} \right) + \frac{\partial}{\partial y} \left(\frac{ph^3}{12\mu} \frac{\partial p}{\partial y} \right) = \frac{\partial}{\partial x} \left(\frac{ph(u_a + u_b)}{2} \right) + \frac{\partial}{\partial y} \left(\frac{ph(v_a + v_b)}{2} \right) + \rho(w_a - w_b) - \rho u_a \frac{\partial h}{\partial x} - \rho v_a \frac{\partial h}{\partial y} + h \frac{\partial d}{\partial t}$$

Where p is the fluid film pressure, x and y are the width and length respectively, h is the flim thickness thickness, μ is the fluid viscosity, ρ is a fluid density, u, v, w are the bounding body velocities in all three dimensions of space respectively and the subscripts a and b represent each of the moving bodies.

Reynold's equation cannot be considered for this application since it assumes the pressure distribution through the height of the film thickness is uniform (which, from the get-go was assumed to be false). Furthermore, it also assumes the thickness of the fluid layer is much smaller than its 2 counterparts in space, which, given the problem configuration is not necessarily true since a gear width might only be a few times the teeth height in some instances and thus, in the approximation phase of 2 flanks, the fluid film thickness can be comparable in magnitude to the other 2 dimensions found in space.

Another key element when discarding this version of applied fluid dynamics comes from the reference (Bergseth, 2012). In this PhD thesis, the author explains that a key element in

determining the friction coefficient is the surface boundary layer. On top of that, said surface boundary layer is strongly dependant on the chemical composition of the lubricant and pre-existing conditions, namely, surface roughness after different gear manufacturing operations, which included green-shaving; power honing and grinding, alas, no assumptions about the lubricant can be made, such as the ones in Reynold's equations.

Following traditional Involute straight-gear design, a flank, at any point, can be described as the circumference with radius R_i and centre along the pressure line (with an inclination α with regards to the perpendicular of the line connecting both gear centres), as such, the Navier-Stokes equation can be solved in a cylindrical base.

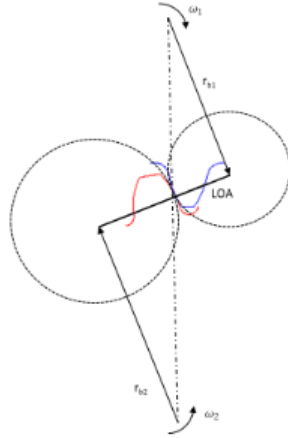


Figure 27 Gear tooth profile representation (Slogén, 2013)

An added benefit on considering line contacts in the middle of the gear flank rather than close to the tip is that the effects of tip reliefs can be largely simplified. As detailed in (Jamali, Sharif, & Snide, 2014), a tip relief can squeeze lubricant out of the contact, leading to a fluid film height reduction and artificially altering the contour conditions so that a rougher contact between the surfaces exists and the lubricated contact hypothesis is no longer applicable.

The fluid continuity equation can be written as:

$$\frac{1}{r} \frac{\partial(r u_r)}{\partial r} + \frac{1}{r} \frac{\partial u_\theta}{\partial \theta} + \frac{\partial u_z}{\partial z} = - \frac{\partial \rho}{\partial t}$$

Where r is the radial direction value, θ is the angle coordinate, z is the vertical coordinate, ρ is the fluid density, t is time, u_r , u_θ and u_z are the fluid velocities in each of the respective directions.

Alas, the Navier-Stokes equation become:

$$\begin{aligned} \vec{r}: \rho \left(\frac{\partial u_r}{\partial t} + u_r \frac{\partial u_r}{\partial r} + \frac{u_\theta}{r} \frac{\partial u_r}{\partial \theta} - \frac{u_\theta^2}{r} + u_z \frac{\partial u_r}{\partial z} \right) &= - \frac{\partial P}{\partial r} + \rho g_r + \mu \left[\frac{1}{r} \frac{\partial}{\partial r} \left(r \frac{\partial u_r}{\partial r} \right) - \frac{u_r}{r^2} + \frac{1}{r^2} \frac{\partial^2 u_r}{\partial \theta^2} - \frac{1}{r^2} \frac{\partial u_\theta}{\partial \theta} + \frac{\partial^2 u_r}{\partial z^2} \right] \\ \vec{\theta}: \rho \left(\frac{\partial u_\theta}{\partial t} + u_r \frac{\partial u_\theta}{\partial r} + \frac{u_\theta}{r} \frac{\partial u_\theta}{\partial \theta} - \frac{u_r u_\theta}{r} + u_z \frac{\partial u_\theta}{\partial z} \right) &= - \frac{\partial P}{\partial \theta} \frac{1}{r} + \rho g_\theta + \mu \left[\frac{1}{r} \frac{\partial}{\partial r} \left(r \frac{\partial u_\theta}{\partial r} \right) - \frac{u_\theta}{r^2} + \frac{1}{r^2} \frac{\partial^2 u_\theta}{\partial \theta^2} - \frac{2}{r^2} \frac{\partial u_r}{\partial \theta} + \frac{\partial^2 u_\theta}{\partial z^2} \right] \\ \vec{z}: \rho \left(\frac{\partial u_z}{\partial t} + u_r \frac{\partial u_z}{\partial r} + \frac{u_\theta}{r} \frac{\partial u_z}{\partial \theta} - \frac{u_\theta}{r} \frac{\partial u_z}{\partial \theta} + u_z \frac{\partial u_z}{\partial z} \right) &= - \frac{\partial P}{\partial z} + \rho g_z + \mu \left[\frac{1}{r} \frac{\partial}{\partial r} \left(r \frac{\partial u_z}{\partial r} \right) + \frac{1}{r^2} \frac{\partial^2 u_z}{\partial \theta^2} + \frac{\partial^2 u_z}{\partial z^2} \right] \end{aligned}$$

Where P is the three-dimensional pressure field across the fluid, g_i is the respective component of the gravity in each coordinate and μ is the dynamic viscosity of the fluid. The simplifications taken for granted when solving these equations were:

$$\begin{aligned}
 u_z &= 0 & \frac{\partial^i u_r}{\partial z^i} &= 0 \mid i \in \mathbb{N} \\
 \frac{\partial u_i}{\partial t} &= 0 \mid i \in [\vec{r}, \vec{\theta}, \vec{z}] & \frac{\partial^i u_\theta}{\partial z^i} &= 0 \mid i \in \mathbb{N} \\
 \vec{g} &= \begin{bmatrix} 0 \\ 3 \times 1 \end{bmatrix}
 \end{aligned}$$

These simplifications imply the fluid does not move across the flank of the tooth, which, as its well known, is inherently false, however, this allows to model the movement of the fluid across the meshing of the flanks more simply. Considering the velocity in both \vec{r} and $\vec{\theta}$ to be independent from \vec{z} allows for a fully decoupled two-dimensional model along the \vec{r} and $\vec{\theta}$ directions, which, represents uniform pressure across the fluid “layers”, thus resulting in varying pressures for two points in different z coordinates but same \vec{r} and $\vec{\theta}$, thus, respecting the pseudo-three-dimensional problem configuration proposed.

Considering the fluid velocity variation to be dependent of the angle position as well as the radius allows for the computation of the fluid compression as the points in the gear surface move closer together, thus 2 points in the same circumference to have different pressures as they would be in different angles and therefore, the fluid will not behave as laminar throughout the model, which, would be a poor definition.

The effects of gravity have been disregarded throughout the model, since, at its core it will operate with the film thickness provided by the corresponding EHL model.

EHL is only one of the three possible lubrication regimes. The lubrication regimes are:

- **Elastohydrodynamic Lubrication (EHL):** There exists a thin layer of fluid between both surfaces so there is no direct contact in between each other. This is the go-to since it prevents surface damage such as scuffing. It is typically associated with an increase of the friction coefficient as shown in the Stribeck curve
- **Mixed Lubrication (ML):** There is some contact between the surfaces, whilst other regions have an oil film in between them. This leads to a decrease of the friction coefficient between both surfaces.
- **Boundary Lubrication (BL):** There is mostly direct contact between the surfaces, with a constant friction coefficient (solid-to-solid contact) whilst some pockets of lubricant may be found.

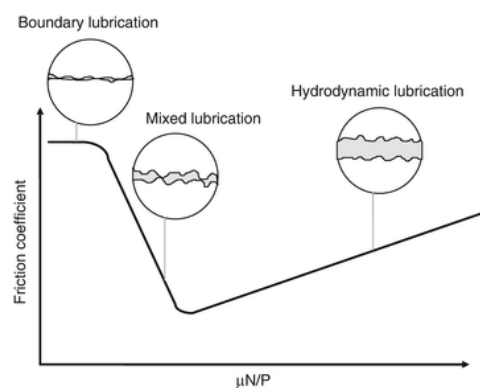


Figure 28 Stribeck curve (Wang, 2013)

Time effects have been disregarded since it would overcomplicate the model and increase the computational cost without adding too much information, since the model itself works by converging a set of stationary events.

Modelling of gear surface roughness impact on electrified transmissions' efficiency
 4. Model adaptation

To further solve the model, a velocity field is required, and for such, being consistent with the previously listed simplifications, the velocity field has been assumed to be turbulent and therefore, it presents a parabolic distribution through the fluid height.

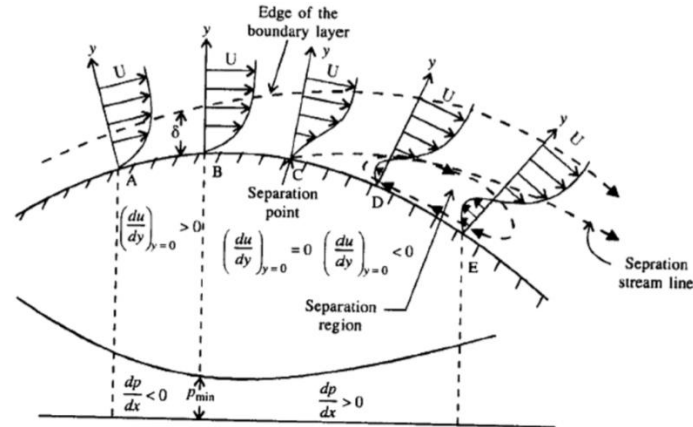


Figure 29 Fluid velocity profile over a rolling cylinder (IIT Bombay Alumni, 2022)

This is applicable when a thick enough fluid layer (fluid total thickness is greater than the boundary layer height) lies on the gear's surface, which can be obtained via normal dipping techniques; jet lubrication or full submersion. Different lubrication techniques are discussed in (Abraham, 2014). In this Master Thesis, the author discusses the different effects of lubrication and their effect on scuffing. He concludes that neither mist nor dip lubrication are sufficient to prevent scuffing, where, overall, mist lubrication is blatantly insufficient for the load cases presented in the report. Jet lubrication was found to have a strong correlation with load and consequently with flow rate. It also showed that jet velocity is more important than volumetric flow rate when preventing scuffing.

The fluid height, at any point of the fluid can be described exclusively as a function of the EHL film thickness and the angle in cylindrical coordinates (with the origin aligned with one of the roller's main axes):

Navier Stokes stand-in variables

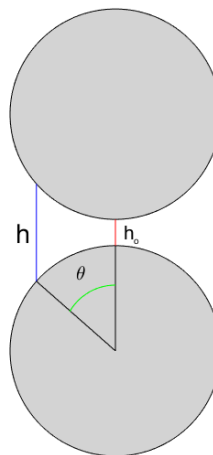


Figure 30 Navier-Stokes stand in contour variables

$$h = h_0 + (1 - \cos \theta)(r_1 + r_2)$$

As such, the fluid velocity can be rewritten as a function of height (and therefore, inherently, θ and the radius), therefore, the following system of equations can be solved:

$$\begin{cases} v(h) = Ah^2 + B^2 + C \\ v(\theta = 0, r = r_2) = \omega_2 r_2 \\ v(\theta = 0, r = r_1) = \omega_1 r_1 \end{cases}$$

Where A, B and C are the coefficients to be calculated, ω_i is the radial speed of the gear tooth (for the driving and driven gears 1 and 2 respectively). To solve the model, it's imperative to rely on a variable denoted as u_∞ which is widely regarded as the fluid velocity far away from the working surfaces (and the boundary layer thereby generated) and thus stable in time and space. The coefficients can thus be solved as:

$$\begin{aligned} A &= \frac{4}{(r_2 + h_o)^2} \left(\frac{\omega_1 r_1 + \omega_2 r_2}{2} - u_\infty \right) \\ B &= \frac{4u_\infty - (\omega_1 r_1 + 3\omega_2 r_2)}{r_2 + h_o} \\ C &= \omega_2 r_2 \end{aligned}$$

Since both A and B are linearly dependent on u_∞ they would be remarkably sensible to it, alas, u_∞ is a key parameter. A commonly accepted simplification assumes this velocity to be 0 or in moving reference, the properties of said base e.g. a transmission solidary to a moving vehicle. Another reasonable assumption would be for u_∞ to be the velocity extracted from solving Bernoulli's equation for any fluid line stemming from a coolant pump (if there are any) considering energy losses due to the changes in surface area and vorticity of the fluid when passing through the gears.

Another, simpler way of approximating u_∞ is by applying Bernoulli's equation backwards once the fluid's pressure field is fully characterized in the meshing point.

Either way, accepting, this definition of the fluid velocity represents u_θ , the continuity equation yields the velocity distribution as a function of the radius:

$$u_r = -\frac{1}{r} (r_1 + r_2) (2hA \sin\theta + B \sin\theta) (r + D) - C$$

Which, when applying the contour conditions whereby, in the meshing point $u_r = 0 \forall r$, then:

$$u_r = 0 \forall r \Leftrightarrow C = 0$$

Alas, the velocity field of the fluid at any point within the boundary layer can be described as:

$$\begin{bmatrix} u_r \\ u_\theta \\ u_z \end{bmatrix} = \begin{bmatrix} -\frac{1}{r} (r_1 + r_2) (2hA \sin\theta + B \sin\theta) (r + D) \\ Ah^2 + B^2 + \omega_2 r_2 \\ 0 \end{bmatrix} \Bigg| \begin{cases} A = \frac{4}{(r_2 + h_o)^2} \left(\frac{\omega_1 r_1 + \omega_2 r_2}{2} - u_\infty \right) \\ B = \frac{4u_\infty - (\omega_1 r_1 + 3\omega_2 r_2)}{r_2 + h_o} \end{cases}$$

Solving for D in turn (the integration constant) could be done so by calculating the boundary layer for a rotating cylinder and stating:

$$u_r(r = \delta) = u_\infty$$

Where δ is the height of the boundary layer at any point of the gear's flank profile.

The boundary layer has been approximated by a number of renowned authors such a Reynold, Prandtl and Von Karman, in this algorithm, the logarithmic implementation (converted to cylindrical coordinates) will be used:

$$u = \sqrt{\frac{\tau_w}{\rho}} \left(\frac{1}{0,41} \ln \frac{r \sin\theta}{y_o} + 5 \right) \Big| y_o = \begin{cases} \frac{3.5D_{84}}{30} \text{ if } Re_w = \frac{u_\tau k_s}{\nu} > 100 \\ \frac{\nu}{9u_\tau} \text{ if } Re_w = \frac{u_\tau k_s}{\nu} < 3 \end{cases}$$

Modelling of gear surface roughness impact on electrified transmissions' efficiency
 4. Model adaptation

Where τ_w represents the shear stress on the wall, which would need to be calculated at every point, however, due to the complexity of the problem when considering real engineering surfaces τ_w will be considered as the average, thus it can be represented as:

$$\overline{\tau_w} = \frac{F_s - \int \mu_{mm} p ds_1}{|s_2|}$$

Where $\int \mu_{mm} p ds_1$ is the sliding of the points of both surfaces in which there is metal-to-metal contact and $|s_2|$ is the physical size of the surface in which there is no metal-to-metal contact.

Furthermore, D_{84} represents the 84-percentile grain size of the surface, however, adapting said parameter to the existing algorithm definition D_{84} will be the 84-percentile of the radius of the surface roughness.

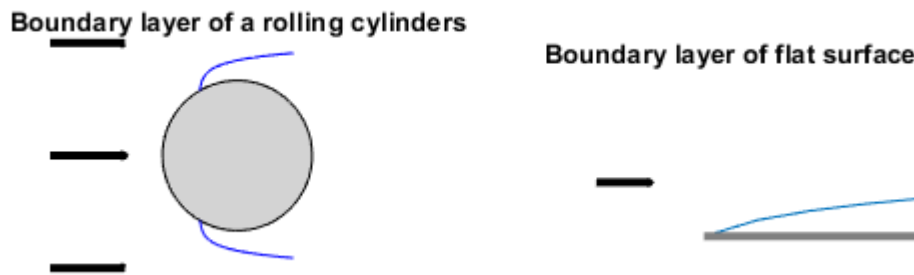


Figure 31 Boundary layer representation

Alternatively, an infinitely thin layer of fluid in contact with a moving solid will always move at the wall's speed, alas, the point at which the boundary layer starts can be described as:

$$P \mid \vec{u} = \begin{bmatrix} u_r = 0 \\ u_\theta = u_{wall} \end{bmatrix}$$

Whereby, due to the solidarity in movement, there is no radial component since the wall has exclusively movement in the $\vec{\theta}$ direction, alas, solving for D we get (assuming the boundary layer starts at the root of the flank since above there is an existing vorticity from the previous tooth):

$$\theta = \frac{2\pi}{z}$$

$$R_b = mz * \cos\alpha$$

$$\vec{u}(P) = \begin{bmatrix} u_r = 0 \\ u_\theta = u_{wall} \end{bmatrix} \Leftrightarrow D = -R_b$$

In turn, the parameter h_o can be estimated from traditional EHL theory if h_o was considered to be the fluid film present between 2 lubricated surfaces. Said parameter, traditionally labelled Δh , relies on the deformation of surface peaks due to pressurization of the fluid as its being entrained, causing a Venturi between both surfaces (M.M.Khonsari, 2015). Said height, would traditionally be used to calculate the parameter Λ , which could partly predict the type of contact between both surfaces.

That prediction was improved upon in (Jonny Hansen, 2021), to the defining parameter Λ^* , said parameter could predict a EHL contribution of 60-80% in mixed lubrication conditions for any ball-on-disc contact and correctly predict a 100% EHL contact when full-film lubrication was tested.

Furthermore, said parameter, Λ^* , accounted for the roughness of real engineering surfaces, although not bilaterally, one surface was considered to be perfectly flat and infinitely rigid (Jonny Hansen, 2021).

Modelling of gear surface roughness impact on electrified transmissions' efficiency
4. Model adaptation

In said publication (Jonny Hansen, 2021) and PhD Thesis (Hansen, 2021), the authors go into a lot of detail explaining this new parameter Λ^* , which can be considered as the ratio between the total surface deformation and the peak surface roughness, with the formulation:

$$\Lambda^* = \frac{h^*}{S_{pk}}$$

Where Λ^* is the aforementioned lubrication regime estimator where $\Lambda^* \geq 1$ implies full EHL lubrication whilst $\Lambda^* < 1$ implies boundary lubrication or mixed lubrication. The total surface separation is represented by h^* and the peak surface roughness is represented by S_{pk} in the equation.

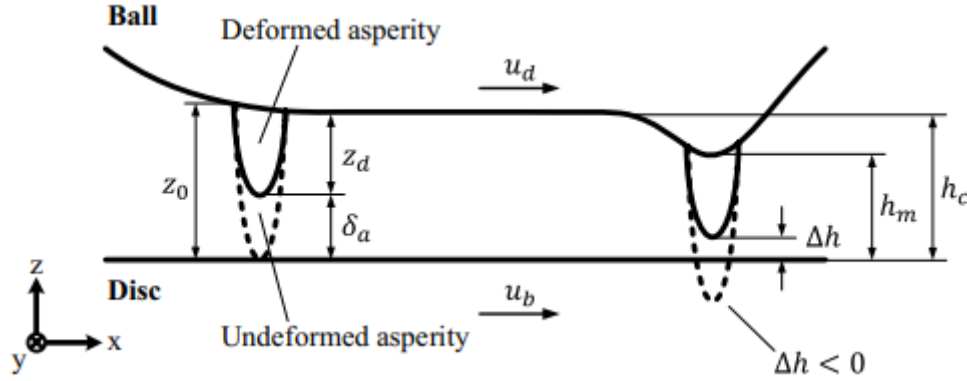


Figure 32 Traditional EHL parameter depiction (Jonny Hansen, 2021)

Furthermore, in the publication (Jonny Hansen, 2021), the authors go into a lot of trouble to describe their newfound height h^* based on traditional EHL parameters, arriving at:

$$h^* = h_m + h_c f_q$$

Where h_m is the minimal surface separation plus the deformed asperity height variation; h_c is the distance between both surfaces (disregarding the asperities) and f_q is an adimensional EHL variable based on the radii, a sort of correction factor. Their respective formulations are (Hansen, 2021):

$$h_m = 3.63U^{0.68}G^{0.49}W^{-0.073}(1 - e^{-0.68k})R'_x | k = 1.03 \left(\frac{R'_y}{R'_x}\right)^{\frac{2}{\pi}}$$

$$h_c = 2.69U^{0.67}G^{0.53}W^{-0.067}(1 - 0.61e^{-0.73k})R'_x | k = 1.03 \left(\frac{R'_y}{R'_x}\right)^{\frac{2}{\pi}}$$

$$f_q = \left(\frac{R'_{x,a}}{R'_{x,b}}\right)^\alpha \frac{1 - \gamma_1 e^{-\gamma_2 \left(\frac{R'_{y,a}}{R'_{x,a}}\right)^{\gamma_3}}}{1 - \gamma_1 e^{-\gamma_2 \left(\frac{R'_{y,b}}{R'_{x,b}}\right)^{\gamma_3}}}$$

In this set of equations, the coefficients α , γ_1 , γ_2 and γ_3 depend on the direction of the surface roughness and its direction with regards to the oil entrainment direction, with the list of values shown below:

Table 1 Adimensional EHL coefficients

Surface roughness direction	α (-)	γ_1 (-)	γ_2 (-)	γ_3 (-)
Isotropic & transversal	1.134 - X	0.61	0.75	2/ π
Longitudinal	1.146 - X	1	1.23	2/3

Modelling of gear surface roughness impact on electrified transmissions' efficiency
 4. Model adaptation

Furthermore, U, G and W are the aforementioned dimensionless speed, material and load variables. The variable X is the corresponding exponent of the dimensionless speed parameter in each equation. The R' represents the effective radii on different directions, where the x and y subindexes represent the oil-entrainment direction and it's perpendicular, respectively and the a and b subscripts represent asperity radius or the macro geometry radius respectively (when no a or b subindexes are present the variable represents the smooth surface effective radius).

This does not necessarily agree the hypothesis proposed in (Kadiric P. R., 2019), where the fluid film thickness was theorized to decrease with an increasing SRR.

When modifying the general formulation to gears, the radius $R'_{y,b}$ and R'_y are ∞ since the gears in the entrainment direction represent a circumference centred in the pressure line, but in the perpendicular direction, they are but a flat line, thus having an infinite radius, alas, the equations can be simplified to:

$$h_m = 3.63U^{0.68}G^{0.49}W^{-0.073}$$

$$h_c = 2.69U^{0.67}G^{0.53}W^{-0.067}$$

$$f_q = \left(\frac{R'_{x,a}}{R'_{x,b}}\right)^\alpha \left(1 - \gamma_1 e^{-\gamma_2 \left(\frac{R'_{y,a}}{R'_{x,a}}\right)^{\gamma_3}}\right)$$

Since:

$$\lim_{R'_{y,b} \rightarrow \infty} e^{-0.68*1.03 \left(\frac{R'_y}{R'_x}\right)^{\frac{2}{\pi}}} = e^{-0.68*1.03 \lim_{R'_y \rightarrow \infty} \left(\frac{R'_y}{R'_x}\right)^{\frac{2}{\pi}}} = e^{-\infty} \rightarrow 0$$

$$\lim_{R'_{y,b} \rightarrow \infty} e^{-0.73*1.03 \left(\frac{R'_y}{R'_x}\right)^{\frac{2}{\pi}}} = e^{-0.73*1.03 \lim_{R'_y \rightarrow \infty} \left(\frac{R'_y}{R'_x}\right)^{\frac{2}{\pi}}} = e^{-\infty} \rightarrow 0$$

$$\lim_{R'_{y,b} \rightarrow \infty} 1 - \gamma_1 e^{-\gamma_2 \left(\frac{R'_{y,b}}{R'_{x,b}}\right)^{\gamma_3}} = 1 - \gamma_1 e^{-\gamma_2 \lim_{R'_{y,b} \rightarrow \infty} \left(\frac{R'_{y,b}}{R'_{x,b}}\right)^{\gamma_3}} = 1 - \gamma_1 e^{-\infty} \rightarrow 1$$

An added benefit of this formulation is the removal of the film thickness as an independent variable when considering micro pitting, as described previously in (Hui Long, 2015).

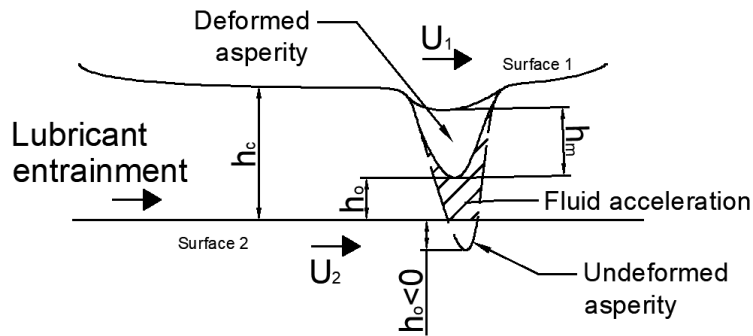


Figure 33 Adapted h^* model representation

Therefore, finally the Navier-Stokes equations can be solved to calculate the pressure field of the fluid, only in the \vec{r} direction since the inevitable consequence of decoupling the \vec{z} direction yields:

$$\frac{\partial P}{\partial z} = 0$$

Therefore, the pressure distribution in any point of the fluid can be expressed as:

Modelling of gear surface roughness impact on electrified transmissions' efficiency

4. Model adaptation

$$\begin{aligned}
 P(r, \theta) = & (16Ar_1^2 \sin(\theta) - R_b^2 \rho + 16Ar_2^2 \sin(\theta) - 4Ar_1^2 (\sin(2\theta) + 2\sin(\theta)) - 4Ar_2^2 (\sin(2\theta) + 2\sin(\theta)) - 4C\mu\theta/2 + 4Br_1 \sin(\theta) + 4Br_2 \sin(\theta) + 4CR_b \rho\theta/2 - 4Bh_0 \mu\theta/2 + 2C^2 r^2 \rho \ln(r) - 4B\mu r_1 \theta/2 - 4B\mu r_2 \theta/2 - \\
 & 4A\mu r_1^2 (\sin(2\theta)/8 + \sin(\theta)/4) - 4A\mu r_2^2 (\sin(2\theta)/8 + \sin(\theta)/4) + 8A\mu r_1^2 + 8A\mu r_2^2 + 8Ah_0 r_1 \sin(\theta) + 8Ah_0 r_2 \sin(\theta) + 2B\mu r_1 \sin(\theta) + 2B\mu r_2 \sin(\theta) + 32Ar_1 r_2 \sin(\theta) - 8Ar_1 r_2 (\sin(2\theta) + 2\sin(\theta)) - 4Ah_0^2 \mu\theta/2 - 6A\mu r_1^2 \theta/ \\
 & 2 - 6A\mu r_2^2 \theta/2 + 5A\mu r_1^2 \sin(\theta) + 5A\mu r_2^2 \sin(\theta) + 2B\mu r_1 + 2B\mu r_2 - 5AR_{br1}^2 \rho \sin(\theta) - 5AR_{br2}^2 \rho \sin(\theta) + 8A\mu r_1^2 \sin(\theta) + 8A\mu r_2^2 \sin(\theta) - 2A\mu r_1^2 (\sin(2\theta) + 2\sin(\theta)) - 2A\mu r_2^2 (\sin(2\theta) + 2\sin(\theta)) + 64A^2 r_1^4 \rho (\cos(\theta)/2 + \\
 & 1/2) + 64A^2 r_2^4 \rho (\cos(\theta)/2 + 1/2) - 96A^2 r_1^4 \rho \cos(\frac{\theta}{2})^4 - 96A^2 r_2^4 \rho \cos(\frac{\theta}{2})^4 + 64A^2 r_1^4 \rho \cos(\frac{\theta}{2})^6 + 64A^2 r_2^4 \rho \cos(\frac{\theta}{2})^6 - 16A^2 r_1^4 \rho \cos(\frac{\theta}{2})^8 - 16A^2 r_2^4 \rho \cos(\frac{\theta}{2})^8 + 8B^2 r_1^2 \rho (\cos(\theta)/2 + 1/2) + 8B^2 r_2^2 \rho (\cos(\theta)/2 + 1/2) - \\
 & 4B^2 r_1^2 \rho \cos(\frac{\theta}{2})^4 - 4B^2 r_2^2 \rho \cos(\frac{\theta}{2})^4 + 4Ah_0 \mu r_1 + 4Ah_0 \mu r_2 + 16A\mu r_1 r_2 + 4BR_b h_0 \rho\theta/2 + 4BR_b r_1 \rho\theta/2 + 4BR_b r_2 \rho\theta/2 + 4AR_b r_1^2 \rho (\sin(2\theta)/8 + \sin(\theta)/4) + 4AR_b r_2^2 \rho (\sin(2\theta)/8 + \sin(\theta)/4) - 8Ah_0 \mu r_1 \theta/2 - \\
 & 8Ah_0 \mu r_2 \theta/2 - 12A\mu r_1 r_2 \theta/2 - 2BR_b r_1 \rho \sin(\theta) - 2BR_b r_2 \rho \sin(\theta) + 4Ah_0 \mu r_1 \sin(\theta) + 4Ah_0 \mu r_2 \sin(\theta) + 4AR_b h_0^2 \rho\theta/2 + 10A\mu r_1 r_2 \sin(\theta) + 2B\mu r_1 \sin(\theta) + 2B\mu r_2 \sin(\theta) - A\mu r_1 r_2 (\sin(2\theta) + 2\sin(\theta)) + 6AR_b r_1^2 \rho\theta/2 + \\
 & 6AR_b r_2^2 \rho\theta/2 + 2A^2 h_0^2 r^2 \rho \ln(r) + 2B^2 h_0^2 r^2 \rho \ln(r) + 64A^2 r_1^4 \rho \ln(r) + 64A^2 r_2^4 \rho \ln(r) + 12B^2 r_1^2 \rho \ln(r) + 12B^2 r_2^2 \rho \ln(r) + 24B^2 r_1 r_2 \rho \ln(r) + 48A^2 h_0^2 r_1^2 \rho (\cos(\theta)/2 + 1/2) + 48A^2 h_0^2 r_2^2 \rho (\cos(\theta)/2 + 1/2) - \\
 & 24A^2 h_0^2 r_1^2 \rho \cos(\frac{\theta}{2})^4 - 24A^2 h_0^2 r_2^2 \rho \cos(\frac{\theta}{2})^4 + 384A^2 r_1^2 r_2^2 \rho (\cos(\theta)/2 + 1/2) - 576A^2 r_1^2 r_2^2 \rho \cos(\frac{\theta}{2})^4 + 384A^2 r_1^2 r_2^2 \rho \cos(\frac{\theta}{2})^6 - 96A^2 r_1^2 r_2^2 \rho \cos(\frac{\theta}{2})^8 - 4AR_b h_0 r_1 \rho \sin(\theta) - 4AR_b h_0 r_2 \rho \sin(\theta) + 48ABr_1^3 \rho (\cos(\theta)/2 + 1/ \\
 & 2) + 48ABr_2^3 \rho (\cos(\theta)/2 + 1/2) - 48ABr_1^3 \rho \cos(\frac{\theta}{2})^4 - 48ABr_2^3 \rho \cos(\frac{\theta}{2})^4 + 16ABr_1^3 \rho \cos(\frac{\theta}{2})^6 + 16ABr_2^3 \rho \cos(\frac{\theta}{2})^6 + 16ACr_1^2 \rho (\cos(\theta)/2 + 1/2) + 16ACr_2^2 \rho (\cos(\theta)/2 + 1/2) - 8ACr_1^2 \rho \cos(\frac{\theta}{2})^4 - 8ACr_2^2 \rho \cos(\frac{\theta}{2})^4 - \\
 & 10AR_b r_1 r_2 \rho \sin(\theta) + AR_b r_1 r_2 \rho (\sin(2\theta) + 2\sin(\theta)) + 4Ah_0 \mu r_1 \sin(\theta) + 4Ah_0 \mu r_2 \sin(\theta) + 16A\mu r_1 r_2 \sin(\theta) - 4A\mu r_1 r_2 (\sin(2\theta) + 2\sin(\theta)) + 4B^2 h_0 r_1 \rho (\frac{\cos(\theta)}{2} + \frac{1}{2}) + 4B^2 h_0 r_2 \rho (\frac{\cos(\theta)}{2} + \frac{1}{2}) + 112A^2 h_0 r^2 r_1^3 \rho \ln(r) + \\
 & 20A^2 h_0^3 r^2 r_1 \rho \ln(r) + 112A^2 h_0 r^2 r_2^3 \rho \ln(r) + 20A^2 h_0^3 r^2 r_2 \rho \ln(r) + 16B^2 r_1 r_2 \rho (\frac{\cos(\theta)}{2} + \frac{1}{2}) - 8B^2 r_1 r_2 \rho \cos(\frac{\theta}{2})^4 + 256A^2 r^2 r_1 r_2^3 \rho \ln(r) + 256A^2 r^2 r_1^3 r_2 \rho \ln(r) + 4BCh_0 r^2 \rho \ln(r) + 10BCr^2 r_1 \rho \ln(r) + 10BCr^2 r_2 \rho \ln(r) + \\
 & 96A^2 h_0 r_1^3 \rho (\frac{\cos(\theta)}{2} + \frac{1}{2}) + 8A^2 h_0^3 r_1 \rho (\frac{\cos(\theta)}{2} + \frac{1}{2}) + 96A^2 h_0 r_2^3 \rho (\frac{\cos(\theta)}{2} + \frac{1}{2}) + 8A^2 h_0^3 r_2 \rho (\frac{\cos(\theta)}{2} + \frac{1}{2}) - 96A^2 h_0 r_1^3 \rho \cos(\frac{\theta}{2})^4 - 96A^2 h_0 r_2^3 \rho \cos(\frac{\theta}{2})^4 + 32A^2 h_0 r_1^3 \rho \cos(\frac{\theta}{2})^6 + 32A^2 h_0 r_2^3 \rho \cos(\frac{\theta}{2})^6 + 72A^2 h_0^2 r^2 r_1^2 \rho \ln(r) + \\
 & 72A^2 h_0^2 r^2 r_2^2 \rho \ln(r) + 256A^2 r_1 r_2^3 \rho (\cos(\theta)/2 + 1/2) + 256A^2 r_1^3 r_2 \rho (\cos(\theta)/2 + 1/2) - 384A^2 r_1 r_2^3 \rho \cos(\frac{\theta}{2})^4 - 384A^2 r_1^3 r_2 \rho \cos(\frac{\theta}{2})^4 + 256A^2 r_1 r_2^3 \rho \cos(\frac{\theta}{2})^6 + 256A^2 r_1^3 r_2 \rho \cos(\frac{\theta}{2})^6 - 64A^2 r_1 r_2^3 \rho \cos(\frac{\theta}{2})^8 - \\
 & 64A^2 r_1^3 r_2 \rho \cos(\frac{\theta}{2})^8 + 384A^2 r_1^2 r_2^2 \rho \ln(r) + 4ABh_0^3 r^2 \rho \ln(r) + 4ACh_0^2 r^2 \rho \ln(r) + 4BCr_1 \rho (\cos(\theta)/2 + 1/2) + 4BCr_2 \rho (\cos(\theta)/2 + 1/2) + 56ABr^2 r_1^3 \rho \ln(r) + 56ABr^2 r_2^3 \rho \ln(r) + 24ACr^2 r_1^2 \rho \ln(r) + 24ACr^2 r_2^2 \rho \ln(r) + \\
 & 8AR_b h_0 r_1 \rho\theta/2 + 8AR_b h_0 r_2 \rho\theta/2 + 12AR_b r_1 r_2 \rho\theta/2 + 10B^2 h_0 r^2 r_1 \rho \ln(r) + 10B^2 h_0 r^2 r_2 \rho \ln(r) + 288A^2 h_0 r_1 r_2^2 \rho (\cos(\theta)/2 + 1/2) + 288A^2 h_0 r_1^2 r_2 \rho (\cos(\theta)/2 + 1/2) + 96A^2 h_0^2 r_1 r_2 \rho (\cos(\theta)/2 + 1/2) - \\
 & 288A^2 h_0 r_1 r_2^2 \rho \cos(\frac{\theta}{2})^4 - 288A^2 h_0 r_1^2 r_2 \rho \cos(\frac{\theta}{2})^4 - 48A^2 h_0^2 r_1 r_2 \rho \cos(\frac{\theta}{2})^4 + 96A^2 h_0 r_1 r_2^2 \rho \cos(\frac{\theta}{2})^6 + 96A^2 h_0 r_1^2 r_2 \rho \cos(\frac{\theta}{2})^6 + 8ACh_0 r_1 \rho (\cos(\theta)/2 + 1/2) + 8ACh_0 r_2 \rho (\cos(\theta)/2 + 1/2) + 72ABh_0 r^2 r_1^2 \rho \ln(r) + \\
 & 30ABh_0^2 r^2 r_1 \rho \ln(r) + 72ABh_0 r^2 r_2^2 \rho \ln(r) + 30ABh_0^2 r^2 r_2 \rho \ln(r) + 32ACr_1 r_2 \rho (\cos(\theta)/2 + 1/2) - 16ACr_1 r_2 \rho \cos(\frac{\theta}{2})^4 + 168ABr^2 r_1 r_2^2 \rho \ln(r) + 168ABr^2 r_1^2 r_2 \rho \ln(r) + 48ABh_0 r_1^2 \rho (\cos(\theta)/2 + 1/2) + 12ABh_0^2 r_1 \rho (\cos(\theta)/2 + \\
 & 1/2) + 48ABh_0 r_2^2 \rho (\cos(\theta)/2 + 1/2) + 12ABh_0^2 r_2 \rho (\cos(\theta)/2 + 1/2) - 24ABh_0 r_1^2 \rho \cos(\frac{\theta}{2})^4 - 24ABh_0 r_2^2 \rho \cos(\frac{\theta}{2})^4 + 144ABr_1 r_2^2 \rho (\cos(\theta)/2 + 1/2) + 144ABr_1^2 r_2 \rho (\cos(\theta)/2 + 1/2) - 144ABr_1 r_2^2 \rho \cos(\frac{\theta}{2})^4 - \\
 & 144ABr_1^2 r_2 \rho \cos(\frac{\theta}{2})^4 + 48ABr_1 r_2^2 \rho \cos(\frac{\theta}{2})^6 + 48ABr_1^2 r_2 \rho \cos(\frac{\theta}{2})^6 + 336A^2 h_0 r^2 r_1 r_2^2 \rho \ln(r) + 336A^2 h_0 r^2 r_1^2 r_2 \rho \ln(r) + 144A^2 h_0^2 r^2 r_1 r_2 \rho \ln(r) + 20ACh_0 r^2 r_1 \rho \ln(r) + 20ACh_0 r^2 r_2 \rho \ln(r) + 48ACr^2 r_1 r_2 \rho \ln(r) + \\
 & 144ABh_0 r^2 r_1 r_2 \rho \ln(r) + 96ABh_0 r_1 r_2 \rho (\cos(\theta)/2 + 1/2) - 48ABh_0 r_1 r_2 \rho \cos(\frac{\theta}{2})^4 / (2r^2)
 \end{aligned}$$

4. Model adaptation

4.3. Stress allocation

In the 2D deformable, rough line contact the fluid pressure influence and other forces acting on the surface is allocated differently depending on the lubrication regime.

When there is full EHL the pressure of the fluid is applied on both surfaces following the Navier-Stokes solution, as such $\sigma = P(r, \theta, \omega_1, \omega_2, \mu, \rho, R_b, h)$ for every point of the line contact of each surface, therefore, the variation of the pressure across the fluid pressure is considered. The shear stress due to rolling and sliding are then divided even across the entire line contact, as the fluid acts equally on the entire surface.

In BL or ML cases, the numerical solver already accounts for the pressure effect of the Navier-Stokes solution. If there is contact between surfaces, points where both surfaces, the formulation for allocating sliding and rolling resistance varies, such that the rolling resistance is allocated to said points, as for rolling resistance there needs to be surface engagement and the sliding forces are slightly modified to accommodate metal to metal contact, therefore, the surface stress follows the allocation logic and convergence equations:

$$\begin{cases} F_m = \sum \mu_m a^2 w_{con} \\ F_{s_no} = \sum \mu a^2 w_{no} \\ F_s = F_{s_no} + F_m \end{cases}$$

Where F_m is the sliding resistance from a metal-to-metal contact, along with the metal-to-metal friction coefficient, μ_m and w_{con} is the load experienced by every differential in contact with the opposing surface. On the other hand F_{s_no} represents the friction due to the fluid action and it's entirely dependent on the square differential size, a , the fluid's friction coefficient μ and the load in differentials which are not in contact with the other surface. Ensuring thus that the macroscopically calculated forces are verified by the model, since those are the precise formulations.

4.4. Fluid model testing

After solving the Navier-Stokes equations under the given hypothesis, the results need to be evaluated and compared against the Reynold's equations to verify, if, indeed, the pressure variation across the fluid film is insignificant.

After some literature review (Kadiric P. R., 2019), the minimum calculated film thickness lubrication was 43 nm, as such, the Navier Stokes solutions were evaluated with a maximum film separation of 100nm between the cylinders. Numerical results were computed at the pitch point of each gear tooth in contact and the results are shown below:

Modelling of gear surface roughness impact on electrified transmissions' efficiency
 4. Model adaptation

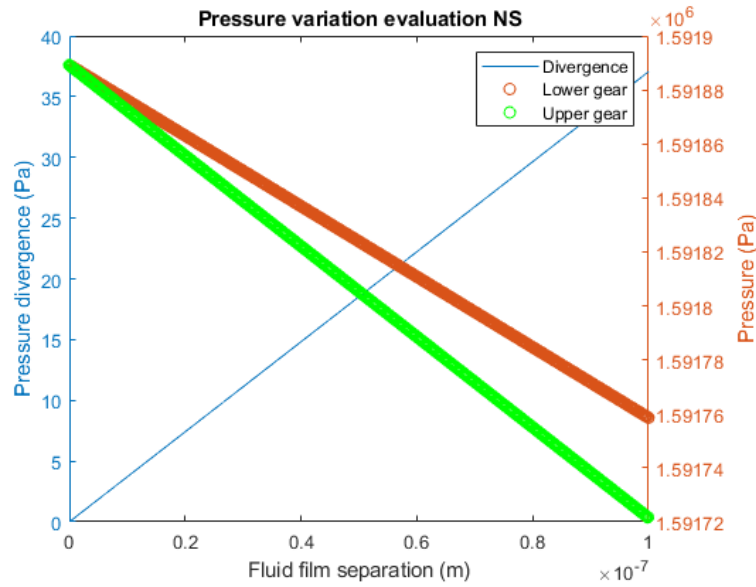


Figure 34 Navier Stokes surface pressure divergence

As can be seen above, the divergence of pressure has a maximum variation of 37.05 Pa at 100nm, insignificant when compared to the 1.59 MPa the lower gear experiments, alas, the solution verifies the Reynold's equations solution where the pressure variation across the film thickness is negligible (for thin films).

When considering large thicknesses (the film cannot be neglected in comparison to the other dimensions) the equation's divergence follows a quadratic reason as seen below:

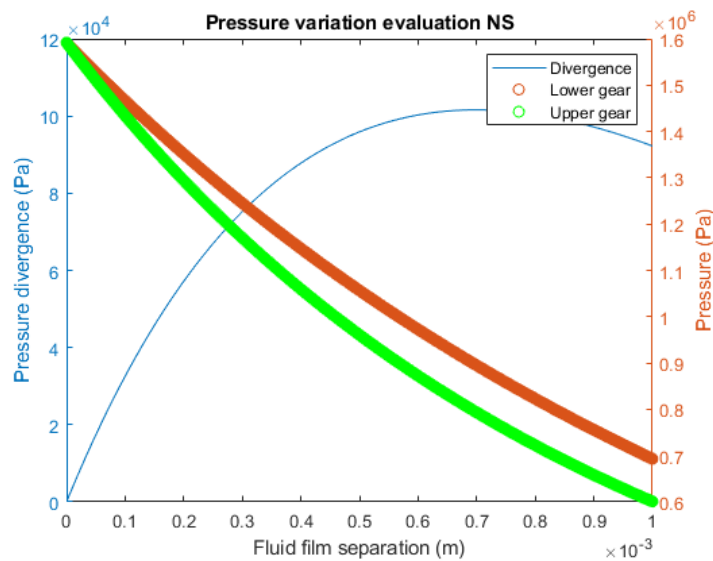


Figure 35 Navier Stokes surface pressure divergence in large gaps

In this case, for gear teeth with an equivalent circumference radius below 6mm the maximum divergence is of 16% between both surfaces, thus, the pressure variation is significant but this configuration escapes Reynold's definition since, the height is not significantly smaller than the other dimensions and said pressure (equivalent to energy) loss is due to the turbulence and vorticity of the fluid.

When verified against existing literature, most rely on Reynold's equations to calculate a patch contact (Jamali, Sharif, & Snide, 2014) and fluid film distribution in a three-dimensional workspace. It was found that transient dependent terms were of larger significance and influence

4. Model adaptation

than in quasi-static approximations of the same calculations, alas, it is safe to say, the model is inherently wrong until transient terms can be implemented appropriately. However, this would break model concordance since it is quasi-static in nature, based on the dry rough contact models approximations already made. Although, in the reference (Jamali, Sharif, & Snide, 2014), to determine the fluid film thickness, the traditional parameter Λ was used instead of the new parameter Λ^* as proposed in the reference (Hansen, 2021).

4.5. Thermal effects

It's common knowledge that surfaces in contact heat up due to friction. Said temperature increase is commonly referred to flash temperature (Rowe, 2014). Alas, the surface temperature in a frictional contact is often described as:

$$T_i = T_b + \Delta T$$

Where T_i is the surface temperature; T_b is the bulk temperature of the material and ΔT is the flash temperature increase.

The conundrum now lies on the definition of said flash temperature. As any heat transfer problem, it is strongly dependant on the initial configuration and the mechanisms involved. When both surfaces are in contact a simple Fourier conduction problem can be assumed with the electrical similarity with power being injected in between two resistances:

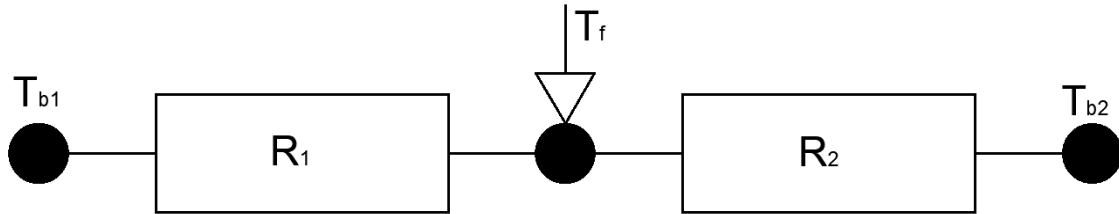


Figure 36 Thermal configuration differential contact

This set up is therefore described by the following simple conduction equations:

$$T_f - T_{b1} = \frac{q_1}{R_1}$$

$$T_f - T_{b2} = \frac{q_2}{R_2}$$

$$q = q_1 + q_2$$

Which when solved, yields the definition of flash temperature as:

$$T_f = \frac{q + T_{b1}R_2 + T_{b2}R_1}{R_1 + R_2}$$

Where q is the friction-generated heat ($q = v_s * \mu W$); R_i represents the thermal conductivity resistance and the subindexes 1,2 correspond to surface 1 and surface2 respectively. Said resistance follows the well-known formula (C-Therm, 2022):

$$R = \frac{L}{Ak}$$

Such that L is the length (in this application the length of a surface differential in meters), A is the area through which the heat is transferred (once again, adapted to a differential, the area of said differential in meters squared) and k is the thermal conductivity of the material (K/W).

In this application, a contact thermal resistance is not considered since by definition it represents the difficulty heat transfer faces when 2 uneven surfaces are in contact and thus the contact area is smaller than the nominal area (Ishizaki & Nagano, 2020). However, since the code only applies the conductivity equations to calculated direct contact, said resistance is redundant.

Modelling of gear surface roughness impact on electrified transmissions' efficiency
 4. Model adaptation

This heat definition also respects the findings made in (Kadiric P. R., 2019) where the temperature increase in the gear surface depends on the sliding speed.

When a thin layer of fluid exists between both surfaces a myriad of models exists, however, one of the latest and better suited for this application along with being backed up by both theory and testing is presented in (Masse, 2019). Starting from Fourier's equations they arrive to the formulation:

$$\Delta T(x, t) = \int_t dt' \int_x \frac{Q(x', t')}{2\pi k_s(t-t')} \exp\left\{\frac{[x-x'-u_i(t-t')]^2}{4\alpha_s(t-t')}\right\} dx'$$

Where u_i is the sliding velocity of each surface; k_s is the thermal conductivity of each surface and α_s is the thermal diffusivity of each surface.

When solving this equation, knowing the heat generated is independent of both variables x' and t' , the solution presents stability problems since, the solver, assuming a static problem, $t-t'$ yields an uncertainty, as $x-x'$ can easily be divided into differentials of the surface so for any point $X = 2a_L$. As such, a simplified solution can be reached if the following assumption is made: $t-t' \approx t \rightarrow dt' \approx dt$, which can also be applied to the x domain as such that $x-x' \approx x \rightarrow dx' \approx dx$, the equation becomes:

$$\Delta T(x, t) = \frac{Q}{2 * k_s \sqrt{\pi}} \int \frac{1}{\sqrt{t}} \operatorname{erfi}\left(\frac{x-v_i t}{\sqrt{4\alpha_s t}}\right) dt$$

Reaching this stage is possible since $Q(x', t')$ is independent of both x and t , however, this second integral cannot be solved. Alas, to employ this method, a new definition for the friction-generated heat would be needed.

An alternative formulation is proposed in (Zhou, Xing, & Hu, 2021), where the heat flux across a gear tooth is divided into circular differentials across the height of the tooth and a set of linear heat transfer problems, as seen below:

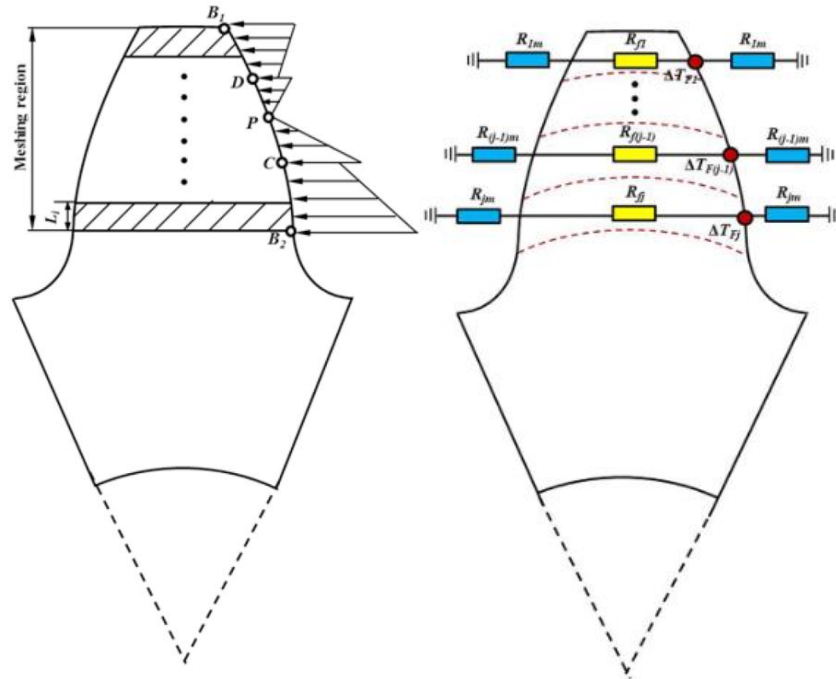


Figure 37 Heat flux distribution across the meshing flank (left) and flash temperature solver proposal (right) (Zhou, Xing, & Hu, 2021)

Modelling of gear surface roughness impact on electrified transmissions' efficiency
 4. Model adaptation

In this publication (Zhou, Xing, & Hu, 2021), this novel model is compared against both Blok's model and ISO standard model, achieving satisfactory results. As such, the problem can be rewritten following the electrical model equivalent as:

$$T_f - T_b = \frac{Q}{A} \left(\frac{1}{h_1} + \frac{L}{k_s} + \frac{1}{h_2} \right)$$

In the reference the formulation of an appropriate convection coefficient definition is discussed, reaching the formulation:

$$h_m = 0.288Re^{0.731}Pr^{1/3} * \frac{k_f}{d_i}$$

Where Pr is Prandtl's number. As such, the flash temperature can be computed as:

$$T_f = T_{bi} + \frac{Q_i}{A} \left(\frac{2}{h_i} + \frac{L}{k_s} \right)$$

Where the i subindexes indicate each surface respectively. To understand how the heat generated due to friction divides amongst both surfaces the equations presented in (Masse, 2019) were used:

$$T_{b1} - T_{b2} = \frac{h}{2k_f} (1 - 2\vartheta)Q \quad | \quad h = h_1 + h_2$$

$$Q_1 = \vartheta Q$$

$$Q_2 = (1 - \vartheta)Q$$

Where ϑ is the fraction heat coefficient.

After having described and implemented the inner workings of this module, it was tested on the existing surface measurements of a pitch line of a gear. The results are shown below:

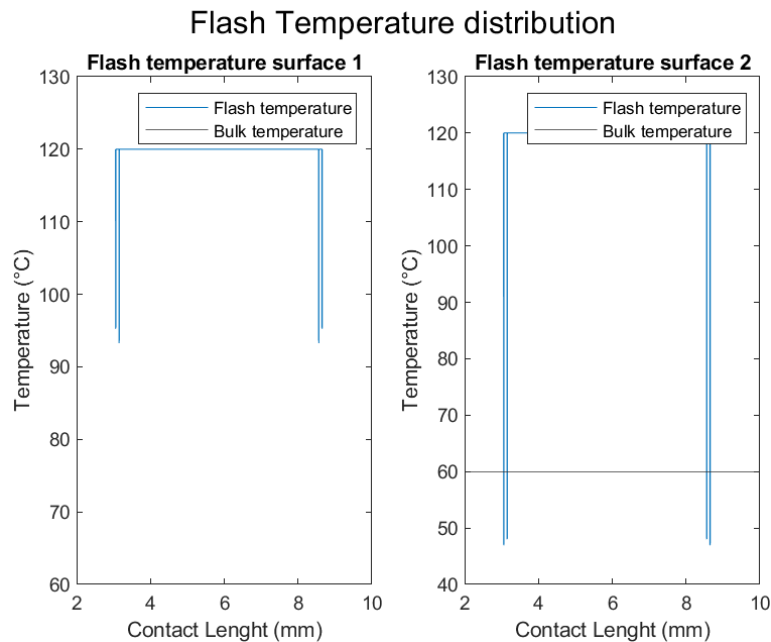
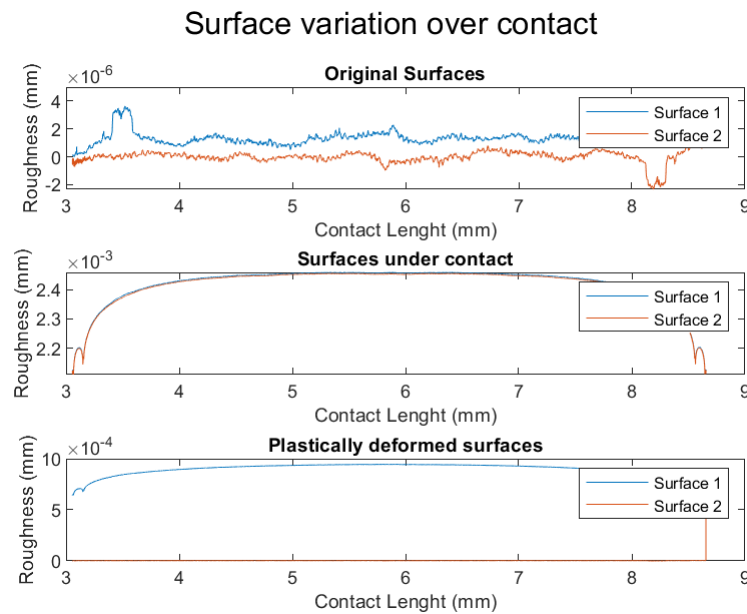


Figure 38 Flash temperature across the contact

4. Model adaptation



This surface configuration has specifically been chosen to portray the effect of direct contact and a wide gap between both surfaces at certain elements of the pitch line. It's evident from the figures above the temperature raises about 60 degrees in the points where there exists contact between both surfaces, whilst the temperature increase for differentials where there exists a lubricant film between both surfaces the increase is remarkably smaller. On top of that, surface 2, with a greater module and thus more mass and length, therefore a greater thermal resistance, which redirects the heat towards surface 1, hence why it heats up whilst the other, due to the effect of the treading lubricant cools down. The temperature range is by far smaller than the ones found in the literature with it only being 70K compared to the 100-200K found in the references (Zhou, Xing, & Hu, 2021) and (Masse, 2019) over the whole surface. However. The flash temperature prediction it's fairly similar at the pitch line as shown with the 130K in (Kahraman, 2021), (Zhou, Xing, & Hu, 2021) and (Masse, 2019). Since this model only looks at line contacts it is thus considered valid.

The temperature increase, although not high enough to cause scuffing by itself upon one contact, is high enough to deteriorate the lubricant properties (normally lubricants are kept below 100°C), which, over the course of the gear lifecycle can result in surface damage and scuffing as the lubricant degrades.

Furthermore, the temperature increase is correlated to the tribological mechanism present and the contact stress just as in the reference (González-Pérez, 2021) where they validate their findings via FEM across an entire flank, although the smooth contact approximation is used. Another paper used for validation is the reference (Anisetti, 2016), in this paper a dynamic system modelling the gear is coupled with a mixed-lubrication regime and the temperature studied at a wide range of temperatures, they found, as expected, that the temperature varied significantly when dynamic effects were considered, increasing the temperature beyond that of the static approximation, specially near resonance frequencies, however, physical verifications is still pending. Overall, to appropriately and accurately characterize the surface temperature increase a full 3D model such as the one presented in (Lyu, Meng, & Wen, 2021).

4.6. Churning and Windage Losses

The differences between churning and windage losses lies in the fluid definition, churning considers fluid mixture (multiphase) whilst windage involves single phase fluids (Gorla, 2016).

Several churning and windage loss models have been proposed over the years, of which, the most prominent ones are promptly collected and analysed in (Gorla, 2016) and (Nosko, 2017). Starting

Modelling of gear surface roughness impact on electrified transmissions' efficiency
 4. Model adaptation

from Ohlendorf's single gear losses model (Ohlendorf, 1962), going through Richter's adaptation to approximate 2 gears in contact (Richter, 1964) to arrive at Terekhov's model (Terekhov, 1975), more complex and complete model which together with the ISO 14179 (ISO, 2001) standard are both considered in (Pandurangi, 2020). Another noteworthy model presented and discussed in the reference (Gorla, 2016) is the one proposed in (Velex, 2007), which is considered one of the most accurate to date. However, the authors choose to evaluate the model proposed by Mauz in (Mauz, 1987) as it is widely regarded as the most comprehensive of all, albeit the author admits inaccuracies ranging from 5% to 15% with torque levels above 5Nm and below said threshold they can skyrocket to 50%. The model's inaccuracies are shown below:

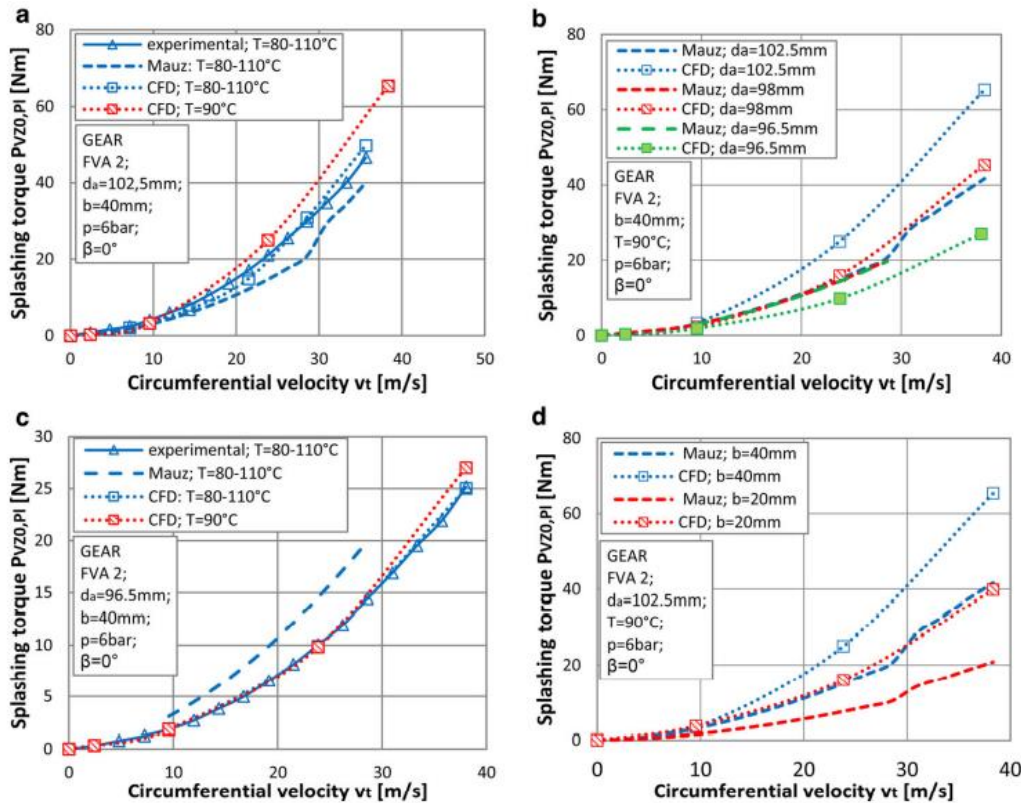


Figure 40 CFD-Mauz comparison (Gorla, 2016)

The authors (Gorla, 2016) recommend finite element modelling with remeshing on a case-by-case scenario to model churning losses as it's the most accurate of all solutions reviewed. Alternatively, (al M. N., 2020) evaluate Velex & Changenet's model; Terekhov's model; Boness' and Lauster & Boos' model against CFD and experimental data, only to find Velex & Changenet's model to perfectly match the experimental data until 100 rad/s and with small deviation thereafter, alas, Velex & Changenet's model will be employed in this paper.

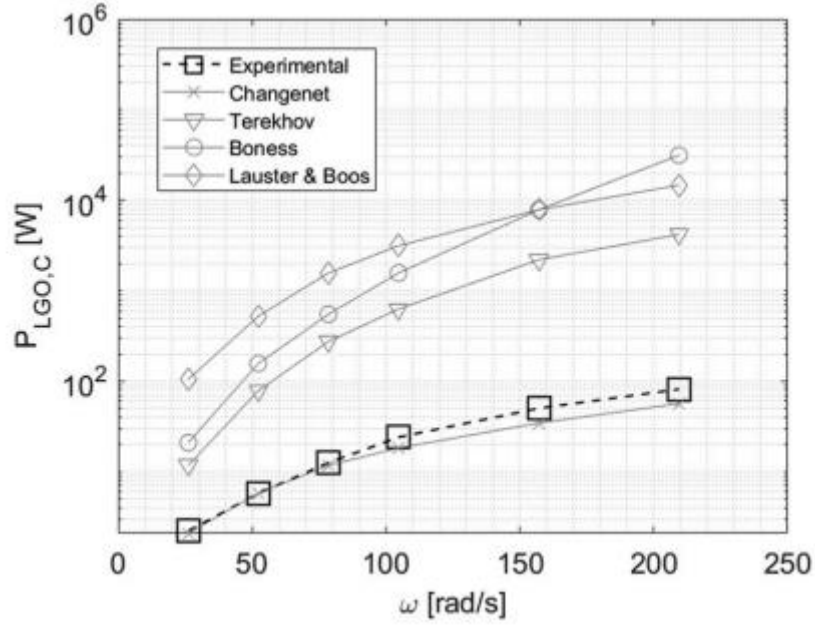


Figure 41 Changenet & Velex model validation (al M. N., 2020)

The model is described as (Gorla, 2016):

$$T_{VZ_o,C} = \psi_1 \left(\frac{m}{d_p}\right)^{\psi_2} \left(\frac{b}{d_p}\right)^{\psi_3} \left(\frac{h}{d_p}\right)^{\psi_4} \left(\frac{V_o}{d_p^3}\right)^{\psi_5} Re^{\psi_6} Fr^{\psi_7}$$

Where ψ_i are coefficients dependent on the speed regime; m is the module; d_p is the pitch diameter; b is the width, h is the immersion depth; V_o is the volume of lubricant; Re is Reynold's number and Fr is Froud's number. $T_{VZ_o,C}$ represents the torque lost due to churning, which can be easily converted into power by virtue of:

$$P_{VZ_o,C} = \omega T_{VZ_o,C}$$

Where ω is the rotational speed in rad/s. The coefficients to fully describe the model can be seen below:

Table 2 Velex and Changenet's coefficients

	ψ_1	ψ_2	ψ_3	ψ_4	ψ_5	ψ_6	ψ_7
Low and medium speeds	1.366	0	0	0.45	0.1	-0.21	-0.6
High speeds	3.644	0	0.85	0.1	-0.35	0	-0.88

The high-to-low speed barrier will be set by the turbulent Reynold's number, just as with the windage losses model below.

To evaluate windage losses the authors (Gorla, 2016) also provide a plethora of models, perhaps, the most comprehensive of which is Diab's model proposed in (al Y. D., 2004) which models windage losses as (al Y. D., 2004):

$$P_{VZ_o,W} = \frac{1}{2} C_t \rho \omega^3 R^5 \quad | \quad C_t = C_f + C_l$$

$$C_l = \xi \frac{z}{4} \left(\frac{b}{R}\right) \left[\frac{1 + 2(1 + x)}{z}\right]^4 (1 - \cos \phi)(1 + \cos \phi)^3 \quad | \quad \phi = \frac{\pi}{z} - 2(inv(\alpha_p) - inv(\alpha_a))$$

$$C_f = \frac{2n_1\pi}{5 - 2m_1} \frac{1}{(R^*)^{m_1}} \left(\frac{R^*}{R}\right)^5 + \frac{2n_2\pi}{5 - 2m_2} \left[\frac{1}{Re^{m_2}} - \frac{1}{(R^*)^{m_2}} \left(\frac{R^*}{R}\right)^5\right]$$

Modelling of gear surface roughness impact on electrified transmissions' efficiency
 4. Model adaptation

Where ρ is the lubricant's density; ω is the rotational speed; R is the pitch radius of the gear; ξ is a reduction factor for obstacles near the gear; b is the gear width; X is the profile shift coefficient, z is the number of teeth, α_p is the pressure angle at the pitch point and α_a is the pressure angle at the tooth tip.

$$\xi = \xi_1 + \xi_2 | \xi_{1,2} = \begin{cases} \left(\frac{h}{R}\right)^{0.56} & \text{in the presence of deflectors, flanges ...} \\ 0.5 & \text{otherwise} \end{cases}$$

The subindexes 1 and 2 represent each side of the gear when bisected. As per (Gorla, 2016), in gear pairs $\xi = 0.5$ always.

The coefficients n_1 , m_1 , n_2 and m_2 are coefficients depending on the fluid flow. The 1 subindexes are valid when there is a laminar regime and the 2 subindexes for turbulent flow ($Re^* \cong 3 * 10^5$). The radius separating laminar and turbulent sections is represented by R^* and can be computed as:

$$R^* = \sqrt{\frac{\mu Re^*}{\rho \omega}}$$

Finally, Re is Reynold's number which can be calculated as (Reynolds, 1886):

$$Re = \frac{\rho u D}{\mu} = \frac{u D}{\nu}$$

Where u is the speed of the surface of the cylinder (applied to the pitch diameter in this case); D is the diameter of the cylinder (pitch diameter in this application); ρ is the fluid density; μ is the dynamic viscosity and ν is the kinematic viscosity.

Yi Diab's validates his model proposal in his PhD thesis (Diab, 2005), directed by Prof. Vexel and Dr. Ville, comparing his "Dimensionless numbers model" against both pre-existing models and experimental data. As such, a series of test as presented as the one shown below:

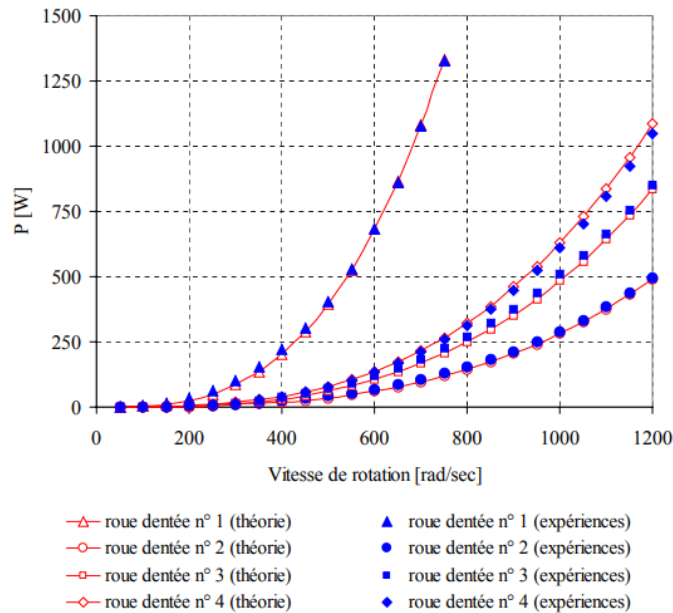


Figure 42 Comparison between tests and modeled windage losses (Diab, 2005)

4. Model adaptation

4.7. Model's lubricant sensitivity analysis & validation

Having already discussed the different model modules concerning efficiency, a sensitivity analysis based on the properties of known lubricants was performed, with the secondary aim of considering or not windage and churning losses, since, although they are known to exist in reality, available software (LDP) does not consider them, and thus, their validity in this scenario cannot be guaranteed.

Alas, the model was tested for a range of lubricant densities (from 100 to 1000 kg/m³) and a range of absolute viscosities (ranging from 0.01 to 0.5 Pa*s) with a standard pressure-viscosity coefficient of 2·10⁻⁸ m²/N and a convergence step of 1µm (rather on the larger scale since it allowed for speed at the expense of accuracy).

To evaluate the model, 2 segments of a real surface measurement were inserted into the program since the focus of this test was the model performance (Santos, 2022).

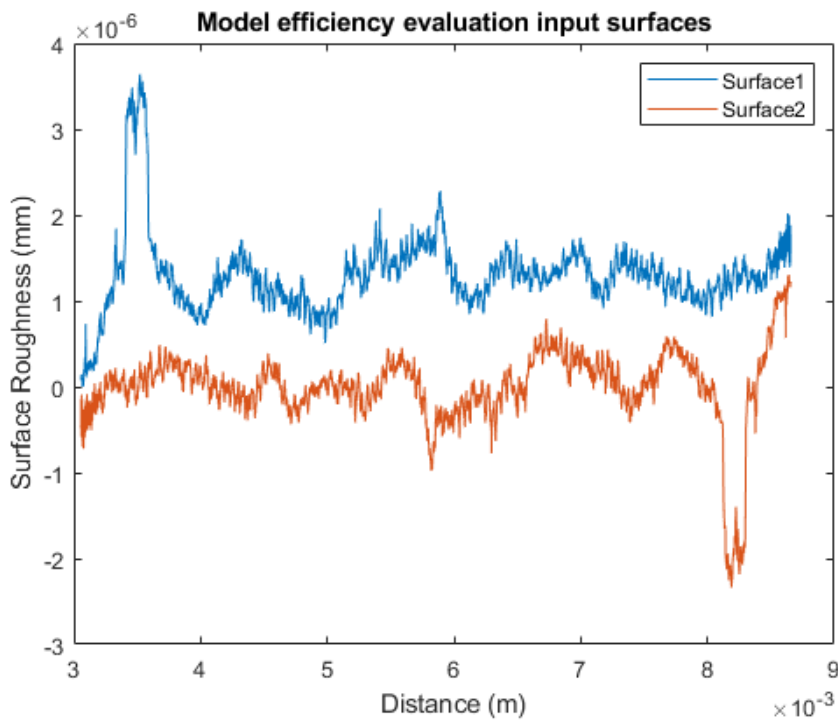


Figure 43 Real surface measurement example

The surface shown above clearly contained a surface defect which can be seen on either the beginning of surface 1 or the end of surface 2. To avoid a pure rotation of the surface, each were cut with 1mm difference from the original measurement.

The model was tested twice, with and without the Navier Stokes contribution to evaluate the effect on the accuracy and computation costs. The efficiency results are shown below:

Modelling of gear surface roughness impact on electrified transmissions' efficiency

4. Model adaptation

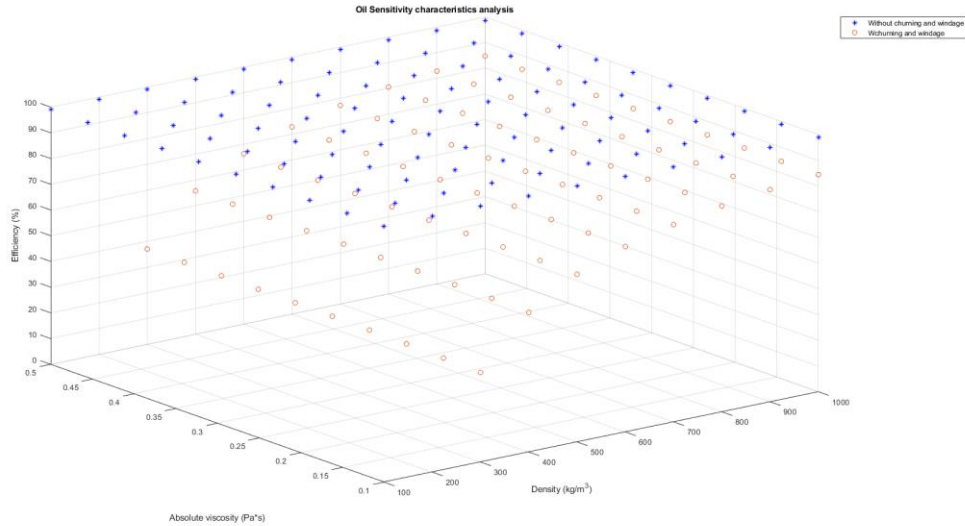


Figure 44 Efficiency sensitivity analysis to lubricant properties

As seen above, the maximum efficiency (99.4635%) coincides both with and without Navier-Stokes since the pressure contribution to the surface deformation energy is low when compared to the other contributions. Windage and churning losses also coincide and are greatly affected by the lubricant properties and drive efficiencies down enormously (when more realistic lubricant properties are considered).

In light of such a behaviour along with the impossibility to fully characterize the lubricants used windage and churning losses will be disregarded in the model since their effects exceeds the aim of any surface contact.

Similarly, the efficiencies are somewhat high ranging from 99.4635% to 98.4188% whereas a typical gear-to-gear transmission has an efficiency of about 98%, this is most likely due to the lubricant's density and absolute viscosity pairing since said maxima are found at the minimum density and minimum absolute viscosity, whilst, for more realistic lubricants (in both terms of viscosity and density) the efficiencies range from 98.9345% and 98.5325%, thus very close to the output shown by the various LDP models of this type of gears.

It's worth noting the real absolute efficiency of the gear pairing is not known since LDP only offers approximations on different types of lubricants and therefore a small variation within the efficiency results are to be expected.

Upon evaluating and reviewing this gear meshing efficiency model, the reference (Alfredsson, 2020) was found. Although said reference does employ a similar approach to this model: Using EHL calculations as a first determination of whether there exists contact or not, solving the Reynold's equation and using the compliance matrix developed in (Sosa, 2017) along with the solution of thermal equations. It does not operate on the same multivariate space as this one, since it looks at a 3D surface with a 12th degree polynomial (unsuited for a 2D surface) with a special emphasis on the azimuthal direction whilst this model focuses on efficiency rather than fatigue and thermal effects (even though both are considered in this model). The solid-to-solid contact deformation and pressure is also defined differently in both models, since in (Alfredsson, 2020) it described as points less than 1nm apart whilst in this model implements a step-by-step lowering of the surface until there is a negative distance and adjusts it to have a zero-separation contact. Furthermore, the reference (Alfredsson, 2020) employs Businessq potential functions to approximate the stress at the contact whilst this model uses a more direct approach.

4. Model adaptation

4.8. Efficiency and losses calculations

Windage and churning losses, although they were reviewed, were not implemented in this model since they are themselves external to a pair of gears meshing.

The sliding and rolling resistance losses were described as:

$$P_{\mu} = F_s V_s$$

$$P_r = F_r V_e$$

Where P_{μ} are the losses due to sliding friction (F_s) and it's dependent on the sliding speed of the contact between gear teeth (V_s), whilst the rolling resistance losses are dependent on the aforementioned rolling resistance (F_r) and the entrainment speed (V_e).

The surface deformation losses followed the formula:

$$P_{si} = \frac{\iint \sigma \delta \cdot ds}{T} \rightarrow \frac{\sigma \delta a^2}{T}$$

Where P_{si} are the losses due to surface deformation of each surface, σ is the Von Mises surface stress, which can be elastic or plastic, δ is the deformation depth at every point, T is the period of rotation of the gears. The theoretical formulation with a surface integral was substituted in the code with a multiplication of stress and deformation at every point in the line measurements, with a squared differential with side a to concord with the rough deformation contact model.

Finally, the efficiency is thus calculated as:

$$\eta = \frac{M_1 \omega_1 - P_{\mu} - P_r - P_{s1} - P_{s2}}{M_1 \omega_1}$$

4.9. Sintered gears implementation

To incorporate sintered gears in the model, after it's been verified for normally manufactured wrought steel gears (cutting, heat treatment, honing and/or grinding) the following changes were made to the model:

Redefined Young's modulus following the equation (Flodin, 2016):

$$E = E_o \left(\frac{\rho}{\rho_o} \right)^{3,4}$$

Where E_o is the material's known Young's modulus, ρ is the powder metal part density and ρ_o is the material's known density and E

A similar formulation for the Poisson coefficient is accepted, developed in (Li, 2016):

$$v = \left(\frac{\rho}{\rho_o} \right)^{0.16} (1 - v_o) - 1$$

Where v is the part's Poisson coefficient and v_o the material's original Poisson coefficient.

Alas, any model originally configured for wrought steel gears can easily be converted to powder metal gears, given that there are no significant sub-surface defects of voids which may compromise the surface's behaviour, allowing to compare the behaviour and characteristics of both.

4.10. Model outputs

A table containing the inputs for the example and the obtained results is presented below:

Modelling of gear surface roughness impact on electrified transmissions' efficiency
 4. Model adaptation

Table 3 Variables portrayed example

Variable	Value	Units	Variable	Value	Units
Module	1.3	mm	Elastic limit 2	235	MPa
Pressure angle	20	deg	Bulk temperature 1	60	K
Helix angle	30	deg	Bulk temperature 2	60	K
Number teeth 1	50	-	Lubricant conductivity	0.135	W/m/K
Number teeth 2	120	-	Lubricant heat capacity	2	J/g/K
Width 1	50	mm	Thermal conductivity 1	45	W/m/K
Width 2	50	mm	Thermal conductivity 2	45	W/m/K
Input moment	285	Nm	Lubricant density	998	Kg/m ³
Input rotational speed	3000	rpm	Lubricant load loss dependent coefficient	0.84	-
Metal-to-metal friction coefficient	0.3	-	Reference load loss dependent coefficient	0.9069	-
Young's modulus 1	210	GPa	Lubricant absolute pressure	0.0975	Pa·s
Young's modulus 2	210	GPa	Lubricant's pressure viscosity coefficient	2e-08	mm ² /N
Poisson Coefficient 1	0.3	-	Numerical error	1	%
Poisson Coefficient 2	0.3	-	Delta step	80	nm
Elastic limit 1	235	MPa			

Sample surface, if the inputs are surface parameters, the model will output a sample surface generated from those parameters using the GPR module included. If the input are already surfaces, then those same surfaces will be shown.

The surface variation in 2 separate stages will also be calculated and shown, the surface under contact (allowing to for calculation of real surface deformation) and the surface after contact, where the result of the plastic deformation of the surface will be outputted.

Modelling of gear surface roughness impact on electrified transmissions' efficiency
 4. Model adaptation

Surface variation over contact

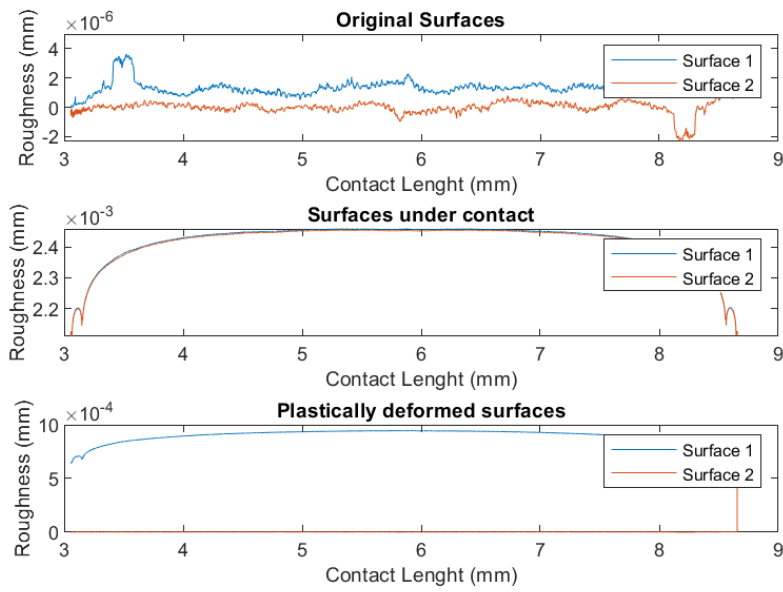


Figure 45 Sample surface module output

The contact stress will also be computed and shown on screen and the shear sub surface stress at various depths.

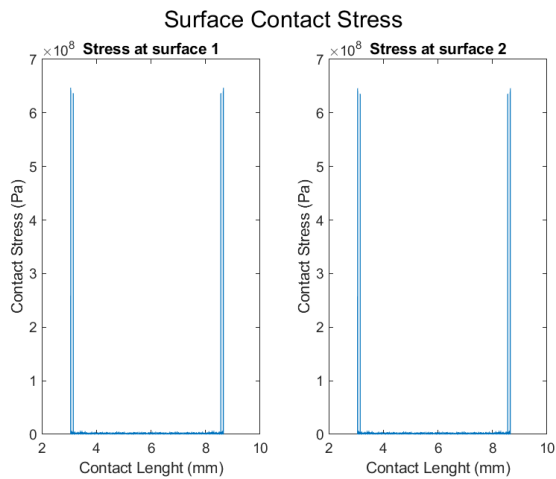


Figure 46 Sample contact stress output

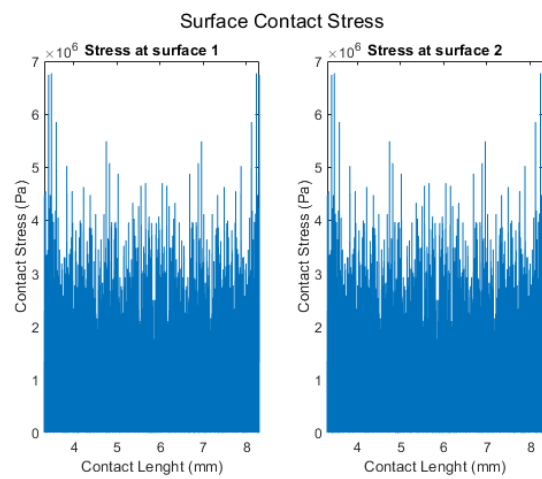


Figure 47 Sample detail output of contact stress

Modelling of gear surface roughness impact on electrified transmissions' efficiency
 4. Model adaptation

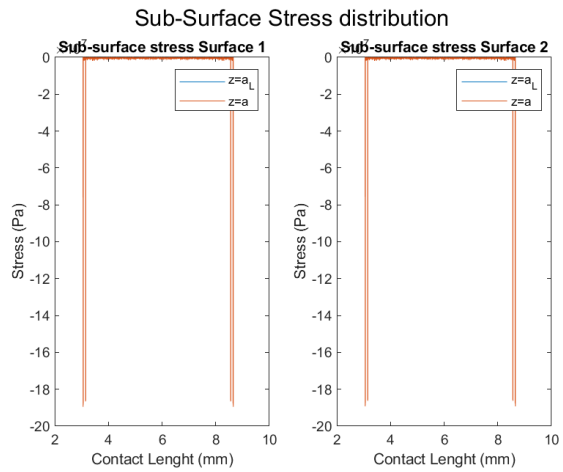


Figure 48 Sample sub-surface stress output

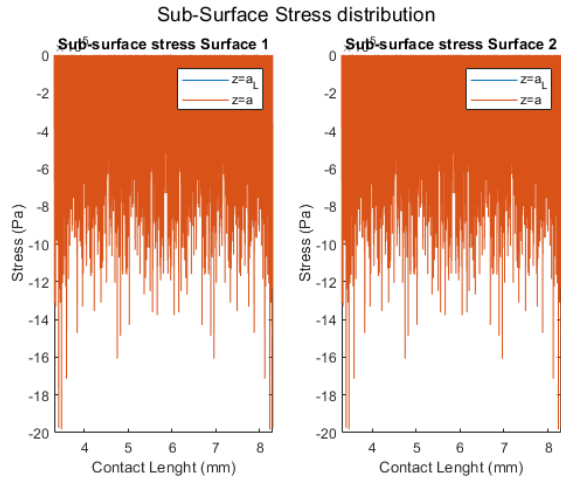


Figure 49 Sample detail output of sub-surface stress

The temperature variations are also shown as figures:

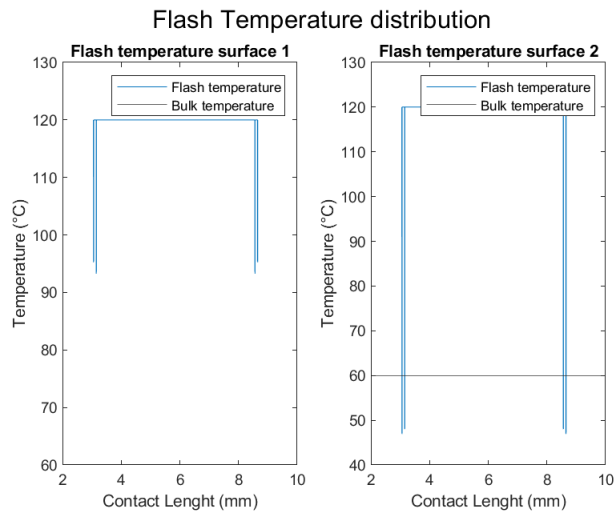


Figure 50 Sample flash temperature output

The losses due to various reasons will also be shown as figures, in 2 separate events, during and after the contact, allowing the user to understand how energy is lost at various instants:

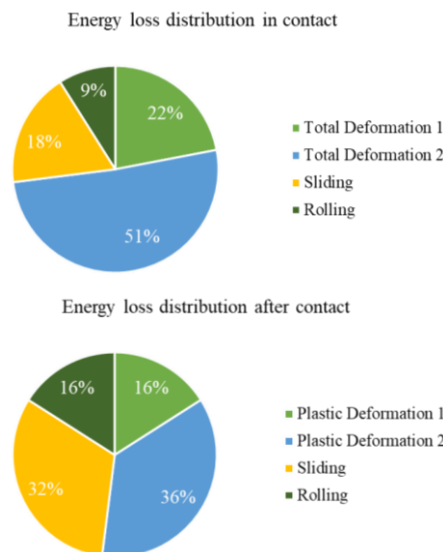


Figure 51 Sample energy loss distribution output

Modelling of gear surface roughness impact on electrified transmissions' efficiency
4. Model adaptation

A final graph will be generated with the convergence history of the model to verify its behaviour and allow for optimization algorithms:

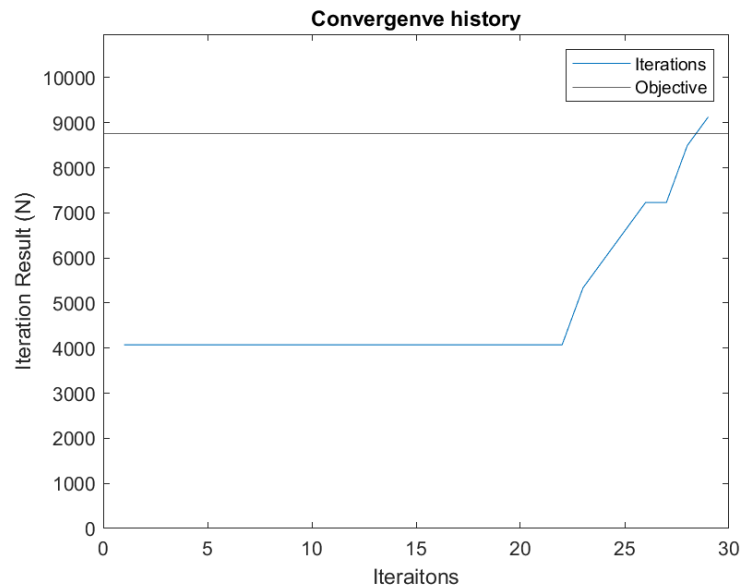


Figure 52 Sample convergence history output

The entire workspace will then be saved in a folder named as the date and time of when the model was launched for easy identification. Furthermore, the entire workspace will be saved in that folder.

Throughout the execution of the model, a series of messages will be shown in the command prompt detailing where the model is at every moment, and it will finish with a summary of all relevant data as well as the computing time it required to solve. An image of said final summary can be seen below:

```
Gear parameters loaded successfully
Lubricant parameters loaded successfully
Load parameters loaded successfully
Material parameters loaded successfully
Convergence parameters loaded successfully
New output folder created:2022_05_03_11_52_49
Hertzian module completed successfully
Surface calculations completed successfully
Friction coefficient calculated successfully
Adimensional numbers calculated successfully
EHL calculations completed successfully. Lamda_star=0.00010942
Fluid film thickness=5.4043e-10m
Churning losses calculated successfully
Windage losses calculated successfully
Rolling force calculated successfully
Slidding calculated successfully
Building compliance matrix
Compliance matrix built successfully
C is symmetric and invertible
Contact between the surfaces, numerical solver
```

Figure 53 Command prompt messages 1

Modelling of gear surface roughness impact on electrified transmissions' efficiency
4. Model adaptation

The current iteration is also displayed but it has been removed for the sake of brevity.

```
The error was of: 4.053%
Surface equivalent stress calculated successfully
Plastic deformation of surfaces calculated successfully
Working deformation of surfaces calculated successfully
Sub-surface stress calculated successfully
Total contact energy successfully calculated
Plastic deformation energy successfully calculated
```

Figure 54 Command prompt messages 2

```
Elapsed time is 74.960032 seconds.
The plastic deformation power losses are : 531.1W
The sliding power losses are : 318.6382W
The rolling power losses are : 159.1579W
The churning power losses are : 16.0279W
The windage power losses are : 12960.5148W
The output torque is : 117.4119Nm
The efficiency considering Windage and Churning is: 84.38%
The efficiency considering Windage and Churning is: 98.8732%
```

Figure 55 Final model output summary

As shown by the model, there is a stress concentration in the vicinity of either surface defect which agrees with known effects of surface damage as stress concentrations, which is in turn reflected in the contacting and plastically deformed surfaces. As expected from the literature review, the sub-surface stress mimics the contact stress, and both are shown to be asymmetric and dependant on the contact and fluid pressure effects.

The temperatures show a rise of up to 60 K due to flash temperature, which, upon further review and comparison with other known models seems a bit too low (normally reaching up to 140K) whilst the effect of the surface damage (acting as a lubrication pocket) is evident and prevents the temperature from raising as much as with a direct surface contact, although, the model estimates one of the surface will decrease in temperature, which could largely be due to the lack of dynamic and transient effects of this formulation.

The losses upon the contact constitute unusable energy, since they include the elastic deformation, whilst the loss after contact are the real losses, since the elastic deformation, although unavailable, are recovered when the surface relaxes. Most of the permanent losses are divided amongst surface deformation and the sliding.

The model at first has a constant force in the convergence history since it's the overall effect of the oil film pressure, as the surfaces are not yet in contact, whilst, later on it starts to increase as each surface runs into each other.

4.11. Model Summary

Having validated all the building blocks of the model, the layout would be as follows:

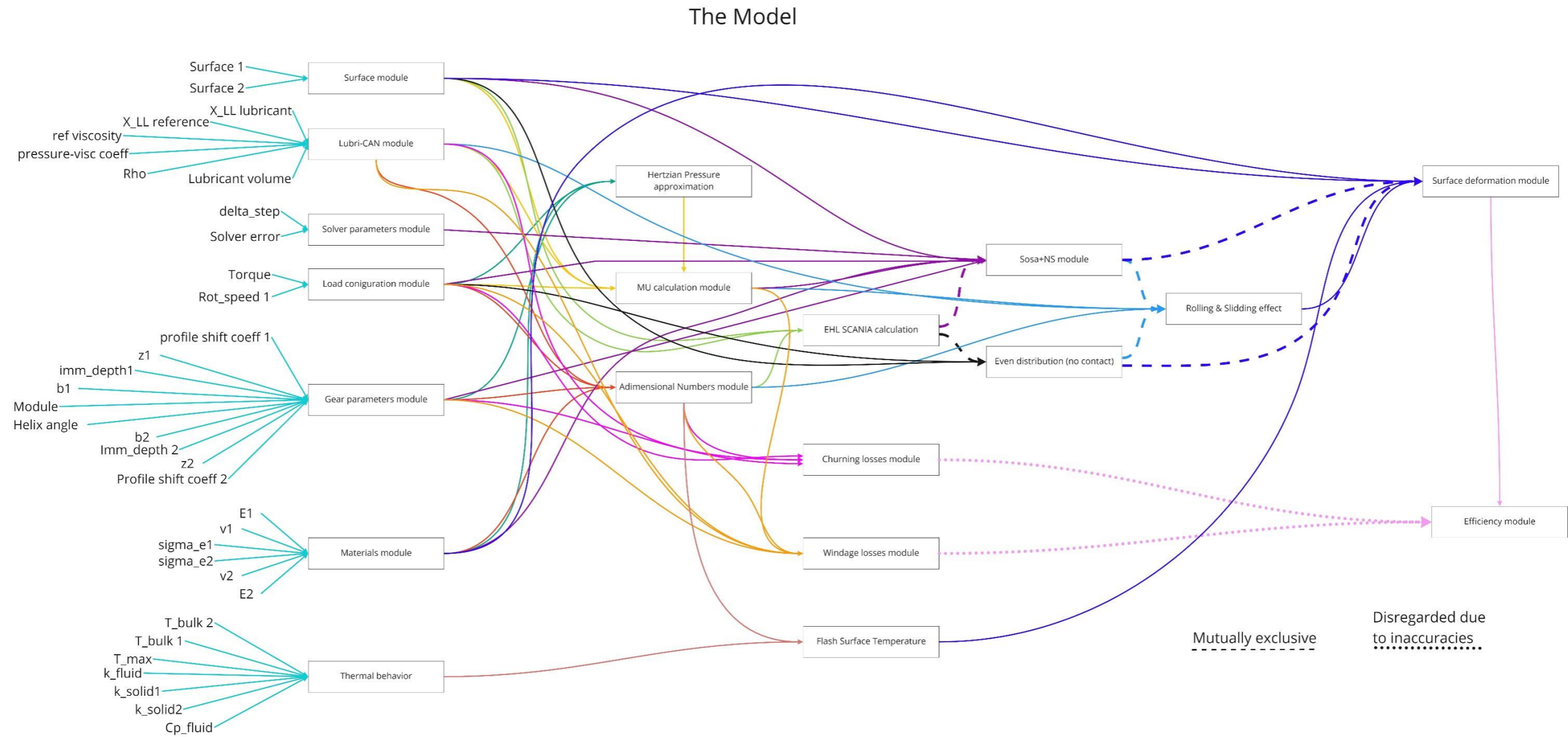


Figure 56 Model block diagram

5. Surface measurement & characterization

The problem now arises when inputting surfaces into the model, since no surface measurement spans the entirety of a gear flank for a number of reasons ranging from the interference between the helix angle and the profilometer (in 2D measurements) or the fillet radius being too tight for the probe to the impossibility of achieving a good enough alignment of the curved flank surface with the observation lens in 3D measurements. As with the reference (Rathi, 2013), both methods will be considered, analysed and characterized.

5.1. 2D measurements

The first set of measurements were collected in a MarSurf GD 120 with a 1 μm probe and a 60° cone angle. From it, all surface parameters were extracted, and the raw measurement data was exported.

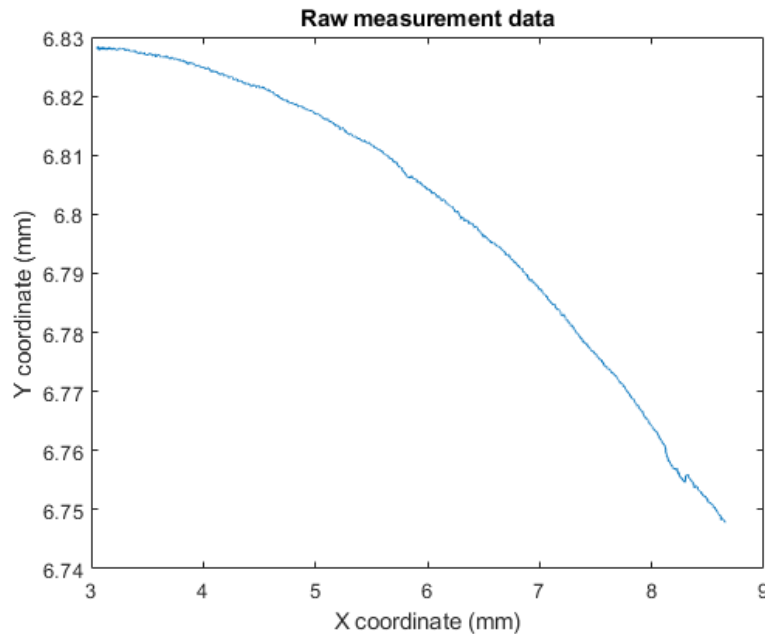


Figure 57 Raw surface measurement data

In the figure above the helix angle of the gear flank is remarkably evident, even the surface damage which can be seen towards the end of the measurement.

To extract the surface roughness from the raw measurement a code was set up in MATLAB R2021b to automatically select the most efficient linear regression model up to order 10 whilst minimizing the error. Thus, the model 2 orders of magnitude higher than the bend in the RMSE plot was selected provided it had minimum variation with the previous iteration.

Modelling of gear surface roughness impact on electrified transmissions' efficiency
 5. Surface measurement & characterization

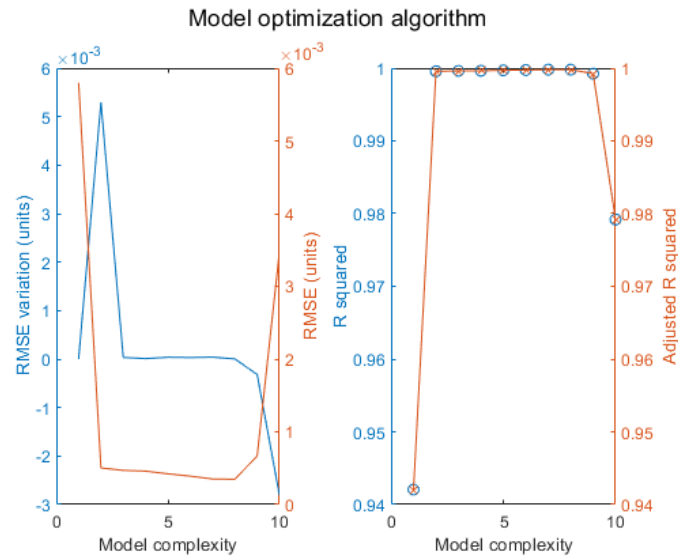


Figure 58 Automatic model accuracy selection

As seen above, this measurement benefited the most from a linear regression with an order of magnitude of 4, having a small enough RMSE with a stable variation with its neighbouring iterations and having a maximal R-squared. However, compared to (Alfredsson, 2020), where a 12th order polynomial was employed, in light of the Adjusted R-Square and RMSE drop, it was not well suited for this type of data, since in the afore mentioned reference (Alfredsson, 2020), the input data was a 3D surface, whilst here it's a 2D vector.

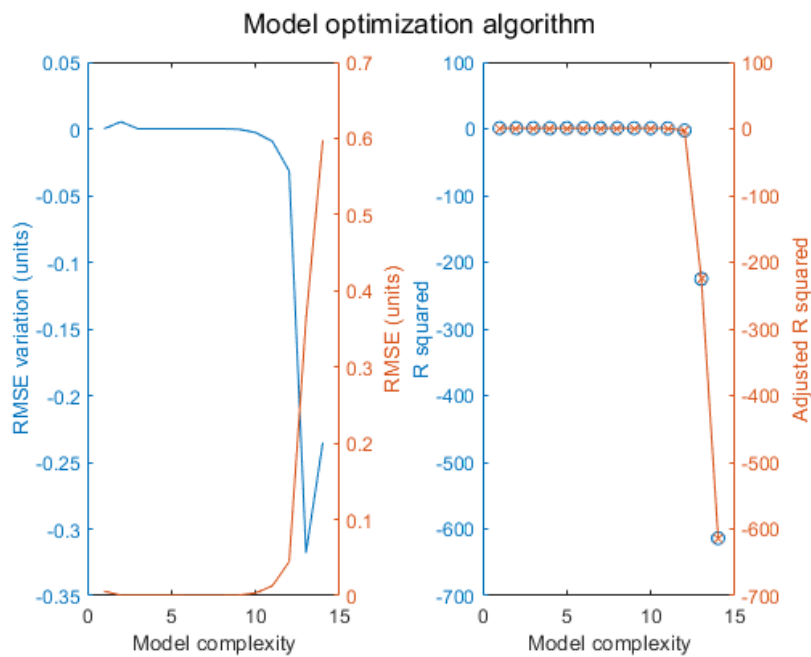


Figure 59 Nominal form polynomial extracting comparison

The fact the code still selects a 4th degree polynomial verifies the selector logic employed for future use when extracting the nominal surface out of the roughness measurements, as seen in the above figure, the R-squared and RMSE point to the inadequacy of the 14th degree polynomials.

The resulting model for this example had an R-squared and Adjusted R-square of 1; a p-value of 0 and the maximum p-value of the coefficients was in the range of 10^{-17} . Alas, overall, it can be

Modelling of gear surface roughness impact on electrified transmissions' efficiency
 5. Surface measurement & characterization

considered a remarkably accurate model. The resulting surface roughness was extracted and can be seen below:

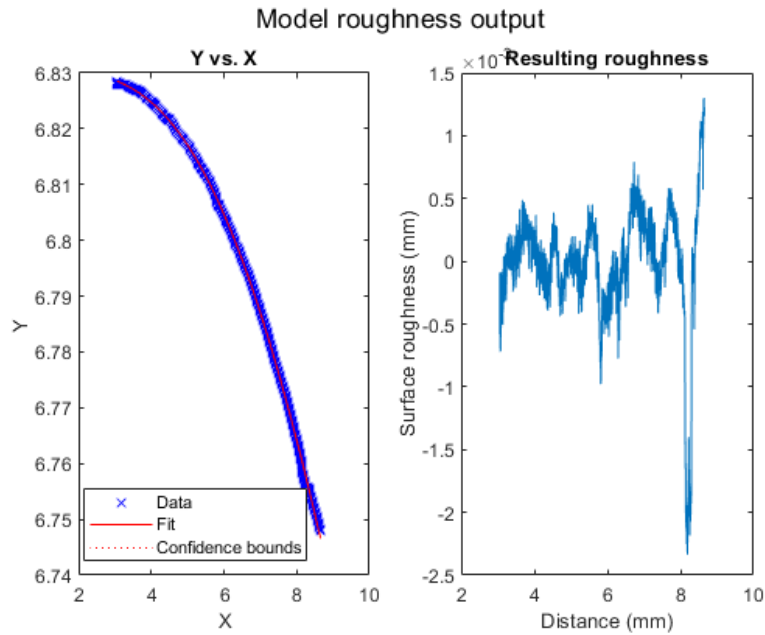


Figure 60 Surface measurement regression and extracted roughness

From the above picture, the afore mentioned surface damage is evident (-2 μm dip). The surface can also be characterized as a probability distribution and its corresponding probability density:

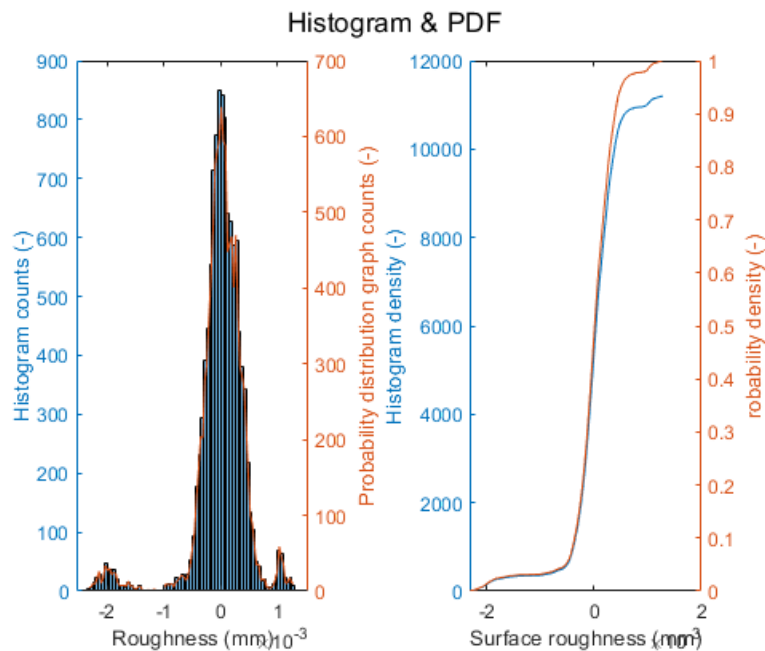


Figure 61 Surface measurement distribution and cumulative distribution

Due to the nature of surface measurements, they can be approximated as noise around the surface, thus, traditional probability distribution fittings are not well suited to characterize them. Additionally, every surface may have a different distribution, thus, when scaling the surface analysis tool, having to iterate between a list of possible distribution types which may or may not be representative of the surface seems too costly and unreliable since some may even not be accurately represented by any of the pre-defined distributions.

Modelling of gear surface roughness impact on electrified transmissions' efficiency
5. Surface measurement & characterization

Therefore, other techniques need to be considered. Clearly classification techniques are not suitable since the algorithm will need to work either in a label-to-sequence or in a sequence-to-sequence manner alas, regression type algorithms seem far more suitable.

At the lab 2 technologies were readily available to acquire surface roughness measurements:

- Contact profilometry (equipment: MarSurf GD 120).
- White light interferometry (equipment: KEYENCE VR-500).



Figure 62 Surface roughness calibration sample



Figure 63 Line roughness calibration sample 1



Figure 64 Line roughness calibration sample 2

An additional challenge is the randomness of the data, since any engineering surface can be considered to be made up of three distinct types of waves (J. Raja, 2002):

- Roughness: High frequency components of the surface.
- Waviness: Medium frequency components of the surface.
- Form: Low frequency components of the surface.

Historically, in surface metrology the line between surface roughness and waviness was derived from the sample cut-off length, normally set at 0.25 mm or 0.8mm. A shorter cut-off length allows for more measurements in the same sampling length (benefitting repeatability) whilst longer cut-off lengths give a better understanding of the surfaces since they are able to capture longer wavelength defects as explained in detail in (Spectrum Metrology, 2017).

Traditional surface parameters are calculated from sampling the roughness and treating it as a random distribution, therefore, traditional parameters refer to averages (R_a) and standard deviations (R_q) within the cut-off length, alas, roughness has never been fully characterized since there also lies the precision & filtering dilemma. In contact profilometry the tip diameter of the probe acts as a first filter where roughness with a wavelength smaller than the tip diameter will not be detected (al J. S., 2014) whilst non-contact profilometry can easily loose precision if the surface isn't perfectly aligned (Michaud, 2015).

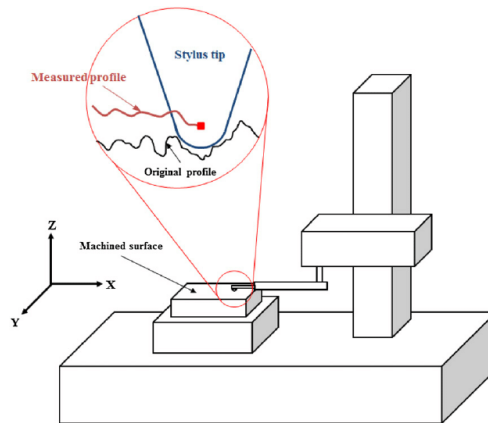


Figure 65 Smoothing effect in contact profilometry (Cho, 2012)

Contact profilometry is the traditional surface roughness measurement method, where a series of styli are skated across the surface, tracking in a single measurement the form, waviness and roughness. Afterwards, the signal is filtered, firstly with some kind of fitting (as of today it's not standardized) to remove the nominal shape. The resulting signal will be a compound of roughness and waviness.

There is no set standard when removing the nominal form from the measurement since it's remarkably dependant on the shape of the element and the path taken by the instruments, alas, there are several different techniques to filter out the longer-wavelength elements of the acquired signal, primarily multi-variable regression as already discussed (if only the raw data is available) or in more recent times, the measurement equipment is capable of tracking and controlling the position and velocity errors of the measuring equipment with the dawn of advanced controls, although, in theory it could be done with a simple PID controller although the measurement would be less reliable (Delta Computer Systems, 2022).

5.2. 3D measurements

On the other hand, with the dawn of the new millennia contactless interferometry was refined. In this new measurement technique, no probe is needed. White light interferometry relies on collimating light beams (accurately parallel) employing one as a reference whilst the other is employed as a measurement tool, thus being called object beam (AZO Optics, 2017).

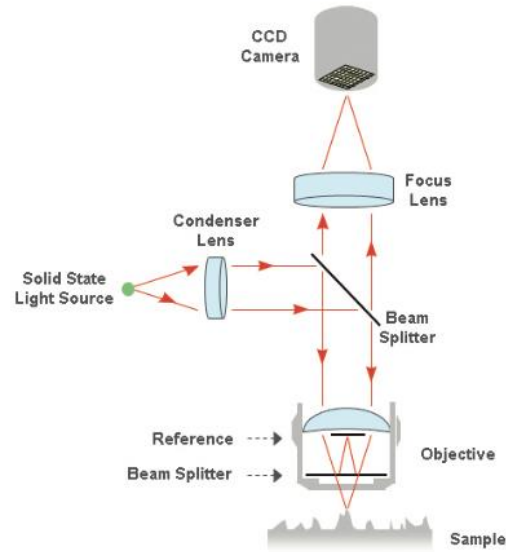


Figure 66 White light interferometry assembly (nanoScience Instruments, 2022)

The object beam is reflected off the object whilst the reference beam is reflected from a reference mirror. Both beams are thus captured and combined at the CCD camera, resulting in wave interference, which in turn, can be constructive, the maxima of both waves are added together, or destructive, the maxima if both waves subtract from one-another, resulting in an attenuated amplitude (Swinburne University of Technology, 2022).

This interference is a direct result of the reflection phase shift that any light beam experiences when moving from a medium with faster wave speed (such as air) to a medium with slower wave speed (any solid). This phase shift is directly correlated with the wavelength of the light beam with the equation (Nave, 2022):

$$u^{inc}(x, t) = Ae^{i(k_1x - \omega t)}$$

Where k_1 is directly correlated with the spatial component of the reflectance (the reflecting surface height variation) and ω is the angular frequency (therefore correlated with the wavelength).

Alas, by subtracting both light beams, the machine need only process the phase shift due to the reflectance, which in turn is closely related to the height variation as already discussed (nanoScience Instruments, 2022).

White light interferometry simply employs all the wavelengths (therefore all the colours and as such white light) and stitches the results together to obtain a more detailed profile of the surface (AZO Optics, 2017).

There currently is a debate in metrology as to which technique is better, since non-contact interferometry can lead to errors depending on the lighting and surface finish of the workpiece whilst it also requires re-calibrations more often, since the measuring is purely via electronic components. Contact interferometry on the other hand may slightly damage the piece due to the high contact stress which is concentrated at the stylus tip (Schuetz, 2021). There is another debate as to losing the contact between the object and measuring equipment is beneficial or not even though there exists a subtle attenuation of the surface roughness when employing a probe (Santos, 2022).

Since different data acquisition techniques will undoubtedly yield slightly different roughness results, a test ought to be conducted to understand the extent of this variation. Due to the equipment limitations the same reference surface could not be measured in both the 2D

measurement machine (MarSurf GD 120) and the optical surface roughness tool (KEYENCE VR-500) alas, a 2D roughness measurement was extracted from the raw data of an optical measurement without any kind of filtering:

- S-filter: None.
- L-filter: None.
- F operator: Automatic.

The S-filter removes unwanted small-scale lateral components on aerial 3D acquisition methods. The L-filter removes unwanted large-scale components of the surface. Finally, the F operator removes the nominal form of the surface; it's described as an operator since it is first optimized to fit the nominal form and then removes said form from the data (Santos, 2022).

A code mimicking the effect of several types of probes was written in MATLAB to understand how it may affect the surface parameters.

The model imports a line measurement from the Keyence VR-500 and mimics different styli effects and the effect they have on the output surface and its corresponding parameters by first building a set of stylus tips and then skating them through the surface.

The model receives a surface roughness vector from the Keyence VR-500 and a myriad of parameters to define the different stylus properties, namely:

- Tip diameter (in micrometres).
- Cone angle (in degrees).
- Base diameter (in micrometres).

The styli are initially divided into 4 segments: left-side tangent; left-side circular segment; right-side circular segment and right-side tangent. The tangents have a slope determined by the cone angle of the stylus and expand from the contact point with the stylus tip and the base diameter of the stylus.

Said 4 vectors are then merged for ease of operation.

For every point in the surface, a range defined by the base diameter of the probe is defined and all surface points whose x-coordinate belong to said interval are considered. The stylus is then placed directly at height 0, aligned vertically with the defined point and the height difference between the probe and the surface is computed at every point in the interval. The extracted surface roughness measurement as every point will therefore be the minus minimum height difference (assuming there is interference between the probe and the stylus). If there the probe needs to be lowered further the resulting roughness measurement will again be the minus minimum height difference.

Finally, the software records the location of the contact point on the probe, to evaluate if it's occurring in the tip region or elsewhere.

5.3. Acquisition system comparison and equivalence

The imported measurement from KEYNECE VR-500 had a cut-off length of 0.8mm and the probes in the MATLAB model were set to a 60° and tip diameters of 1 and 2 microns respectively.

Modelling of gear surface roughness impact on electrified transmissions' efficiency
 5. Surface measurement & characterization

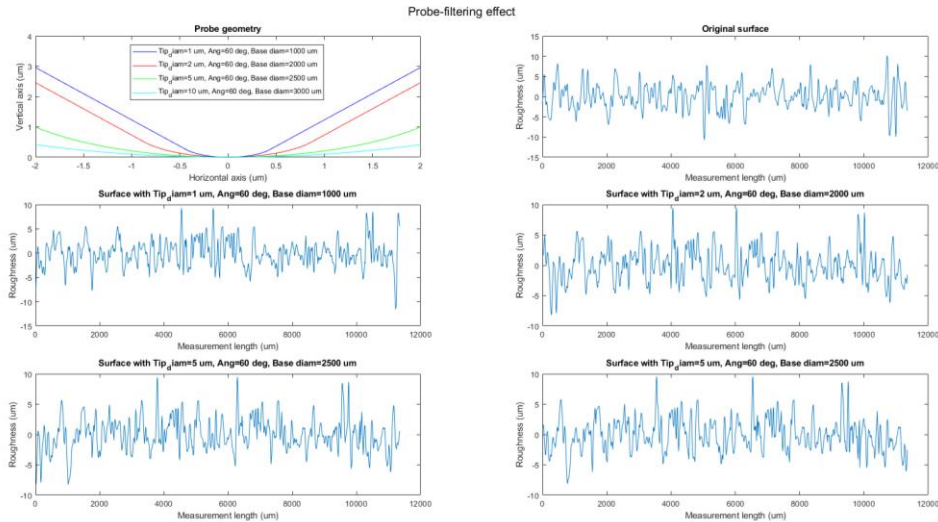


Figure 67 Probe mimicking surface roughness

As a result, the output surface parameters were:

Table 4 Surface roughness probe filtering output

Surface	Cut-off length (mm)	Tip diam (um)	Tip ang (deg)	Base diam (um)	Ra (um)	Rq (um)
3D surface	0.8	-	-	-	7.55E-02	3.06
Probe1	0.8	1	60	1000	-1.23E-13	2.73
Probe2	0.8	2	60	2000	-3.17E-13	2.70
Probe3	0.8	5	60	2500	2.58E-13	2.67
Probe4	0.8	10	60	3000	-7.65E-13	2.67
Probe5	0.25	2	60	2000	-3.17E-13	2.70
Surface	Rz (um)	Rzi (um)	Rsk (-)	Rku (-)	Rvi (um)	Rpi (um)
3D surface	12.22	20.87	-1.47	-1.82	10.72	10.15
Probe1	11.17	20.87	8.31	13.04	11.55	9.32
Probe2	10.80	17.68	-0.50	-3.27	8.22	9.46
Probe3	11.06	17.70	-0.20	-3.85	8.24	9.46

As seen in table directly above, several parameters such as Ra are far more sensible to the probe dimensions. Other sensible ones include Rsk and Rku. The rest seem to be more stable and unaffected by the variation of the probe size, alas, optically acquired surface roughness data seems reliable when compared to traditional 2D measurements. Although it might seem a bold statement, Ra, which is the one with the largest relative variation is large disregarded as a reasonable parameter to consider when studying roughness across a surface.

It was also observed that the sensible parameters were greatly dependant on the base diameter of the probe, suggesting there exists contact outside the tip of the stylus due to the roughness.

Furthermore, it's evident that beyond 2 microns of tip diameter the surface roughness remains mainly unchanged suggesting the prime sensitivity is below 2 microns, for all above listed standard probes.

To train the surface generation model a total of 80 measurements were taken from 4 planet gears and 4 sun gears from a planetary electrified transmission after testing (having each being manufactured with different technologies). In the tested gears the data was collected from 2 measurements in the lead direction and 2 measurements in the profile direction on both the drive and coast side of each gear tooth (thus a total of 8 measurements from each gear denture), except

Modelling of gear surface roughness impact on electrified transmissions' efficiency
 5. Surface measurement & characterization

in 2 gears where only the measurements of the smaller dentures was recorded due to a machine malfunction. A breakdown of the gear properties is shown below:

Table 5 Measured Gears' characteristics

Gear train	Type	Finishing	Material
1	Sun	Honing	Wrought steel
1	Planet Stage 1	Continuous grinding	Wrought steel
1	Planet Stage 2	Honing	Wrought steel
2	Sun	Continuous grinding	Wrought steel
2	Planet Stage 1	Honing	Wrought steel
2	Planet Stage 2	Honing	Wrought steel
3	Sun	Continuous grinding	Wrought steel
3	Planet Stage 1	Honing	Wrought steel
3	Planet Stage 2	Honing	Wrought steel
4	Sun	Grinding	Powder metal
4	Planet Stage 1	Honing	Powder metal
4	Planet Stage 2	Honing	Powder metal

The ring gear was not studied due to the difficulty in transportation (size and weight).

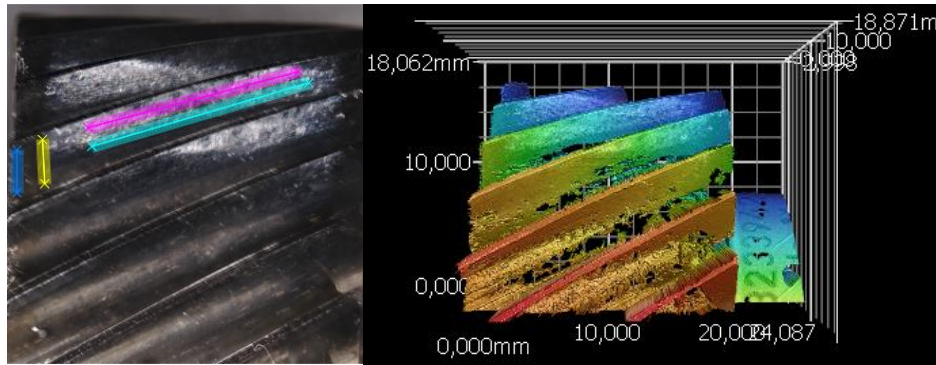


Figure 68 Optical measurement acquisition: Lead and profile measurements (right) and surface capture (left of a sun gear)

As the planet gears have 2 sets of teeth (with different module) the process resulted in a total of 16 measurements per planet gear and 8 per sun gear (for the 4 tested gears).

This procedure was then repeated with the untested gears with 3 teeth being measured, bringing the total to 24 measurements of untested gears. As such the entire data sample consists of 96 measurements.



Figure 69 Meshed sun gear & planet gear

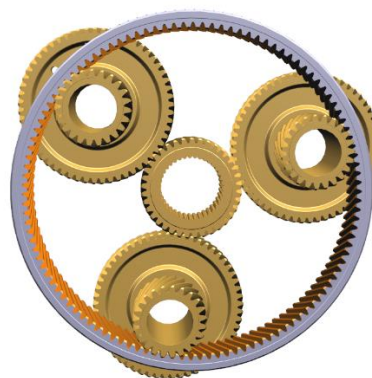


Figure 70 Planetary assembly CAD

The selected input parameters were based on a shortlist defined jointly with (Santos, 2022):

Table 6 Input variables for the surface model

Variable	X	Z	Gear	Type	Size	Flank	Direction	Rz	Rp
Type	Cont.	Cont.	Cat.	Cat.	Cat.	Cat.	Cat.	Dis.	Dis.
Units	μm	μm	-	-	-	-	-	μm	μm
Variable	Rt	Rq	Rsk	Rv	Rku	Rpk	Rvk	Rmax	Sm
Type	Dis.	Dis.	Dis.	Dis.	Dis.	Dis.	Dis.	Dis.	Dis.
Units	μm	μm	-	μm	-	μm	μm	μm	μm

“Cont.” refers to continuous variables; “Cat.” implies categorical variables and “Dis.” means discrete variables. “X” is the x-coordinate of the measurement; “Z” is the surface roughness of the measurement (it’s the variable to be modelled by the model); “Gear” is a categorical variable that accounts for the gear being a sun or a planet gear. “Flank” refers to the drive of coast flank; “Direction” refers to the measurement acquisition direction, either lead or profile direction, the rest refer to commonly used surface parameters with the following descriptions (Santos, 2022):

- Rz: Average maximum height of the profile, is the average of all the Rti values over the evaluation length
- Rp: Maximum profile peak height, is the height of the largest peak of the profile from the mean line.
- Rv: Maximum profile valley depth, is the depth of the largest valley from the mean line.
- Rt: Maximum height of the profile, is the vertical distance between the highest peak and the lowest valley.
- Rq: RMS roughness, is the root mean square average of the roughness profile.
- Rsk: Skewness, represents the asymmetry of the profile roughness distribution.
- Rku: Kurtosis is the “peakedness” of the profile from the mean line.
- Rpk: Reduced peak height, is the distance between the highest peak and the core roughness.
- Rvk: Reduced valley depth, is the distance between the lowest valley and the core roughness.
- Rmax: Maximum roughness depth, refers to the largest of the successive values of Rti through the evaluation length.
- Sm: Mean spacing of profile irregularities, is the mean spacing on irregularities within the evaluation length considered.

As there are 2 modules present in the planet gears, the module must be considered as a categorical variable since it only presents 2 values, thus it can be substituted for a 0, 1 value instead of the actual module, thus preserving proprietary information, said approach could also be implemented for the helix angles although in this model it was overlocked. The face width is not considered since no measurement can span the entirety of the face width; therefore, any generated surface must be obtained from the stitching of several generated lines, alas, it would falsify the results.

Some parameters which could be considered, however, are the profile shift coefficient (generating an undercut starting from the root) and tip relief (resulting in a tip relief). Neither are considered in order for the model to focus on surface finishing requirements and extract from said model the most relevant surface parameters to better define production requirements since neither reflect on the gears’ active profile and therefore, they would never transfer torque.

Modelling of gear surface roughness impact on electrified transmissions' efficiency
5. Surface measurement & characterization

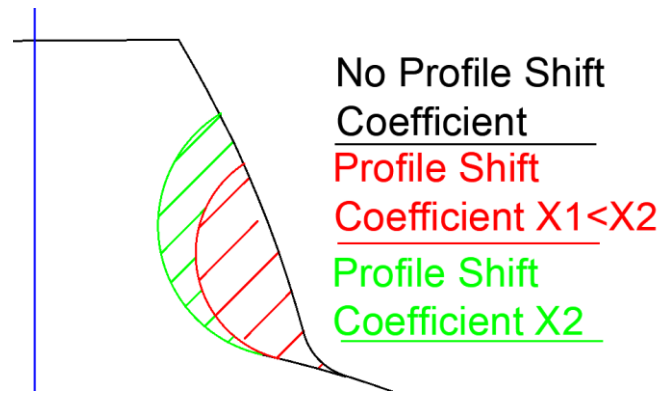


Figure 71 Profile shift coefficient visualization

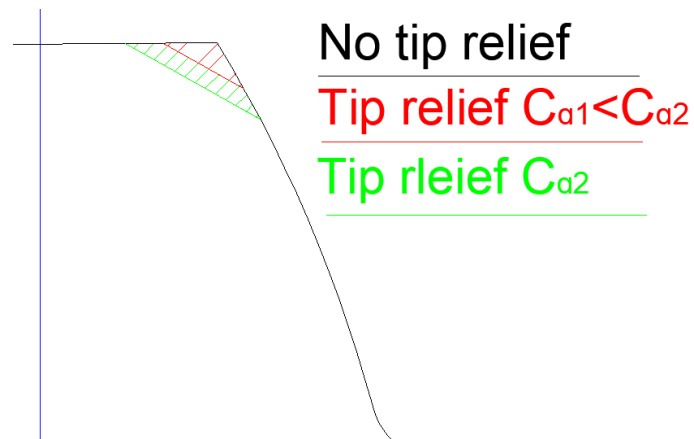


Figure 72 Profile crowning visualization

In both of the above figures, the effect of the profile shift coefficient and tip relief have been exaggerated and are not to scale, its merely to represent the reduction of the active profile both entail.

6. Surface modelling and generation

When it comes to surface modelling there are 2 reasonable approaches, either, generating a surface at every interest point or generating a surface at first and tracking its deformation as time progresses. The latter, although more instructive is not necessarily correct since it always needs a reference point. It would seem reasonable to assume only the peaks of the roughness measurements would plastically deform and the valleys would remain unchanged as the change of both peaks and valleys could imply a waviness or form shift, therefore, a full surface change. However, as stated in (Tiwari, Wang, & Persson, 2019), upon plastic deformation of the surface peaks, the fluent material comes to rest on the valleys, therefore, using valleys as surface reference would lead to an absolute error in surface measurement. Alas, it's safer to generate surfaces at different points of the transmission's lifecycle.

Furthermore, during the lifecycle of the gear, the flank may change due to unwanted grinding in the gear pair meshing, which can be prominent enough to warrant a waviness or form change in the gear as seen below:

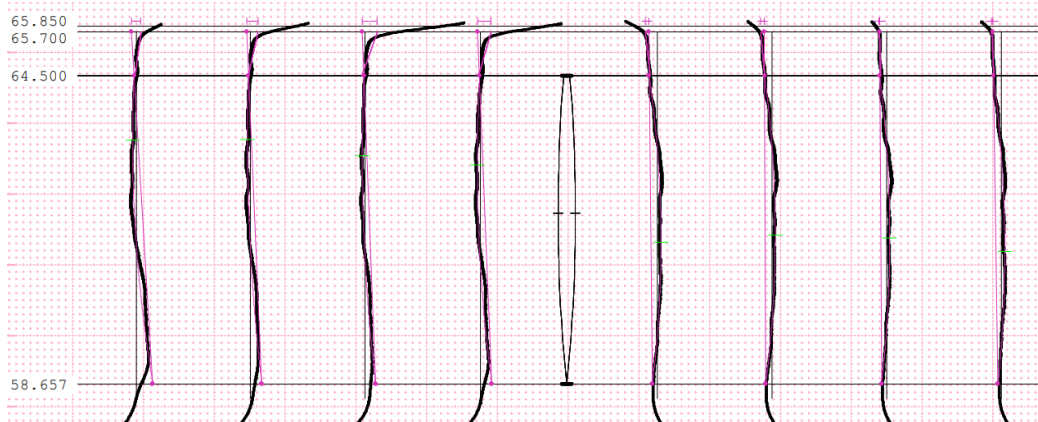


Figure 73 Gear profile deviation after testing

On the right side is the coast flank, which, although it has suffered some grinding and deformation, it's not as prevalent as in the drive flank (on the left side of the image). The curve represents deviation from the involute. As it's made obvious by the leftmost measurement, there is a pretty significant deviation towards the root (or dedendum) of the teeth, where sliding between both gears is prevalent (in the active profile).

The deviations shown above, especially on the root of the first measurement in the drive flank warrant not only a roughness change, but a waviness and form change too, as already discussed.

6.1. Model selection and discussion

Therefore, the model not only requires a regression component but also a random component to more realistically represent surfaces. To accurately capture both components a shortlist of suitable candidates was composed, and a literature review was performed. The candidates were:

- Recurrent Neural Networks (RNN)
- Generalized Adversarial Networks (GAN)
- Multivariable Linear regression
- Gaussian Process Regression (GPR)

Both RNN and GAN are neural networks commonly used for image classification and generation, but support sequence-to-sequence capabilities as described in (Fumo, 2017) and (Brownlee, Machine Learning Mastery, 2019). The key difference lies on how they operate internally. RNN supports an internal memory function which is carried throughout the model remembering the most relevant elements of both the input and the previous iteration of calculations (Donges, 2021),

known as Long-Short Term Memory (LSTM). This cell is able to both generate an output or iterate in itself to refine the output, thus the name, recurrent. To validate and train the network a technique known as backpropagation is used, which simply put is moving from the output layer to the input layer of the neural network (Seth, 2021), in other words, verifying the bijectivity of the neural network.

RNN can be summarized as complex feedforward neural networks with a small internal memory. It's called recurrent since it performs the same function on every input, but the output depends on the previous iterations of the data (Mittal, 2019), although not only on the previous output, thus why it's not a Markov chain, which strictly follows the formula $h_t = f(h_{t-1})$.

Unlike standard feedforward networks, their internal memory (or internal state) allows them to process a sequence of inputs, hence, why it's well suited to model continuous data or more commonly speech recognition, where every word (or input in the case of data) is related to the one immediately before and right after and all ensemble create a sentence with meaning (likewise with data).

When in image recognition and classification applications it's commonly used with a convolutional layer to extend the pixel recognition capabilities to a neighbourhood of pixels, in other words, looking a forest rather than individually at each tree. This merges with the other mainstream neural network model, the convolutional neural network (CNN) which unlike RNN is remarkably good at extracting features (usually from images, an application of a common classification problem) but its oblivious to time-dependant data.

RNN

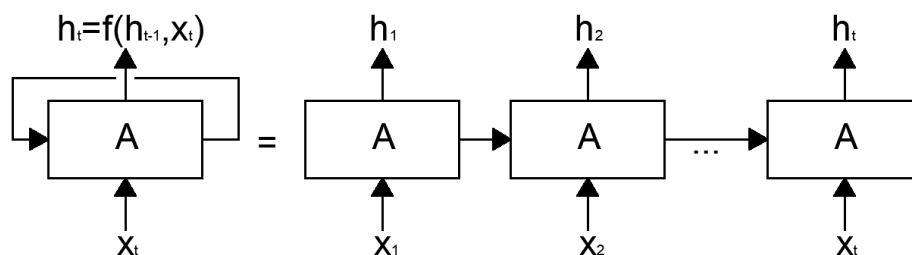


Figure 74 Unfolded RNN

LSTMs are a modification of RNN, they incorporate a memory at every cell which makes it easier to remember past data which solves the vanishing gradient problem found in RNN (SuperDataScience, 2018). The vanishing problem arises from training itself. At first, each cell is randomly assigned a weight close to zero when building the optimizer. The issue lies on the definition of RNN, as every output depends on the previous one, when building the error function to optimize the network, as it grows the weight of each neuron becomes the product of all previous states, as such, as the series progresses said product implements more and more close-to-zero elements, which drastically reduces the error function, thus failing to optimize the neural network (SuperDataScience, 2018):

$$\frac{\partial x_t}{\partial x_k} = \prod_{t \geq i \geq k} \frac{\partial x_i}{\partial x_{i-1}} = \prod_{t \geq i \geq k} \vec{w}_{rec}^T \text{diag}(\sigma'(x_{i-1}))$$

If however, the relative weights (\vec{w}_{rec}) were large rather than close to zero, the gradient would explode.

LSTM cells have a very particular architecture which allows them to overcome the vanishing (or exploding) gradient problem. The input gate decides which value from the input should be used to update the memory with a combination of a sigmoid and tanh function. The sigmoid

discriminates between inputs (whether it's accepted as a valid input or not) whilst the tanh function assigns a weight between -1 and 1 (SuperDataScience, 2018). Both, as any RNN inherently depend on previous output and the current input. The general formulation is:

$$i_t = \sigma(W_i \cdot [h_{t-1}, x_t] + b_i)$$

$$\tilde{C}_t = \tanh(W_c \cdot [h_{t-1}, x_t] + b_c)$$

For reference, the sigmoid function is described as:

$$\sigma(x) = \frac{1}{1 + e^{-x}}$$

The catch is in the next block, the forget gate, which decides, via a sigmoid function which details to forget from the block. For every number at the cell state (all the previous iterations, C_{t-1}), considering both the previous state (h_{t-1}) and the current input (x_t) to generate a number between 0 (forget) or 1 (keep), with the formula (SuperDataScience, 2018):

$$f_t = \sigma(W_f \cdot [h_{t-1}, x_t] + b_f)$$

Finally, the output gate decides which values to let through and which to drop. Once again, it does so via the sigmoid function, yielding values between 0 and 1. This is in turn paired with a tanh function that gives the output weight (relevance) between -1 and 1, following the formulation (SuperDataScience, 2018):

$$o_t = \sigma(W_o \cdot [h_{t-1}, x_t] + b_o)$$

$$h_t = o_t \tanh(C_t)$$

Below the schematic of a LSTM cell is provided:

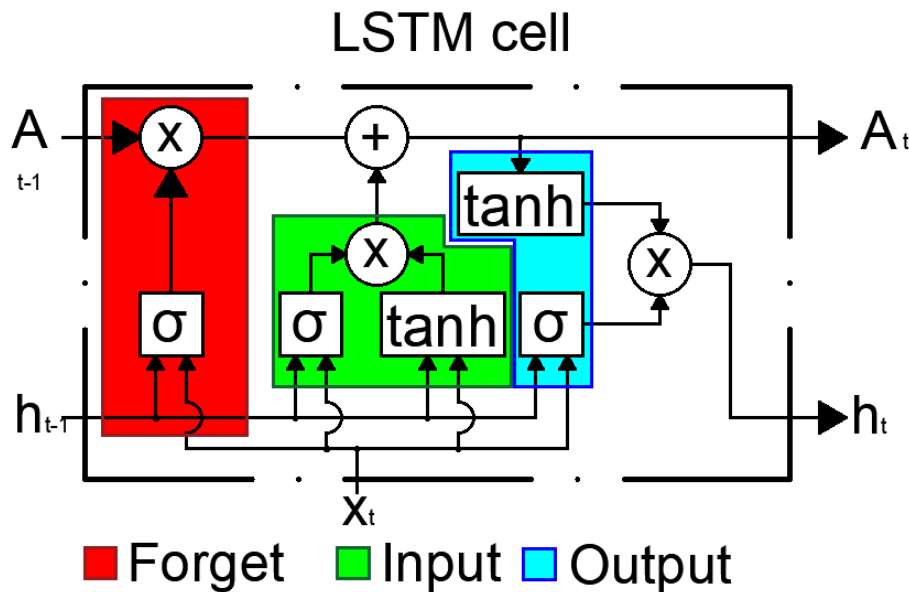


Figure 75 LSTM architecture

GANs on the other hand rely on a cat and mouse game or zero-gain game between two neural networks (Brownlee, Machine Learning Mastery, 2019). These are generally referred to as the Generator (a label-to-sequence neural network) and a Discriminator (a sequence-to-label neural network). Based on a training dataset, both networks are pitted against each other, the Generator aiming to create data as realistic looking as possible based on the training dataset whilst the Discriminator must determine which of the samples which it's been fed are in fact real or false, created by the Generator (al I. G., 2014). They compete in each iteration and whomever losses must improve before the next round. Generally, once the generator has been trained the Discriminator is discarded (Hui, 2018). Although GANs are generally used to recreate or enhance

images there are several examples of GANs used to generate sample numerical vectors and random number generators (RNG) as shown in (Rocca, 2019) and (Marcello De Bernardi, 2018).

The generator takes a fixed length vector as input and generates a sample of the working domain. This vector is full of random values extracted from a Gaussian distribution to generate a seed which kickstarts the process (Brownlee, Machine Learning Mastery, 2019). After extensive training the point pool for the seed will correspond to real points in the domain of the training sample, this is known as latent space, the variables herein although not observable are key for the model's correct performance (Brownlee, Machine Learning Mastery, 2019).

Latent variables are a projection of the initial data, storing the high-level concepts of the dataset. In GANs the generator gives the extracted latent points a meaning (Brownlee, Machine Learning Mastery, 2019) so that they can mix with the original data and kickstart the cat and mouse game, in other words, it translates the latent variables into something the others can use.

GANs typically use CNNs as generators and discriminators (Brownlee, Machine Learning Mastery, 2019), thus, are better suited for classification problems. Relying in CNNs also means they are remarkably ill-suited to sample continuous variables but excel at computer vision applications.

An important subproduct of GANs is their ability to generated conditional outputs with what's known as Conditional GANS or CGANs in short. This model can be trained with a standard dataset and a vector of conditions as an additional input which tends to be a classification label or a discrete variable (Brownlee, Machine Learning Mastery, 2019). To properly train the generator, the discriminator is also conditioned, meaning, it too receives the supplementary condition ridden vector. This adds a layer of complexity to the discriminator, since not only does it discern if the data is real or not based on the structure and reasonable values but also has to agree on the class label (or other existing conditions). After n iterations this will have taught the generator to create fake data according to the labels (Brownlee, Machine Learning Mastery, 2019). This could probe particularly useful when generating surface roughness vectors according to different surface parameters but the fact it relies in CNNs is a great drawback.

Another reasonable GAN version is a Wasserstein GAN (WGAN in short), not only does it improve the stability when training, but it also provides a loss function which is in turn correlated with the quality of the output (Bronlee, 2021). However, it relies in deep CNNs and therefore is not well suited for this application, alas, its usage was discarded.

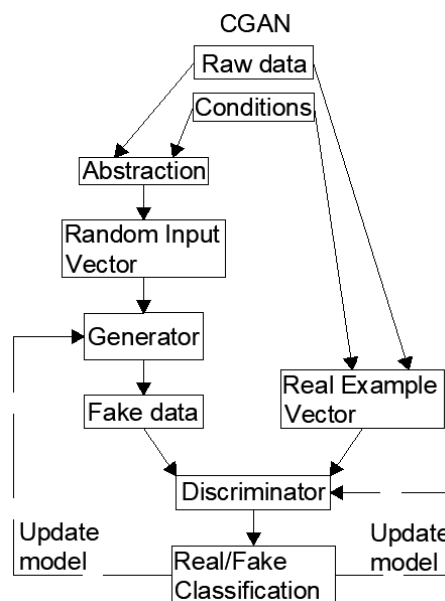


Figure 76 CGAN structure

Modelling of gear surface roughness impact on electrified transmissions' efficiency

6. Surface modelling and generation

The other two alternatives fall in the machine learning realm, with multivariable linear regression being the simpler of the two and its formulation being well known, however, the biggest setback is the lack requirement of predetermining the variables to adjust and the order of magnitude of said variables, thus being a parametric study (Williams, 2010). Furthermore, randomness of any given value is inherently removed from any regression since it will always output a function $Y = f(X)$ (Tim, 2017), therefore any line surface generated with this technique will always be equal (given the same input parameters) unless the confidence intervals are considered, and a random value is selected from the range.

It is well known linear regression is not well suited for very noisy large datasets without a clear structure, centred around 0, such as these samples for instance (James, 2020), since the confidence intervals will tighten around the regression model and thus excluding real original values. See example below with a sample surface measurement.

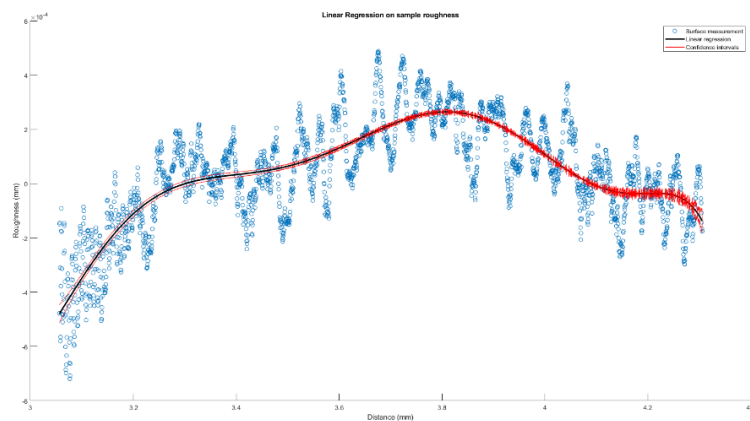


Figure 77 Linear regression on surface sample

The confidence interval at 95% leaves out most of the data for the regression of order 10. This lack of randomness leads the research efforts towards Gaussian Process Regression.

GPR combines the smoothing techniques of a linear regression with confidence intervals adjusted to the sample data (Scikit learn, 2022), thus allowing for a random selection of values within.

GPR is a non-parametric regression, thus rather than calculating the probability distribution of a parameter it calculates the probability across all possible functions for said parameter (Sit, 2019) and compare those to the sample data, thus, calculating the posterior probability of that function being representative with a Bayesian approach. Thanks to the associated probability of each generated function, the mean function can be derived along with the confidence intervals at every point of the function (Optimization Geeks, 2021).

Due to its very nature, GPR models have “flexible” confidence intervals and contain all the sample data (MathWorks, 2021). Alas, it’s reasonable to assume any random value within the determined confidence intervals will respect all high-level parameters which characterize the surface yet allow for the randomness component demanded of any real surface.

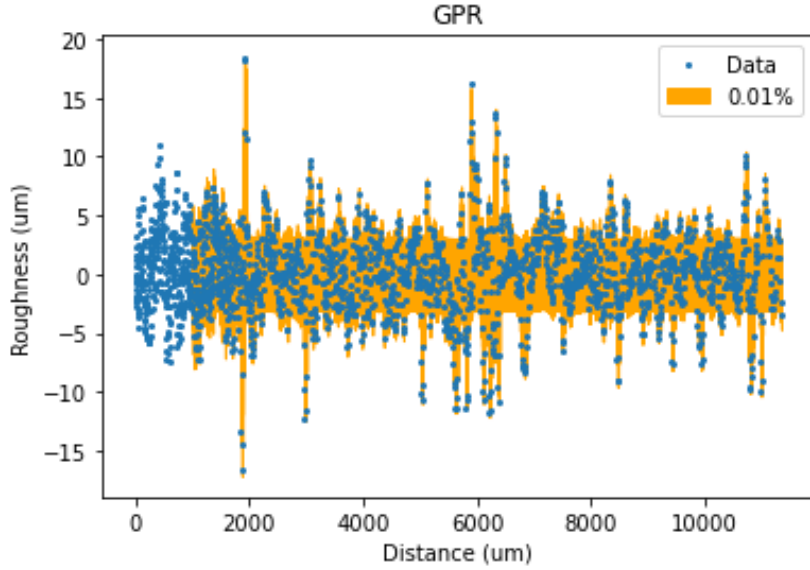


Figure 78 GPR confidence intervals at 99.9% of a real measurements

Therefore, GPR was selected to analyse and study surfaces for their posterior characterization. Neural networks, although at first seemed promising were discarded since it's remarkably hard to fully characterize how the hidden layer is operating and therefore if there was a deep underlying error it would have been too complex to fix in a reasonable timeframe.

Any GPR model is extremely reliant on its kernels, or covariance of the GPR random variables, which, together with the mean function of the GPR completely defines the model (Roelants, 2022). Any GPR model can be written as:

$$y \sim GP(m(x), k(x, x')) = N \left(\begin{bmatrix} m(x_1) \\ \vdots \\ m(x_n) \end{bmatrix}, \begin{bmatrix} k(x_1, x_1) & \cdots & k(x_1, x_n) \\ \vdots & \ddots & \vdots \\ k(x_n, x_1) & \cdots & k(x_n, x_n) \end{bmatrix} \right)$$

So that $m(x)$ is the mean function and $k(x, x')$ is the kernel or covariance between each random variable pair. Hence a GPR is nothing more than a multi-mean, multi-variance normal distribution adapted to the existing data.

In order for the model to have a valid kernel matrix $k(x, x')$, this must be positive definite, implying it must be symmetric and invertible. There are several re-defined kernels available in Scikit-learn 0.24.2, the most commonly used ones are:

Constant kernel, this tends to be use as a smaller part of a more complex product kernel (combination of several kernels), where it scales the magnitude of the other kernel or as part of sum kernel where it modifies the mean of the GP (Gaussian process)

White noise kernel represents independent and identically distributed noise added to the GP distribution. With the formula (Roelants, 2022):

$$k(x_a, x_b) = \sigma^2 I_n$$

Where σ^2 is the variance of the noise and I_n is the identity matrix. This results in a zero-filled matrix except for the diagonal, which contains the variances of each variable, considering the noise between variables is uncorrelated (Roelants, 2022).

Exponentiated quadratic kernel or radial-basis function kernel (RBF). This is a stationary kernel, it's dependent on the length-scale parameter $l > 0$ which can be a scalar (isotropic variant) or a vector with the same number of dimensions as the input random variables, the anisotropic variance (Scikit-learn, 2022). It follows the equation:

$$k(x_a, x_b) = \exp\left(-\frac{d(x_a, x_b)^2}{2l^2}\right)$$

Where the d operator is the Euclidean distance, other distance functions have been reviewed in literature, such as the Manhattan distance but they do not necessarily result in a positive definite matrix, thus, for stability's sake is better not to use them (Noco, 2020). This type of kernel yields the smoothest functions since they are infinitely differentiable and thus it has mean square derivatives in all orders (Scikit learn, 2022). They have a maximum at $x_a = x_b$ and exponentially decreases towards 0 as the function moves further away from that point (Roelants, 2022).

Rational quadratic kernels are similar to the exponentiated quadratic kernels yielding smoother curves (Roelants, 2022) resulting from an infinite sum of RBFs with different characteristic length-scales. Not only are they characterized by the length-scale parameter $l > 0$ but also by the scale mixture parameter $\alpha > 0$ (Scikit-learn, 2022). When $\alpha \rightarrow \infty$ then the rotational quadratic kernel converges to and RBF kernel (Roelants, 2022). It follows the function:

$$k(x_a, x_b) = \sigma^2 \left(1 + \frac{\|x_a - x_b\|^2}{2\alpha l^2}\right)^{-\alpha}$$

Where σ^2 is the overall variance or squared amplitude. Only the isotropic variant is supported at the moment in Scikit-learn 0.24.2 (Scikit learn, 2022).

Periodic kernel or Exp-Sine-Squared kernel allows for the use of periodic functions. It's characterized by the length scale parameter $l > 0$ and a periodicity parameter $p > 0$ (Roelants, 2022). Currently only the isotropic variant where l is a scalar is supported in Scikit-learn 0.24.2 (Scikit learn, 2022). It follows the function:

$$k(x_a, x_b) = \sigma^2 \exp\left(-\frac{2}{l^2} \sin^2\left(\pi \frac{|x_a - x_b|}{p}\right)\right)$$

Kernels also have operators, as such a new kernel can be obtained from simpler versions, the most commonly used ones include the sum kernel; the product kernel and the exponentiation kernel. The sum kernel adds 2 kernels together; the product kernel multiplies them and the exponentiation kernel creates a power function with the kernel as the base and the scalar p as the exponent (Scikit learn, 2022).

Local periodic kernel is the multiplication of a periodic and an exponentiated quadratic kernel, this allows the periods to vary over longer distances, combining both variance terms into one (Roelants, 2022).

Dot-Product kernel is non-stationary, meaning it has a mean which frows around a fixed trend constantly and independently from any time function (Iordanova, 2022). This kernel can be generated by putting $N(0,1)$ priors on the coefficients and a prior of $N(0, \sigma_o^2)$ on the bias of any linear regression. In other words, making both the linear regression coefficients and the bias follow normal distributions (Scikit learn, 2022). This kernel is invariant to a rotation of the coordinates about the origin, but it is sensible to translations. It's parametrized by σ_o^2 and in any case where $\sigma_o^2 = 0$ it is called the homogeneous linear kernel, otherwise, inhomogeneous (Scikit learn, 2022). It is commonly paired with an exponentiation as it tends to widen the confidence intervals as the independent variable increases. It follows the formula (Scikit learn, 2022):

$$k(x_a, x_b) = \sigma_o^2 + x_a \cdot x_b$$

Matérn kernel is a stationary kernel and a generalization of the RBF kernel, dependant on the additional parameter ν which controls the smoothness of the end result. It is also characterized by the length-scale parameter $l > 0$ which can be a scalar (isotropic variant) or a vector with the same number of dimensions as the independent random variables (anisotropic variant). It follows the equation (Scikit learn, 2022):

$$k(x_a, x_b) = \frac{1}{2^{\nu-1}\Gamma(\nu)} \left(\frac{\sqrt{2\nu}}{l} d(x_a, x_b) \right)^\nu K_\nu \left(\frac{\sqrt{2\nu}}{l} d(x_a, x_b) \right)$$

Where $d(x_a, x_b)$ is the Euclidean distance (no reference to other distance formulae has been found in the literature); K_ν is a modified Bessel function and Γ is the gamma function. As $\nu \rightarrow \infty$, this kernel converges to an RBF kernel. When $\nu=1/2$, the Matérn kernel transforms into an absolute exponential kernel. Another couple of common smoothness factors are $\nu=3/2$ and $\nu=5/2$ resulting in an RBF kernel which is once or twice differentiable respectively (Scikit learn, 2022).

The big advantage of the Matérn kernel lies on the flexibility control the smoothness parameter ν grants the function, adapting it to the real underlying properties of the correlation between functions (Scikit learn, 2022). In other words, it's the most flexible kernel available.

The default kernel (RBF multiplied by a constant value) and default optimization the L-BFGS-B algorithm, minimize the hyperparameters within the provided default bounds (Nocedal, 1989) and the default optimizer restarts (none) to find the kernel parameters which maximize the log-marginal likelihood (Scikit learn, 2022).

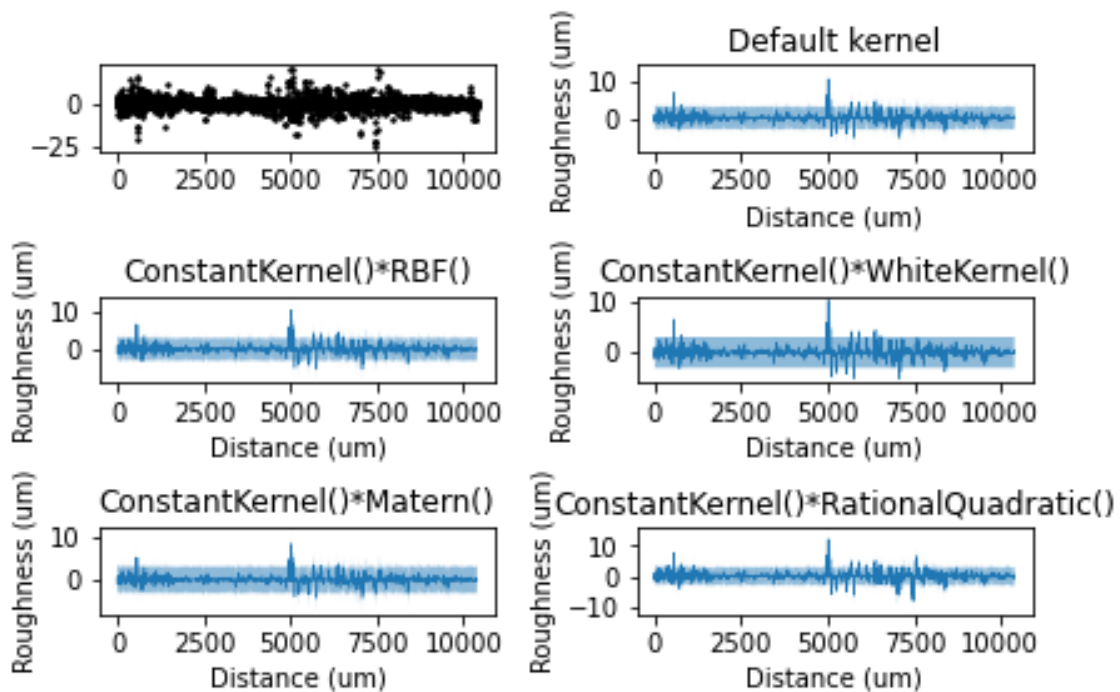


Figure 79 Fixed boundary optimization kernel comparison

As seen above, the constrained optimization of the kernel's hyperparameters greatly affects the confidence interval, largely due to the contact value kernel not being optimized. However, this is an illustrative sample of the effect each kernel has on the GPR model. The default kernel represents a fairly smooth model, whilst the White Kernel is the noisiest (as expected due to its nature). The RBF and Matérn kernels represent the surface slopes much better than any other (again, as expected) whilst the rotational quadratic is a bit more aggressive with the slopes, due to the default α . These kernel samples were performed with the processed data from the gear measurements. The sample evaluation parameters obtained were:

Table 7 Sample kernel evaluation

Kernel Type	Default	RBF	White	Matérn	Rational Quadratic
Optimization cycles	1	1	1	1	1
Scores	1	1	-0.00603	1	1
Log Marginal Likelihood	-65894.8	-65894.8	-70239.3	-66460.2	-62764.8

All kernels have a score of 1 (except the White kernel due to its noisiness), thus, their modelling can explain the sample, however the likelihood does vary significantly. The negative value of the function is due to a plethora of values being smaller than one, therefore, the logarithm of said marginalized variable will be negative. As per the results, the worst model would once again be the White kernel, whilst the best would be the rotational quadratic. These results are far from absolute since the models were not allowed to optimize, this was merely to point out their behaviour.

It's worth noting the native python description lack the σ^2 multiplier, alas, it will be supplied by a multiplying constant kernel on all models. After some previous tests the Exp-Sine-Squared kernel was unable to perform due to the chaotic nature of the data unless it was allowed to optimize (unbounded optimization rather than fixed bounds such as the results shown in the sample figure above).

After careful study and consideration, the following kernel set-ups were tested (using their score and log-marginal likelihood to rate them):

- Default: RBF with length-scale parameter equal to 1 and fixed bounds (hyperparameters will not be optimized) and a single optimization run.
- Model 1: RBF with optimizable hyperparameters; a starting length-scale parameter of 1 and 10 optimization runs.
- Model 2: White kernel with optimizable hyperparameters; a starting noise level of 1 and 10 optimization runs.
- Model 3: Matérn kernel with optimizable hyperparameters; a starting length-scale parameter of 1; a nu of 3/2 (starting as an absolute exponential kernel) and 10 optimization runs.
- Model 4: Rational Quadratic kernel with optimizable hyperparameters; a starting length-scale parameter of 1; a starting alpha of 1 (scale mixture parameter) and 10 optimization runs.
- Model 5: Exp-Sine-Squared kernel with optimizable hyperparameters; a starting noise level of 1 and 10 optimization runs.

Since the Dot Product kernel yields ever-expanding confidence bounds it was discarded as the surface roughness is clearly contained within the geometrical tolerance.

As indicators to discern between each model's behaviour 2 parameters are available: score and the log marginal likelihood.

The score of the model is the coefficient of determination of the prediction based on the test data which is defined as:

$$R^2 = 1 - \frac{u}{v} \quad \left| \quad \begin{cases} u = \sum (y_{true} - y_{prediction})^2 \\ v = \sum (y_{true} - \bar{y}_{prediction})^2 \end{cases} \right.$$

Where u is the residual sum of squares and v is the total sum of squares (in which $\bar{y}_{prediction}$ is the mean of the predictions). The best possible score is 1 although the score may be negative (arbitrarily worse) with a minimum score of 0, a constant model disregarding all of the input characteristics (Scikit learn, 2022).

The log marginal likelihood can be described as the coefficient of the stochastic complexity or the learning degree of the model (Rusin, 2022); in other words, for every input parameter the likelihood of each value is calculated and that is in turn multiplied by the probability density of that parameter and that value occurring, this is un turn performed for al input parameters and added (Bruno Nicenboim, 2022). Simply put the log likelihood, it's the goodness of fit of a model having marginalized each variable separately (having taken them out of the equation by integrating them), the higher the value the better (Zach, 2021). The marginal likelihood is how well the data is explained given all parameters (ofer-a, 2022).

To analyse the parameters significance with regards to the recorded surface roughness two separate validation procedures were considered: Regression trees and Automatic Relevance Detection (ARD).

Regression trees evaluate is an unsupervised learning tool which seek to, at every iteration split the data at a variable value which minimizes the sum of the square deviation errors (Frontline Solver, 2022). Therefore, the first split is the one which minimizes the sum of square deviations the most, and so on for subsequent cuts, alas, the first few split variables can be considered to be the most relevant for the data.

ARD is a useful tool when it comes to pruning large amounts of irrelevant data. It regularizes the solution space (dependent variable) into a set of reference coordinates based on the input variables, which, effectvely removes irrelevant parameters (Nagarajan, 2007). To distinguish between relevant and irrelevant data ARD relies in a set of hyperparameters determined by the variance of the input space (Nagarajan, 2007). Mathematically, each coefficient is marginalized and studying the maximum type II likelihood, equivalent to the formulation:

$$-\min(\log(p(y; \gamma))) = -\min \int p(y|\gamma)p(x; \gamma)dx$$

In other words, minimizing the minus log marginal likelihood or maximizing the log marginal likelihood of the data, alas, it is particularly well suited to evaluate GPR data as pointed out in (g, 2021).

6.2. Data preparation

To train the model, 80% will be allocated to the training set and 20% to the test set, no validation set was defined since the current implementation of the GPR model automatically fits the hyperparameters, making its own train/validation split internally (Scikit learn, 2022).

The model and training environment were coded in Spyder (Anaconda) with Python 3.9, using the libraries:

- Pandas: Dataset management library (release: 1.3.4).
- Numpy: Vector and matrix operations library (release: 1.20.3).
- Matplotlib: Graphs and plots library (release: 3.4.3).
- Scikit-learn: Machine learning library (release: 0.24.2).
- Scipy: Statistics library (release: 1.7.1).

An added benefit of this training set-up and implementation is the default warning against underfitting in case there isn't enough data or the optimization cycles are not enough, thus, the only real challenge the training cycle could face would be overfitting.

Modelling of gear surface roughness impact on electrified transmissions' efficiency

6. Surface modelling and generation

```
Increase the number of iterations (max_iter) or scale the data as shown in:  
https://scikit-learn.org/stable/modules/preprocessing.html  
_check_optimize_result("lbfgs", opt_res)  
C:\ProgramData\Anaconda3\lib\site-packages\sklearn\gaussian_process\_gpr.py:506: ConvergenceWarning: lbfgs failed to converge  
(status=2):  
ABNORMAL_TERMINATION_IN_LNSRCH.
```

Figure 80 Underfitting warning message

Before progressing towards model outcomes, it's worth noting the surface parameters extracted by the measurement acquisition instruments (KEYNECE VR-500) do not expand the entirety of the measurement length but a frame in the middle of the aforementioned, most likely to avoid noise due to the start and ending of the measuring length as seen below:

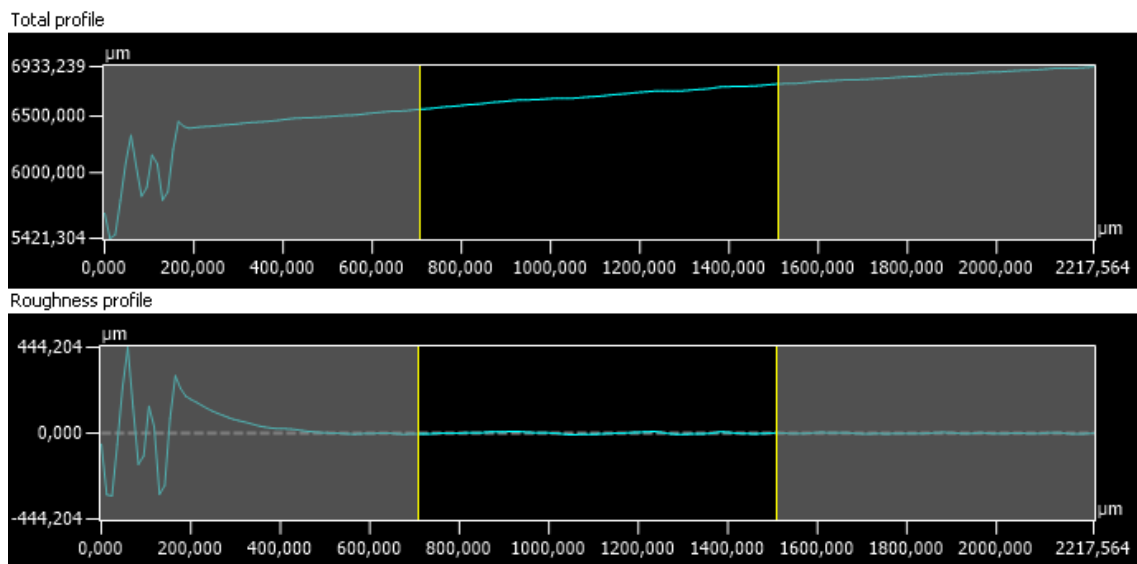


Figure 81 Evaluation length of 2-line measurements in the profile direction

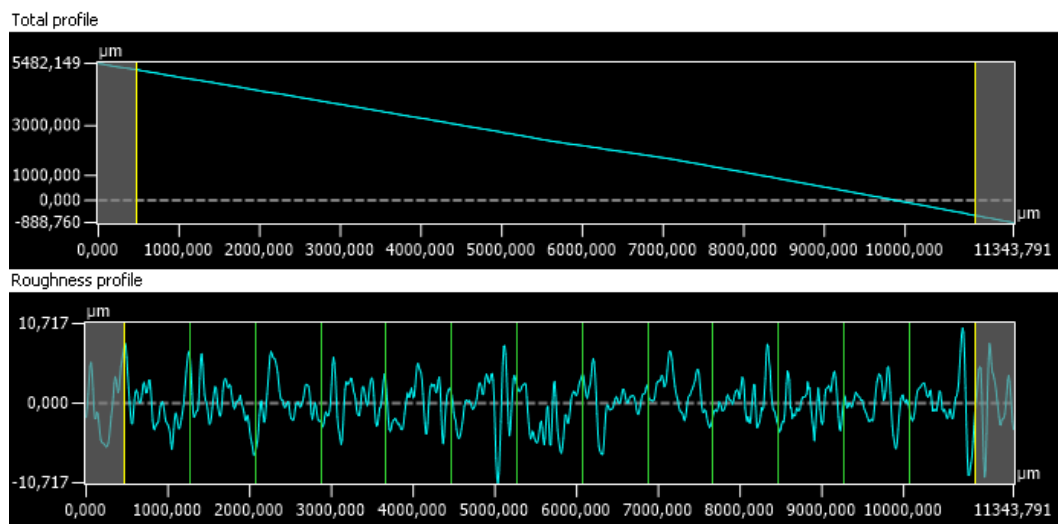


Figure 82 Evaluation length of 1line measurements in the lead direction and its extracted roughness

Alas, the model will only be trained with data from that same range, 0.7 mm to 1.5 mm in the profile direction (there isn't enough distance along the tooth's involute to measure more than 1 cut-off length) and 0.5 mm to 10.9 mm in the lead direction (13 cut-off lengths as seen above).

6.3. Surface model output and discussion

The various versions of the GPR model couldn't be executed in the existing computing equipment, alas, more advance processors and power equipment was required. A first modelling batch was calculated using all surface parameters captured by the 3D optical interferometry

Modelling of gear surface roughness impact on electrified transmissions' efficiency
 6. Surface modelling and generation

measurement equipment (KEYNECE VR-500). The scores and log marginal likelihood can be seen below:

Table 8 First GPR model results

Model	Default RBF	RBF	White	Matérn	Rotational Quadratic	ExpSine Squared
Optimization cycles	1	10	10	10	10	10
Score	0.76	0.99	-0.06	0.88	0.89	0.76
Log Margin	-12087	-5988	-7075	-6881	-6601	-7075

As seen above, the scores are remarkably high, except the White Kernel, especially for RBF and Rotational Quadratic kernels. The fact the White kernel has such a low test score suggests there is some structure to the data hence why a noise-specialized kernel has so many problems trying to model the data.

The log marginal likelihood explains how all the variables explain or affect the data, since it's the integration of every variable, alas, it should, ideally be positive and as high as possible. In this scenario, the results are far from ideal, which can be due to some overfitting, for which the resulting models and confidence intervals although a part of the error is due to not having enough data since the 3D measurement equipment was unable to capture as many points per measurement as the 2D measurement equipment. The resulting models can be seen below:

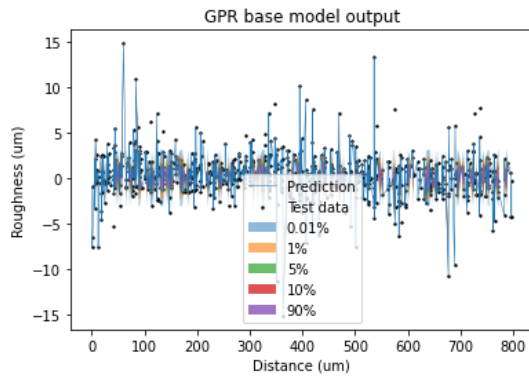


Figure 83 Default GPR model results

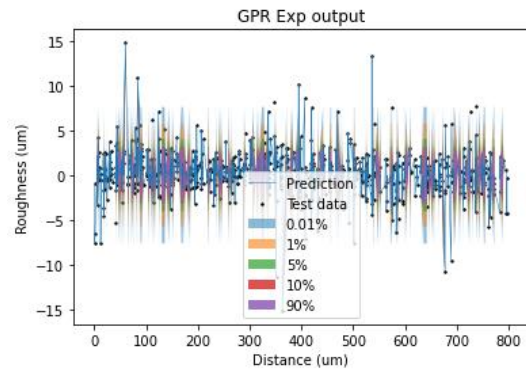


Figure 84 Exponential Sine GPR model results

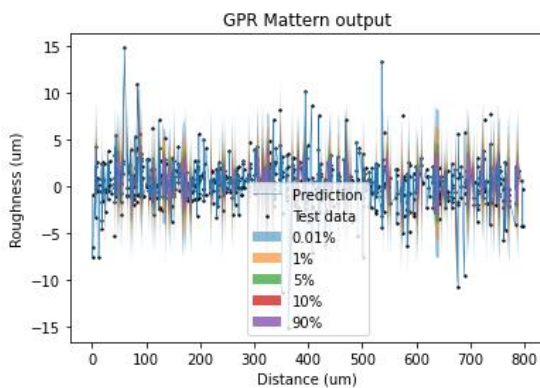


Figure 85 Matérn GPR model results

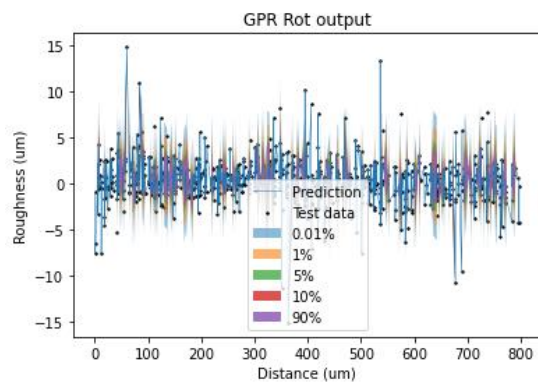


Figure 86 Rotational Quadratic GPR model results

Modelling of gear surface roughness impact on electrified transmissions' efficiency
 6. Surface modelling and generation

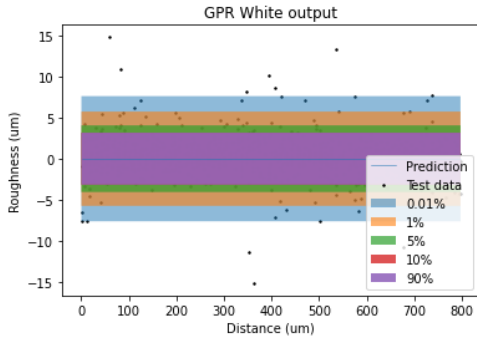


Figure 87 White GPR model results

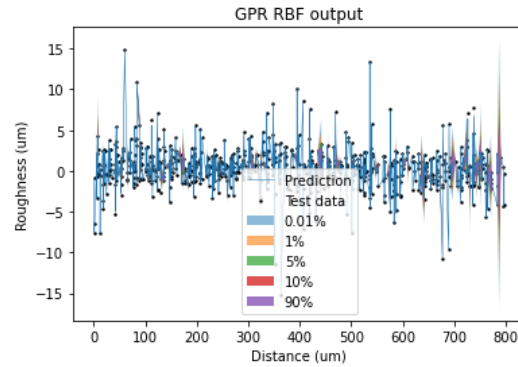


Figure 88 RBF GPR model results

Thanks to the model outputs the White kernel shows no compliance with the data and thus, very wide confidence intervals, whilst the others, have very narrow confidence intervals with the model and the confidence intervals both tracing the data, pointing towards a blatant overfitting, thus, GPR could be assumed to be too precise for this application, since this modelling aims at attaining realistic confidence interval bounds to then randomly generate surface points within those bounds.

The data was then evaluated with ARD (Automatic Relevance Determination) and decision trees to understand which were the key players in determining the data.

ARD suggested the most relevant variable was Rsk (in module).

Table 9 ARD significance results 1

Parameter	Rz	Rp	Rv	Rt	Rq	Rsk	Rku	Sm	Rpk
ARD score	-6e-4	-6e-4	1e-4	-6e-4	-6e-4	0.03	0.02	-6e-4	-6e-4
Parameter	Rvk	Type	Size	Flank	Direction	Rmax	Id1	Id2	
ARD score	-6e-4	0.003	0.004	-6e-4	-0.002	-6e-4	-0.002	-5e-4	

To determine the second most relevant parameter Rsk was suppressed from the dataset and the ARD procedure repeated, yielding Sm as the second most relevant variable (in module):

Table 10 ARD significance results 2

Parameter	Rz	Rp	Rv	Rt	Rq	Rku	Sm	Rpk
ARD score	9e-5	-5e-5	-5e-5	-9e-5	-4e-4	-5e-6	-0.03	-2e-4
Parameter	Rvk	Type	Size	Flank	Direction	Rmax	Id1	Id2
ARD score	-1e-3	-5e-4	-6e-4	-6e-4	-6e-4	-6e-4	-6e-4	-6e-4

To verify this result, a regression tree was modelled from the data and the three first branches were dependant on Rsk, Rmax and Sm. The tree can be seen below (with a prune to 5 levels):

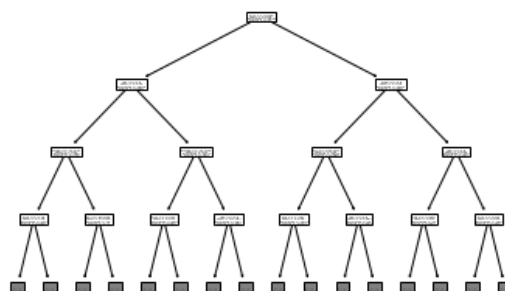


Figure 89 Regression tree for variable significance

Modelling of gear surface roughness impact on electrified transmissions' efficiency
 6. Surface modelling and generation

These results are thus related with and validated by the reference (Marghalani, 2010) where S_m and R_{max} were also selected to represent the surface roughness in 2 dimensions, but instead of R_{sk} (which represents the surface's skewness), to centre the distribution the author relies on R_a . A representation can be seen below:

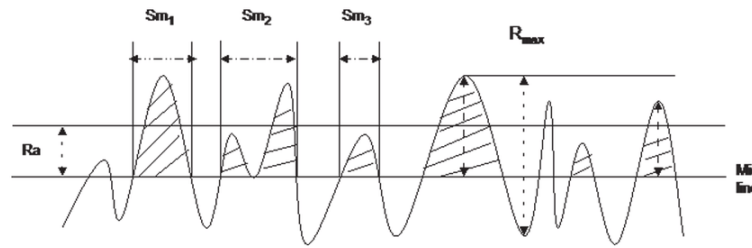


Figure 90 Parameter selection representation (Marghalani, 2010)

The GPR models were then repeated with the afore mentioned parameters and the X-coordinates of the surfaces as the input space, resulting in:

Table 11 Refined GPR training with different kernels

Model	Default RBF	RBF	White	Matérn	Rotational Quadratic	ExpSine Squared
Optimization cycles	1	10	10	10	10	10
Score	-0.061	-0.061	-0.061	0.122	-0.070	-0.061
Log Margin	-7075	-7075	-7075	-6918	-14285	-7075

As seen above, the scores drop significantly as most variables have been dropped from the model, which hinders accuracy, and the log marginal likelihood remains abysmal. It is worth noting the White kernel has not changed in between input configurations which points towards the kernel not being adequate for this application. However, the confidence intervals enlarged and were now capable of encompassing most of the surface data:

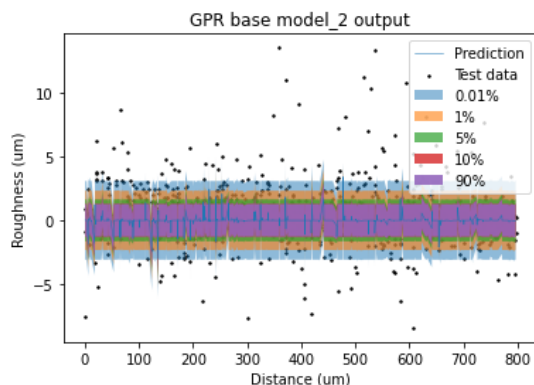


Figure 91 Reduced default GPR model results

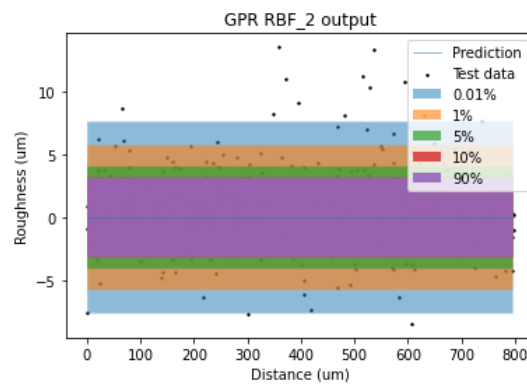


Figure 92 Reduced RBF GPR model results

Modelling of gear surface roughness impact on electrified transmissions' efficiency
 6. Surface modelling and generation

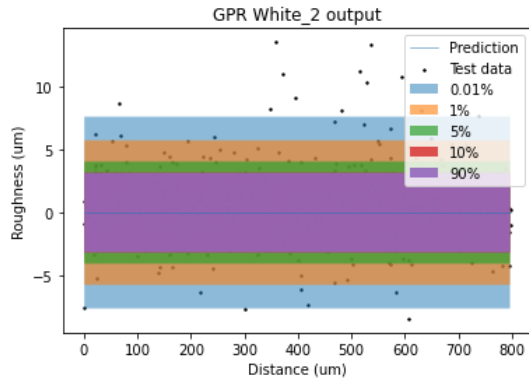


Figure 93 Reduced White GPR model results

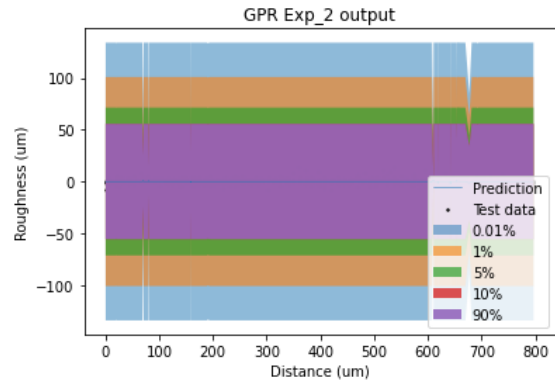


Figure 94 Reduced Exponential Sine GPR model results

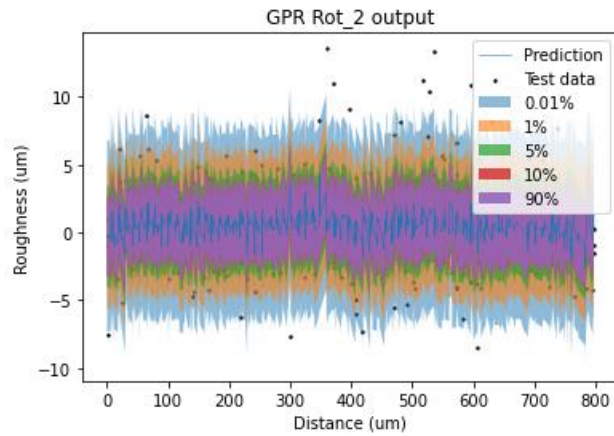


Figure 95 Reduced Rotational Quadratic GPR model results

As seen above, the confidence intervals have enlarged significantly, with White's and RBF's not seemingly optimized, suggesting the optimization cycle number should have been increased or in White's case most likely it's unsuited for this type of optimization. However, since the base RBF and Rotational Quadratic have confidence intervals which contain the data and most importantly, adapts to it, a new modelling round with these 2 kernels will be trained with the 3 relevant parameters and gear labels, as such, this previous iteration run allows for the selection of appropriate modelling kernels. These second models considering labels resulted in the following scores and log marginal likelihood:

Table 12 Relevant parameters and kernels optimization with labels

Model	Score	Marginal Log Likelihood
RBF	-0.037	-7087
Rotational Quadratic	0.153	-6918

The models' confidence intervals are depicted below:

Modelling of gear surface roughness impact on electrified transmissions' efficiency
 6. Surface modelling and generation

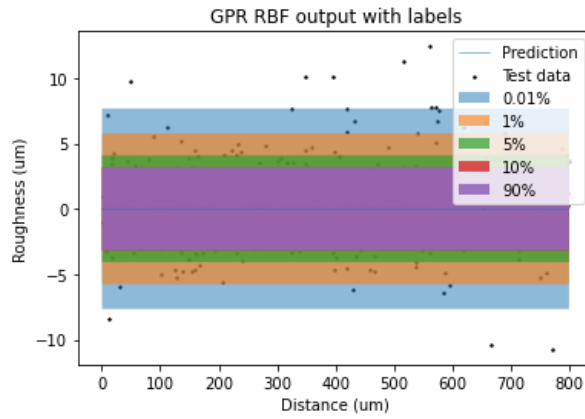


Figure 96 Labelled input RBF GPR model

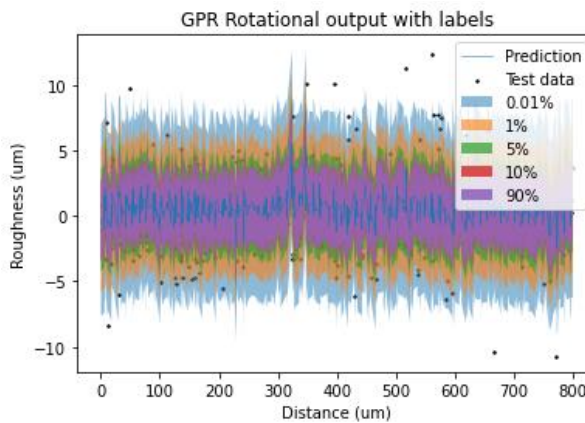


Figure 97 Labelled input Rotational Quadratic FPR model

Although the scores are still low, the 12% increment is significant compared to previous results, alas, the labels can greatly increase the model accuracy to predict the surfaces generated.

In parallel, to verify the robustness of the decision trees and ARD outputs, a combination of all the shortlisted parameters was run on 5 optimization cycles for both a RNF and Rotational Quadratic kernels, with identifier labels such as gear type, module, flank...

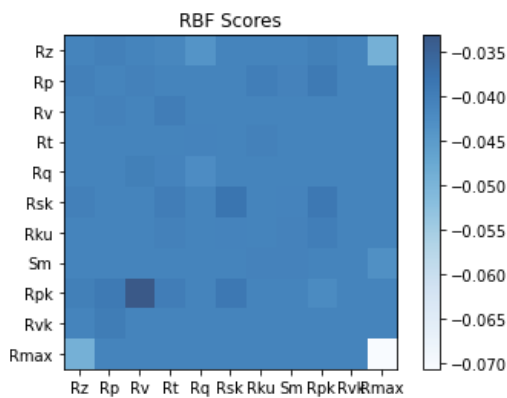


Figure 98 RBF scores colour map without labels

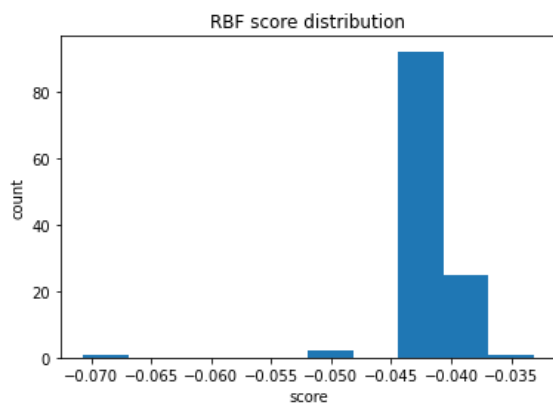


Figure 99 RBF score distribution without labels

Modelling of gear surface roughness impact on electrified transmissions' efficiency
 6. Surface modelling and generation

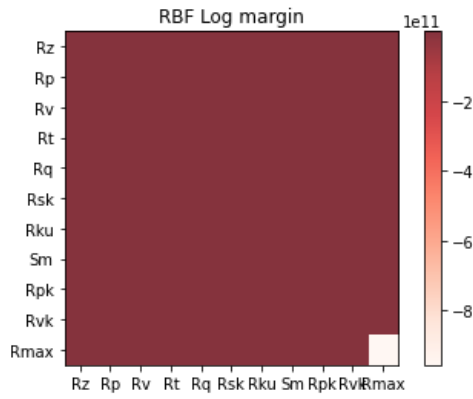


Figure 100 RBF Log Margin colour map without labels

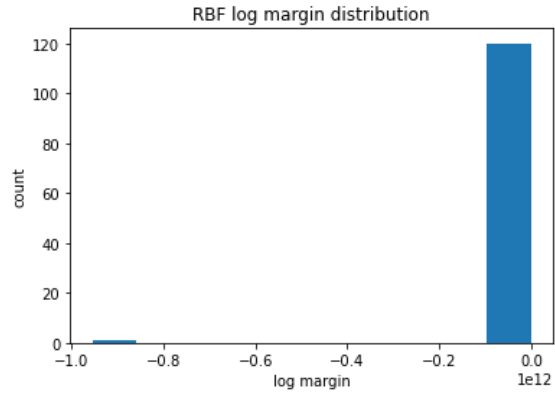


Figure 101 RBF Log Margin distribution without labels

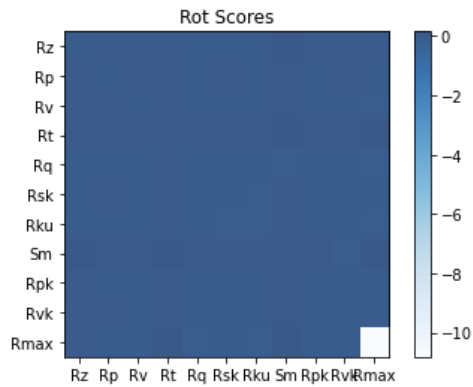


Figure 102 Rot scores colourmap without labels

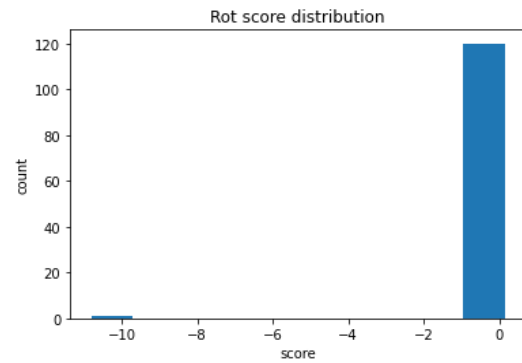


Figure 103 Rot score distribution without labels

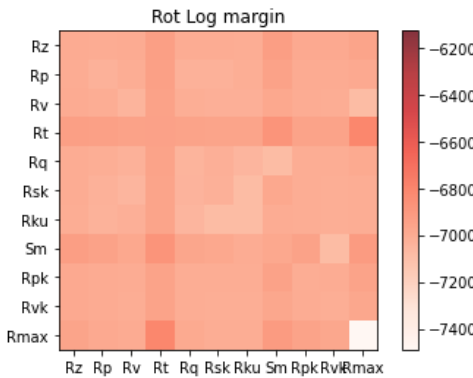


Figure 104 Rot Log Margin colour map without labels

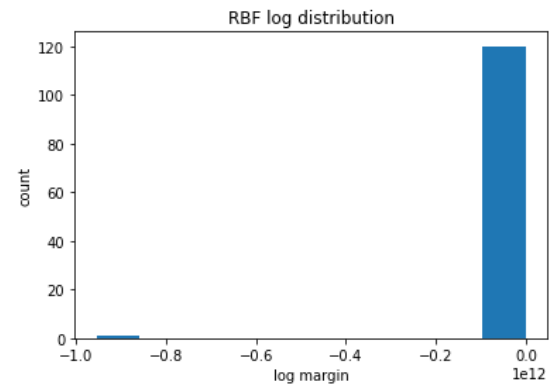


Figure 105 Rot Log Margin distribution without labels

The models without labels and over a 10% score were:

Table 13 Unlabelled model details

Variable 1	Variable 2	Kernel	Log margin	Score
Rz	Sm	Rotational Quadratic	-6929	0.117
Rt	Sm	Rotational Quadratic	-6873	0.154
Rt	Rmax	Rotational Quadratic	-6808	0.146
Rmax	Sm	Rotational Quadratic	-6914	0.129

Overall, the only model which improves the previous' iteration based on labelled data and the variables Rsk, Rmax and Sm is the model based on Rt and Sm, improving by 0.1% the score and the log marginal likelihood by 45 (0.65% improvement at best) but relying in only 2 variables.

Modelling of gear surface roughness impact on electrified transmissions' efficiency
 6. Surface modelling and generation

Additionally, the score and log marginal likelihood and score colour maps for RBF suggest it needs further optimization cycles whilst the Rotational Quadratic kernel is better suited for modelling with fewer iterations. Once again, such poor log marginal likelihoods can be mostly explained due to the lack of data.

R_t is a new variable to consider based on this results, although it represents something very similar to R_{max} , since their definitions are:

- Maximum Height of the Profile (R_t): Total height of the roughness profile described as the highest peak (R_{pi}) minus the lowest valley (R_{vi}) within the evaluation length (Santos, 2022).
- Maximum Roughness Depth (R_{max}): Largest of the successive values of R_{ti} calculated over the evaluation length (Santos, 2022).

Alas, R_t and R_{max} can be considered to be equivalent, if R_t is overall more stable and commonplace within traditional surface roughness parameters, as R_{max} is more prone to errors as it relies in one “peak” measurement rather than values over evaluation lengths.

There is a debate to be had on which of the 2 is better suited for contact or optical interferometry, since R_{max} and R_t will inevitably grow if the filtering effect of the probe is removed (the valleys will be deeper for instance) as discussed previously in this publication.

The modelling results from labelled data are presented below:

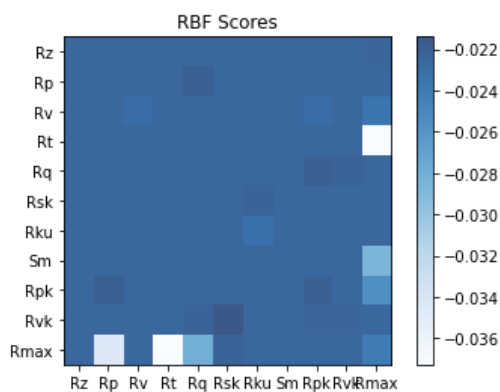


Figure 106 RBF scores colourmap with labels

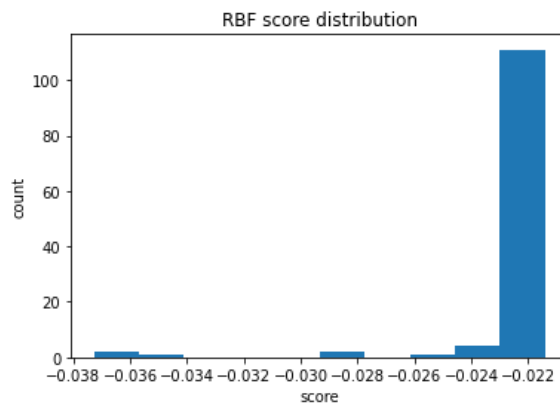


Figure 107 RBF score distribution with labels

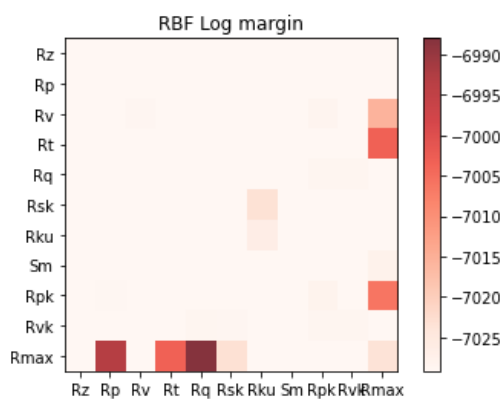


Figure 108 RBF Log Margin colour map with labels

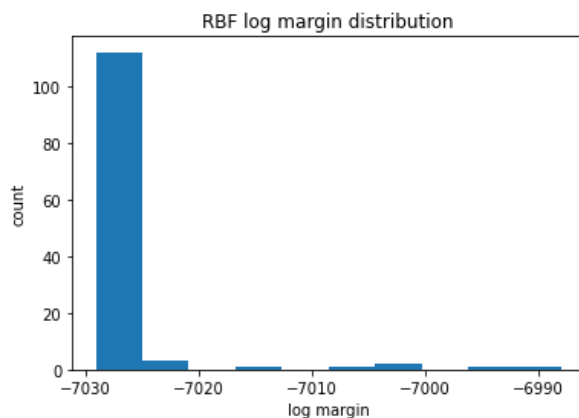


Figure 109 RBF Log Margin distribution with labels

Once again, RBF show clear signs of underfitting, completely attributed to the few optimization runs it was allowed to minimize computing resources (5 optimization runs).

Modelling of gear surface roughness impact on electrified transmissions' efficiency
 6. Surface modelling and generation

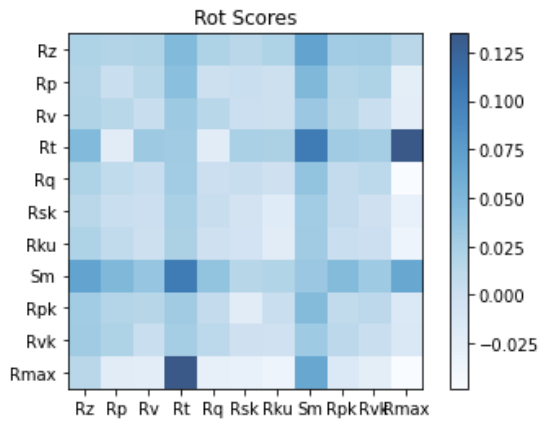


Figure 110 Rot scores colourmap with labels

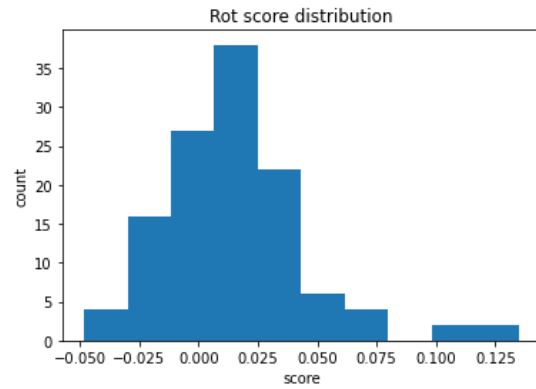


Figure 111 Rot score distribution with labels

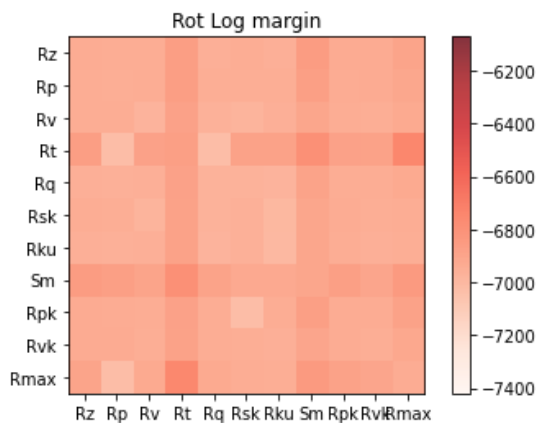


Figure 112 Rot Log Margin colour map with labels

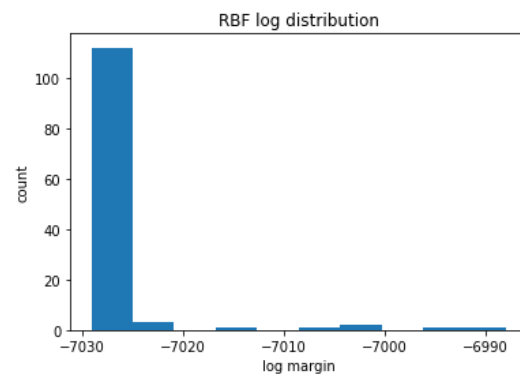


Figure 113 Rot Log Margin distribution with labels

There are, once again, a couple models with a score above 10%, their details are presented below:

Table 14 Labelled model details

Variable 1	Variable 2	Kernel	Log margin	Score
Rt	Sm	Rotational Quadratic	-6790	0.104
Rt	Rmax	Rotational Quadratic	-6745	0.135

The log marginal likelihoods have improved marginally whilst the scores have dropped, suggesting the labels have split the data into subsets far too small for modelling. This splitting can also explain the improvement of the log marginal likelihood since there is less noise in the data.

Further efforts should focus on fully characterizing a single gear, removing manufacturing variances and other nuances as the low scores suggest the data is too noisy for this approach to comfortably work with this limited dataset as explained in the reference (Santos, 2022).

As already discussed, the three extracted parameters to determine a surface are: Sm, Rmax/Rt and Rsk, which, point towards a material ratio positioning in space. Any line in space requires a starting point (Rsk) and a vector, whose coordinates are provided vertically by Rt/Rmax and horizontally by Sm.

An alternative formulation, simpler and more stable, would be correlating this surface parameters to the abbot curve

7. Sustainability and SDG alignment

This project fit into the following 3 Sustainable Development Goals (United Nations, 2022):

- Goal 9: Industry, Innovation and Infrastructure
- Goal 12: Responsible Consumption and Production
- Goal 13: Climate Action



Figure 114 SDG 9 (United Nations, 2022)



Figure 115 SDG 12 (United Nations, 2022)



Figure 116 SDG 13 (United Nations, 2022)

The project is clearly encompassed into “Goal 9: Industry, Innovation and Infrastructure” since it the better understanding of gear behaviour when running and straight out of manufacture allow to push forward any electric vehicle transmission efforts, thus dealing with innovation. Since a better surface definition and a deeper understanding of its behaviour benefit industrial manufacturing processes, allowing for more appropriate and accurate surface requirements, alas, the industry segment of the goal. Having already comprehended the importance of surface roughness and its effect on efficiency the next step is clearly the adequacy of the manufacturing process and value creation chain, thus, yielding an infrastructure optimization to accommodate this new gear surface requirement reality since some current production techniques will undoubtedly be made redundant as they fail to meet requirements.

Understanding of the effect of the several factors hereby discussed on gear efficiency falls in the category of “Goal 12: Responsible Consumption and Production” since it aims to provide all attainable benefits whilst minimizing natural resources utilization. A prime example is the more accurate definition of surface roughness requirements, since all production equipment parameters can be adjusted to increase utilization whilst reducing waste: speeds, cutting depths, pre-emptive maintenance, manufacturing deviation within specifications...

By better understanding the relevance of surface roughness and the manufacturing optimization thus reduces material consumption as the input requirements of the gear blanks can be redefined requiring less raw materials; energy and overall work performed.

Finally, Goal 13: Climate Action is present across the entire project. From the manufacturing end of the project, where a reduction in material consumption and energy usage amongst others inherently reduces the carbon footprint and ameliorates the lifecycle assessment of any and all electric driveline transmissions. Furthermore, with the number of electric vehicles set to increase as the CAFE Requirements tighten on OEMs and combustion engines are left behind, any efficiency increase through the entire power delivery chain not only would increase the drivable range of vehicles but would also reduce wasted energy and thus reduce energy desideratum and associated undesirable climatic side effects as energy production is still not 100% renewable, thus, every time an electric vehicle is recharged, new CO₂ is released, although less than with and ICE.

8. Conclusions

Going back to the starting research questions, all have been answered in a satisfactory manner both the primary research question and the secondary questions.

What is the relationship between the surface and performance (scuffing and efficiency) of a gear mesh?

The model built in MATLAB can accurately predict the efficiency of a pair of meshing gears and compute the correlation between surface roughness and performance (energy lost upon plastic deformation for instance). The model also included the effect of lubricant pressure fields, thermal effects, sliding and rolling losses... Windage and churning were also considered although they were ultimately discarded due to the low accuracy of the models and these effects not being strictly meshing-related.

What are the lubrication mechanisms for a given lubricant and can it be accurately predicted?

Based on the aforementioned lubrication theory, ideally, all gears should work under EHL (elastohydrodynamic lubrication), however, that is not always the case, as such, several theories, parameters and approximations have been proposed throughout the years, with the most accurate being Λ^* . Said approximation was built into the model and it seems to correlate with the existing literature (based on the results). Furthermore, the full effects of the lubricant were linearly approximated by the load-loss-dependent coefficient, which is far from ideal. To fully understand the effects of each type of lubricant on gear meshing efficiency a full-fledge lubricant study would be required. A lineal approximation was selected based on the available thermal benchmarking data after several regression models; ANOVA; Regression trees; PCA and Clustering techniques failed to yield accurate or appropriate models.

Can the surface behaviour in different lubrication regimes be accurately modelled?

Surface behaviour in different lubrication regimes could indeed be accurately modelled, from the full separation and even fluid film pressure acting on the surface in EHL to the partial or extended contact in mixed or boundary lubrication.

Can a surface be directly correlated to a small set of surface characterization parameters?

As already discussed, several literature references do suggest the possibility of fully characterizing a surface with merely 2 or 3 parameters. As per this paper's results, it is possible, based on the GPR models with a rotational quadratic kernel to model surfaces based on S_m and R_{max}/R_t (or an Abbot curve or a set of material consolidation parameters) but a lot more data than the one available would be required, to increase the score of the models.

9. Outlook and future work

Clearly, the model can be further improved to accommodate a more accurate temperature module beyond the current one from essentially, adaptations of Fourier's law to better mimic the results of both ROMAX and LDP (commercially available software used in the automotive industry to design, simulate and analyse transmissions).

The model could also be upgraded from a 2D stationary line contact model to a pseudo3D or full 3D by considering the area around the studied contact point (in the case of a pseudo 3D) as every line in the lead direction is considered (with the software running along the profile direction of the gear tooth) or a full 3D by considering the gear flank as a surface body (which would undoubtedly require FEM).

Perhaps is more pressing the software be made transient and implement time-dependent factors directly into both the contact dynamics and specially in the lubrication definitions, as already discussed.

The surface generating model should also be re-trained with heaps of data from a myriad of surface roughness measurements before, during (different stages) and after testing so a more complete picture of how the surface deforms (especially in the first cycles were running-in takes place) and thus it would be able to generate surfaces as they deform and change in real life, helping in the design and understanding of test definition and in turn improve real-life performance of electric transmissions.

Furthermore, a refined powder metal gears module should be implemented to allow for further R&D efforts to study their applications in future transmissions, reducing material usage and associated environmental impacts.

The modular nature of the model allows for further developments and introduction of additional functions such as NVH evaluation.

10. References

- Abraham, R. M. (2014). *AN EXPERIMENTAL STUDY OF SCUFFING PERFORMANCE OF A HELICAL GEAR PAIR SUBJECTED TO DIFFERENT LUBRICATION METHODS*. Columbus: Ohio State University.
- al, G.-E. e. (2018). Prediction of micropitting damage in gear teeth contacts considering the concurrent effects of surface fatigue and mild wear. *Wear*, 398-399, pages 99-115.
- al, H. e. (2007). Prediction of Mechanical Efficiency of Parallel-Axis Gear Pairs. *Journal of Mechanical Engineering* 129, 58-68.
- al, I. G. (2014). Generative Adversarial Nets. *Proceedings of the International Conference on Neural Information Processing Systems* (pp. 2672-2680). Montréal: International Conference on Neural Information Processing Systems.
- al, J. S. (2014). The Effect of Tip Size on the Measured Ra of Surface Roughness Specimens with Rectangular Profiles. *Precision Engineering*, 38 (1):217-220.
- al, M. N. (2020). Oil distribution and churning losses of gearboxes: Experimental and numerical analysis. *Tribology International* 106496, 151:1-9.
- al, N. B. (2022, 05 03). *Gear Solutions*. Retrieved from Heat treat processes for gears: <https://gearsolutions.com/features/heat-treat-processes-for-gears/>
- al, P. K. (2021). Grinding and fine finishing of future automotive powertrain components. *CIRP Annals*, 70:2:589-610.
- al, P. M. (2021, 04 15). *Gear Solutions*. Retrieved from Predicting Gear Sliding Losses: <https://gearsolutions.com/features/predicting-gear-sliding-losses/>
- al, S. W. (1991). A Frictional Model of Partial-EHL Contacts and its Applications to Power Loss in Spur Gears. *Tribology Transactions* 34, 398-407.
- al, T. P.-J. (2008). An Experimental Investigation of Spur Gear Efficiency. *Journal of Mechanical Design* 130, 1-10.
- al, Y. D. (2004). Windage Losses in High-Speed Gears. Preliminary Experimental and Theoretical Results. *Journal of Mechanical Design*, 126(5):903-908.
- Alfredsson, C.-M. E. (2020). The influence of gear surface roughness on rolling contact fatigue under thermal elastohydrodynamic lubrication with slip. *Tribology International*, 151: 106394.
- Anisetti, S. L. (2016). On the flash temperature of gear contacts under the tribo-dynamic condition. *Tribology International*, 97:6-13.
- Apex Dynamics. (2022, 05 02). *ApexDyna*. Retrieved from GEAR HISTORY – WHERE DO GEARBOXES ORIGINATE?: <https://www.apexdyna.nl/en/gear-history>
- AZO Optics. (2017, 03 22). *AZO Optics*. Retrieved from The Basics of White Light Interferometry: <https://www.azooptics.com/Article.aspx?ArticleID=1204>
- Bergseth, E. (2012). *On tribological design in gear tooth contacts*. Stockholm: Royal Institute of Technology.
- Bergstedt, E. (2021). *A comparative Investigation if Gear Performance Between Wrought and Sintered Powder Metallurgical Steel*. Stockholm: KTH Royal Institute if Technology.
- Björklund, S. (1995). *Elastic contacts between rough surfaces*. Stockholm: KTH.

10. References

- Bodycote. (2019). *Bodycote*. Retrieved from Austempering: <https://www.bodycote.com/services/heat-treatment/hardening-and-tempering/austempering/>
- Bronlee, J. (2021, 01 18). *Machine Learning Mastery*. Retrieved from How to Develop a Wasserstein Generative Adversarial Network (WGAN) From Scratch: <https://machinelearningmastery.com/how-to-code-a-wasserstein-generative-adversarial-network-wgan-from-scratch/>
- Brownlee, D. J. (2019, 07 17). *Machine Learning Mastery*. Retrieved from A Gentle Introduction to Generative Adversarial Networks (GANs): <https://machinelearningmastery.com/what-are-generative-adversarial-networks-gans/>
- Brownlee, D. J. (2019, 07 19). *Machine Learning Mastery*. Retrieved from A Gentle Introduction to Generative Adversarial Networks (GANs): <https://machinelearningmastery.com/what-are-generative-adversarial-networks-gans/>
- Bruno Nicenboim, D. S. (2022, 02 21). *An Introduction to Bayesian Data Analysis for Cognitive Science*. Retrieved from 1.7 An important concept: The marginal likelihood (integrating out a parameter): <https://vasishth.github.io/bayescogsci/book/sec-marginal.html>
- Chapter 2: Overall Methodology. (2005). In H. Xu, *DEVELOPMENT OF A GENERALIZED MECHANICAL EFFICIENCY PREDICTION METHODOLOGY FOR GEAR PAIRS* (p. 30). Columbus: Ohio State University.
- Cho, D.-H. L.-G. (2012). Assessment of surface profile data acquired by a stylus profilometer. *Measurement Science and Technology*, 23: 105601.
- C-Therm. (2022, 04 25). *C-Therm*. Retrieved from Thermal Resistance and Thermal Conductance: <https://ctherm.com/resources/helpful-links-tools/thermalresistanceandconductivity/>
- Delta Computer Systems. (2022, 04 28). *RMCTools*. Retrieved from Position PID: https://deltamotion.com/support/webhelp/rmctools/Controller_Features/Control_Modes/Position_PID.htm#:~:text=Position%20PID%20is%20the%20algorithm,Proportional%2C%20Integral%2C%20and%20Differential.
- Diab, Y. (2005). *Analyse des pertes de puissance dans les transmissions par engrenages à grande vitesse. Applications aux réducteurs industriels et aux machines textiles*. Lyon: L'Institut National des Sciences Appliquées de Lyon.
- Dizdar, D. S. (2012). High-Performance Sintered-Steel Gears for Transmissions and Machinery: A Critical Review. *GEARTECHNOLOGY*, 60-65.
- Donges, N. (2021, 07 29). *Builton*. Retrieved from A Guide to RNN: Understanding Recurrent Neural Networks and LSTM Networks: <https://builton.com/data-science/recurrent-neural-networks-and-lstm>
- Espinel, J. (2021, 12 07). *Fictiv*. Retrieved from The 3 essential methods for gear machining: <https://www.fictiv.com/articles/the-3-essential-methods-for-gear-machining>
- European Commission. (2022, 04 25). *European Commission*. Retrieved from CO₂ emission performance standards for cars and vans: https://ec.europa.eu/clima/eu-action/transport-emissions/road-transport-reducing-co2-emissions-vehicles/co2-emission-performance-standards-cars-and-vans_en
- European Powder Metallurgy Association. (2020, 07 01). *EPMA*. Retrieved from Life Cycle Analysis (LCA): <https://www.epma.com/environment-health-quality-and-safety-group/life-cycle-analysis>

10. References

- FGM. (2022, 05 02). *Federal Gear and Machine*. Retrieved from A Short History of Gears and Where Gear Manufacturing Is Today: <https://fg-machine.com/blog/a-short-history-of-gears-and-where-gear-manufacturing-is-today/>
- Flodin, A. (2016). Powder Metal Gear Technology: A Review of the State of the Art. *Power Transmission Engineering*, 38-43.
- Fontanari, V., Molinari, A., & Pahl, M. M. (2019). Tooth Root bending fatigue strength of high-density sintered small-module spur gears: The effect of porosity and microstructure. *Metals*, 9:5:599.
- Frontline Solver. (2022, 05 19). *FrontlineSolver*. Retrieved from Regression Trees: <https://www.solver.com/regression-trees#:~:text=A%20regression%20tree%20is%20built,method%20moves%20up%20each%20branch.>
- Fumo, D. (2017, 08 04). *Towards Data Science*. Retrieved from A Gentle Introduction To Neural Networks Series — Part 1: <https://towardsdatascience.com/a-gentle-introduction-to-neural-networks-series-part-1-2b90b87795bc>
- g, g. (2021, 09 05). *Stack Exchange*. Retrieved from Gaussian Process Regression: Is it possible to determine significance of terms?: <https://stats.stackexchange.com/questions/542211/gaussian-process-regression-is-it-possible-to-determine-significance-of-terms>
- Gears Mechon. (2022, 05 09). *Gears*. Retrieved from Pitting of gears: <https://gearsmechon.wordpress.com/pitting-of-gears/>
- Glinsky, C. (2022, 05 02). *Drivetrain Hub*. Retrieved from Geometry/Involute: <https://drivetrainhub.com/notebooks/gears/geometry/Chapter%201%20-%20Involute.html>
- González-Pérez, V. R.-C. (2021). Investigation of the effect of contact pattern design on the mechanical and thermal behaviors of plastic-steel helical gear drives. *Mechanisms and Machine Theory*, 164:104401.
- Gorla, F. C. (2016). Windage, churning and pocketing power losses of gears: different. *Forsch Ingenieurwe*, 80:85-99.
- Hansen, J. (2021). *Elasto-hydrodynamic film formation in heavily loaded rolling-sliding contacts*. Gothenburg: Lulea University of Technology.
- Hui Long, I.-T. a. (2015). Analytical and Experimental Study of Gear Surface Micropitting due to Variable Loading. *Applied Mechanics and Materials*, 750: 96-103.
- Hui, J. (2018, 06 19). *Jonathan Hui*. Retrieved from GAN — What is Generative Adversarial Networks GAN?: <https://jonathan-hui.medium.com/gan-whats-generative-adversarial-networks-and-its-application-f39ed278ef09>
- IIT Bombay Alumni. (2022, 03 15). Boundary layer basics. Mumbai, Maharashtra, India.
- imbema. (2022, 05 09). *Imbema*. Retrieved from PITTING ON GEARS; HOW DO YOU PREVENT THIS LUBRICATION PROBLEM?: <https://www.imbema.com/en/offshore-maritime-and-process-industry/pitting-on-gears-how-do-you-prevent-this-lubrication-problem/#:~:text=Pitting%20or%20pitting%20corrosion%20on,lots%20of%20heat%20being%20generated.>
- Iordanova, T. (2022, 01 05). *Investopedia*. Retrieved from An Introduction to Non-Stationary Processes: <https://www.investopedia.com/articles/trading/07/stationary.asp>

10. References

- Ishizaki, T., & Nagano, T. I. (2020). Measurement of local thermal contact resistance with a periodic heating method using microscale lock-in thermography. *Review of Scientific Instruments*, 91: 064901.
- ISO. (2001). *ISO/TR 14179-1:2001*. Genève: ISO.
- J. Raja, B. M. (2002). Recent advances in separation of roughness, waviness and form. *Journal of the International Societies for Precision Engineering and Nanotechnology*, 26: 222-235.
- J.C. Vasco, P. B. (2006). Laser micromachining for mould manufacturing: I. The influence of operating parameters. *Assembly in Automation*, 227-234.
- Jamali, H. U., Sharif, K., & Snide, H. E. (2014). Transient EHL analysis of helical gears. *International Gear Conference 2014* (pp. 721-730). Lyon: Elsevier Ltd.
- James. (2020, 06 24). *Stats Exchange*. Retrieved from Linear Regression for Noisy Data: <https://stats.stackexchange.com/questions/473850/linear-regression-for-noisy-data>
- Jeong, M.-S., & Lee, G. M.-K. (2014). Sustainable Production of Helical Gears: Environmental Effects and Product Quality. *International Journal of Precision Engineering and Manufacturing-Green Technology*, 37-41.
- Johnson, K. (1987). *Contact Mechanics*. Cambridge: Cambridge University Press.
- Jonny Hansen, M. B. (2021). A New Film Parameter for Rough Surface EHL Contacts with Anisotropic and Isotropic Structures. *Tribology Letters* 69:37, 1-17.
- José M.C. Azevedo, A. C. (2018). Energy and material efficiency of steel powder metallurgy. *Powder Technology*, 328:329-336.
- Kadiric, P. R. (2019). The influence of side-roll ratio on the extent of micropitting damage in rolling-sliding contacts pertinent to gear applications. *Tribology Letters*, 67:1-20.
- Kadiric, P. R. (2019). The Influence of Slide-Roll Ratio on the Extent of Micropitting Damage in Rolling-Sliding Contacts Pertinent to Gear Applications. *Tribology Letters* 67, 63:1-21.
- Kahraman, S. L. (2021). A scuffing model for spur gear contacts. *Mechanism and Machine Theory*, 156: 104161.
- Kapil Gupta a, R. L. (2015). Recent developments in sustainable manufacturing of gears: a review . *Journal of Cleaner Production* , 3321-3329.
- Kelly, P. (2022). Anisotropic Elasticity. In P. Kelly, *Solid Mechanics Lecture Notes Part I* (pp. 156-166). Auckland: University of Auckland.
- KHK Stock gears. (2022, 05 02). *KHK Gears*. Retrieved from Basic Gear Terminology and Calculation: https://khkgears.net/new/gear_knowledge/abcs_of_gears-b/basic_gear_terminology_calculation.html
- Kianian, B. (2019). *A comparative cost analysis of conventional wrought steel and powder metallurgy (PM) gear manufacturing technologies*. Lund: Department of Mechanical Engineering, Lund University.
- Kianian, B. (2019). Comparing Acquisition and Operation Life Cycle Costs of Powder Metallurgy and Conventional Wrought Steel Gear Manufacturing Techniques. *52nd CIRP Conference on Manufacturing Systems* (pp. 1101-1106). Ljubljana: Elsevier.
- Kianian, B. (2019). Comparing Acquisition and Operation Life Cycle Cost of Powder Metallurgy and Conventional Wrought Steel Gear Manufacturing Techniques. *52nd CIRP Conference on Manufacturing Systems* (pp. 1101-1106). Ljubljana: Procedia.

10. References

- Koenig, J., Hoja, S., Tobie, T., & Stahl, F. H. (2019). Increasing the load carrying capacity of highly loaded gears by nitriding. *6th International BAPT Conference "Power Transmissions 2019"* (p. 287:02001). Borovets: MATEC Web of Conferences.
- Kolivand, S. L. (2020). On the dynamic of a lubricated roller contact. *Mechanism and Machine Theory*, 153:103959.
- Kotthoff, D. G. (2018). NVH Potential of PM Gears for Electrified Drivetrains. *GEARTECHNOLOGY*, 40-43.
- Krömer, M., Sari, D., & Brecher, C. L. (2016). Surface Characteristics of Hobbed Gears. *6th WZL Gear Conference in the USA 2016* (pp. 10:1-6). Aachen: Apprimus Verlag.
- L. Xiao, S. B. (2007). The influence of surface roughness and the contact pressure distribution on friction rolling/sliding contacts. *Tribology international*, 40:4:694-698.
- Li, X. (2016). *Efficiency and wear properties of spur gears made of powder metallurgy materials*. Stockholm: KTH Royal Institute of Technology.
- Lyu, B., Meng, X., & Wen, R. Z. (2021). A deterministic contact evolution and scuffing failure analysis considering lubrication deterioration due to temperature rise under heavy loads. *Engineering failure analysis*, 123: 105276.
- M.M.Khonsari, m. M. (2015). The high pressure rheology of some simple model hydrocarbons. *Tribology International* 82, 228-244.
- Madhusanka, G. (2021, 01 16). *Mech heart*. Retrieved from Gear Manufacturing Process Step by Step: <https://mechheart.com/gear-manufacturing-process-step-by-step/>
- Mallipeddi, D., Norell, M., & Nyborg, M. S. (2019). Influence of running-in on surface characteristics of efficiency tested ground gears. *Tribology International*, 115:45-58.
- Marcello De Bernardi, M. K. (2018). Pseudo-Random Number Generation using Generative Adversarial Networks. *Nemesis 2018, UrbReas 2018, SoGood 2018, IWAISe 2018, and Green Data Mining 2018* (pp. 1-10). Dublin: Springer International Publishing.
- Mar-Dustrial Sales. (2022, 05 03). *Mar-Dustrial Sales*. Retrieved from How Gears are Hardened for Industrial Machinery: <https://www.mardustrial.com/blog/how-falk-gearbox-gears-are-hardened-for-industrial-machinery-10-24-2011/#:~:text=The%20basic%20procedure%20for%20hardening,in%20greater%20hardness%20and%20strength.>
- Marghalani, H. Y. (2010). Effect of filler particles on surface roughness of experimental composite series. *Journal of applied oral science*, 18 (1):59-67.
- Masse, S. L. (2019). On the flash temperature under the starved lubrication condition of a line Contact. *Tribology International*, 136: 173-181.
- Materion Bursh Performance Alloys. (2012). Yield Strength and Other Near-Elastic Properties. *Technical Tidbits Issue 47*, 1-2.
- MathWorks. (2021, 08 19). *Youtube*. Retrieved from Machine Learning Basics | MATLAB's Best Model with Heather Gorr: <https://www.youtube.com/watch?v=Wf2N2Glc2ls>
- Matk Devlin, T. a. (2006). Influence of Surface Roughness on Gear Pitting Behavior. *Gear Technology*, 3:30-38.
- Mauz, W. (1987). *Hydraulische Verluste von Strinradgetrieben bei*. Stuttgart: IMK.
- Michaud, M. (2015). Roughness measurement: Optical vs. contact stylus profilometry. *Materials Matter*, 22-24.

- Mittal, A. (2019, 10 12). *Medium*. Retrieved from Understanding RNN and LSTM: <https://aditi-mittal.medium.com/understanding-rnn-and-lstm-f7cdf6dfc14e>
- Myunster, Y. M. (2002). Determination of power losses in gear transmissions with rolling and slidding friction incorporated. *Mechanisms and Machine Theory*, 37: 167-174.
- Nagarajan, D. W. (2007). A New View of Automatic Relevance Determination. In J. Platt, D. Koller, & Y. S. Roweis, *Advances in Neural Information Processing Systems 20 (NIPS 2007)* (p. 1735). Red Hook: Curran Associates, Inc.
- nanoScience Instruments. (2022, 04 28). *nanoScience Instruments*. Retrieved from White Light Interferometry: <https://www.nanoscience.com/techniques/optical-profilometry/white-light-interferometry/>
- Nave, R. (2022, 04 28). *HyperPhysics*. Retrieved from Reflection Phase Change: <http://hyperphysics.phy-astr.gsu.edu/hbase/phyopt/interf.html#c2>
- NHTSA. (2022, 04 25). *NHTSA*. Retrieved from Corporate Average Fuel Economy: <https://www.nhtsa.gov/laws-regulations/corporate-average-fuel-economy#:~:text=The%20final%20rule%20establishes%20standards,annually%20for%20model%20year%202026.>
- Nocedal, D. C. (1989). On the limited memory BFGS method for large scale optimization. *Mathematical Programming*, 45: 503-528.
- Noco. (2020, 05). *stats Exchange*. Retrieved from {Squared exponential kernel with Manhattan distance does not result in positive semi-definite matrix: <https://math.stackexchange.com/questions/3660546/squared-exponential-kernel-with-manhattan-distance-does-not-result-in-positive-s>
- Nosko, O. B. (2017). Power losses of gear systems. *Problem of Friction and Wear*, 107-116.
- ofer-a. (2022, 01 17). *Stack Exchange*. Retrieved from In the most basic sense, what is marginal likelihood?: <https://stats.stackexchange.com/questions/519422/in-the-most-basic-sense-what-is-marginal-likelihood>
- Ohlendorf, H. (1962). *Verlustleistung und Erwärmung von Stirnrädern*. München: TU München.
- Optimization Geeks. (2021, 10 31). *Youtube*. Retrieved from Easy introduction to gaussian process regression (uncertainty models): <https://www.youtube.com/watch?v=iDzaoEwd0N0>
- Pandurangi, A. B. (2020). *Electric Transmission System efficiency Simulation*. Gothenburg: Chalmer's University of Technology.
- Rackov, M., Veres, M., & Kuzmanovic, Z. K. (2013). HCR Gearing and Optimization of Its Geometry. *Advanced Materials Research*, 633:117-132.
- Rathi, D. T. (2013). A Review On Internal Gear Honing. *International Journal of Engineering Research & Technology*, 2:5: 973-983.
- Reynolds, O. (1886). *On the Theory of Lubrication and Its Application to Mr. Beauchamp Tower's Experiments, Including an Experimental Determination of the Viscosity of Olive Oil*. London: Royal Society of London.
- Richter, W. (1964). *Stirnradgetriebe Zahnreibung*. Braunschweig: Braunschweig Vieweg.
- Rocca, J. (2019, 01 07). *Towards Data Science*. Retrieved from Understanding Generative Adversarial Networks (GANs): <https://towardsdatascience.com/understanding-generative-adversarial-networks-gans-cd6e4651a29>

10. References

- Roelants, P. (2022, 04 29). *My Notes*. Retrieved from Gaussian processes (3/3) - exploring kernels: <https://peterroelants.github.io/posts/gaussian-process-kernels/>
- Rowe, W. B. (2014). 18 - Energy Partition and Temperatures. In W. B. Rowe, *Principle of Modern Grinding Technology* (pp. 381-420). Norwich: William Andrew Publishing.
- Rusin, M. (2022, 04 29). *Quora*. Retrieved from In a Gaussian process, what is the intuitive explanation of log-marginal likelihood?: <https://www.quora.com/In-a-Gaussian-process-what-is-the-intuitive-explanation-of-log-marginal-likelihood>
- Santos, D. J. (2022). *A study on surface characterization of gears and the measurement problem*. Győr: Széchenyi István University.
- Schuetz, G. (2021, 01 14). *Modern Machine Shop*. Retrieved from When to Use 2D or 3D Surface Measurement: <https://www.mmsonline.com/articles/when-to-use-2d-or-3d-surface-measurement>
- Scikit learn. (2022, 04 08). *Scikit learn*. Retrieved from Gaussian Processes: https://scikit-learn.org/stable/modules/gaussian_process.html
- Scikit learn. (2022, 04 29). *Scikit learn*. Retrieved from [sklearn.gaussian_process.GaussianProcessRegressor](https://scikit-learn.org/stable/modules/generated/sklearn.gaussian_process.GaussianProcessRegressor.html): https://scikit-learn.org/stable/modules/generated/sklearn.gaussian_process.GaussianProcessRegressor.html
- Scikit-learn*. (2022, 04 29). Retrieved from Gaussian Processes: https://scikit-learn.org/stable/modules/gaussian_process.html
- Seth, N. (2021, 06 01). *Analytics Vidhya*. Retrieved from How does Backward Propagation Work in Neural Networks?: <https://www.analyticsvidhya.com/blog/2021/06/how-does-backward-propagation-work-in-neural-networks/#:~:text=Forward%20Propagation%20is%20the%20way,is%20called%20the%20Backward%20Propagation.>
- Sit, H. (2019, 06 19). *Towards Data Science*. Retrieved from Quick Start to Gaussian Process Regression: [https://towardsdatascience.com/quick-start-to-gaussian-process-regression-36d838810319#:~:text=Gaussian%20process%20regression%20\(GPR\)%20is,uncertainty%20measurements%20on%20the%20predictions.](https://towardsdatascience.com/quick-start-to-gaussian-process-regression-36d838810319#:~:text=Gaussian%20process%20regression%20(GPR)%20is,uncertainty%20measurements%20on%20the%20predictions.)
- Sklenak, S., & Brecher, J. B. (2021). Dry lubricated rolling-sliding contact-operation behavior and calculation of local frictional energy. *Gear Technology*, November/December 2021: 60-67.
- Slogén, M. (2013). *Contact Mechanics in Gears A Computer-Aided Approach for Analyzing Contacts in Spur and Helical Gears*. Gothenburg: Chalmers University, Department of Product and Production Development.
- Snidle, R., Evans, H., & Holmes, M. A. (2004). *Understanding Scuffing and Micropitting of Gears*. Cardiff: NATO.
- Sosa, M. (2017). *Running-in of gears- surface and efficiency transformacion*. Stockholm: KTH.
- Spectrum Metrology. (2017, 07 01). *Spectrum Metrology*. Retrieved from An Introduction to surface roughness measurement: <https://www.spectrum-metrology.co.uk/surface-roughness/theory.php#:~:text=Cut%2Doff%3A%20The%20wavelength%20at,is%20always%20set%20to%20Lc.>
- Spikes, H. (n.d.). *Basics of EHL for practical application*. London: Tribology Group, Department of Mechanical Engineering, Imperial College London.

10. References

- SuperDataScience. (2018, 08 23). *SuperDataScience*. Retrieved from Recurrent Neural Networks (RNN) - The Vanishing Gradient Problem: <https://www.superdatascience.com/blogs/recurrent-neural-networks-rnn-the-vanishing-gradient-problem>
- Swinburne University of Technology. (2022, 04 28). *Cosmos*. Retrieved from Constructive Interference: <https://astronomy.swin.edu.au/cosmos/c/Constructive+Interference#:~:text=Constructive%20interference%20occurs%20when%20the,the%20waves%20would%20be%20aligned.>
- Tasgetiren, K. A. (2004). A study of spur gear pitting formation and life prediction. *Wear*, 257:1167-1175.
- Tengzelius, J. (2000). LIFE CYCLE ASSESSMENT (LCA) OF POWDER METALLURGY. *PM2000* (pp. 1-6). Tokyo: Höganäs.
- Terekhov, A. (1975). Hydraulic losses in gearboxes with oil immersion. *Russian Engineering Journal*, 55:7-11.
- Tim. (2017, 01 17). *Stackexchange*. Retrieved from Understanding the randomness of y in linear regression model: <https://stats.stackexchange.com/questions/256998/understanding-the-randomness-of-y-in-linear-regression-model>
- Tingskog, T. (2018). *Metal AM Vol 2*. Shrewsbury: MetalAM. Retrieved from An introduction to metal powders for AM: Manufacturing processes and properties.
- Tiwari, A., Wang, A., & Persson, M. H. (2019). Contact Mechanics for Solids with Randomly Rough Surfaces and Plasticity. *Lubricants*, 7:90.
- Tomanickova, Z. L. (2007). Choosing the most appropriate mathematical model to approximate the Abbott Curve. *Tribology International*, 40(9):1319-1334.
- Tosic, M. (2019). Model of Thermal EHL Based on Navier-Stokes Equations: Effects of asperities and Extreme Loads. *Lulea University of Technology*, 1-82.
- Tribonet. (2016, 12 11). *Tribonet*. Retrieved from Reynold's Equation-An Overview: <https://www.tribonet.org/wiki/reynolds-equation/>
- UGEARS. (2022, 05 02). *UGEARS*. Retrieved from History of Gears: <https://ugears.online/blogs/news/history-of-gears#:~:text=Gears%20are%20considered%20as%20one,matter%20how%20it%20was%20turned.>
- United Nations. (2022, 05 02). *United Nations Development Program*. Retrieved from What are the Sustainable Development Goals?: https://www.undp.org/sustainable-development-goals?utm_source=EN&utm_medium=GSR&utm_content=US_UNDP_PaidSearch_Brand_English&utm_campaign=CENTRAL&c_src=CENTRAL&c_src2=GSR&gclid=EAIaIQobChMIx5zmm6_A9wIVB28YCh0WPQMKEAAYASAAEgIQ1vD_BwE
- Velex, C. C. (2007). A Model for the Prediction of Churning Losses in Geared Transmissions—Preliminary Results. *Journal of Mechanical Design*, 129:128-133.
- Wang, Y. W. (2013). Stribeck Curves. In Y. W. Wang, *Encyclopedia of Tribology* (pp. 3365-3370). Boston: Springer.
- Wei, J. (2015). A Study of Spur Gear Pitting under EHL Conditions: Theoretical Analysis and Experiments. *Tribology International* 94, 146-154.

10. References

- Williams, D. (2010, 09 21). *Talk Stats*. Retrieved from Is there a non parametric alternative to multiple linear regression?: <http://www.talkstats.com/threads/is-there-a-non-parametric-alternative-to-multiple-linear-regression.13721/>
- Xi-Hui Liang, Z.-L. L. (2017). Spur Gear Tooth Pitting Propagation Assessment Using Model-based analysis. *Chinese journal of mechanical engineering*, 30:1369-1382.
- Zach. (2021, 08 31). *Statology*. Retrieved from How to Interpret Log-Likelihood Values (With Examples): <https://www.statology.org/interpret-log-likelihood/>
- Zhang, Y., & Berhrens, S. F. (2022, 05 02). *Introduction to Mechanisms*. Retrieved from Gears: <https://www.cs.cmu.edu/~rapidproto/mechanisms/chpt7.html>
- Zhou, C., Xing, M., & Hu, H. W. (2021). A novel thermal network model for predicting the contact temperature of contact gears. *International Journal of Thermal Sciences*, 161:106703.